2016

Sediment Transport and Bedform Dynamics in Rip Currents

Thorpe, Antony

RESEARCH DEGREES WITH PLYMOUTH UNIVERSITY

SUSPENDED SEDIMENT TRANSPORT AND BEDFORM DYNAMICS IN A RIP CURRENT

ANTONY THORPE

A thesis submitted to Plymouth University in partial fulfilment for the degree of

DOCTOR OF PHILOSOPHY

School of Marine Science and Engineering
Faculty of Science and Engineering

August 2016

Abstract

Simultaneous *in-situ* measurements of waves, currents, water depth, suspended sediment concentrations and bed profiles were made in a rip channel on Perranporth Beach, Cornwall, UK. Perranporth is a high energy beach (annual offshore H_s = 1.6 m) which is macro-tidal (mean spring range = 6.3 m) and the grain size is medium sand (D_{50} = 0.28 – 0.34 mm). It can be classified as a low tide bar – rip beach and exhibits a relatively flat inter-tidal zone with pronounced rhythmic low tide bar - rip morphology. Data were collected over two field campaigns, totalling 14 tidal cycles and including 27 occurrences of rip currents, in a range of offshore wave heights (H_s = 0.5 – 3 m). The *in-situ* measurements were supplemented with morphological beach surveys. Sediment samples were taken for grain size analysis.

The rip current was found to be tidally modulated. The strongest rip flow (0.7 m/s) occurred at mid to low tide, when waves were breaking on the adjacent bar. Rip flow persisted when the bar had dried out at the lowest tidal elevations. The rip was observed to pulse at a very low frequency (VLF) with a period of 15 - 20 minutes, which was shown to be influenced by wave breaking on the adjacent bar. The rip was completely in-active at high tide.

Bedforms were ubiquitous in the rip channel and occurred at all stages of the tide. Visual observations found bedforms to be orientated shore parallel. When the rip was active, mean bedform length and height was 1.45 m and 0.06 m respectively. The size and position of the bedforms in the nearshore suggested that they were best classified as megaripples. When the rip was not active, the mean bedform length and height was 1.09 m and 0.06 m respectively. In rip conditions, with typical mean offshore flow rates of > 0.3 m/s, the bedforms migrated in an offshore direction at a mean rate of 0.16 cm/min and a maximum rate of 4.6 cm/min. The associated mean bedform sediment transport rate was 0.0020 kg/m/s, with a maximum rate of 0.054 kg/m/s. In the rip, migration rates were correlated with offshore directed mean flow strength. In non-rip conditions, bedform migration was onshore directed with a mean rate of 0.09 cm/min and a maximum rate of = 2.2 cm/min. The associated mean bedform transport rate was 0.0015 kg/m/s, with a maximum rate of = 0.041 kg/m/s. The onshore bedform transport was correlated with incident wave skewness, and was weakly correlated with orbital velocity. Over a tidal cycle, the offshore directed bedform transport was only marginally larger in rip currents than when it was when onshore directed in non-rip conditions.

Sediment suspension in the rip current was shown to be dependent on the presence of waves. Suspended sediment transport was dominated by the mean flux. The mean flux contributed > 70% of total suspended transport on 19 out of the 27 observed rip current occurrences. The net contribution of the oscillatory flux was small compared to the mean flux. Within the oscillatory component, a frequency domain partitioning routine showed that the VLF motion was an important mechanism for driving offshore directed sediment transport. This was balanced by onshore directed sediment transport at incident wave frequency of a similar magnitude. Depth integration showed that the mean total suspended sediment transport was in the range of 0.03 kg/m/s to 0.08 kg/m/s. At high tide, when the rip was inactive suspended sediment transport rates were minimal compared to when the rip was active. Bedform transport was (on average) 6% of the total suspended sediment transport in a rip current.

The new results presented here show that rip currents make an important contribution to offshore directed sediment transport. The magnitudes of transport indicate that future improvements to morphology change models should include rip driven offshore sediment transport.

Acknowledgements

I would like to thank my supervisors, Professor Gerd Masselink and Professor Paul Russell and in particular my Director of Studies, Doctor Jon Miles for their advice support and encouragement throughout the process of this investigation.

The data collection was labour intensive at times and would not have been possible without the assistance of Richard Kenyon and my fellow PhD students, particularly Claire Earlie, Erwin Bergsma, Ellie Woodward, Kit Stokes and Luis Melo de Almeida. Also, a big thanks is due to Peter Ganderton and Megan Sheridan for invaluable support with all technical aspects of the fieldwork involved with this project.

I would also like to acknowledge Tim Scott and Martin Austin who were lead investigators on the Dynamics of Rip Currents and Implication for Beach Safety (DRIBS) project (Grant Ref No: NE/H004262/1). Working alongside this project afforded me many opportunities to collect my own data whilst surrounded by a world class field research team. Martin and Tim were also kind enough to supply some data presented in this study.

On a personal level I would like to thank my Mum and my girlfriend, Jess for helping me keep positive through this process.

I gratefully acknowledge the funding from the Natural Environment Research Council (NERC) for the studentship that made the completion of this investigation possible and for the financial support for the cost of field experiments and the attendance at numerous conferences (Ref No: NE/I528550/1).

AUTHOR'S DECLARATION

At no time during the registration for the degree of Doctor of Philosophy has the author been registered for any other University award.

Work submitted for this research degree at the Plymouth University has not formed part of any other degree either at Plymouth University or at another establishment.

This study was financed with the aid of a studentship form the Natural Environment Research Council.

Relevant scientific seminars and conferences were regularly attended at which work was often presented. The author presented at three internal seminars to fellow PhD students and members of academic staff.

The material in this thesis has been presented at five external conferences:

- Young Coastal Scientist and Engineers (YCSEC) 2011, Liverpool, UK
- Young Coastal Scientist and Engineers (YCSEC) 2012, Bangor, UK
- International Conference on Coastal Engineering (ICCE), 2012, Santander, Spain
- International Coastal Symposium (ICS), 2013, Plymouth, UK
- International Coastal Symposium (ICS), 2014, Durban, South Africa.

The following conference paper has been published:

- Thorpe, A., Miles, J., Masselink, G., Russell, P., Scott, T., Austin, M., 2012. Field Measurements of Bedforms in a Rip Channel on a Macro-tidal Beach. 33rd International Conference on Coastal Engineering, Santander, Spain.

The following refeered journal papers have been published:

- Thorpe, A., Miles, J., Masselink, G., Russell, P., Scott, T., Austin, M., 2013. Suspended sediment transport in rip currents on a macrotidal beach. Journal of Coastal Research. SI, 65, 1880-1885
- Thorpe, A., Miles, J., Masselink, G., Russell, P., 2014. Bedform Dynamics in a Rip Current. Journal of Coastal Research. SI, 66, 700-705
- Miles, J., Thorpe, A., Russell, P., Masselink, G., 2014a. Megaripple dynamics on a dissipative sandy beach. Journal of Coastal Research, 187-192
- Miles, J., Thorpe, A., Russell, P., Masselink, G., 2014b. Observations of bedforms on a dissipative macrotidal beach. Ocean Dynamics, 64, 225-239. 10.1007/s10236-013-0677-2
- Miles, J., Thorpe, A., 2015. Bedform contributions to cross-shore sediment transport on a dissipative beach. Coastal Engineering, 98, 65-77. http://dx.doi.org/10.1016/j.coastaleng.2015.01.007

Word count of main body of thesis: **62,249 (not including bibliography)**

Signed ……..

Date ……

List of Contents

CHAPTER 1: INTRODUCTION……..1

1.1: The Importance of rip currents…..……..…….....1

1.2: Rip Currents and Sediment Transport…..……...…….....2

1.3: Aims and Objectives.....…… ……..…….....3

1.4: Specific Processes Studied……...……...…….....4

1.5: Structure of Thesis…….……...…….……6

CHAPTER 2: LITERATURE REVIEW…….……..8

2.1: Introduction……...…….....8

2.2: Cross-shore Sediment Transport……..…….....8

2.2.1: The effect of undertow on cross-shore sediment transport……..…….....…9

2.2.2: The effect of incident wave processes on cross-shore sediment transport.....10

2.2.3: The effect of different frequency motion on cross-shore sediment transport.....11

2.2.4: The effect of the presence of bedforms on cross-shore sediment transport.....12

2.2.5: Sediment transport in the swash zone…….....…..….....12

2.2.6: Cross-shore sediment transport models…….....12

2.3: Rip Currents.....13

2.3.1: Rip current theory…….....……...13

2.3.2: Rip current morphodynamcis…….....…….....16

2.3.3: Rip current flow dynamics……...……..….....19

2.3.4: Sediment transport in rip currents…….....21

2.4: Bedforms.....23

2.4.1: Bedform classification…….....…….....….24

2.4.2: Wave forced bedforms…...…….....…...24

2.4.3: Current forced bedforms …….....……...26

2.4.4: Bedform measurements in the surfzone and nearshore…...….....…27

2.4.5: Bedforms in rip currents…….....…….....…..29

2.4.6: Bedform sediment transport…….....…….....…...30

CHAPTER 3: METHOD…….....32

3.1: Site description…….....32

3.2: Instrumentation…….....….34

3.2.1: Pressure Transducer (PT)…….....….....34

3.2.2: Acoustic Doppler Velocimeter (ADV)…….....……..35

3.2.3: Optical Backscatter Sensor (OBS)……36
3.2.4: Sand Ripple Profiling (SRP) Sonar……37
3.2.5: Total station……40
3.3: Experiment Techniques……40
3.3.1: Beach surveys……40
3.3.2: GPS drifter data……41
3.3.3: Total station surveys……42
3.3.4: Sediment sampling……42
3.4: Experiment Design……43
3.4.1: SRP trial; Porthtowan, November 2010……44
3.4.2: Full equipment trial; DRIBS 1, Perranporth, May/June 2011……46
3.4.3: Sediment Transport in Rip Currents (STIR) 1; Perranporth, October 2011...49
3.4.4: Sediment Transport in Rip Currents (STIR) 2; Perranporth, April 2011.....51
3.5: Data Processing……54
3.5.1: De-spiking hydrodynamic data……54
3.5.2: OBS calibration……55
3.5.3: Processing SRP data……57
3.6: Data Analysis……58
3.6.1: Spectral analysis……58
3.6.2: Filtering……60
3.6.3: Waves……61
3.6.4: Currents……62
3.6.5: Partitioning of suspended sediment flux……63
3.6.6: Depth integration of suspended sediment flux……64
3.6.7: Bedform parameters ……66

CHAPTER 4: FIELD OBSERVATIONS OF RIP CURRENTS……69
4.1: Introduction……69
4.2: Beach Morphology……69
4.2.1: Beach classification……70
4.2.2: Whole beach scale morphology……72
4.2.3: Individual rip scale morphology……73
4.2.4: Spatial variability of rip flow……74
4.3: Grain Size Analysis……76
4.4: Quantification of Environmental Parameters……77
4.4.1: Offshore wave climate……77

4.4.2: *In-situ* velocity measurements……..……..80
4.4.3: Sensitivity of velocity measurements…….....…..85
4.4.4: Pressure statistics on the bar…….....86
4.5: Rip Current Forcing…….....…….....…..87
4.5.1: Tidal forcing…….....……...87
4.5.2: Forcing by offshore wave climate…….....88
4.5.3: Forcing by nearshore wave activity……..….....……..89
4.5.4: Summmary of flow characteristics ……..….....91
4.6: Rip current pulsing…….....…….....….....93
4.6.1: Identification of Very Low Frequency (VLF) pulsing…….....…..93
4.6.2: Occurrence of Very Low Frequency (VLF) pulsing…….....95
4.6.3: Processes controlling Very Low Frequency (VLF) motions pulsing.....99
4.7: Discussion of Results on Rip Current Dynamics..…….....101
4.8: Summary of Results: Field Observations of Rip Currents....…….....……107

CHAPTER 5: BEDFORM DYNAMICS IN RIP CURRENTS……..…….....110
5.1: Introduction……..…….....110
5.2: Environmental Conditions……..…..…….....110
5.3: Bedform Dimensions…….....112
5.3.1: Bedform dimensions from SRP data…….....……..112
5.3.1: Bedform dimensions from total station transect data…….....…..…..113
5.4: Hydrodynamic Conditions for the Existence of Bedforms…….....…..115
5.4.1: Bedform dimensions as a function of water depth..……...……..115
5.4.2: Bedform dimensions as a function of mean cross-shore flows..…,.....…..115
5.4.3: Bedform dimensions as a function of orbital velocity..……...…..……..116
5.4.4: Bedform dimensions as a function of Froude number and Mobility number.....117
5.4.5: Rate of change of bedform dimensions…...…….…..…..118
5.5: Bedform Classification…….....…..119
5.6: Bedform Migration……,,,,,,,,,,,,,,,,,,,.....….121
5.5.1: Quantification of bedform migration…….....……..……..121
5.5.2: Bedform migration as a function of tidal elevation…..…….....……..121
5.5.3: Bedform migration as a function of mean cross-shore flows…….....122
5.5.4: Bedform migration as a function of incident wave processes..….....……..123
5.5.5: Investigation of the combined forcing of bedform migration..…….....124
5.5.6: A simple predictive model for bedform migration …….....…..125

5.7: Bedform Transport Rate……..…..126
5.8: Discussion of Results on Bedform Dyanmics.....127
5.9: Summary of Results: Bedform Dynamics....…….....133

CHAPTER 6: SUSPENDED SEDIMENT TRANSPORT IN RIPCURRENTS.....136
6.1: Introduction…….....……..136
6.2: Sediment Suspension…….....…..137
6.1.1: An example of suspended sediment concentrations.…….....…..137
6.6.2: Sensitivity of suspended sediment concentration measurements…..….....138
6.6.3: Investigation into sediment suspension processes..……....139
6.3: Mean Flux…….....…..140
6.3.1: An example of mean suspended sediment flux……..…….....140
6.3.2: Mean cross-shore flux as a function of mean cross-shore flows..…….....141
6.3.3: Quantification of mean and oscillatory flux…….....……...142
6.3.4: Total flux as a function of mobility number…….....……..147
6.4: Temporal Variability in Suspended Sediment Transport Dynamics…….....147
6.4.1: Very Low Frequency (VLF) effects on suspended sediment transport dynamics.....147
6.4.2: Infra-gravity (IG) frequency effects on suspended sediment transport dynamics.....154
6.4.3: Gravity (G) frequency effects on suspended sediment transport dynamics.....157
6.5: Quantification of all Suspended Sediment Transport Processes…….....161
6.6: Quantification of Depth Integrated Suspended Sediment Transport...….....168
6.6.1: Justification of depth integration method…….....……168
6.6.2: Quantification of depth integrated suspended sediment flux..…….....…170
6.6.3: Validity of depth integration method…….....……171
6.6.4: Forcing of depth integration sediment transport…….....….172
6.7: Discussion on Rip Current Sediment Transport Dynamics........……..173
6.8: Summary of Results: Suspended Sediment Transport in Rip Currents.......181

CHAPTER 7: INTERPRETATION AND SYNTHESIS…….....……..184
7.1: Introduction…….....……..184
7.2: Summary of Results…….....……..184
7.2.1: Summary of rip current sediment transport results.....184
7.2.2: A comparison between results collected in rip and non-rip conditions.....186
7.3: Context of Results…….....……..187

7.3.1: Wave climate……187

7.3.2: Morphology……190

7.4: Mode of Transport……195

7.4.1: Total suspended sediment transport and bedform transport….196

7.4.2: All modes of suspended sediment transport……197

7.5: Overall Relevance of Results……198

7.6: Limits of Applicability……201

7.6.1: Method……201

7.6.2: Instrumentation……202

7.7: Suggestions for Further Work……203

CHAPTER 8: CONCLUSIONS……209

REFERENCES……203

APPENDIX……223

- Thorpe, A., Miles, J., Masselink, G., Russell, P., Scott, T., Austin, M., 2013. Suspended sediment transport in rip currents on a macrotidal beach. Journal of Coastal Research. SI, 65, 1880-1885

- Thorpe, A., Miles, J., Masselink, G., Russell, P., 2014. Bedform Dynamics in a Rip Current. Journal of Coastal Research. SI, 66, 700-705

- Thorpe, A., Miles, J., Masselink, G., Russell, P., Scott, T., Austin, M., 2012. Field Measurements of Bedforms in a Rip Channel on a Macro-tidal Beach. 33rd International Conference on Coastal Engineering, Santander, Spain.

List of Figures

CHAPTER 1

Figure 1.1: Photo displaying an example rhythmic low tide bar rip morphology captured at low tide.....1

CHAPTER 2

Figure 2.1: Schematic diagram showing rip current forcing as a result of longshore variations in wave height (Komar, 1998).....14

Figure 2.2: An schematic diagram of topographically arrested megarips from Sydney, Australia coast line (Short, 1985) 15

Figure 2.3: Schematic diagram of a rip current showing direction of different flows (Komar, 1998). 16

Figure 2.4: The Relative Tidal Range conceptual model of Masselink and Short (1993).....

.....18

Figure 2.5: Schematic diagram of a bedform in unidirectional flow highlighting nomenclature from (Masselink and Hughes, 2003) 23

Figure 2.6: Stability diagram of current forced bedforms (Southard and Boguchwal, 1990b) 27

CHAPTER 3

Figure 3.1: Map showing the location of the study site within the UK and a panoramic photograph of Perranporth.....33

Figure 3.2: Time-averaged image of Perranporth captured with an ARGUS camera.....34

Figure 3.3: Schematic diagram of Acoustic Doppler Velocimeter head and its key components (SonTek, 2009). 36

Figure 3.4: OBS beam pattern and exploded view of OBS-3 sensor (Downing, 2006) 37

Figure 3.5: Schematic of an SRP showing typical mounting configuration (Marine-Electronics, 2006).....38

Figure 3.6: Map of the inter-tidal area showing surveyed with an GPS-RTK.....41

Figure 3.7: Orientation of bedform measurements made by walking cross-shore transects in the rip channel. The approximate transect measured (solid line) and the instrument frame (red circle) are marked…….....……..…42

Figure 3.8: Photograph showing instrument frame with SRP and data-logger battery pack.....45

Figure 3.9: A 30-minute time-stack of bedform evolution.....45

Figure 3.10: Photograph of instrument frame showing position of instrumentation.....46

Figure 3.11: Contour plot of beach morphology from combined topographic and bathymetric surveys.....47

Figure 3.12: Time-stack of bed evolution and associated hydrodynamics and suspended sediment fluxes 48

Figure 3.13: Photo of instrument frame and the position of instruments.....50

Figure 3.14: Photo of instrument frame and the position of instruments.....52

Figure 3.15: Schematic diagram showing plan view of study area.....54

Figure 3.16: OBS calibration curves with R^2 value displayed for all sensors used in both *STIR 1* and *STIR 2*. 56

Figure 3.17: An example of a bed scan (solid line) with a 1 % Tukey window applied.....57

Figure 3.18: Relationship between *ndf* and multiplication factors.....59

Figure 3.19: Schematic diagram of low-pass, high-pass and band-pass filters. 60

Figure 3.20: An example of rip current identification method.....63

Figure 3.21: Schematic diagram showing the partial method of processing depth integrated suspended sediment transport from point measurements.....64

Figure 3.22: Schematic diagram showing the integrated method of processing depth integrated suspended sediment transport from point measurements.....64

Figure 3.23: Schematic diagram showing methods applied to calculate velocity and concentration profiles.....65

Figure 3.24: Calculation of bedform length and migration rate.....67

CHAPTER 4

Figure 4.1: Time averaged ARGUS image showing quasi-regular bar - rip morphology at low tide at Perranporth.....69

Figure 4.2: Cross-shore beach profiles taken during each of the two collection periods, in spring and autumn.....70

Figure 4.3: Time averaged photos captured with an ARGUS camera during (a) *STIR 1* and *STIR 2*.....71

Figure 4.4: Contour plots showing morphology of Perranporth Beach..... 72

Figure 4.5: Rectified ARGUS images of Perranporth Beach 73

Figure 4.6: Contour plots showing localised morphology of Perranporth beach.....74

Figure 4.7: Longshore profiles through the instrument location.....74

Figure 4.8: Contour plot showing beach morphology and averaged GPS drifter tracks.....75

Figure 4.9: Contour plot showing the location of sediment samples.....76

Figure 4.10: Percentage of sediment retained within each band of the Wentworth scale; (a) mean and (b) individual sub-samples (collected on three consecutive days).....77

Figure 4.11: Offshore wave parameters collected from a DWR buoy during *STIR 1*.....78

Figure 4.12: Offshore wave parameters collected from a DWR buoy during *STIR 2*.....79

Figure 4.13: *In-situ* velocity parameters calculated from 10-minute sections of data collected during *STIR 1*.....81

Figure 4.14: I*n-situ* velocity parameters calculated from 10-minute sections of data during *STIR 2*.....82

Figure 4.15: Vector plot showing direction mean flows throughout each entire tidal cycle (a - f) during *STIR 1*.....83

Figure 4.16: Vector plot showing direction mean flows throughout each entire tidal cycle (a - h) during *STIR 2*.....84

Figure 4.17: Example of a velocity time series and comparison of velocity recorded at 0.45 m and 0.25 m above the bed.....85

Figure 4.18: Summary of pressure statistics measured on the bar crest.....86

Figure 4.19: Local relative wave height (H_s/h) on bar crest as a function of variance.....87

Figure 4.20: Mean cross-shore flow as a function of water depth in the rip channel.....…...88

Figure 4.21: Mean cross-shore velocity as a function of H_o (a & b) and T_p (c & d) during *STIR 1*.....89

Figure 4.22: Mean cross-shore (a, d & e), longshore (b, e & h) and resolved (c, f & i) current velocities in the rip channel.....90

Figure 4.23: A summary of the mechanisms that drive rip flow at different stages of the tide.....92

Figure 4.24: Time series of (a) u and (b) v velocity data showing VLF oscillations with a 2 minute running mean. (c) Power spectral density (PSD) of u and v with 2 non-overlapping windows and 1 overlapping window and (d) with 8 non-overlapping and 4 overlapping windows, a linear axis is used so energy at high frequencies can be visualised. 94

Figure 4.25: From top; Water depth (h), cross-shore (<u>) and longshore (<v>) mean velocity, cross-shore and longshore VLF variance (σ^2), cross-shore and longshore IG variance and cross-shore and longshore G variance for all tides during *STIR 1*. Vertical lines represent the boundary between tides. 97

Figure 4.26: From top; Water depth (h), cross-shore (<u>) and longshore (<v>) mean velocity, cross-shore and longshore VLF variance (σ^2), cross-shore and longshore IG variance and cross-shore and longshore G variance for all tides during *STIR 2.* Vertical lines represent the boundary between tides. 98

Figure 427: VLF variance as a function of mean flows during *STIR 1*.....99

Figure 4.28: VLF variance as a function of mean flows during *STIR 2*.....100

Figure 4.29: Maximum cross-shore VLF velocity variance as a function of offshore wave height.....100

Figure 4.30: Local relative wave height (H_s/h) as a function of cross-shore VLF variance (σ^2). H_s/h = 0.3 is marked, the point at which wave broken was shown to commence.....101

Figure 4.31: Schematic diagram illustrating the coupling of processes occurring in and around a rip system that may influence VLF rip current pulsing.....107

CHAPTER 5

Figure 5.1: 5-minute averaged hydrodynamic parameters.....111

Figure 5.2: Bedform dimensions; (a) length (λ) and (b) height (∆) for all SRP bedform data.....113

Figure 5.3: Cross-shore bed profiles measured with the total station in the rip channel.....114

Figure 5.4: Bedform (a) length (λ) and (b) height (∆) as a function of water depth (*h*).....115

Figure 5.5: Bedform (a) length (λ) and (b) height (∆) as a function of mean cross-shore velocity (<u>*)* 116

Figure 5.6: Bedform length (λ) as a function of (a) Froude number (Fr) and (b) mobility number (Ψ).....117

Figure 5.7: (a & c) Bedform length (λ) and (b & d) height (∆) as function orbital velocities (U_m).....118

Figure 5.8: (a) Rate of change of bed elevation (δΔ/δt) as a function of water depth.....118

Figure 5.9: Bedform observations were classified as (a) anorbital, sub-orbital or orbital following Wiberg and Harris (1994).....119

Figure 5.10: Bed state observations placed in the conceptual model of Boguchwal and Southard (1990) 120

Figure 5.11: (a) Water depth (*h*), (b) mean cross-shore flows (*U*) and (c) migration rates (M_r) for all bedform data collected.....121

Figure 5.12: (a) Migration data (bars) collapsed by re-sampling data in 0.5 m increments of water depth and (b) bedform migration as a function of water depth.....122

Figure 5.13: Bedform migration rate (M_r) as a function of mean cross-shore velocity (*U*) ..... .123

Figure 5.14: Bedform migration (M_r) as a function of (a & b) incident wave skewness (*S*), (c & d) velocity cubed ($<u'^3>$) and (e & f) orbital velocity (U_m).....124

Figure 5.15: Bedform migration rate (cm/min) as a function of cross-shore velocity and wave skewness.....125

Figure 5.16: (a) Model of bedform migration rate based on mean flow, normalised incident wave skewness plotted against measured migration rate and (b) the same model with orbital velocity as an additional forcing component..... 126
.

Figure 5.17: Bedform transport rate calculated from bedform all data. The shaded areas mark periods when the rip current was deemed to be active, the centre line in the shaded area represents the boundary between tides. 127

Figure 5.18: Schematic diagram showing the mechanism for which bedforms migrate upstream (Dumas et al., 2005). 132

CHAPTER 6

Figure 6.1: An example of instantaneous velocity and concentration data.....137

Figure 6.2: Instantaneous suspended sediment concentration data at z = 0.45 and 0.25.....138

Figure 6.3: Factors determining mean suspended sediment concentration (z = 0.25 m) in the rip channel in *STIR 1* and *STIR 2*.....140

Figure 6.4: An example of the contribution of (a) mean flows (<u>) and (b) sediment concentrations (<c>) to (c) mean suspended sediment transport (<uc>).....141

Figure 6.5: Mean sediment transport (<uc>) as a function of mean flows (<uc>) in (a) *STIR 1* and (b) *STIR 2.* 142

Figure 6.6: (a) Mean flux (<uc>), (b) oscillatory flux (<u'c'>) and (c) total flux (<uc> + <u'c'>) during *STIR 1*.....144

Figure 6.7: (a) Mean flux (<uc>), (b) oscillatory flux (<u'c'>) and (c) total flux (<uc> + <u'c'>) during *STIR 2*.....145

Figure 6.8: Percentage contribution to the gross total flux from the mean flux (UC) and oscillatory flux (uc).....146

Figure 6.9: Total transport (<*uc*> + <*u'c'*>) as a function of the mobility number.....147

Figure 6.10: An example of VLF pulsing in the (a) cross-shore velocity time series.....149

Figure 6.11: Closer examination of (a) instantaneous velocity (u) and (b) concentration (c) data.....150

Figure 6.12: (a) Power Spectra Density (PSD) of cross-shore velocity ($m^2/s^2/Hz$) and suspended concentration ($((kg/m^3)^2/Hz$) (b) Co-spectrum, showing direction and magnitude of sediment transport at different frequencies ($kg/m^2/s/Hz$). (c) Coherence spectrum with 95% confidence level marked.....152

Figure 6.13: Example of 68 minute of instantaneous (a) velocity (u) and (b)concentration (*c*) data at high tide when the rip current was inactive..... 153

Figure 6.14: An example of wave groups present in the instantaneous (a) velocity (u) and associated (b) suspended sediment concentrations (*c*) .....154.

Figure 6.15: (a) Power Spectra Density (PSD) of cross-shore velocity ($m^2/s^2/Hz$) and suspended concentration ($((kg/m^3)^2/Hz$) (b) Co-spectrum, showing direction and magnitude of sediment transport at different frequencies ($kg/m^2/s/Hz$). (c) Coherence spectrum with 95% confidence level marked.....156

Figure 6.16: An example of individual waves present in the (a) instantaneous velocity (u) and associated (b) suspended sediment concentrations (*c*).....157

Figure 6.17: (a) Power Spectra Density (PSD) of cross-shore velocity ($m^2/s^2/Hz$) and suspended concentration ($(kg/m^3)^2/Hz$) (b) Co-spectrum, showing direction and magnitude of sediment transport at different frequencies ($kg/m^2/s/Hz$). (c) Coherence spectrum with 95% confidence level marked.....158

Figure 6.18: Auto-correlation between instantaneous velocity (u) and concentration (c) for data.....159

Figure 6.19: Oscillatory suspended transport (<u'c'>) in *STIR 1* (a, c & e) and *STIR 2* (b, d, & e) as a function of (a & b) asymmetry (*Asym*), (c & d) normalised skewness (*S*) and (e & f) un-normalised skewness ($<u^{'3}>$) 160

Figure 6.20: (a) Mean flux (<uc>), (b) VLF flux ($<u'c'>_{VLF}$),(c) IG flux ($<u'c'>_{IG}$) and (d) G ($<u'c'>_{G}$) during *STIR 2*.....162

Figure 6.21: (a) Mean flux (<uc>), (b) VLF flux ($<u'c'>_{VLF}$),(c) IG flux ($<u'c'>_{IG}$) and (d) G ($<u'c'>_{G}$) during *STIR 1*.....163

Figure 6.22: Quantification of suspended sediment transport from the mean flux, the VLF flux, IG flux and G flux for the entire period the rip current was active on the flood and ebb tide during *STIR 1* and *STIR 2*. 164

Figure 6.23: Percentage contribution to total sediment transport from the mean flux, the VLF flux, IG flux and G flux for the entire period the rip current was active on the flood and ebb tide during *STIR 1* and *STIR 2*.....165

Figure 6.24: Correlation of VLF flux ($<u'c'>_{VLF}$) and gravity frequency flux ($<u'c'>_{G}$) transport. ($R^2 = 0.64$).....167
.
Figure 6.25: Oscillatory suspended sediment flux from different modes of transport (mean, VLF IG and G) as a function of mean flows for periods when the rip current was active.....168.

Figure 6.26: Time series of vertical diffusivity (L_s) calculated from sediment concentrations at z = 0.25 m and 0.45 m in *STIR 1*. 169

Figure 6.27: Time series of vertical diffusivity (L_s) calculated from sediment concentrations at z = 0.25 m and 0.45 m in *STIR 2*. 169

Figure 6.28: Time series of depth integrated suspended sediment transport (Q_s) during *STIR 1*.....170
.
Figure 6.29: Time series of depth integrated suspended sediment transport (Q_s) during *STIR 2*.....170

Figure 6.30: Correlation of point measurments of total suspended sediment transport (<UC> + <u'c'>) and depth integrated flux in *STIR 1*.....171

Figure 6.31: Correlation of point measurments of total suspended sediment transport (<UC> + <u'c'>)and depth integrated flux in *STIR 2*.....171

Figure 6.32: (a) Depth integrated suspended sediment flux (Q_s) and (b) mobility number (Ψ) averaged over every period the rip current was active. X-axis refers to rip current number (STIR 1 = 1 to 12, STIR 2 = 14 to 28). (c) Correlation of Q_s and Ψ for data points from observation in *STIR 1* and *STIR 2*. $R^2 = 0.77$. 172

CHAPTER 7

Figure 7.1: Wave height (H_o) and peak period (T_p) for the month preceding and during (a) *STIR 1*, deployment 1, (b) *STIR 1,* deployment 2 and (c) *STIR 2*. 188

Figure 7.2: Offshore wave spectra during *STIR 2* (third deployment), demonstrating the presence of wind sea (6.7 s) and swell component (11.1).....190

Figure 7.3: Dimensionless fall velocity (Ω) the month preceding and during each deployment. 191

Figure 7.4: Four ARGUS images captured each week in the four weeks leading up to each deployment and one ARGUS image during each period of data collection.....194

Figure 7.5: ARGUS images captured at low tide showing low tide morphology at Perranporth during *STIR 1* (October, 2011) and *STIR 2* (April 2013) and for three other years during the same months.....196

Figure 7.6: Bedform transport rate (Q_b) for periods when bed scans were collected (indicated by the solid thick line) and depth integrated suspended sediment transport rate (Q_s) for the entire study period.....199

List of Tables

CHAPTER 2

Table 2.1: Beach classification.....17

CHAPTER 3

Table 3.1: Total SRP footprint size and horizontal resolution.....39

Table 3.2: Instrument heights relative to the bed level at the beginning of the first deployment in *STIR 1*.....51

Table 3.3: Instrument heights relative to the bed level at the beginning of the deployment in *STIR 2*.....53

Table 3.4: R^2 values of OBS calibration.....56

CHAPTER 4

Table 4.1: Summary of beach classification model outputs during *STIR 1* and *STIR 2*.....71

Table 4.2: Grain size analysis results.....77

Table 4.3: Summary of offshore wave parameters during *STIR 1*.....78

Table 4.4: Summary of offshore wave parameters during *STIR 2*.....79

Table 4.5: Environmental conditions for each 68 minute section of data of a rip current with VLF pulsing and at high tide when pulsing was absent.....93

Table 4.6: Boundaries for frequency bands (in Hz and Seconds) used in spectral analysis.....95

CHAPTER 5

Table 5.1: Bedform dimension statistics for rip and non-rip conditions.....113

Table 5.2: Bedform lengths and heights from cross-shore total station survey.....114

Table 5.3: Summary of field measurements of bedforms in the rip currents, the surf zone and for comparison uni-directional flow.....130

Table 5.4: Bedform height, migration rate and transport rate compared to work by other authors.....133

CHAPTER 6

Table 6.1: Hydrodynamic parameters for examples highlighting the effect of VLF motions on suspended sediment dynamics.....148

Table 6.2: Suspended sediment transport fluxes from different modes of suspended sediment transport each example.....153

Table 6.3: Hydrodynamic parameters for example time series presented in Figure 6.9.....154

Table 6.4: Hydrodynamic parameters for example time series presented in Figure 6.12.....157

Table 6.5: R^2 values for the correlation of point measurements of suspended sediment and depth integrated flux.....172

Table 6.13: Comparison of depth integrated suspended sediment transport at different locations within the nearshore.....180

CHAPTER 7

Table 7.1: Direction and relative contribution to sediment transport in a rip current from all modes of transport.....185

Table 7.2: A comparison of offshore wave height(H_o) and peak period (T_p) during, and prior to the experiment.....188

Table 7.3: A comparison of dimensionless fall velocity (Ω) during, and prior to the experiment and the historical average for the month of the deployment.....192

Table 7.4: Summary of sea conditions for the peak period and significant wave height from the wave spectra example.....193

Table 7.5: Mean and maximum Q_b and Q_s during all periods the rip current was active and when bed data were collected.....

Table 7.6: Hydrodynamics of rip conditions on the flood tide of Tide 3, *STIR 1*.....198

Table 7.7: Percentage contribution to (net) total sediment transport from mean transport, oscillatory transport and bedform transport for rip current data from the flood of Tide 3, *STIR 1*.....198

Table 7.8: Percentage contribution to (gross) total sediment transport from mean transport, VLF, IG, G frequency transport and bedform transport.....198

Table 7.8: A comparison of mass onshore and offshore sediment transport (kg/s) at low tide Perranporth calculated by multiplying literature values of depth integrated suspended sediment and measurements made in this study with mean bar width and mean rip channel width.....200

List of Symbols

< >	- time averaged
a_b	- breaker amplitude ($H_b/2$)
accel	- velocity acceleration
Asym	- velocity asymmetry
c	- instantaneous sediment concentration
<c>	- mean sediment concentration
c’	- de-trended sediment concentration
CI	- confidence limit
D	- grain diameter
d_o	- orbital diameter
DWR	- directional wave rider buoy
f	- frequency
Fr	- Froude number
F_w	- wave friction factor
g	- gravitational constant (9.81 m/s^2)
G	- gravity
D_{50}	- median grain size
h	- water depth
H	- wave height
h_{bar}	- water depth over the bar
h_{rip}	- water depth in the rip
H_{10}	- average height of the highest 10 % of waves
H_b	- breaker height
H_{max}	- maximum wave height
H_o	- offshore wave height
H_s	- significant wave height
$H_{s\ bar}$	- significant wave height on the bar
H_s/h	- ratio of significant wave height to water depth
HT	- high tide

Hz - frequency, *n*/ per sec

IG - infra-gravity

L_s - vertical diffusivity

LT - low tide

MHWS - mean high water springs

MLWS - mean low water springs

mODN - meters relative to ordnance datum Newlyn

M_r - migration rate of bedforms

MSR - mean spring range

ndf - number of degrees of freedom

N_y - nyqvist frequency

^{o} - degree unit of angle

PSD - power spectral density

Q_b - bedform transport rate (kg/m/s)

Q_s - depth integrated suspended sediment transport rate (kg/m/s)

<r> - resolved velocity

R^2 - goodness of fit parameter in linear regression analysis

R_F - frequency resolution

RTR - relative tidal range

s - specific density (a ratio of water to sand density)

S - normalised velocity skewness

S_w - window size

T - wave period

T_p - peak wave period

t - time interval

Tan β - beach slope

T_p - peak wave period

u - instantaneous cross-shore velocity

<u> - mean cross-shore velocity

<u'> - time averaged oscillatory velocity

u' - de-trended cross-shore velocity

$u'c'$ - instantaneous cross-shore suspended sediment transport

U_{10} - Fastest 10 % of mean cross-shore velocity

$\langle uc \rangle$ - mean cross-shore suspended sediment transport

$\langle u'c' \rangle$ - time averaged instantaneous cross-shore suspended sediment transport

$\langle u'c' \rangle_G$ - time averaged gravity frequency instantaneous cross-shore suspended sediment transport

$\langle u'c' \rangle_{IG}$ - time averaged infra-gravity frequency instantaneous cross-shore suspended sediment transport

$\langle u'c' \rangle_{VLF}$ - time averaged Very Low Frequency instantaneous cross-shore suspended sediment transport

$\langle u'^3 \rangle$ - un-normalised cross-shore velocity skewness

U_m - orbital velocity

U_{rip} - cross-shore rip current velocity

$U_{undertow}$ - cross-shore undertow velocity

VLF - very low frequency

$\langle v \rangle$ - mean longshore velocity

$\langle v' \rangle$ - time averaged longshore velocity

λ - bedform wavelength

z - elevation

Δ - bedform height

δ - change

θ - angle of wave incidence

ξ - surf scaling parameter

ρ_s - sediment density (2650 kg/m^3)

σ^2 - variance

σ - standard deviation

Ψ - mobility number

Ω - dimensionless fall velocity

ω_s - sediment fall velocity

w - radian frequency

CHAPTER 1: INTRODUCTION

1.1 The Importance of Rip Currents

Around half of the world's population is concentrated within 100 km of the coast (Turner and Luisetti, 2015). Beaches offer protection as a natural barrier from the sea and are often considered recreational environments. They are desirable places to live near, attract visitors and can sustain a local tourist industry. In addition to this they offer a physical barrier to the sea, which can protecting against flooding and erosion. This implies that beaches have a social and economic relevance within coastal areas and therefore understanding their dynamics is important.

Rip currents are described as strong uni-directional currents that originate close to the shoreline and flow offshore, dissecting the wave dominated surfzone (Shepard et al., 1941; Bowen, 1969; Cook, 1970; MacMahan et al., 2006). They are of great interest due to their potential to exchange water (Fowler and Dalrymple, 1990) and sediment (Cook, 1970) across the nearshore. They also have important implications for the safety of recreational beach users (Short and Hogan, 1994; Scott et al., 2007; Scott et al., 2009a). Although rip currents can occur in a range of environments, they are particularly important features of intermediate state beaches (Short, 1985; Masselink and Short, 1993). In this setting they are a significant feature of the low tide morphology as they flow offshore through a cross-shore orientated channel that is cut through adjacent sandbars. Rip systems often exhibit a rhythmic pattern (Short, 1985), where they are evenly spaced along the entire length of open coast beaches (Figure 1.1), although rhythmicity is not always present (Turner et al., 2007).

Figure 1.1: Photo displaying an example of rhythmic low tide bar rip morphology captured at low tide. Rip channels can be seen to dissect inter-tidal bars and morphology transcends inter-tidal and sub-tidal zones. Image captured at Whitsand Bay, SE Cornwall in June, 2014.

Much of the coast of Cornwall and Devon in SW England receives high energy wave conditions from the North Atlantic as swell and wind-sea. Scott et al. (2009a) showed that in the summer months, 59% of this stretch of coastline exhibited Low Tide Terrace (LTT) or Low Tide Bar-Rip (LTBR) beach morphology (sub states of the intermediate classification), of which rip currents are an important feature.

The beaches of Cornwall and Devon are macro-tidal with mean spring tidal ranges in excess of 6 m. This plays a significant role in driving beach morphology and rip current dynamics. Generally, the inter-tidal part of the beach is planar and featureless as the large tidal range ensures this area of beach receives only a short period in which the waves and currents are able to shape the morphology. Pronounced bar – rip morphology forms across the low water position, due to the increased duration of tidal stationarity (Scott et al., 2009a). Therefore low tide bar – rip morphology is often a feature of the sub-tidal and seaward part of inter-tidal sections of the beach.

Rip currents have been studied for decades (Shepard et al., 1941; McKenzie, 1958; Cook, 1970; Short and Brander, 1999; Scott et al., 2014). In recent times there has been a considerable effort to improve understanding in order to assist beach managers and improve beach safety (Austin et al., 2012; McCarroll et al., 2014; Scott et al., 2014). In the UK, 71% of incidents recorded by the lifeguard service in 2005 were attributed to rip currents (Scott et al., 2007). The danger posed by rip currents is particularly acute in the SW of England in summer months, due to the large numbers of visitors to the area. The large changes in tidal elevation can catch each users unaware as the rip current becomes active when water depth over the bar reaches a critical level (Austin et al., 2010).

1.2: Rip Currents and Sediment Transport

Sustainable management of the coast relies upon on our ability to model coastal evolution and erosion. There has been increasing concern in recent times about the effects of global warming. This may include beach erosion as a consequence of more severe storms, or more directly with the rising of sea levels. Current estimates of sea level rise, due to thermal expansion and melting of the ice caps, are from between 0.28 to 0.98 m by 2100 depending on emission scenarios (Church et al., 2013). The simple model of Bruun et al. (1962), based on beach elevation and the active cross-shore width of the beach, predicts that beach erosion will increase in direct proportion with sea level rise. Prediction of beach response requires all mechanisms of cross-shore sediment transport (both onshore and offshore) to be quantified and understood. This information can be used to validate models which can predict shoreline change.

The general understanding of cross-shore sediment transport in the nearshore zone is that seaward of the breakpoint transport is predominantly onshore, whilst shoreward of the breakpoint transport is predominantly offshore (Tinker et al., 2009). In high energy conditions, a wider surfzone and strong bed return flow lead to net erosion of sediment as the beach moves towards a dissipative state. In low energy conditions, onshore transport tends to dominate as a result of incident wave processes and the beach undergoes accretion as it moves towards a more reflective state. These processes have been well studied and quantified in a range of conditions in the macro-tidal environments of the UK and abroad (Russell, 1990; Davidson et al., 1993; Russell, 1993; Kroon and Masselink, 2002; Aagaard et al., 2006; Austin et al., 2007; Mariño‐Tapia et al., 2007; Masselink et al., 2007).

Rip currents provide an important contribution to coastal circulation patterns (Masselink and Short, 1993; MacMahan et al., 2006; Austin et al., 2010), but the fundamental processes that link sediment transport in rips to sediment transport and beach erosion remain poorly understood. Initial measurements of sediment transport in rip currents suggest that they have the potential to transport significant amounts of sediment offshore (Aagaard et al., 1997; Brander, 1999b). However, measurements of the processes that drive transport in rips are particularly limited, due to the practical difficulties in making measurements in such a dynamic environment (Aagaard et al., 1997; Greenwood et al., 2013).

In addition, the 1st International Conference on Rip Currents held in Florida, in February 2010, identified sediment transport in rip currents as a major topic in need of international research; this provides the niche for the proposed study (Leatherman and Fletemeyer, 2011).

1.3: Aims and Objectives

The aim of this study is to increase the understanding of rip currents and their contribution to offshore sediment transport and beach erosion. This is achieved through extensive field research campaigns. To focus on this ultimate aim two research questions will be answered:

- Are rip currents a major mechanism for sediment transport?
- What is the dominant mode of sediment transport within a rip system?

To answer these broad research questions a series of objectives have been identified, with the aim to further knowledge on the importance of rip currents as a mode of offshore sediment transport. The objectives are as follows:

- Make new measurements of rip current hydrodynamics, suspended sediment concentrations and bedform dynamics in a rip current.
- Investigate the processes responsible for suspended sediment transport in a rip current.
- Quantify different modes of suspended sediment transport and their relative importance to total suspended sediment transport in a rip current.
- Quantify sediment transport associated with migrating bedforms in a rip current.
- Make a comparison of suspended sediment transport and bedform transport in rip currents.

Resulting from these research questions and objectives the following hypotheses will be addressed:

- Rip currents transport a significant quantity of sediment in 'normal' or equilibrium conditions.
- Due to the strong mean flows the mean suspended flux is the dominant mode of suspended transport in a rip current.
- Offshore migrating bedforms make a significant contribution to total offshore transport of sediment in a rip current.

The first hypothesis suggests that when the beach is in, or close to an equilibrium state in terms of wave energy received, that rip currents will be a significant transporter of sediment. The justification of the second hypothesis is that rip currents are known to exhibit strong mean flows, and therefore it is logical that the flow has the potential to be a significant transporter of sediment. The third hypothesis is commensurate with observations in the nearshore zone of migrating bedforms contributing to the sediment budget (Huntley et al., 1991; Hoekstra et al., 2004; Masselink et al., 2007). However, as the existing understanding of the topic is limited, the research is by nature investigative and the approach is designed to yield a more detailed insight than suggested by simple hypothesis testing. Deeper insight into the processes measured will be obtained by interrogation of the results collected.

1.4: Specific Processes Studied

Broad ideas of the key processes were identified from the literature prior to the planning of the field campaigns. The experiment design targeted the following processes:

- Analysis of flow characteristics and rip current forcing mechanisms relevant to this study site.
- New measurements of the mean and oscillatory (wave) components of suspended sediment flux and investigation of the associated hydrodynamic forcing.
- New measurements of bedform length, height and migration rate in a rip current.
- New measurements of bedform transport rate in a rip current.
- Quantification of total sediment transport and the relative contribution from the suspended load and from the bedform transport rate.

The study went through an evolution in terms of intended outcome of each field campaign. Results presented in this study are from two field campaigns, termed *STIR 1* and *STIR 2* (Sediment Transport in Rip Currents). In addition extensive laboratory tests and two preliminary experiments were carried out. A brief description of each field experiment is as follows:

Preliminary experiment, Porthtowan (North Coast of Cornwall, UK), November 2010

- A Sand Ripple Profiler (SRP), an instrument with an acoustic pencil beam scanner for measuring bed profiles, was trialled to test its performance for measuring bedforms in the nearshore. The results showed that an SRP deployed at approximately 1 m above the bed was able to give bedform dimensions and migration rates in a rip channel.

Full instrument trial, Perranporth (North Coast of Cornwall, UK), June 2011

- The original intention of this experiment was that the measurements would make up part of the data used in this study. The instrumentation was secured to a scaffold frame on the seabed at the approximate mean low water springs (MLWS) position. However, analysis showed that by the time the instruments were sufficiently covered by the flooding tide to record the data the rip current had become inactive. Observations of megaripple dynamics in the surf zone in non-rip conditions were published from this data (Miles et al., 2014a, b; Miles and Thorpe, 2015)

First data collection, Perranporth (North Coast of Cornwall, UK), *STIR 1*, October, 2011

- In order to ensure measurements could be made in a rip current, a mobile frame was constructed that could be carried into a pre-determined active rip current. Data collected included measurements of waves and currents, point measurements of suspended sediment concentration, and scans of the bed

profile. During this field campaign 6 tides of data were recorded and from this 12 occurrences of rip currents were identified in wave heights ranging from 0.5 to 1.5 m.

Second data collection, Perranporth (North Coast of Cornwall, UK), *STIR 2*, April, 2013

- A second intensive field experiment was carried out to provide results from a larger range of conditions. A mobile frame was again deployed but designed in a way that extra velocity and sediment concentration measurements could be made in a vertical orientation. A second SRP was deployed in the cross-shore plane, therefore increasing the footprint of the scan of the bed. During this field campaign 8 tides of data were collected and from this 15 occurrences of rip currents were identified in wave heights ranging from 0.9 to 3 m.

In total this study comprises of 14 tides of data in which 27 occurrences of rip currents were identified. The full instrument trial and *STIR 1* were carried out alongside the NERC (Natural Environment Research Council) DRIBS (Dynamics of Rip Currents and Implications for Beach Safety) project (Austin et al., 2010; Austin et al., 2012; Austin et al., 2014; Scott et al., 2014). DRIBS was a large scale, internationally leading field project, focusing on the hydrodynamics of rip currents, with the findings being disseminated to the Royal National Lifeboat Institution (RNLI) to help improve lifeguarding services. Rip current sediment dynamics were exclusively the remit of this study. However, working alongside the DRIBS project was of benefit to the completion of this study in terms of available infrastructure and expertise in surfzone field work. The final experiment (*STIR 2*) was planned and carried out by the author independently of the DRIBS project.

1.5: Structure of Thesis

In **Chapter 2** a comprehensive review of all relevant literature is given. It is structured so that initially some theory on cross-shore sediment transport is provided. This is followed by sections on rip currents, rip current specific sediment transport and finally bedform dynamics. Gaps in the knowledge relevant to sediment transport in rip currents are identified. **Chapter 3** describes the method. The study site is identified and classified and the instrumentation reviewed. This is followed by a chronological description of each field study showing the evolution of the experiment. The last part of the method is a description of the analysis techniques.

In **Chapter 4** results on rip current dynamics are presented with the purpose of providing a spatial and temporal context of the study site for results presented in subsequent chapters. Surveys and drifter track experiments are described to indicate

the spatial scale of the rip, and to put the measurements in context. Point measurements of hydrodynamics are used to illustrate the temporal variability of rip dynamics. In **Chapter 5** bedform dynamics are quantified and the forcing is investigated by comparing rip with non-rip conditions. Sediment transport associated with migrating bedforms is quantified. **Chapter 6** investigates suspended sediment transport processes and the frequency dependent nature of suspended sediment transport in rip currents. Additionally, suspended sediment transport is quantified.

The results of this study, incorporating observations from the previous three chapters, are drawn together and discussed as a whole in **Chapter 7**. The limits of applicability and suggestions for further work are also discussed here. Finally the conclusions of the investigation and analysis are given in **Chapter 8**.

CHAPTER 2: LITERATURE REVIEW

2.1: Introduction

In this chapter relevant literature relating to sediment transport and bedform dynamics in rip currents is reviewed to provide a background to the project and highlight the gaps in the existing body of knowledge surrounding the topic.

The literature review is made up of three sections. Firstly, a section on cross-shore sediment transport is presented to provide a context for the measurements made in this study and how they fit into the existing knowledge of cross-shore sediment transport on sandy beaches (Section 2.2). The focus of this section is on the processes responsible for cross-shore transport in different hydrodynamic conditions and their relative importance to the overall cross-shore sediment transport budget. The following two sections focus on rip currents and bedform dynamics respectively. The rip current section includes a review of the existing knowledge on rip current forcing, beach morphology associated with rip currents, rip current flow dynamics and finally the existing work on sediment transport in rip currents is summarised (Section 2.3). Measurements of bedform dynamics in rip currents are limited, and for this reason the general theory of both current forced and wave forced bedforms are identified in Section 2.4. This section summarises field studies of bedform dynamics carried out in the nearshore zone and in rip currents. Finally the use of bedform migration as a proxy for sediment transport is explored.

2.2: Cross-shore Sediment Transport

A major focus of nearshore research has been to improve the understanding of sediment dynamics. The spatial scale varies from whole beach morphology to the behaviour of individual grains of sand. Reasonably robust models exist for predicting longshore sediment transport rates; however, the same level of model detail is not reproduced for cross-shore transport, which has a potentially more important role in influencing the beach morphology (Aagaard et al., 2002). The reason for this is because multiple different mechanisms may transport sediment simultaneously in opposing directions (Aagaard and Greenwood, 1994). The mechanisms can broadly be categorised into oscillatory processes and transport resulting from mean flows. Work by Jaffe et al. (1984) demonstrated the co-existence of oscillatory and mean flow driven transport by partitioning the cross-shore velocity *(u)* and the suspended sediment concentration (*c*) into mean and fluctuating components.

Sediment transport and morphology change can also vary on much larger time scales. Masselink et al. (2014) identified multiyear variability in bar dynamics that correlated well with the North Atlantic Oscillation (NAO). Seasonal variability in sediment transport is common in coastal zones in mid to higher latitudes due to the increased occurrence of storms in winter months (Poate et al., 2009; Scott et al., 2011; Masselink et al., 2014). Tidal asymmetry of sediment dynamics has been observed in certain circumstances (Davidson et al., 1993; Masselink and Pattiaratchi, 2000). This has been attributed to the effects of beach de-watering and to a lag between hydrodynamics and bedform alteration (Davidson et al., 1993).

Through field (e.g. Russell and Huntley, 1999) and modelling (e.g. Bailard, 1981) studies, there is now a general consensus on the direction of cross-shore transport and the processes responsible within the near shore zone in a two-dimensional on-offshore frame of reference. Transport tends to occur in opposing cross-shore directions at different cross-shore locations within the nearshore zone (Aagaard and Greenwood, 1994, 1995b; Masselink et al., 2008; Tinker et al., 2009). Within the surfzone, sediment transport is offshore due to undertow near the bed returning sediment seaward and potentially resulting in beach erosion (Elgar et al., 2001). Offshore of the break point sediment transport is onshore due to incident wave skewness and asymmetry (Gallagher et al., 1998b; Elgar et al., 2001; Miles, 2013) which can result in onshore bar migration (Aagaard et al., 2002; Hoefel and Elgar, 2003; Aagaard et al., 2006; Masselink et al., 2007). Morphological response is dependent on the balance between the onshore and offshore sediment transport processes. This in turn is dependent on the hydrodynamic forcing, and to a lesser extent, the grain size and the water depth (Vincent and Osborne, 1995; Miles, 2013).

2.2.1: The effect of undertow on cross-shore sediment transport

In the surfzone, sand is preferentially transported offshore due to the combination of wave stirring (that results in sediment suspension) and offshore directed mean flows as a result of undertow, sometimes referred to as bed return flow (Russell, 1993; Masselink and Black, 1995; Russell and Huntley, 1999). This is a quasi – steady, offshore directed flow near the bed and is a mass balance response to onshore drift associated with shoreward travelling broken waves and the decay of radiation stress (Aagaard et al., 2002).

In high energy, storm conditions beaches tend to undergo erosion due to the large width of the surfzone resulting in a greater portion of the nearshore zone subjected to undertow. The strength of the undertow also increases with increasing wave energy. Aagaard and Greenwood (1995b) measured undertow at 0.34 m/s in a storm, and

concluded that it was a major mechanism for offshore sediment transport. Offshore transport associated with undertow can result in large scale beach erosion, and the offshore migration of bars (Masselink et al., 2008).

2.2.2: The effect of incident wave processes on sediment transport

In the shoaling zone sand is preferentially transported onshore as a result of incident wave skewness (Elgar et al., 2001; Ruessink et al., 2007). Wave skewness is a measure of wave shape. Skewed waves have larger peaks than troughs, and positively skewed waves have a faster, albeit shorter onshore stroke (Miles, 2013) which can result in onshore sediment transport (Gallagher et al., 1998a). As waves move shoreward through the shoaling zone the leading edge steepens and the wave starts to take on a 'saw-tooth' profile, these are called asymmetric waves (Drake and Calantoni, 2001; Elgar et al., 2001; Hoefel and Elgar, 2003; Miles, 2013). Laboratory and field studies have found skewed and asymmetric waves to have the potential to contribute to bedload transport (Gonzalez-Rodriguez and Madsen, 2007), sheet flow sediment transport (Hsu and Hanes, 2004; Nielsen, 2006) and suspended sediment transport (Elgar et al., 2001; Gallagher, 2003; Masselink et al., 2007; Austin et al., 2009). Huntley and Hanes (1987) identified cross-shore acceleration as a mechanism for sediment suspension, similarly Masselink et al. (2007) found enhanced sediment suspension (D_{50} = 0.69 mm) as a result of wave asymmetry.

An important factor in determining the magnitude of suspended sediment transport by incident waves is the phase lag effect between passing waves and sediment settling and re-suspension. This is influenced by the grain size and wave period. Finer grains will remain in suspension longer and require smaller critical velocities for initial suspension and are likely to move further than coarser grains, therefore increasing the potential for increased transport rates (Ruessink et al., 2009). For these reasons Ruessink et al. (2009) suggested that phase lags are the most important factor for sediment transport when the sediment has a D_{50} of < 0.25 mm. During shorter period waves the critical velocity is sustained for a shorter time and therefore suspension and onshore transport is likely to be limited. However, during shorter waves there is less time for sediment settling to occur and therefore sediment can stay in suspension longer. It can be difficult to separate the effects of skewness, asymmetry, and infer the importance of other factors such as wave velocity variance, wave period and grain size on sediment transport dynamics (Miles, 2013).

Sediment transport by incident wave skewness and asymmetry can result in the onshore migration of sub tidal bars in periods of calm conditions or recovery phases (Gallagher et al., 1998b; Elgar et al., 2001; Hoefel and Elgar, 2003). Inter-tidal bars are

thought to migrate onshore due to onshore flow associated with cell circulation in low energy conditions (Aagaard et al., 2006; Masselink et al., 2008). Masselink et al. (2008) observed a maximum threshold for this of wave heights (H) of approximately 1 m. In larger waves cell circulation ceased, this was supported with visual observations that suggested the water circulation pattern went from three-dimensional to two-dimensional.

2.2.3: The effect of different frequency motions on cross-shore sediment transport

Sediment transport dynamics can respond to different hydrodynamic frequency motions ranging from incident wave time scale (gravity) to wave group (or infra-gravity) time scale to very low frequency (VLF) scale, sometimes referred to as far infra-gravity (FIG) (Lippmann et al., 1999).

Hanes and Huntley (1986) found suspended sediment to be well correlated with the passage of individual waves, though the effect of wave groups was also significant and resulted in suspension higher up in the water column. Similarly, Miles et al. (2002) observed suspension to occur at incident wave frequencies, though it was modulated by shear waves at VLF (< 0.004 Hz), meaning suspension was maximised during offshore directed pulses in the velocity. Subsequently a threshold of 0.5 m/s was identified. Aagaard and Greenwood (1995a) also observed sediment suspension at VLF.

The contribution of motion in the infra-gravity band to sediment transport has been found to often be of lesser importance in calmer conditions than mean transport and transport at incident wave timescales (Conley and Beach, 2003). However, in high energy storm conditions it may be an important mechanism for beach erosion (Davidson et al., 1992; Russell, 1993) particularly close to the shoreline as incident waves decay (Butt and Russell, 1999) and on flatter beach morphologies (Miles et al., 2006). Russell (1993) found that strong flows (~ 1 m/s) associated with infra-gravity motion (0.01 Hz) dominated the surfzone and resulted in suspension events of up to 70 g/l lasting 30 to 40 seconds in storm conditions. Co-spectral analysis found that the infra-gravity component of the oscillatory flow, along with a mean offshore directed flow (undertow) was responsible for the erosion of the beach.

Miles et al. (2002) observed offshore directed suspended sediment transport by the offshore travelling part of shear waves (< 0.004 Hz) on the inter-tidal bar of a macro-tidal beach to be an important mechanism for offshore directed sediment transport. This accounted for up to 16% of the total transport and 37% of the oscillatory transport. Aagaard and Greenwood (1995a) also observed suspended sediment transport at VLF

to account for up to 65% of the total flux, again, indicating that transport at VLF can make up a significant portion of total sediment transport.

2.2.4: The effect of the presence of bedforms on cross-shore suspended sediment transport

The presence of bedforms decreases the near-bed velocities due to an increase in friction and thus, results in increases in bed shear stress and vorticity, and therefore leads to greater sediment mixing and a larger volume of suspended sediment in the water column (Van Rijn, 1993; Vincent and Osborne, 1995; Osborne and Vincent, 1996). Bedforms also introduce spatial variability in suspended sediment concentration, with concentrations around 50% higher over crests than troughs (Nielsen, 1986). Wave stirring over bedforms can lead to increased vertical diffusivity, thus resulting in a change in settling times and potentially a change in the phase between settling and velocity (Nielsen, 1992).

The presence of bedforms can result in suspended sediment transport occurring in an offshore direction in onshore propagating waves. Inman and Tunstall (1972) described a mechanism whereby during the onshore stroke of the wave, sediment is carried a small distance onshore close to the bed and becomes trapped in a vortex in the lee of the ripples. As the flow reverses the sediment is ejected into the water column and transported offshore.

2.2.5: Sediment transport in the swash zone

Within the swash zone it is well established that the sediment concentrations and thus sediment transport are more than an order of magnitude larger than elsewhere in the nearshore (Beach and Sternberg, 1991; Miles et al., 2006).

2.2.6: Cross-shore sediment transport models

The commonly applied model of Bailard (1981) is based on the energetics approach of Bagnold (1963). When used to predict sediment transport rates in the nearshore zone the model correctly predicts the direction of cross-shore transport, though measured volumetric beach response shows that it often under predicts transport rates (Gallagher et al., 1998b; Masselink et al., 2008). The original model does not include bore turbulence (Butt et al., 2004b) or exfiltration (Conley and Inman, 1992) for example, which are important for factors in sediment transport prediction. However, improvements to the model, such as the inclusion of flow accelerations (Hoefel and Elgar, 2003) and different friction factors for oscillatory and mean flows (Hsu et al., 2006) have improved model output.

Modern models are multi-functional and are able to provide estimates for a whole range of nearshore processes. For example, XBeach is a numerical model intended to be used to predict natural coastal response to time varying storm and hurricane conditions (Roelvink et al., 2010). However, the practical uses extend beyond predicting storm response (Roelvink et al., 2009), and the model has been used to investigate the hydrodynamics of rip currents (Austin et al., 2012; Castelle et al., 2013) and gravel beaches dynamics (Jamal et al., 2014).

2.3: Rip Currents

Rip currents are strong, narrow jets (Shepard and Inman, 1950; Bowen and Inman, 1969; MacMahan et al., 2005; MacMahan et al., 2006; Austin et al., 2010) that originate close to the shore and flow offshore, dissecting the wave dominated surfzone (Brander, 1999a). They are important mechanisms for surf zone circulation (Austin et al., 2010; MacMahan et al., 2010; Scott et al., 2014), water exchange in the nearshore zone (Fowler and Dalrymple, 1990) and beach morphodynamics (Brander, 1999a; Turner et al., 2007). Rips have also been recognised as a mechanism for the offshore transport of significant volumes of sediment (Cook, 1970; Aagaard et al., 1997; Brander, 1999b; Short and Brander, 1999). The strong offshore flows have implications for beach safety (Short and Hogan, 1994; Scott et al., 2009b; Austin et al., 2010; MacMahan et al., 2010). Specifically, Scott et al. (2007) found that 71% of all recorded incidents on UK beaches during the summer of 2005 were due to rip currents.

Rip position is most often controlled by the beach morphology (Sonu, 1972; Brander, 1999a; Brander and Short, 2000) and modulated by the hydrodynamic conditions. This includes the wave climate (Shepard et al., 1941; Cook, 1970; Aagaard et al., 1997; MacMahan et al., 2006; Austin et al., 2010), the wave period (Austin et al., 2010) and the tidal state, with rip circulation favouring low tide (Aagaard et al., 1997; Brander, 1999a; Short and Brander, 1999; MacMahan et al., 2005; Castelle and Bonneton, 2006; Castelle et al., 2006) which is most pronounced in macro-tidal settings (Austin et al., 2010; Austin et al., 2012; Austin et al., 2014; Scott et al., 2014).

2.3.1 Rip current theory

Rip currents on long, open coast beaches are typically forced by longshore variations in wave height (MacMahan et al., 2006). There have been various mechanisms to explain this, such as wave – wave interaction, either between incident waves and edge waves (Bowen and Inman, 1969) or between interacting incident wave groups (Dalrymple, 1978; Fowler and Dalrymple, 1990). However, in most instances the

longshore variability in wave height is a result of bathymetry, with wave breaking focused on sandbars on open sandy coasts (Short, 1985).

This longshore variation in wave height creates a longshore variation in momentum flux, termed radiation stress (Longuet-Higgins and Stewart, 1964). Larger waves generate set-up/down both inside and outside the surfzone. The shoreline set up gradient drives longshore currents. Outside the surfzone, set down causes a longshore pressure gradient which is balanced by the longshore radiation stress. However, inside the surfzone the longshore gradient in set up results in water flowing from areas of where waves are high to areas where waves are relatively lower (Figure 2.1). At this point longshore flows converge before flowing offshore as a rip current (Bowen, 1969; MacMahan et al., 2006).

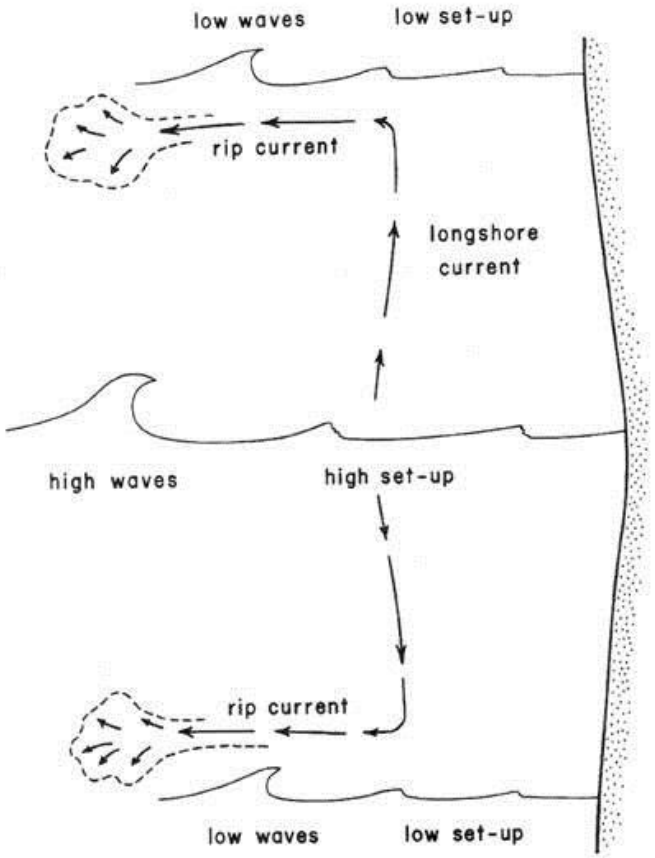

Figure 2.1: Schematic diagram showing rip current forcing as a result of longshore variations in wave height (Komar, 1998).

Rip currents can also form against headlands, where they are driven by wave shadowing (Castelle and Coco, 2012) or by the deflection of a longshore current (Dalrymple et al., 2011). Headland rips may be reinforced by the presence of a rip channel (Castelle and Coco, 2012). In a similar way, rip currents can also form against man-made structures, such as groynes (Pattiaratchi et al., 2009; Scott et al., 2016). Rips can exist in embayed beaches as a result of wave divergence (Wright and Short,

1984) or as a result of longshore deformities in wave height due to wave refraction around headlands and the coastal topography (Short, 1985). Rips in embayed beaches often exist as mega rips in large wave conditions (Figure 2.2) with velocities up to 2-3 m/s, with one or two rip currents draining the whole embayment (Short, 1985). Globally, the most common type of rip currents are those that are controlled by nearshore bathymetry on open coasts (MacMahan et al., 2011). These are the focus of this study, and accordingly the majority of this section will focus on the dynamics of these types of rip currents.

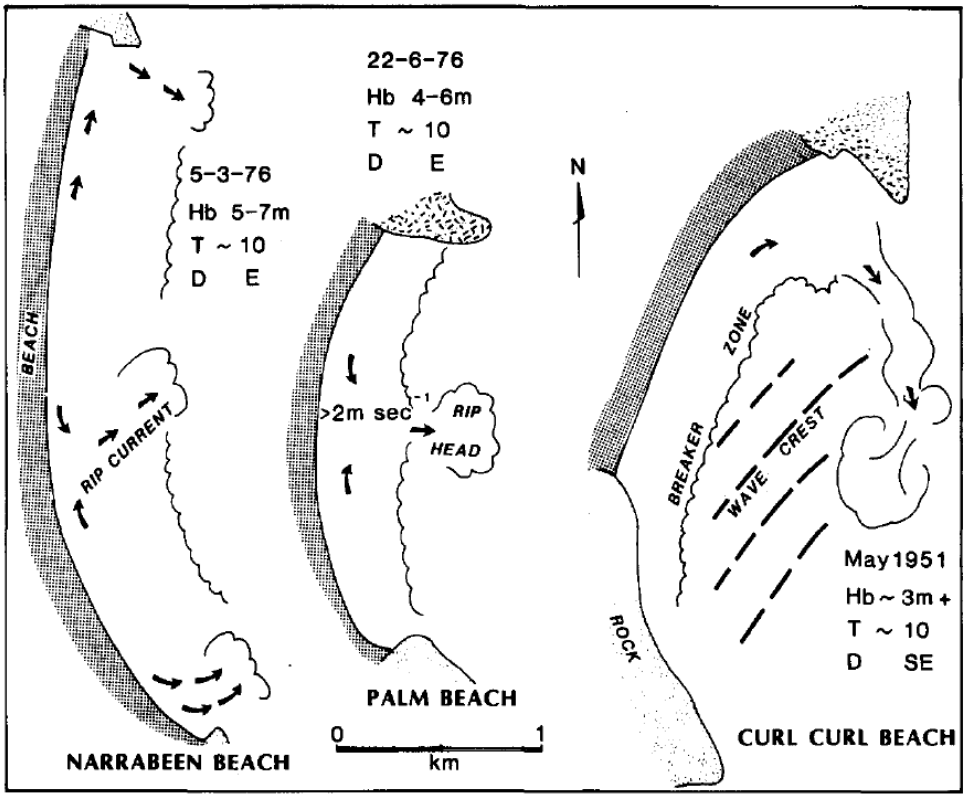

Figure 2.2: A schematic diagram of topographically constrained megarips from Sydney, Australia coast line (Short, 1985).

Wave breaking characteristics play an important role in rip circulation (Shepard et al., 1941; Cook, 1970; Aagaard et al., 1997; MacMahan et al., 2005; Austin et al., 2010), with rip flow strength found to correlate with increasing wave height (Shepard et al., 1941; McKenzie, 1958; Harris et al., 1964; Cook, 1970). Aagaard et al. (1997) identified a threshold for the commencement of rip activity via a ratio of wave height over water depth (H_s/h) of 0.35 within the rip neck. Similarly, Austin et al. (2010) found a good scaling relationship between H_s/h on the bar and rip speed ($R^2 > 0.77$). Harris et al. (1964) and Komar (1998) observed that when angle of wave incidence was large, rips did not form as the flow was longshore dominated. However, when the angle of wave incidence is low rips have been observed to migrate in a longshore direction at rates of between 4 to 18 m/day (MacMahan et al., 2008; Orzech et al., 2010).

Rip currents are also modulated by the tidal level, with rip currents most active at low tide. Castelle et al. (2006) and Bruneau et al. (2009) found rip currents favoured mid to low tide on the French Aquitaine Coast, an area with a meso/macro tidal range (mean spring tidal range = 3.7m). In low waves, Bruneau et al. (2009) observed the rip current stopped flowing at higher tidal elevations, however, in high energy conditions (H_s = 2.5 to 3 m) the rip was active throughout the tide. The likely reason for this is that the larger waves are able to interact with the beach morphology that drives rip flow in deeper water than the smaller waves were able to. On a macro-tidal beach, Austin et al. (2010) observed two stages of rip flow, below mid tide the rip is driven by wave breaking on the bars creating the variation in setup required to drive the rip. However, at spring low tide, the bar completely dries out, but the rip continues to flow. The continued rip flow is attributed to morphological constriction of the flow, a process observed by Brander (1999a) in an accreting rip system.

2.3.2 Rip current morphodynamics

Rips are often observed to be well coupled with beach morphology (Cook, 1970; Aagaard et al., 1997; Brander, 1999a; Austin et al., 2010; MacMahan et al., 2010; Scott et al., 2014) and once formed they are then controlled by the bathymetry (Ranasinghe et al., 2000). Numerous numerical models use bottom topography to drive rip circulation (Noda, 1974; Haller, 1999; Haas et al., 2002; Reniers et al., 2007). Generally a rip system is composed of either one or two feeder channels that run parallel to the shoreline, before converging and flowing offshore in the rip neck. Rip channels may cut through longshore bars (Figure 2.3) or the channel may be skewed with a shore connected shoal on one side of the rip and a dominant feeder channel on the other side (MacMahan et al., 2006).

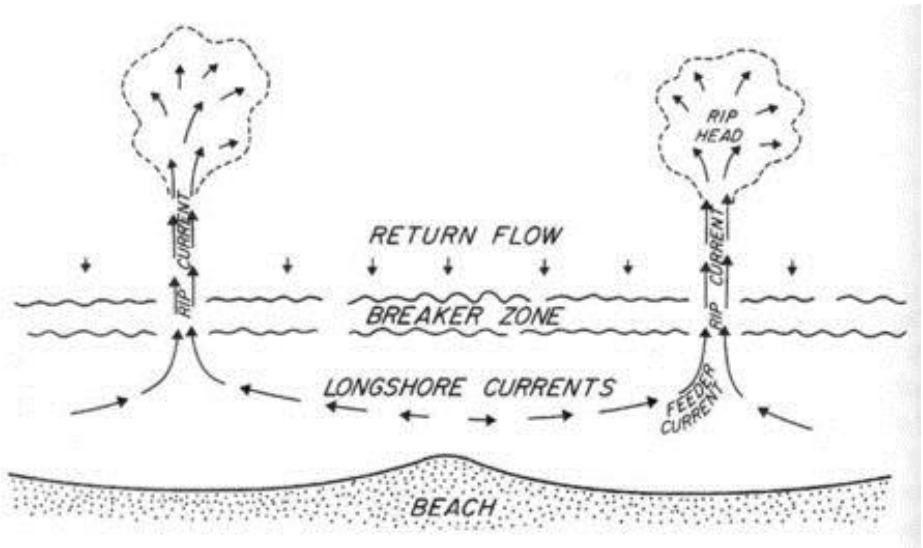

Figure 2.3: Schematic diagram of a rip current showing direction of different flows (Komar, 1998).

Morphologically controlled rips on open costs are typically found on intermediate state beaches that are characterised by a three-dimensional profile, where waves are focused on the sandbars and away from the channels that separate them, thus creating the variation in longshore wave height to drive rip flows (Bowen, 1969). Intermediate beaches are made up of four sub states, which can be classified using the breaker height (H_b), period (T) and sediment fall velocity (w_s) when combined to give the dimensionless fall velocity (Wright and Short, 1984):

$$\Omega = \frac{H_b}{\mathrm{w}_s T} \tag{2.4}$$

The characteristics of each beach state are described in Table 2.1. This parameter is sensitive to errors as it predicts a beach state based on a temporal and spatial scale that may not be indicative of the longer term wave climate (Anthony, 1998). The classification scheme of Wright and Short (1984), whilst providing a useful frame work, does not account for all types of rip configuration and beach state (Brander, 1999a).

Table 2.1: Beach classification (Wright and Short, 1984)

State	Acronym	Ω	Characteristics
DISSIPATIVE	D	> 5.5	Flat profile, with a wide surf zone, fine sediment.
INTERMEDIATE			
Longshore Bar & Trough	LBT	~ 5	Significant bar-trough relief & steeper beach face compared to dissipative beach.
Rhythmic Bar & Beach	RBB	~ 4	Crescentric bars, maybe dissected by rip currents, rhythmic spacing.
Transverse Bar & Rip	TBR	~ 3	Strongest rip circulations of all states. Longshore profile alternates between dissipative bars and fast flowing rips.
Low Tide Terrace	LTT	~ 2	Reflective at high tide, deep trough and offshore bar, small weak irregular rips.
REFLECTIVE	R	< 1.5	Steep beach, typical of coarser grained sediment, waves surge rather than break, berm present.

The Wright and Short (1984) model has been adapted and modified to develop conceptual models for other study areas or conditions. Brander (1999a) developed a model of rip configuration from observations during a field study in a decreasing energy environment. In a down state (LBT > LTT), accretionary trend the model described a decrease in the cross-sectional area of the channel and the creation of a rip head bar. Initially, constraining the flow in a narrower channel may accelerate rip flow, but as this leads to a change in wave dissipation patterns, infilling of the rip channel may occur.

Davis Jr (1985) suggested that changes in tidal elevations play an important role in beach morphology by altering the period of time a section of beach is exposed to waves. During a tidal cycle the position of the swash zone, surfzone and shoaling zone is shifted and therefore the same section of beach is subject to a range of processes (Masselink and Short, 1993). It is reasonable to assume that the morphology of macro-tidal beaches will be affected most by the tide. Masselink and Short (1993) developed a conceptual model (Figure 2.4) that was applicable to macro-tidal environments, which put the classifications of Wright and Short (1984) in context of the Relative Tidal Range (RTR = MSR/H_b). This is achieved by combining wave height and mean spring tidal range (MSR) into a single dimensionless value (RTR). The applicability of the parameter was calibrated with field data and data reported in other literature.

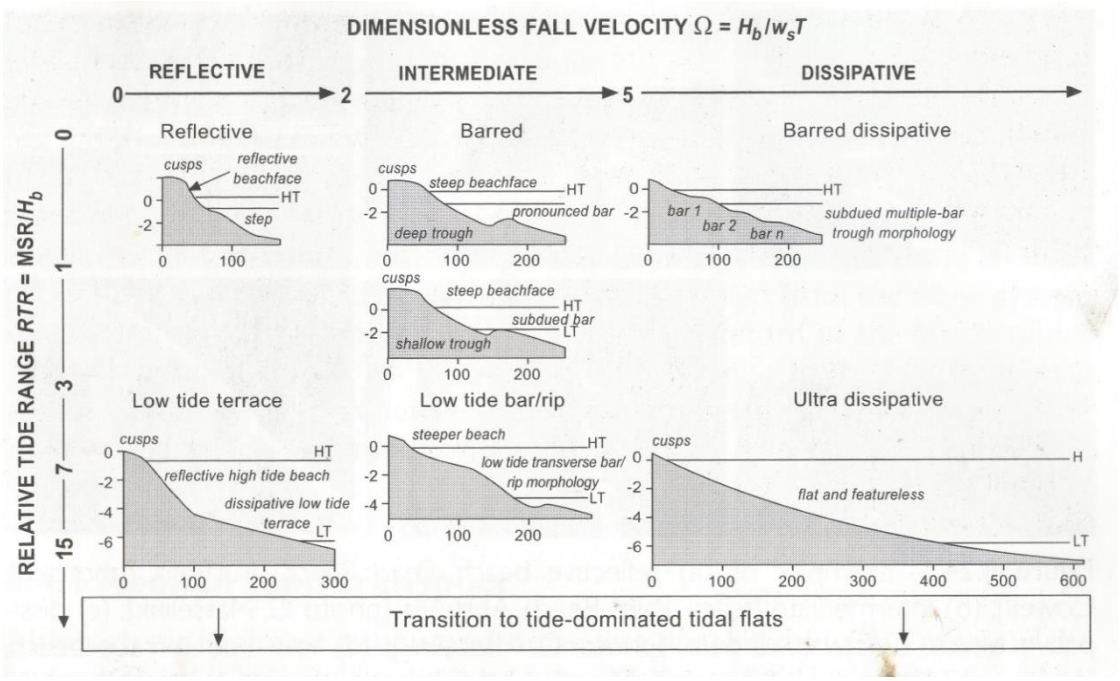

Figure 2.4: The Relative Tidal Range (RTR) conceptual model of Masselink and Short (1993).

Beaches will have a theoretical modal state based on the dominant wave climate and its sediment properties, but will move between erosional and accretionary phases depending on short term changes in the wave climate (Short, 1985). McKenzie (1958)

and Cook (1970) suggested that rips were a result of storm induced bathymetry. Various conceptual models (Short, 1985; Masselink and Short, 1993; Brander, 1999a) contradict this, stating that in storm conditions beaches become flat and featureless as the beach morphology may undergo a reset (Thornton et al., 2007), moving towards a fully dissipative state (Short, 1985). On the macro-tidal coastline of North Cornwall in the UK, beaches have a flat inter-tidal zone and pronounced low tide bar-rip morphology that is generally stable in low energy summer conditions, similar to observations made by Kroon et al. (2003) on the Dutch Coast. However, in high energy conditions, typical of winter months, mass offshore transport maintains the planar inter-tidal beach and leads to the development of offshore parallel bars (Scott et al., 2014). Rips may also disappear through infilling in fair weather conditions. According to Short (1985) sediment exiting the rip will be exceeded by the import of sediment from the adjacent bars in low energy conditions. Brander (1999a) observed the infilling of a rip channel and reduction of cross-sectional area led to an increase in rip velocities as flow was restricted. Sediment transported out of the rip in a transverse bar-rip system is deposited on a rip head bar. Eventually this can become welded to shoreline, and this contributes to a narrowing of the channel. This initiates a feedback mechanism which can maintain the bar-rip morphology as the morphological relief (height of bars versus depth of channel) is maximised, though if low energy conditions persist the flow may be reduced and infilling of the rip system may occur (Brander, 1999a).

Rip currents are often observed to exhibit quasi – regular spacing on open coasts (Short, 1985; MacMahan et al., 2005; Holman et al., 2006; Turner et al., 2007; Orzech et al., 2011) and subsequently have been the subject of much modelling effort (Ranasinghe et al., 2000; Dodd et al., 2003; Reniers et al., 2004b; Orzech et al., 2011). Rip spacing is often said to scale with wave climate (McKenzie, 1958; Bowen and Inman, 1969; Short, 1985; Huntley and Short, 1992; Short and Brander, 1999), surfzone width (Noda, 1974) and the width of the bar crest (Hino, 1974). Short and Brander (1999) found spacing increased with wave energy, but found no explanation of why differences exist between beaches. An alternative mechanism for rip spacing is that it is a controlled by the antecedent morphology (Holman et al., 2006; Turner et al., 2007) and not the wave climate, thus rip spacing is not always regular (Turner et al., 2007).

2.3.3 Rip current flow dynamics

Typical velocities in low energy rip currents range from 0.3 to 0.8 m/s (Bowman et al., 1989; Kraus et al., 1989; Sherman et al., 1993; Aagaard et al., 1997; Brander, 2001; MacMahan et al., 2005; Bruneau et al., 2009; Austin et al., 2010; Austin et al., 2014;

Scott et al., 2014). In a high energy environment (where H_s > 2.5 m, T_p = 10 – 15) Brander and Short (2000) measured velocities in excess of 1 m/s.

Spatially, rip current flows exhibit a circulation pattern in which water that comes onshore over the bar, travels longshore in the feeder channel before returning offshore in the rip neck (Harris et al., 1964; Komar, 1998) as seen in Figure 2.3. Circulation patterns have been well studied in recent times using drifters with fitted GPS trackers deployed in the rip system (Castelle et al., 2006; Austin et al., 2010; MacMahan et al., 2010), often with a focus on beach safety (Austin et al., 2010; Austin et al., 2012; Austin et al., 2014; McCarroll et al., 2014; Scott et al., 2014). Eddy cells have been found to be associated with TBR beach states in micro/meso tidal environments (MacMahan et al., 2008) and LTBR and LTTR in macro-tidal areas (Austin et al., 2010). In these conditions drifter behaviour was characterised by rotating within the surfzone and occasionally exiting the surfzone, when offshore directed pulses in the rip flow occurred. As well as beach state, water levels and wave energy are known to be key controls on circulatory patterns. Drifter exit frequency is reduced in larger waves, as material is held within the surfzone (MacMahan et al., 2010) and exits are much more common in low energy conditions (Scott et al., 2014).

The vertical structure of the flow has been found to be depth uniform when the water depth is > 1 m by Bruneau et al. (2009) using acoustic velocity profilers. Brander (1999b) found the fastest velocities occurred at around the middle of the water column. Cook (1970), identified the importance of wind slippage on the water surface. This was also identified by Bruneau et al. (2009) on windy days in the velocity depth profiles**.**

Rip current flows can be partitioned into the mean, infra-gravity and very low frequency components, all of which can contribute significantly to total flow (MacMahan et al., 2006). Infra-gravity pulses in the rip current flow occur on the time scale of wave groups (0.004 to 0.04 Hz) (Shepard et al., 1941; Shepard and Inman, 1950; Aagaard et al., 1997; Brander and Short, 2000). Infra-gravity pulses have been hypothesised to be caused by high set up created as water ponds in the inner surfzone after a wave group. The ponded water is returned offshore through the rip channel and can be observed as a pulse in the rip flow (Munk, 1949; Shepard and Inman, 1950). More recently rip pulses have been found to arise from cross-shore standing infra-gravity waves (MacMahan et al., 2005; Reniers et al., 2007). During the 'RIPEX' experiment (MacMahan et al., 2005) the infra-gravity contribution to the total flow was calculated during a period in which morphological profile changes were minimal. Large longshore differences were observed in the infra-gravity component of the flow and were found to be associated with the bathymetry, with infra-gravity contributions observed to be smaller in the deeper water of the rip channel than on the surrounding bars.

Rip currents have also been observed to exhibit velocity fluctuations at time scales far exceeding that of wave groups time scale (Haller, 1999; Brander and Short, 2000; Haller and Dalrymple, 2001; MacMahan et al., 2004b; Reniers et al., 2007). These fluctuations are usually described as Very Low Frequency (VLF), or occasionally termed Far Infra-Gravity (FIG). The phenomenon of rip current pulsing is regularly attributed to instabilities in the flow field (Smith and Largier, 1995; Haller, 1999; Haller and Dalrymple, 2001; Bruneau et al., 2009). The first documented field observations of VLF oscillations in the nearshore were made by Oltman-Shay et al. (1989) during the Super Duck experiment in North Carolina. They observed regular oscillations of the longshore flow within the surfzone with a period of 200 to 400 s. The occurrence of these oscillations was explained by Bowen and Holman (1989); they proposed that a uniform wave driven longshore current was assumed to develop a small perturbation that was liable to grow causing the longshore current to become unstable, leading to the observed oscillations, which they termed shear waves. Further research on shear waves within the surfzone (Reniers and Battjes, 1997) found that instabilities were more likely to occur on beaches that exhibited longshore bars, than beaches that were more planar. Bruneau et al. (2009) measured rip current oscillations with a velocity of > 1 m/s and a period of 10 to 30 minutes, which was most prevalent when wave breaking occurred over well-developed bars. They also observed lagrangian drifters to be retained in a rip circulation cell 80% of the time, with drifter exits occurring sporadically. This observed drifter behaviour is similar to drifter behaviour in a rip current to that recorded by MacMahan et al. (2005) and Austin et al. (2010); Bruneau et al. (2009) linked the drifter exits to rip current pulsing. Bruneau et al. (2009) also reproduced their results in a numerical model and showed that shear instabilities of the rip current could be solely responsible for drifter exits via a pulsating jet. Similarly, Haller and Dalrymple (2001) also attributed observed rip current pulsing to be a result of shear instabilities of the rip current, with Haller (1999) describing the rip current as a meandering cross-shore current. Smith and Largier (1995) observed rip current pulsing to occur on a timescale of around 15 minutes, they also attributed these instabilities to be features of the longshore flow rather than the rip current itself. Other authors have linked observed VLF rip current pulsing to characteristics of the wave climate. Bonneton et al. (2006) measured pulses in the rip flow with a 27-minute period, they observed an increase in the significance of VLF pulses with increasing wave height and proposed that the pulses may result from wave groups. This is similar to the findings of Callaghan et al. (2005). In a modelling study Reniers et al. (2004a) linked VLF pulsing to a directionally spread incident wave field and suggested VLF oscillations were driven by temporal and spatial variations in wave groups that developed pressure gradients and radiation stresses within the surfzone (Reniers et al., 2007). In numerous field studies

(MacMahan et al., 2004b; Callaghan et al., 2005; MacMahan et al., 2005) it has also been observed that the VLF motion was well coupled with the underlying morphology, this has supported by model results of Reniers et al. (2007).

2.3.4: Sediment transport in rip currents

Rip currents are often described as important mechanisms for the offshore transport of sediment (Shepard et al., 1941; Ingle Jr, 1966; Cook, 1970; Nielsen, 1992; Aagaard et al., 1997; Brander, 1999b; MacMahan et al., 2006). Rip current induced sediment transport has implications for beach erosion (Cook, 1970; Thornton et al., 2007) and beach morphology (Short, 1985; Brander, 1999b).

The first measurements of sediment transport in rip currents were made by Ingle Jr (1966). He used a fluorescent sand tracer released upstream of a rip current (where $<u>$ = 0.34 m/s as a 5-minute mean). The tracer clearly portrayed the influence of the rip on sediment transport, with sand being interrupted as it moved longshore and deflected offshore with the rip flow. Cook (1970) found rip currents offered an important mechanism to transport beach sand to the inner continental shelf and that rips carried sediment of the same size independent of rip strength. Cook (1970) stated that rip channels should be preserved within the geologic record as coarse bands of sediment orientated normal to the paleo-shoreline. Gallagher et al. (2011) found rip channels contained coarser sediment than areas surrounding the rip channel due to finer sediment being preferentially transported offshore.

Ingle Jr (1966) suggested a rip current specific study on sediment dynamics would be worthwhile, and proposed that with sufficient quantities of tracer his method would allow the sedimentary cycle of the rip system to be quantified. Somewhat surprisingly, it was not until relatively recently that any work was done on the transport of sediment in a rip channel. Studies by Aagaard et al. (1997) and Brander (1999b) focus on suspended sediment transport in rip currents, using OBS sensors and sediment traps respectively to quantify sediment transport. Aagaard et al. (1997) and Brander (1999b) found significant volumes of offshore transport occurred at lower tidal elevations when rip flow was strongest. At higher tidal elevations transport was negligible (Brander, 1999b) or weakly onshore (Aagaard et al., 1997).

Using the Shields (1936) parameter, Brander (1999b) found that the combined contribution of waves and currents was sufficient to entrain sediment, as was the contribution from the waves alone. However, in certain instances the Shields value of the currents alone did not exceed the critical Shields value of 0.05 required to suspend beach sand. Furthermore, the combined Shields parameter varied on a temporal and spatial scale. An entrainment maximum occurred in the rip neck at low tide, whilst it

was minimised in the feeder channel at low tide due to the lack of wave breaking as wave energy dissipated on the bars. This observation was reversed at high tide. The implications of this observation are that at low tide when currents are strongest in a feeder channel, sediment transport will be restricted by the lack of wave driven entrainment. In the rip channel, entrainment and flow is maximised around low tide, hence this being the most significant period for sediment transport (Brander, 1999b).

Aagaard et al. (1997) found in a moderate energy environment (H_s = 1.4 m, T_p = 8 s) that pulses in the rip flow within the infra-gravity band were sufficient for suspending sediment when the rip was active at lower tidal elevations. Mean concentrations where 3.9 g/l in, however this increased to 10 to 50 g/l during offshore pulses in the rip flow.

In mean rip current flows of up to 0.52 m/s Brander (1999b) measured suspended sediment fluxes were offshore directed close to the bed and averaged 0.13 kg/m^2/s, and were up to 0.73 kg/m^2/s. The experiment design involved deployment of a vertical array of sediment traps, from this the total depth averaged suspended sediment flux was calculated by interpolating between fluxes measured at 7 sediment traps using the method of Rosati and Kraus (1989). Total transport was found be offshore directed and to average 0.05 kg/m/s with a maximum rate of up to 0.17 kg/m/s. The flux was found to decay exponentially away from the bed with approximately 50% of all transport occurring in the lower 10% of the water column. Brander (1999b) found a relationship between total suspended sediment transport (Q_s) and $<u'^3>$ (R^2 = 0.83), similar to the model of (Bagnold, 1963) and developed the following expression by least squares regression

$$Q = 27.6\,(< u'^3 >) + 0.92 \tag{2.5}$$

Aagaard et al. (1997) made point measurements of concentration at different heights above the bed (z = 0.05 m, 0.1 m and 0.2 m) and velocity at a single position (z = 0.3 m). They found the direction, magnitude and importance of different modes of transport varied cyclically with the tide. At low tide, when the rip was active ($<u>$ = 0.5 m/s) the mean offshore flux was the dominant mode of transport with maximum rates of 0.8 kg/m^2/s. Incident waves played a secondary but an important role in sediment transport. Infra-gravity motion, though important for sediment suspension was only of minor importance for its subsequent transport. At high tide, transport was onshore due to incident wave processes. The results of Aagaard et al. (1997) showed that over an entire tidal cycle the net flux was offshore directed, this ultimately lead to the morphological enhancement of the rip system as sediment flushed from the rip neck maintained the rip channel.

2.4: Bedforms

Bedforms are quasi-steady sedimentary structures (Clifton, 1976) that are often present on erodible beds that are subjected to waves and/or currents (Fredsoe and Deigaard, 1993). Bedform dynamics (crest pattern, dimensions and migration behaviour) are principally governed by the flow characteristics. They have a large range of size and shape, ranging from ripples with a length of a few tens of centimetres to bars and sand waves with lengths of tens of meters (Masselink and Hughes, 2003). The nomenclature of bedforms in a unidirectional environment is shown in Figure 2.5.

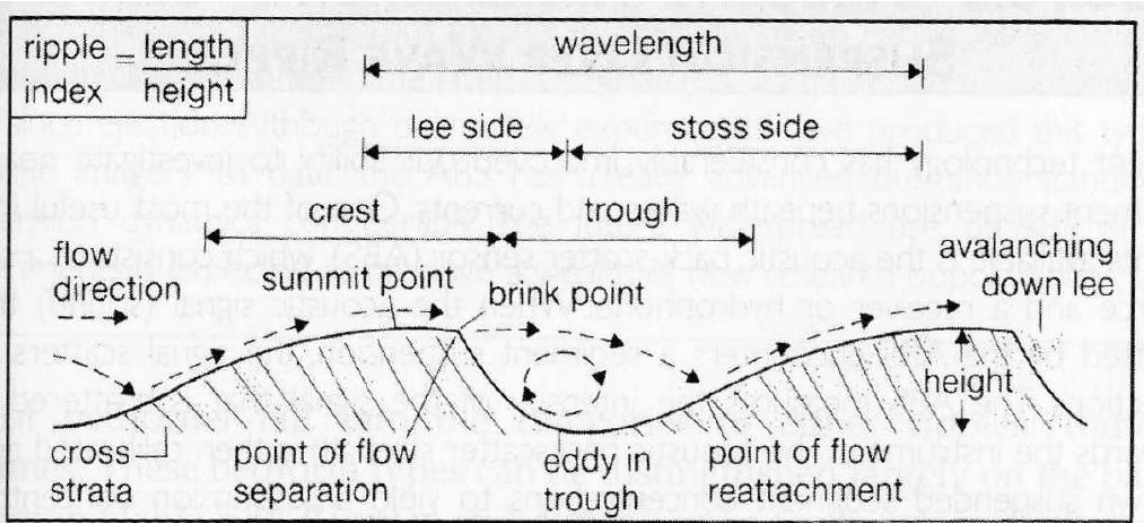

Figure 2.5: Schematic diagram of a bedform in unidirectional flow highlighting nomenclature, from Masselink and Hughes (2003).

Bedforms are important features of the nearshore zone. They introduce bed roughness which has the effect of modifying the flow, reducing the energy in the waves and currents, and in turn affecting suspended sediment transport dynamics, as the bottom boundary layer is modified (Dyer, 1986). The presence of bedforms is an expression of bedload transport (Allen, 1985). Bedform migration may be used as a proxy for estimating bedload transport rate (Hoekstra et al., 2004), or a more conservative approach is to estimate bedform transport rate (Huntley et al., 1991).

2.4.1: Bedform classification

Bedforms are primarily classified based on their scale (ripples, dunes/megaripples and sand waves) and as a secondary classification, the environment in which they are located (oscillatory flow or uni-directional flow), their profile (asymmetric or symmetric) or their plan form (2-dimensional or 3-dimensional). Classifications are based on *in-situ* observations, from measurements made in the field (Osborne and Vincent, 1996; Traykovski et al., 1999; Masselink et al., 2007), in laboratories (Nielsen, 1981; Thorne et al., 2003) and also from empirical models (Yalin, 1964; Clifton, 1976; Boguchwal and Southard, 1990).

2.4.2: Wave forced bedforms

In oscillatory environments bedform formation commences as a flat bed first experiences orbital wave motion just exceeding the threshold of motion, causing grains to roll back and forth forming small triangular ridges. While the bed shear stress is close to the critical value these rolling grain ripples will remain in equilibrium. As the orbital velocities increase the size of the ripples will increase (Allen, 1985; Camenen, 2009), until washout conditions occur. The progression of bedforms in oscillatory conditions, according to Clifton (1976) is: Lower plane flat bed > symmetric ripples > asymmetric ripples > megaripples > higher stage flat bed (sheet flow). Whilst a change in the wave climate can lead to a modification of the bedform state, bedforms of different states may also be dependent on position within the nearshore zone (Nielsen, 1992). Offshore, where the bed first experiences wave motion, bedforms are likely to exist as long crested symmetrical features (Masselink and Hughes, 2003). Moving shoreward these features can become increasingly asymmetric, irregular and feature shorter crests as wave motion near the bed becomes elliptical and flows become horizontal and asymmetric due to waves taking on an asymmetric form (Clifton, 1976). According to Clifton (1976) megaripples, features with typical lengths of 1-2 m and heights of around 0.1 to 0.2 m and rounded crests (Nielsen, 1992), are found around the breaker zone. Within the surfzone, shoreward of the break point, the bed is often flat and featureless (Clifton, 1976).

Wave ripples have a typical length (λ) of 0.2 m and in most instances scale with wave motion (Nielsen, 1992). Clifton and Dingler (1984) classified symmetrical ripples on their relationship with orbital diameter (d_o) and wavelength (λ). Ripples that scaled positively with orbital diameter were termed orbital ripples, typically they are found in shallower water and in short period wave conditions. They were identified as having a ratio of orbital diameter to grain size (d_o/D) of between 100 and 3000 and a ratio of wave length to grain size (λ/D) of between 100 and 2000. Further work by Miller and Komar (1980) identified an approximate relationship for the formation of orbital ripples where;

$$\lambda = 0.65\ d_o \tag{2.6}$$

Sub-orbital ripples are inversely related to orbital diameter and form when d_o/D = 1000 to 3000. Anorbital ripples have no relation to orbital diameter and form when d_o/D > 5000. Anorbital ripples may form in long period wave conditions (>12 seconds) and may include reversing ripples which alternate direction of asymmetry with flow reversal of a passing wave (Inman, 1957). The classification of Wiberg and Harris (1994) states that when a ratio of orbital diameter to bedform height (d_o/Δ) is > 100 the ripples were anorbital, d_o/Δ > 12 and < 100 they were sub-orbital and when d_o/Δ < 12 the ripples

were orbital. In field conditions, Nielsen (1981) related the wavelength to the mobility number (ψ), a variable that accounts for the contribution of d_o, *T* and *D*, with

$$\lambda = \frac{d_o}{2}\exp\left(\frac{693 - 0.37\ \ln^{8}\ \psi}{1000 + 0.75\ \ln^{7}\ \psi}\right) \tag{2.7}$$

where the mobility number (ψ) is given b

$$\psi = \frac{(A\ \omega)^2}{(s-1)\ g\ D}$$

and *A* is the orbital amplitude, ω is the radian frequency, s is the relative sediment density, g is the acceleration due to gravity.

Ripple steepness (∆/λ) can used to classify wave ripples (∆ = bedform height) as either post vortex ripples when ∆ /λ < 0.15, or vortex ripples when ∆ /λ > 0.15 (Dingler and Inman, 1976). Additionally, O'Hara Murray et al. (2011) showed that post vortex ripples occurred when $\lambda/d_o > 0.83$ and vortex ripples occurred when $\lambda/d_o < 0.83$. Vortex ripples are so called as a vortex forms in the lee side of the ripple during each passing wave (Nielsen, 1992). Vortex ripples are particularly important in terms of suspended sediment dynamics as the boundary layer scales with their spacing (Nielsen, 1992). Post-vortex ripples occur when sand is stripped from the ripple crest when the orbital diameter is very large and can signal the onset of sheet flow conditions (Clifton and Dingler, 1984). Nielsen (1981) proposed that ripple steepness is also a function of the mobility number.

$$\Delta/\lambda = 0.342 - 0.34\ (1/2\ f_w\ \psi)^{0.25} \tag{2.8}$$

Where f_w is a wave friction factor given by:

$$f_w = \exp[5.213\ (5D/d_o)^{0.194} - 5.977] \tag{2.9}$$

Megaripples can form abruptly from wave driven ripples with an increase in bed shear stress (Clifton, 1976). They are often found immediately offshore of the break point (Nielsen, 1992).

2.4.3 Current forced bedforms

Current ripples are initiated from a planar bed when the onset of a unidirectional current causes the formation of small clusters of grains. These modify the flow and the cluster grows to form a crest. As the flow velocity increases, the ripples will grow as a vortex is formed in the leeside of ripples, strong enough to initiate sediment movement between ripples (Nichols, 2009).

In unidirectional currents, bedforms evolve as shear stress increases, through a sequence of: lower stage flat bed > ripples > current dunes (2D > 3D) > upper stage

plane bed > anti-dunes (Dyer, 1986; Nielsen, 1992). The height and length of current ripples is a function of grain diameter, and is modulated by the flow (Yalin, 1964; van Rijn, 1984; Camenen, 2009). Large scale features such as dunes and sandwaves scale with water depth and the flow velocities (Yalin, 1964). Current ripples typically have lengths and heights of 0.2 m and 0.06 respectively (Allen, 1968) and are asymmetrical in shape with a steeper downstream face (Nielsen, 1992). Yalin (1964) suggested the wavelength of ripples was approximately 1000 times the grain diameter and their height 1/7 of the wavelength;

$$\lambda = 1000D \tag{2.10}$$

$$\Delta = \lambda/7 \tag{2.11}$$

Current dunes have typical wavelengths of 0.6 to 30 m, and heights of 0.06 to 1.5 m. Dune length is governed by water depth, and dune height scales to maximum of one sixth of dune length (Yalin, 1964).

$$\lambda = 2\pi h \tag{2.12}$$

$$\Delta = \lambda/6 \tag{2.13}$$

A conceptual model devised by Southard and Boguchwal (1990) identified predicted bedform state based on the flow strength and grain size for a given flow depth.

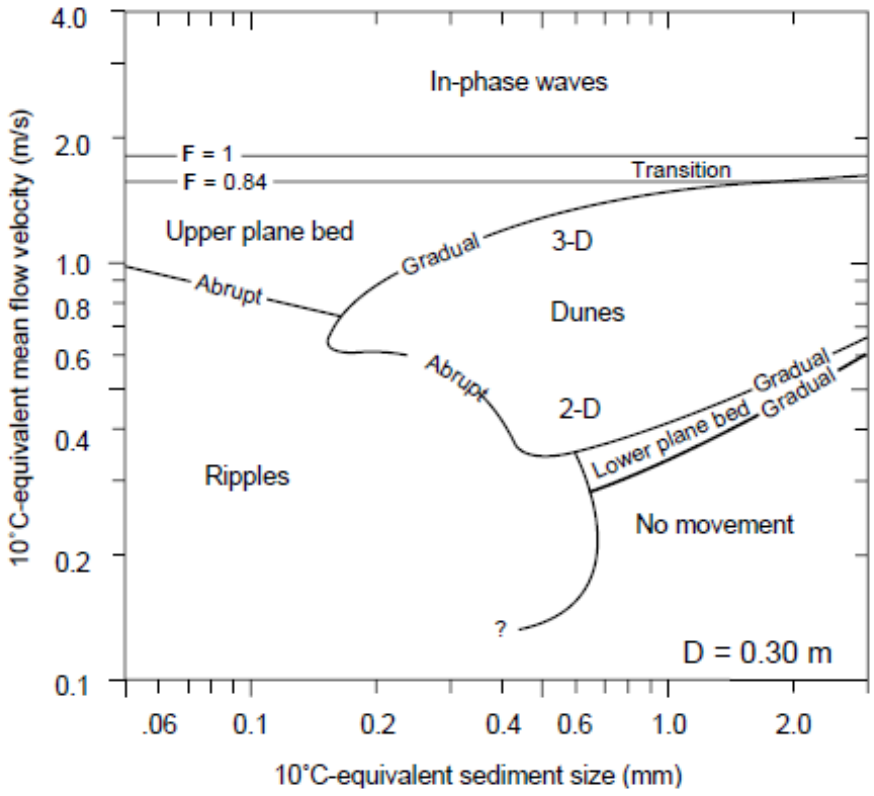

Figure 2.6: Stability diagram of current forced bedforms (Southard and Boguchwal, 1990).

In high flows and shallow depths, under supercritical flow conditions (Froude number > 1), bedforms may migrate against the flow direction, in which case they are known as anti-dunes (Dyer, 1986; Nielsen, 1992).

In the surfzone and nearshore zone it is likely that both unidirectional and oscillatory flows will exist simultaneously. Dyer (1986) and Blondeaux et al. (2000) identified that in conditions with both waves and currents, the bed may display features of both wave and current ripples, and ripples may and co-exist with residual bedforms (Thornton et al., 1998). When megaripples were present (Δ = 0.1 m, λ = 1 m) in low energy conditions, Miles et al. (2014a) found wave ripples were superimposed on top and contributed up to 35% of the total bed roughness. Bedform alignment follows the driving mechanism, therefore in orthogonal wave-current conditions a complex three-dimensional lattice may exist (van Rijn, 1984).

2.4.4: Bedform measurements in the surfzone and nearshore

Megaripples are ubiquitous in the nearshore zone (Gallagher, 2003; Clarke and Werner, 2004). They are recognised as important features, contributing to bed roughness (Gallagher, 2003) and having implications for sediment transport (Aagaard et al., 2000; Gallagher, 2003; Clarke and Werner, 2004) and large scale morphodynamics (Gallagher, 2003; Swales et al., 2006).

Gallagher et al. (1998a) measured megaripples with lengths of 2 to 5 m and heights of 0.2 to 0.3 m. They were present 60% of the time during a six week field study and in a range of wave heights (H_s = 0.5 to 4 m) in ~ 2 m water depth. Gallagher (2003) proposed that the megaripples observed in the surfzone are similar features to those found in unidirectional conditions. A key difference is that in a wave dominated environment that they are symmetrical in shape with a broad, flat crest, whilst in current conditions the bedform takes on an asymmetric profile. This is because over the course of a wave cycle sediment is moved in both directions smoothing the profile. Gallagher (2003) found megaripples to be most common in shallow water (< 2 m), though occasionally present in patches in deeper water (2 – 5 m). Thornton et al. (1998) observed megaripples of 1 to 2 m in length that preferentially formed in rip channels and troughs and not across the rest of the beach. The spatial variability of megaripples in the nearshore has been observed often and is more pronounced in high energy conditions (Greenwood and Davidson-Arnott, 1979; Sherman et al., 1993; Swales et al., 2006). Aagaard et al. (2000) measured megaripples with heights of 0.2 to 0.3 m with bed level sensors in wave heights ranging from 0 to 1.5 m. The method used by Aagaard et al. (2000) only provided a value for bedform height, therefore by using the mean height of 0.24 m and a megaripple steepness (Δ/λ) of 0.1 to 0.2 as given

elsewhere in the literature (Davidson-Arnott and Greenwood, 1974; Clifton, 1976; Sherman et al., 1993; Gallaher et al., 1998; Swales et al., 1999) bedform lengths of between 1.2 and 2.4 m were calculated. In contrast to other measurements, Aagaard et al. (2000) found megaripples to be stable on the bar crest in high energy wave conditions, supporting observations of Hay and Bowen (1993). Nielsen (1992) stated large bedforms, such as megaripples may be present in large oscillatory flows.

Gallagher et al. (1998a) observed average migration rates of 30 cm/hr and maximum rates of 150 cm/hr in an onshore direction. Similar to migration rates measured by Aagaard et al. (2000) of 45 to 90 cm/hr, also in an onshore direction. Migration was attributed to skewed waves or a superimposed steady flow (Gallagher, 2003). Ngusaru and Hay (2004) identified megaripple migration in the onshore direction when orbital velocity was between 0.5 and 0.8 m/s, though when an offshore directed mean flow of > 0.2 m/s was superimposed megaripple migration would stop, or the megaripples would migrate in an offshore direction. Crawford and Hay (2001) measured anorbital ripples with lengths of 8.5 cm and heights of 0.3 cm that migrated in an offshore direction in waves with negative velocity skewness, and migrated in an onshore direction when the velocity skewness was positive at maximum rates of 42 cm/hr. Masselink et al. (2007) investigated variations in ripple migration rates across the surf zone on a relatively coarse grained beach (D_{50} = 0.69 mm) at Sennen Beach in the UK, and found that migration rate depended on surf zone position. Ripples of height of 0.05 m and length of 0.35 m migrated in an onshore direction at rates of 6 cm/hr in the shoaling zone and up to 120 cm/hr and in an onshore direction in the outer surf. They also found onshore directed migration to be impeded by offshore directed mean flows.

Conventional empirical models that predict wavelength and height based on flow conditions do not perform well when compared to field measurements of megaripples (Gallagher, 2011). The empirical models predict an equilibrium bed state for any given flow field. Hay and Mudge (2005) found evidence of various forms of bed state existing in the same conditions. In video observations from a high cliff overlooking the surfzone, Clarke and Werner (2004) observed megaripples to increase with length over time. They observed young bedforms (< 0.5 days) to grow in linear fashion, while older bedforms (> 0.5 days) grew logarithmically. Clarke and Werner (2004) hypothesized that megaripples will grow indefinitely until the flow changes too quickly for them to adapt, or they pass through the swash zone. They developed a self-organisation model based on this principle that correctly predicted bed state for 73% of the measurements. Self-organisation models have also been used by Coco and Murray (2007) and Gallagher (2011) to predict megaripple dynamics. Gallagher (2011) found modelled bedforms to be similar to natural bedforms in cross-sectional shape, plan view, growth

and migration. Consistent with observations of Clarke and Werner (2004), Gallagher (2011) modelled continual bedform growth, as long as conditions were stable. It has been observed that bedforms can exhibit a time lag with hydrodynamic conditions (Austin et al., 2007). This is particularly relevant on macro-tidal beaches where the relative position of the bedform within the nearshore zone changes considerably (Masselink et al., 2007). Miles et al. (2014a) identified that self-organised features dominated in low orbital velocities, but feature scaling was forced at high orbital velocities.

2.4.5 Bedforms in rip currents.

Measurements of bedform dynamics in rip currents are scarce (Sherman et al., 1993; Thornton et al., 1998; Brander, 1999b). This has been attributed to the challenges of making measurements in such a dynamic environment (Aagaard et al., 1997). However, there have been some observations of bedforms within rip channels. Bedforms of megaripple scale (Δ = 0.2 – 0.3 m, λ= 2 – 5 m) have been observed to be present in rip currents (Greenwood and Davidson-Arnott, 1979; Nielsen, 1992; Aagaard et al., 1997; Bruneau et al., 2009), and these features have been suggested to resemble current dunes (Nielsen, 1992).

Brander (1999b) found bedforms in a rip current to be of lengths of 0.8 to 2 m and heights of 0.08 to 0.2 m. Thornton et al. (1998) observed bedforms of approximately 1 to 2 m in length in a rip current. In a more comprehensive study, Sherman et al. (1993) observed megaripples in a rip feeder channel ($\langle v \rangle$ = 0.4 to 0.6 m/s) by visually measuring a pre-selected megaripple with a 'meter long aluminium comb'. Wave heights ranged from 0.37 to 1 m with a period of 6 seconds, mean water depth of 0.71 m, and D_{50} of 0.33 mm. Bedforms were observed to be present throughout the 12 m wide trough, lunate in shape and orientated perpendicular to the beach. Crest height was between 0.15 and 0.2 m, with an average height of 0.16 m and an average wavelength was 1.6 m. The megaripples migrated at an average of 1.65 cm/min in the direction of flow.

Although waves propagate through rip currents, rip channels offer an environment that is current dominated (Nielsen, 1992). According to the classification of current formed bedforms they should be termed dunes if they are current forced (Dyer, 1986). Consistent with previous observations of bedforms in rip channels and the definition of Gallagher et al. (1998a) that megaripples are present within the surfzone, they are referred to in this study as megaripples.

2.4.6: Bedform sediment transport

Bedform migration rate can be used as a proxy for sediment transport. In some cases it has been referred to as bedload transport (Hoekstra et al., 2004), however a more conservative terminology is the bedform transport rate (Huntley et al., 1991; Masselink et al., 2007), which is assumed to be made up of bedload transport and an unquantified amount of saltation.

In low energy conditions Masselink et al. (2007) found the bedform transport rate due to ripples to be comparable to the total suspended flux under shoaling waves, though it was an order of magnitude less in the outer surfzone. Aagaard et al. (2000) found the bedload transport associated with megaripple migration was a minor but significant fraction of the total load transport, with rates of 0.14 to 0.28 kg/m/s. On a steep beach Aagaard et al. (2013) found that bedform transport rate was onshore in 'post-storm' conditions (H = 0.5 m), and offshore directed in 'storm' conditions (H = 1 m). However, in 'post-storm' conditions the net transport was offshore directed as suspended sediment transport was an order of magnitude larger than the bedform transport and in the offshore direction. In storm conditions the dominant mode of transport varied due to variability in suspended sediment transport dynamics. In water depths of 11 m, Traykovski et al. (1999) found that the bedform transport rate was relatively more important than suspended sediment transport. This was because sediment suspension and therefore suspended sediment transport was limited at these water depths, indicating that water depth is a factor that can moderate hydrodynamic influences on the sediment transport and bedform dynamics.

CHAPTER 3: METHOD

In this chapter the study site is described, the instrumentation reviewed and the data collection and the evolution of the experiment design is outlined. Lastly, data processing and analysis techniques are described.

3.1: Site Description

All of the data used in this study were collected from Perranporth Beach on the North Coast of Cornwall, UK (Figure 3.1). Perranporth was chosen as the study site for multiple reasons:

- The beach has pronounced low tide bar-rip morphology (Austin et al., 2010). Evidence suggests that rip currents regularly form on this beach, particularly at mid to low tide (Scott et al., 2009a) with specific locations on the beach known to favour rip formation (Richardson, 2011).
- A large scale field campaign on rip currents was already planned to take place at Perranporth by researchers from Plymouth University. The project, '*Dynamics of Rip Currents and Implications for Beach Safety'* (DRIBS) was a £0.5 million project supported by NERC and the Royal National Lifeboat Institution (RNLI) aimed at improving the understanding of rip current dynamics from a beach safety perspective (DRIBS, 2013). The opportunity existed to carry out data collection whilst this project was running. This meant that a large amount of infrastructure, expertise in surfzone fieldwork and manpower were available for this study. This collaboration improved the opportunity for high quality data collection in the rip and also offered supporting data through surveys of the beach morphology and drifter tracking.
- Perranporth has been, and still is a regularly used field site by the Coastal Processes Research Group (CPRG) of Plymouth University. In recent times work has been undertaken on beach morphology and evolution (Poate et al., 2009; Stokes et al., 2013), rip current dynamics (Austin et al., 2010; Austin et al., 2014; Scott et al., 2014) and swash zone process (Butt and Russell, 1999; Butt et al., 2001; Masselink et al., 2005; Masselink and Russell, 2006; Miles et al., 2006; Puleo et al., 2012).
- Perranporth is part of a worldwide study on beach morphology using video cameras as part of the ARGUS programme (Coastal Imaging Lab, 2009).

- There is a town adjacent to the beach with amenities and accommodation. Perranporth Beach has easy access via main roads and directly on to the beach and is within 90 minutes' drive from Plymouth University.

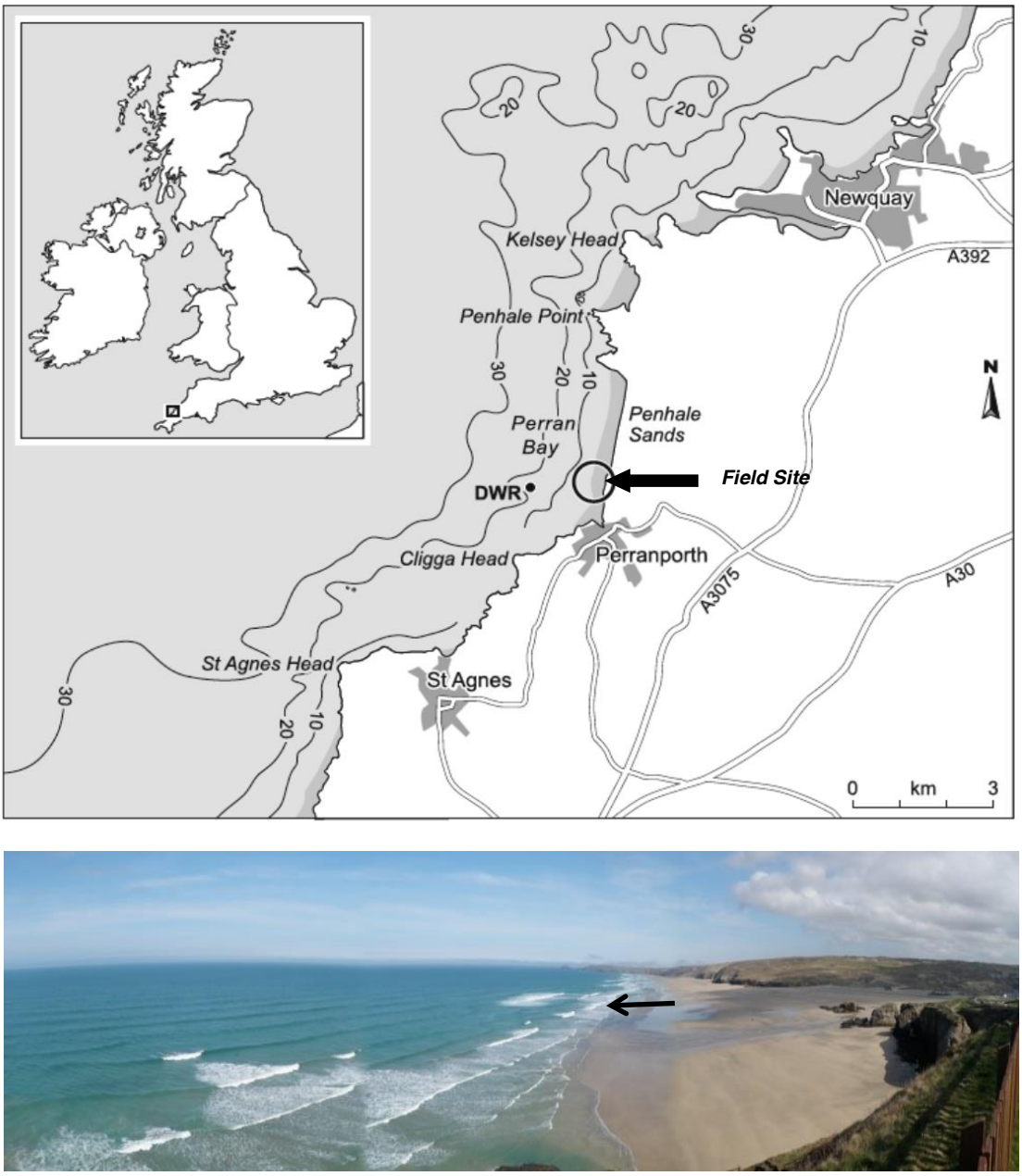

Figure 3.1: From top; Map showing the location of the study site within the UK, the location of the directional wave rider buoy (DWR) (Austin et al., 2010), and a panoramic photograph of Perranporth beach taken from the southern headland, looking in a northerly direction with approximate frame position identified.

Perranporth is a highly energetic beach with an annual significant offshore wave height (H_s) of 1.6 m (maximum H_s > 5 m) and an average peak period (T_p) of 10.5 s (Austin et al., 2010). Located in a macro-tidal environment, the beach experiences semi-diurnal tides with a mean spring range of 6.3 m (Austin et al., 2010), a mean neap range of 2.9 m and consists of medium sized quartz sand (D_{50} = 0.28 – 0.34 mm; w_s = 0.032 m/s (Poate et al., 2009). The beach is 3.5 km long, relatively straight, and is enclosed by

the rocky headlands of Droskyn Point to the south and Ligger Point to the north. The beach faces west-northwest, and is therefore exposed to North Atlantic swells and also receives locally generated wind waves.

Perranporth Beach has a relatively flat inter-tidal zone which can reach 500 m in width (Figure 3.1). It exhibits rhythmic bar-rip morphology (Figure 3.2) that is only partially exposed on the lowest spring tides. The morphology varies temporally and can tend towards a dissipative state under high energy conditions (Austin et al., 2010). Richardson (2011) found rip currents at Perranporth to be spatially persistent at the locations of water outflow, headlands and geological variations, for periods up to 118 days.

Figure 3.2: Time-averaged image of Perranporth captured with an ARGUS camera at low tide looking in a northerly direction during the first data collection period (October, 2011).

3.2: Instrumentation

The processes studied in this thesis are outlined in Section 1.4. The data collection method is developed to measure waves and tidal elevation, flow dynamics, suspended sediment concentration and bedform dynamics. In this section the instruments used to collect this data are reviewed.

3.2.1: Pressure Transducer (PT)

Pressure Transducers (PTs) can be used to measure wave height, mean water depth and tidal height. They are considered to be a robust and practical instrument for *in-situ*

shallow water measurements. They include a piezo-resistive element which is made of a material that accumulates an electrical charge in response to an applied pressure. The electrical response is proportional to the pressure. As pressure is a function of density, gravity and water depth; and density and gravity are constant, a PT can be calibrated to provide water depth and wave height (Hardisty, 1990).

The Tide Wave Recorder-2050 (TWR-2050) is a stand-alone PT; it is self-logging and has replaceable internal batteries. It has two modes than can be used simultaneously: tide averaging or wave recording. Tide averaged data is obtained by removing the effect of waves from the data by only recording water depth. Wave data is recorded as bursts at 1, 2 or 4 Hz as a time series of 512, 1024, 2048 or 4096 data points. The device is vented to facilitate automatic correction with atmospheric pressure. The calibration constants are stored on the instrument making user re-calibration possible. The battery life is dependent on user defined settings, but can last from a few days up to a month (Ruskin, 2011).

3.2.2: Acoustic Doppler Velocimeter (ADV)

Acoustic Doppler Velocimeters (ADVs) are used to study rapid velocity fluctuations in the laboratory or in the field. Field specific ADVs are designed principally to study flow velocities, turbulence, orbital wave motion, bottom boundary layers and mean flows (Nortek, 2010).

An ADV works by emitting a short acoustic pulse from a transmitter, the echo is received in the three acoustic receiver elements (Figure 3.3). The echo is then processed to find the Doppler shift. The calibration is adjusted with the measured speed of sound in the liquid and the velocity is recorded remotely or transmitted in real time to a computer (Nortek, 2010).

In this study both 2D and 3D ADVs were used. The 3D version includes a vertical velocity component. The sampling frequency ranges from 1 to 64 Hz and the instrument has an accuracy of 1 mm/s. Data is either recorded in an XYZ format (relative to the positioning of the sensor) or ENZ format (relative to the on board compass). Therefore it is important to correctly align the ADV head. This is typically done in a cross-shore – longshore orientation. The sensor has pitch and roll sensors making small scale correction possible (Nortek, 2010).

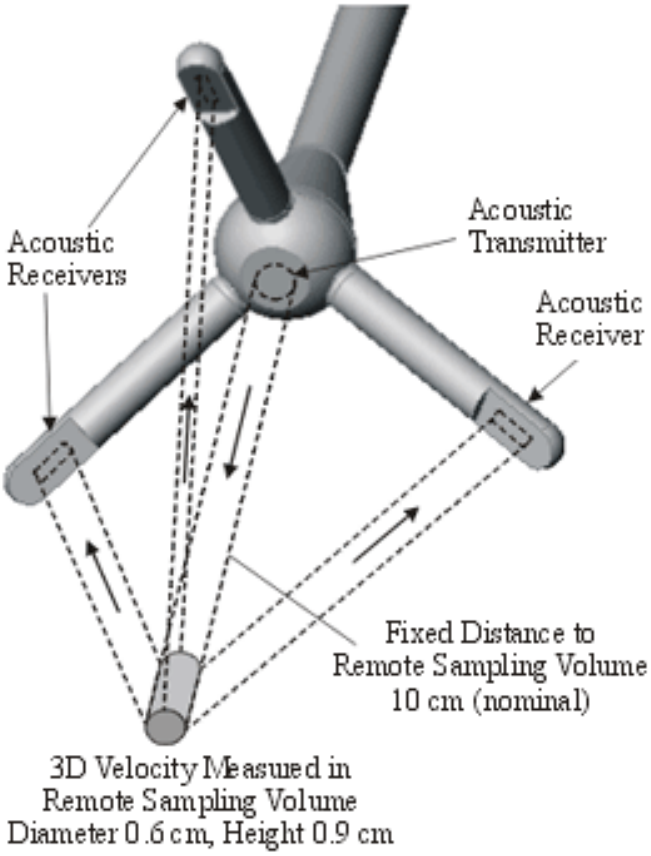

Figure 3.3: Schematic diagram of Acoustic Doppler Velocimeter head and its key components (SonTek, 2009).

The ADV can be cabled to the shore or can be powered and programmed to collect data autonomously. It is fitted with internal batteries with an input for additional external batteries. A function that makes the ADV so versatile is that it is fitted with an internal pressure transducer inside the casing unit and has the capability to power and record from two analogue sensors, such as external PTs or Optical Backscatter Sensors (OBS).

3.2.3: Optical Backscatter Sensor (OBS)

Optical Backscatter Sensors (OBSs) are instruments for measuring turbidity and suspended solid concentrations by detecting light scattered by suspended matter (Downing et al., 1981). They have been widely used in the field to investigate nearshore sediment dynamics (Jaffe et al., 1984; Beach and Sternberg, 1988; Osborne and Greenwood, 1992a, b; Aagaard et al., 1997; Butt and Russell, 1999; Masselink et al., 2007).

OBSs work by producing a short pulse of light that is backscattered by suspended particles in the water. A sensor, consisting of four photo-diode detectors, receives the backscattered light and converts it to photocurrent. The amount of photocurrent depends on the illuminated area of particle, and as area is proportional to volume it is

possible to obtain an indirect measurement of suspended sediment concentration (Downing, 2006). The backscatter is frequency dependent, with the OBS response dependent on the size, shape and composition of suspended particles and therefore it is necessary that they are calibrated with sediment collected at the study site.

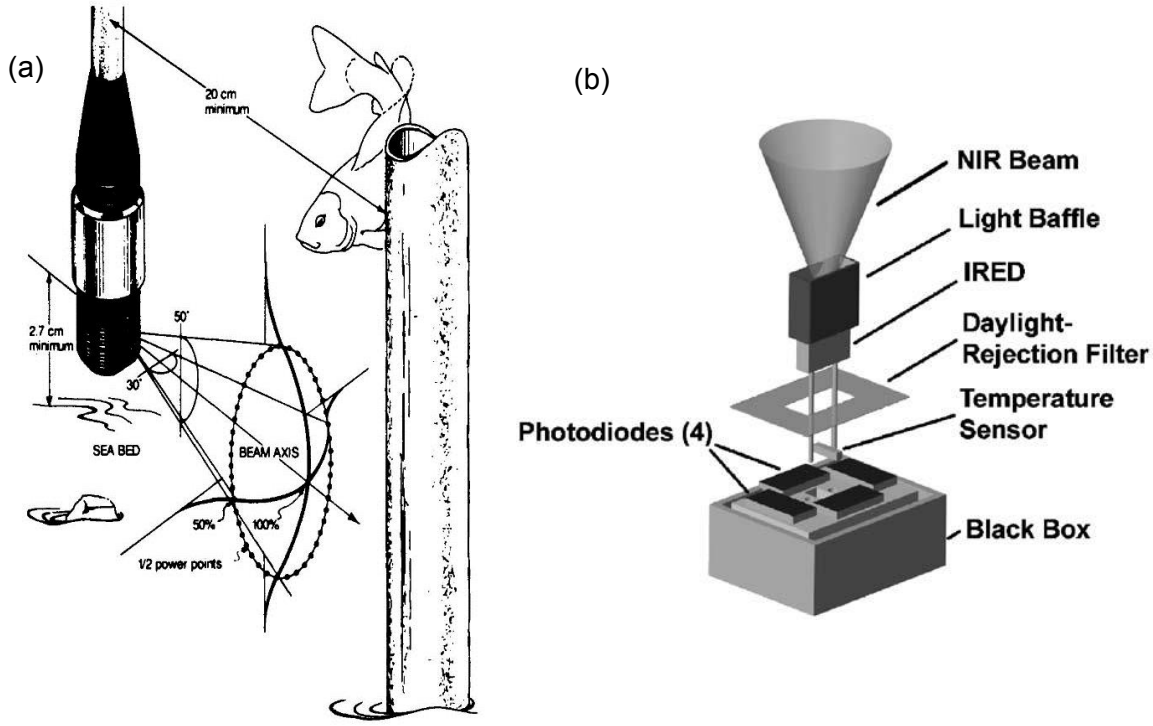

Figure 3.4: (a) OBS beam pattern (from D&A instrument company OBS 1 & 3 instruction manual) and (b) exploded view of OBS-3 sensor (Downing, 2006).

There are several versions of the OBS sensor; an OBS-5 uses a laser diode as a light source. In this study OBS-3+s were used, in which light is emitted via an infra-red emitting diode (IRED). The performance of the OBS sensor is claimed to be superior to most other *in-situ* turbidity sensors due to small size and sample volume, linear response, wide dynamic range and ambient light rejection (Russell, 1990; Downing, 2006).

3.2.4: Sand Ripple Profiling (SRP) Sonar

The Sand Ripple Profiler (SRP) is a pencil beam acoustic scanner with capability to perform regular scans allowing bed evolution to be visualized and quantified. It is fitted with a 1.1 MHz disc transducer and a stepper motor. A directionally focussed acoustic beam is emitted from the transducer and the associated echo received and processed. The motor moves in 0.9^{o} increments until a whole profile is measured. The fastest rate at which scans can be recorded is every 1-minute (Marine-Electronics, 2006).

The SRP is mounted horizontally looking downwards at the bed (Figure 3.6). The size of the footprint of the scan increases by raising the elevation of the SRP and by increasing the size of the swath arc. The programmable settings for the swath arc are 30, 60, 90, 120 and 150 degrees. Raising the height of the SRP is at a cost of reducing the horizontal resolution and if the instrument is being deployed in an inter-tidal environment, the time the instrument is sufficiently submerged to record data will also be affected. Table 3.1 shows the resolution and footprint size for different deployment heights and swath arcs.

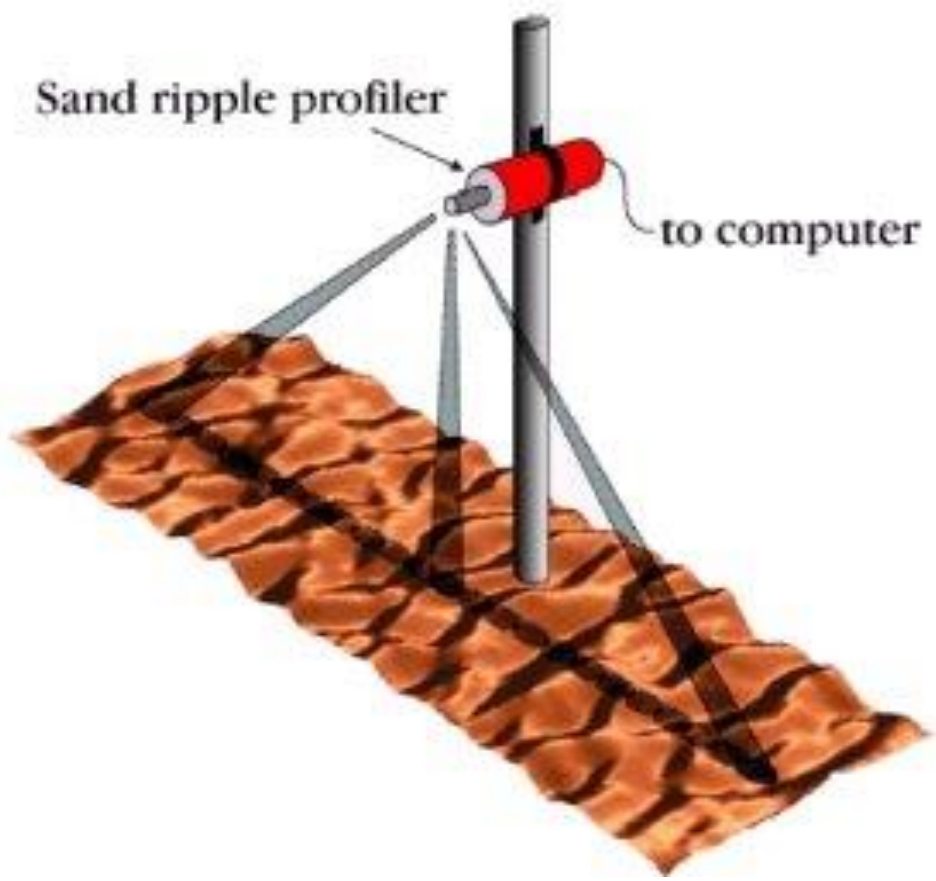

Figure 3.5: Schematic of an SRP showing typical mounting configuration (Marine-Electronics, 2006).

Additionally, increasing the swath arc and therefore the scan footprint also increases the memory capacity required. This was investigated in laboratory tests and it was found that in a wide range of settings that the battery life (when deployed autonomously) was the limiting factor. Battery life was most effected by how often scans were captured, and not by the acoustic settings. The battery is made up of 12 lead acid rechargeable batteries, these make the unit large and very heavy (~ 50 kg), which is an important consideration when planning deployment. When deployed with a data logger, data can be recorded from two SRPs on an internal 8GB memory card. The software for autonomous deployment allows the instrument start time and end time to be specified. It is important to avoid cross contamination of acoustic signals when

using two SRPs. This was done by scanning sequentially, and not simultaneously. Each scan was saved in an individual text file with the option to save in a binary format or an ASCII X, Y format.

Table 3.1: Total footprint size and horizontal resolution for deployment heights of 60, 70, 80, 90, 100, 110 & 120 cm) and swath angles of 90, 120 & 150 degrees (^{o}).

Height (cm)	Swath angle (^{o})	Footprint (cm)	Horizontal resolution (cm)	
			Under SRP	At extremities
60	90	120	0.9	1.8
70	90	140	1.1	2.1
80	90	160	1.2	2.4
90	90	180	1.4	2.7
100	90	200	1.5	3.0
110	90	220	1.7	3.4
120	90	240	1.8	3.7
Height (cm)	**Swath angle (^{o})**	**Footprint (cm)**	**Horizontal resolution (cm)**	
			Under SRP	**At extremities**
60	120	208	0.9	2.6
70	120	242	1.1	3.0
80	120	277	1.2	3.5
90	120	312	1.4	3.9
100	120	346	1.5	4.3
110	120	381	1.7	4.8
120	120	414	1.8	5.2
Height (cm)	**Swath angle (^{o})**	**Footprint (cm)**	**Horizontal resolution (cm)**	
			Under SRP	**At extremities**
60	150	446	0.9	5.0
70	150	522	1.1	5.9
80	150	596	1.2	6.7
90	150	670	1.4	7.5
100	150	746	1.5	8.4
110	150	820	1.7	9.2
120	150	894	1.8	10.1

The SRP has the option for the user to define the acoustic settings. The sample interval is the gap between successive pulses (in 0.8 µsec steps from 0.8 µsec to 100 µsec). The transmit pulse needs to be at least twice the length of the sampling interval. This is because a short pulse may not be detected amongst the noise. These two

variables affect the number of samples taken per scan. In this study a transit pulse of 10 μs and a sample interval of 4 μs was used.

3.2.5: Total station

A total station is an instrument used in surveying to record slope distances and angles from the instrument to a particular point, with data stored as XYZ co-ordinates or in an ENZ format. If the total station is used within a line of site of two or more known points, its location can be deduced by triangulation, and therefore so can any other measurements recorded (Trimble, 2013). A Trimble 5600 station total was used in this study to survey instrument positions, measure beach profiles and to carry out high density surveys on transect of bed that exhibited megaripples.

The total station was used with a Trimble Remote Measuring Target (RMT). These are fitted with prism reflectors. When using a robotic total station, a RMT fitted with one or more tracker diodes will allow one person to carry out the survey. The visible range of the RMT is dependent on weather conditions and the model used, but generally ranges from 350 m to 1500 m (Trimble, 2013), which was ample for the maximums distances surveyed in these experiments of ~ 100 m.

3.3: Experiment Techniques

In addition to measurements made with high frequency instruments deployed in the rip current a range of supplementary data were collected. In this section the methods for the collection of this data are outlined.

3.3.1: Beach surveys

Inter-tidal three-dimensional beach surveys of the beach morphology were carried out on spring low tides during each experiment (a minimum of one per field experiment) using a Real-Time Kinematic Global Positioning System (RTK-GPS) mounted on an All-Terrain Vehicle (ATV) giving centimetre accuracy in the horizontal and vertical. The data were collected on a quasi-regular spaced grid (Figure 3.6) with longshore transects 10 to 15 m apart and cross-shore transects spaced 50 to 100 m apart. The surveys contributed to a larger scale survey programme (Stokes et al., 2013; Austin et al., 2014; Scott et al., 2014).

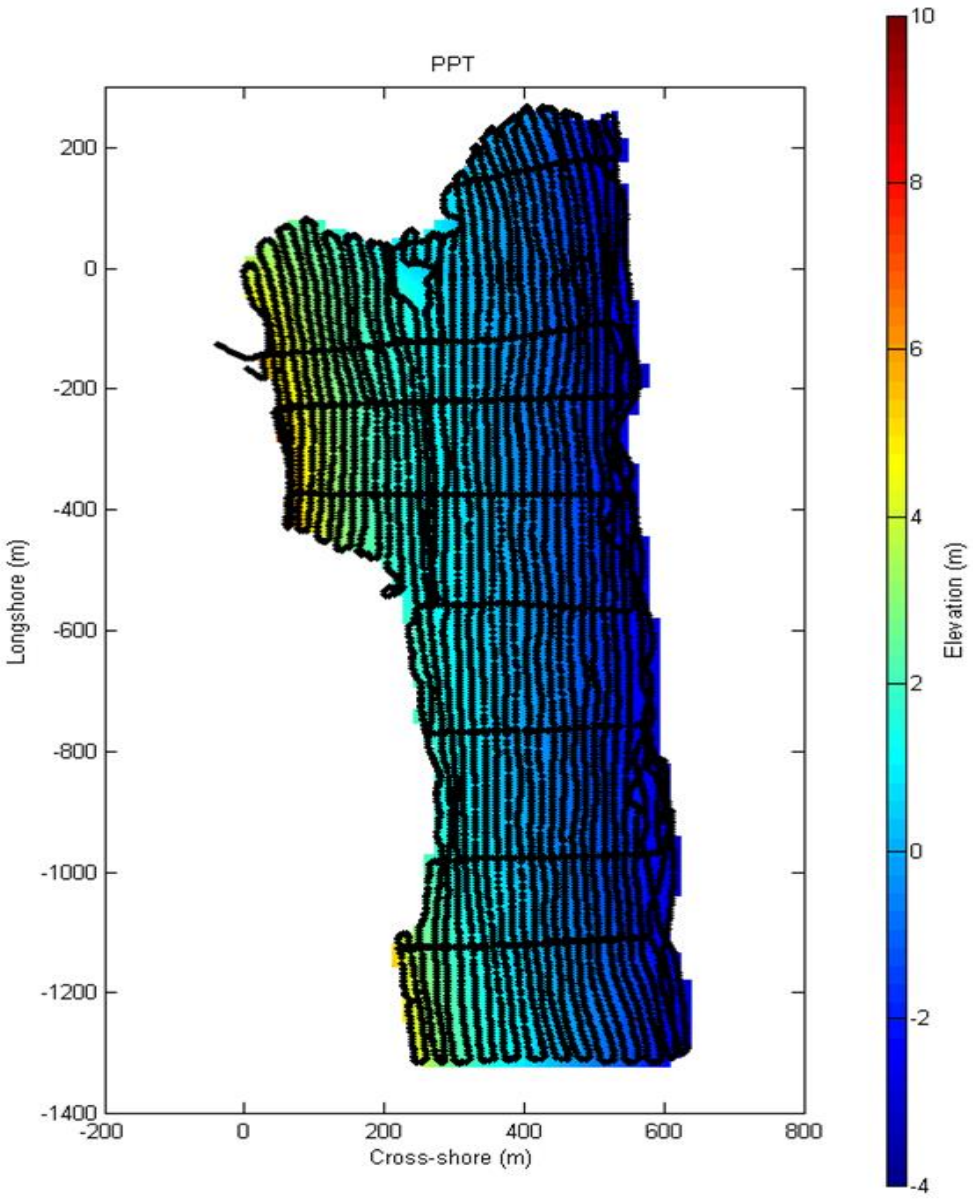

Figure 3.6: Map of the inter-tidal area showing transects measured by GPS-RTK mounted on an ATV (Stokes et al., 2013).

During the DRIBS project sub-tidal surveys were carried out using a RTK-GPS in conjunction with a single beam echo sounder mounted on a jet ski in low wave conditions. The use of jet skis in coastal research was pioneered for surveying nearshore shallow water bathymetry (Dugan et al., 1999; MacMahan, 2001). Depending on depth and slope the estimated accuracies (for sandy bottoms) in water depths ranging from 1 to 10 m are 0.07 to 0.1 m in the vertical and 0.1 to 1 m in the horizontal (Lippmann and Smith, 2008). For maximum overlap, the sub-tidal surveys were performed at neap high tide, and the inter-tidal surveys were performed at spring low tide. The two sets of survey data were combined and interpolated onto a normal grid and fitted to a local co-ordinate system following the method described in Austin et al. (2010).

3.3.2: GPS drifter data

Lagrangian drifters, based on a design by Schmidt et al. (2003), were deployed to measure rip flow strengths, circulation patterns and to identify the overall location of the rip current as part of the DRIBS (2013) project. The drifters were fitted with GPS receivers and data loggers capable of recording raw carrier phase satellite data at 1 Hz. These were subsequently processed from a survey grade base station (Austin et al., 2010). Drifters were deployed across the rip system. If they did not circulate back to the shore they were retrieved by an inflatable boat before being re-deployed.

3.3.3: Total station surveys

Instrument positions and elevations were recorded daily with a total station. Bedform dimensions were measured in the rip channel at spring low tide with the total station. Cross-shore transects were walked as close as possible to the instrument frame at each day light low tide (Figure 3.7). Transects ranged in length from 8 to 23 m. Points were recorded at approximately every 0.1 m, making sure the highest and lowest points of the crests and troughs were recorded.

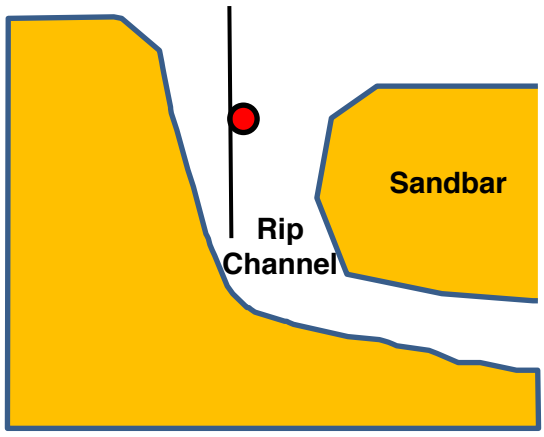

Figure 3.7: Orientation of bedform measurements made by walking cross-shore transects in the rip channel. The approximate transect measured (solid line) and the instrument frame (red circle) are marked.

3.3.4: Sediment sampling

Sediment sampling was carried out for grain size analysis. Samples were taken from the upper beach (high tide limit), the middle of the inter-tidal section of beach, the bar crest, the feeder channel and in the centre of the rip current next to the instrument frame. A map of the sampling locations is provided alongside the analysis in a subsequent chapter (Figure 4.9). Sediment was collected from the surface (to a maximum depth of approximately 30 mm) with a ‘plastic scoop’ at five points at each location (four points of a square and a fifth point in the centre). Approximately 200 g of sand was collected in total. The centre of the rip channel was always submerged so

care was taken that the fine fraction of the sediment did not drain out during sampling. Samples were rinsed and dried, and the analysis was performed using a settling column.

3.4: Experiment Design

Instrument trials and the development of a frame to which instruments could be attached was an ongoing process that took place between October, 2010 and April, 2013. Field experiments contributing to this development were:

- Preliminary experiment: Porthtowan, November, 2010
- Full instrument trial: Perranporth, June, 2011 (alongside DRIBS - part 1)
- First data collection: : Perranporth, *STIR 1*, October, 2011 (alongside DRIBS - part 2)
- Second data collection: : Perranporth, *STIR 2*, April, 2013

Two preliminary field deployments were carried out in November, 2010 and June, 2011 to test instrumentation and the suitability of different frame designs. The data presented in this study were collected in two separate field campaigns, both undertaken at Perranporth on the North Coast of Cornwall, UK. The first campaign, from here on referred to as *STIR 1* (Sediment Transport In Rip Currents) took place between the 14th and 28th of October, 2011, in which 6 tides of data were collected, and 12 occurrences of rip currents were identified. *STIR 2* took place between the 25th and 30th of April, 2013; in which 8 tides of data were collected, and 15 occurrences of rip currents were identified. In total, this study consists of 14 tides of data, including 27 occurrences of rip currents.

The general approach in both *STIR 1* and *STIR 2* was to build a mobile frame out of scaffold bars to which a suite of high frequency instruments were attached to measure hydrodynamics, sediment dynamics and bed profiles. The frame, with instruments attached, was then carried into a pre-determined rip channel at spring low tide, when the sub-tidal morphology was partially exposed. As the tide flooded and ebbed over the frame, the instruments were submerged and data were recorded throughout the tidal cycle, encompassing rip flow at lower tidal elevations and periods when the rip current was inactive at higher tidal elevations. The parameters measured at the instrument frame were cross-shore velocity, longshore velocity, water pressure, suspended sediment concentration at multiple heights above the bed and bed profiles. The frame was extracted some days later. The timescale of frame extraction was dictated by sea conditions, battery life of the sensors and the reduction of the tidal range (making

access to the frame more challenging). This approach allowed instruments to be positioned carefully in a clearly identifiable rip channel.

One of the biggest challenges of planning and undertaking the field experiments was the design and the deployment of a scaffold frame. Due to the large tidal range (> 6 m) and the large dry width of the beach at low tide (> 300 m), cabling the instruments to the shoreline was not possible, therefore external battery packs and loggers were attached to the frame. Furthermore, the SRPs were required to be positioned at least 0.7 m above the bed (Masselink et al., 2007) and in a manner that meant the scaffold frame and other instruments (particularly acoustic instruments) were not visible in the scanning window. This required at least part of the frame to be quite high and therefore potentially unstable.

The design of the scaffold frame underwent constant modifications and improvements in response to the goals of each deployment and lessons learnt during previous deployments. In this section, each experiment is described in chronological order, with the goals and outcomes of each outlined. *STIR 1* and *STIR 2* are described in more detail, as this is where the data for this study came from.

3.4.1: Sand Ripple Profiler Trial; Porthtowan, November 2010

The purpose of this preliminary experiment was to trial the sand ripple profiler in the field after a series of tests in the laboratory. As the instrument would be deployed autonomously, there would be no chance to change instrument settings until the following deployment so this trial offered a chance to see if the same settings that worked in the laboratory were suitable for the field. The trial was undertaken at Porthtowan, an intermediate-dissipative beach of medium sands (D_{50} = 0.38 mm) (Poate et al., 2009) with a W-NW aspect, approximately 10 km south of Perranporth. The offshore wave conditions during the deployment were H_s = 0.6 m and T_p = 10 s (data from the DWR wave rider buoy, 1 km off Perranporth beach)

A scaffold frame was fixed into the sea bed at low tide and the SRP and data logger/battery pack mounted (Figure 3.8). The instrument was located close to the headland on the north end of the beach, an area known to occasionally exhibit a weak topographic rip current. As the tide flooded, the SRP was submerged and data were recorded.

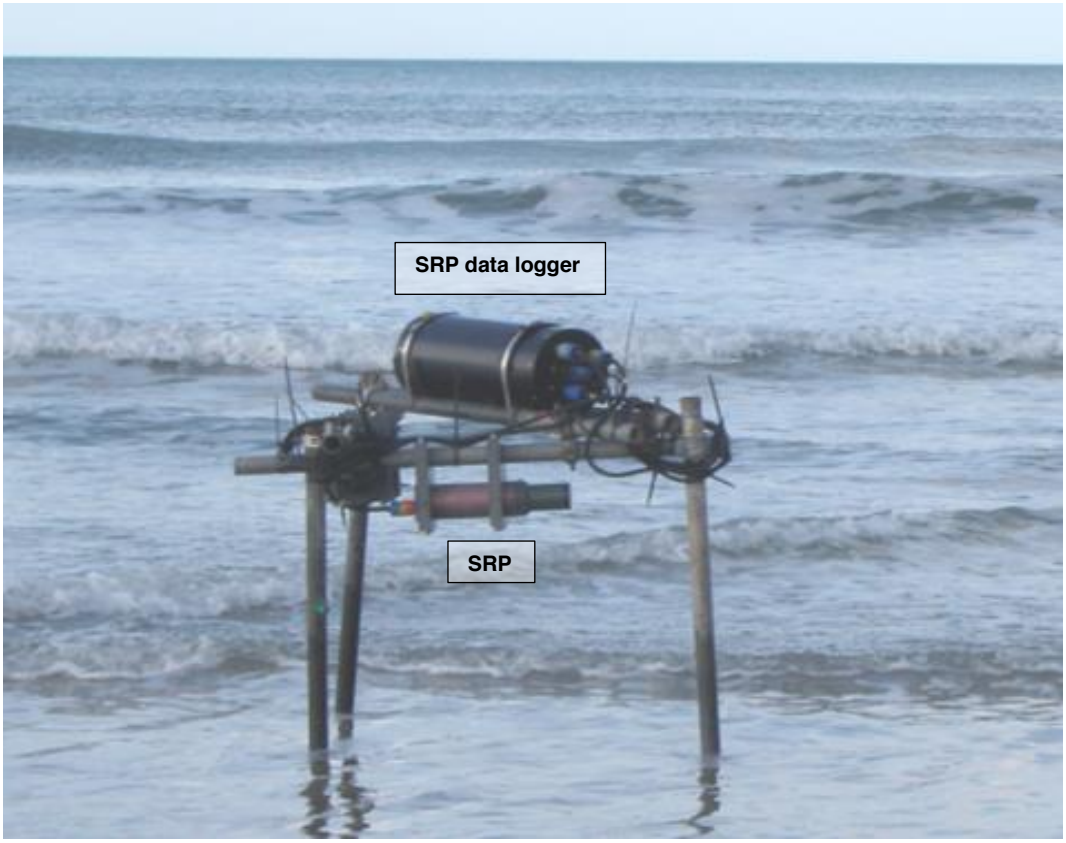

Figure 3.8: Photograph showing instrument frame with SRP and data logger battery pack.

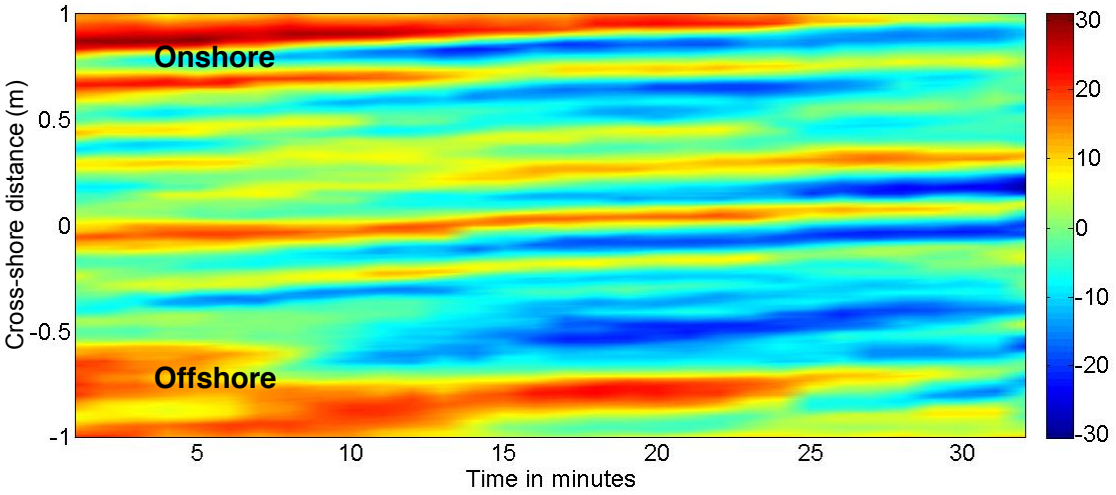

Figure 3.9: A 30-minute time-stack of bedform evolution. The SRP is positioned at a cross-shore position of '0'. The colour bar indicates bed elevation in mm where hot colours represent bedform crests.

The instruments were recovered at low tide the following day. The SRP settings used in the laboratory tests appeared to perform well when deployed in the field. Figure 3.9 shows an example of 30 minutes of data, with results showing ripples (where red colours indicate crests) with a mean height of 0.03 m and a mean length of 0.29 m migrating onshore at a rate of 0.47 cm/min. No rip developed, however the

observations were consistent with previous and subsequent observations of shoreward ripple migration under skewed waves (Miles et al., 2014b).

3.4.2: Full equipment trial, DRIBS *1*
Perranporth, May/June 2011

This experiment was the first attempt to make measurements of suspended sediment concentrations and bedform dynamics in a rip current. These measurements were supplemented with hydrodynamic measurements of water pressure and flow velocities. This experiment was undertaken during the first of two DRIBS field experiments at Perranporth over 6 weeks in May and June 2011. A scaffold frame was fixed into the seabed shoreward of the rip channel in a right angle configuration to offer maximum stability and to minimize flow impedance by the frame itself (Figure 3.10). The SRP battery pack and data logger were secured to the cross-shore orientated scaffold bar so as to limit the effect wave action would have upon it. They were kept as far as possible from the instruments as not to induce a turbulence effect that could interfere with the measurements. All the instrumentation were co-located to make measurements relevant to one another and kept as far as possible from the potential interference of scaffold bars, whilst allowing the frame to maintain its rigidity. Two SRPs were deployed, one to measure longshore bedform profiles (z = 0.8 m) and one to measure cross-shore profiles (z = 0.9 m). An ADV was positioned with the sampling volume at 0.25 m above the bed. The ADV housing unit contained an internal PT (z = 0.8 m) to measure water depth and wave statistics. A pair of OBS 3+s were deployed at 0.25 m and 0.40 m above the bed to measure suspended sediment concentrations.

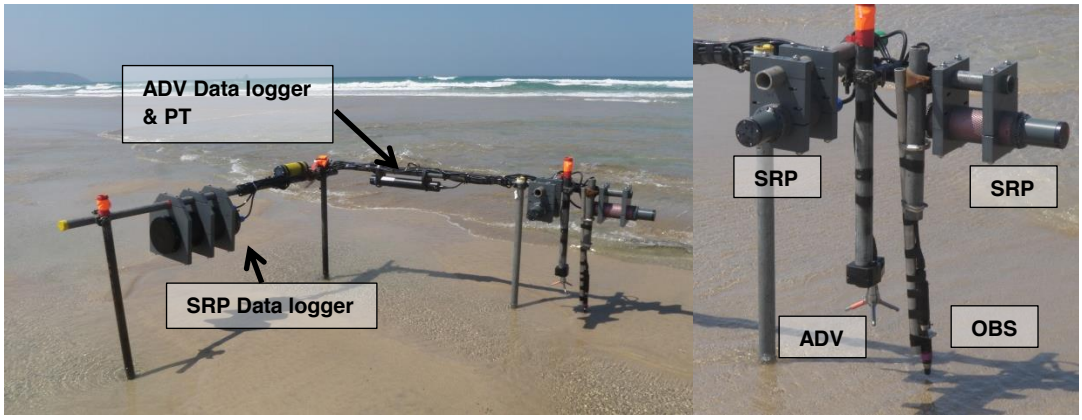

Figure 3.10: Photographs of instrument frame showing position of instrumentation and data loggers and close up of instrumentation.

During this experiment, six tides of data were collected over two separate deployments, between the 20th to 21st May and 2nd to 4th June 2011. The original intention of this experiment was that the data collected would be used in this study. However analysis of the data showed that by the time the instruments were sufficiently covered by the

flooding tide to record the data, the rip was inactive, particularly in the case of the SRP, due to its height above the bed and requirement for greater water depth to operate. Bathymetric data also revealed the instrument frame was not in the centre of the rip channel, as shown in Figure 3.11. The rip channel can be seen between two sand bars with the centre approximately 100 m further offshore and 50 m to the south of the position of the instrument frame.

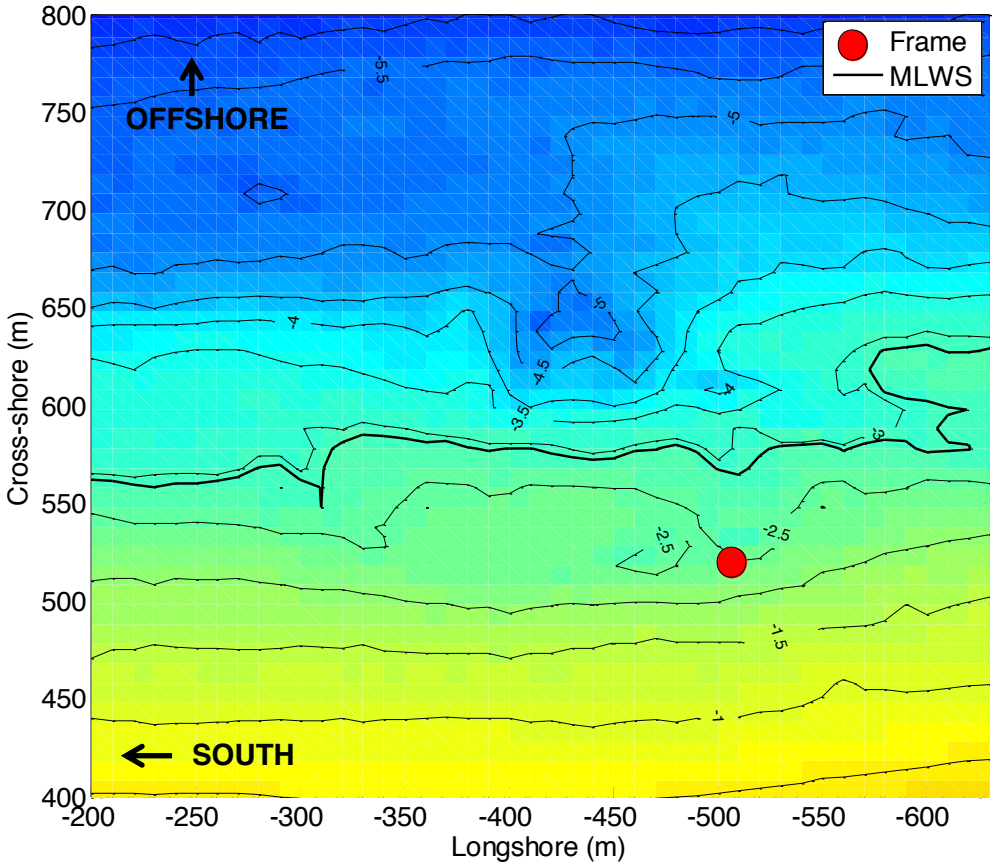

Figure 3.11: Contour plot of beach morphology from combined topographic and bathymetric surveys. Mean low water spring (MLWS) position and location of instrument frame is marked.

The details of the instrument calibration and data analysis are covered in detail in Section 3.5 and 3.6. However, it is useful to present some key observations as at this point, because the results of the preliminary experiments affected the design of subsequent field experiments. An example of one tide of processed data is presented in Figure 3.12. Figure 3.12a shows the bed evolution from the SRP over the tidal cycle. Initially the bed feature has a wavelength of 1.97 m and a height of 0.28 m. The bed shows a flattening throughout the tidal cycle. The hydrodynamic instrumentation was positioned at a lower elevation than the SRP, hence the extra data collected. Mean offshore directed flows of a maximum of approximately 0.3 m/s were measured at lower tidal elevations; this may be either residual rip current flow or bed return flow. Maximum sediment concentrations of 0.9 kg/m^3 were measured at z = 0.25 m on the

ebb tide, once the SRP indicated the bed had flattened out. Accordingly, a point measurement of mean transport was highest at this time with a maximum flux in the offshore direction of 0.2 kg/m^2/s. Wave driven sediment transport was onshore throughout, transport rates decreased with the flattening of the bed from a maximum of 0.04 kg/m^2/s on the flood tide to 0.02 kg/m^2/s on the ebb tide.

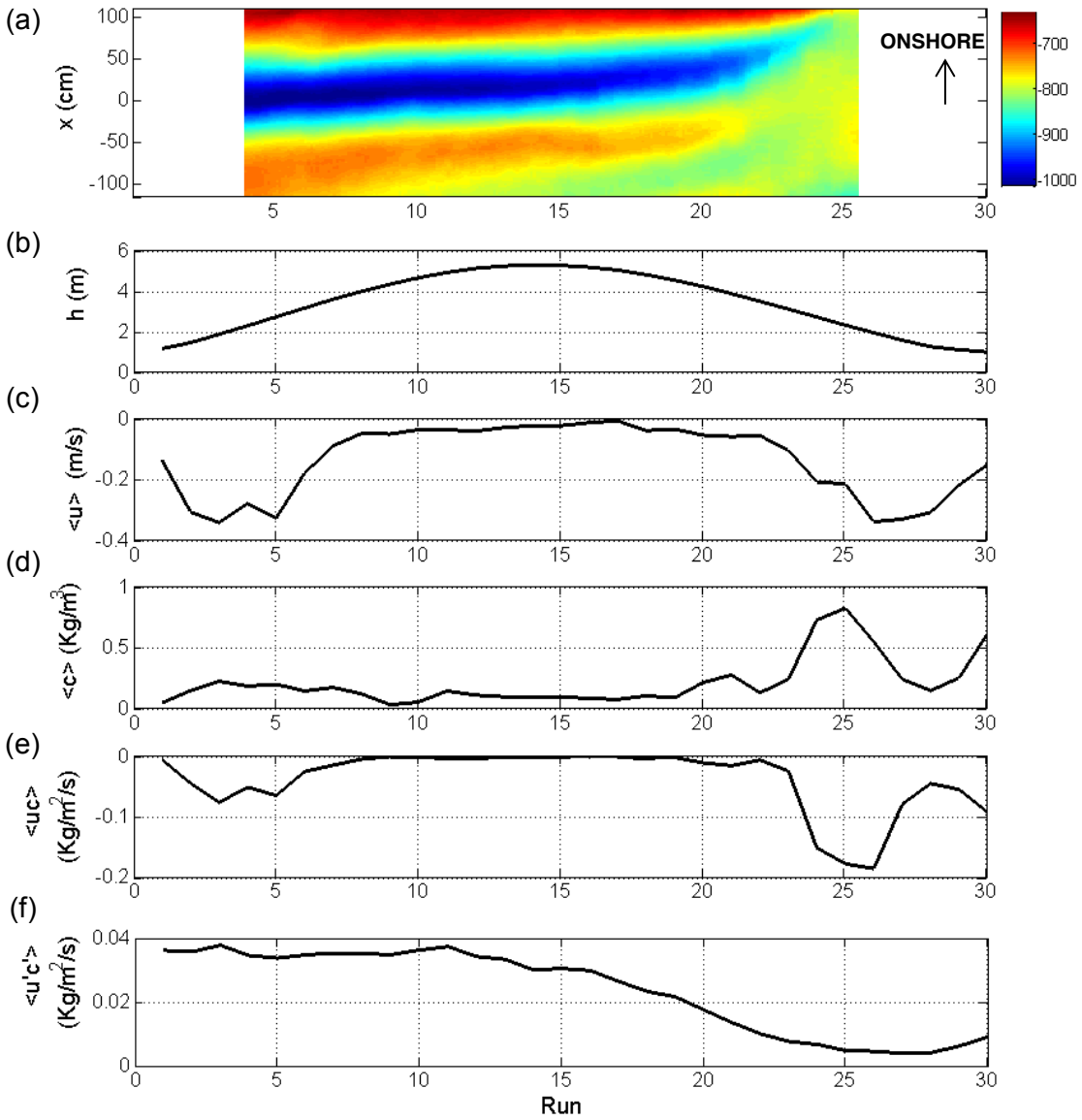

Figure 3.12: (a) Time-stack of bed evolution where hot colours represent crests collected every minute, the colour bar represent distance below the scanner (mm), (b) water depth (*h*), (c) cross-shore velocity (<u>), (d) mean concentration (<c>), (e) mean sediment transport (<uc>) and (f) oscillatory sediment transport (<u'c'>).

Although the instruments did not collect data from rip current conditions in this experiment, the results have indicated that in shoaling and surfzone conditions megaripples; (i) develop in orbital velocities > 0.5 m/s, (ii) migrate onshore and that (iii) migration rates increase with wave skewness and are reduced by undertow (Miles et al., 2014b). Furthermore, the data indicated that ripple sizing is forced by orbital

excursion for large orbital velocities (Miles et al., 2014a). The data also indicates that bedform transport is secondary to suspended sediment transport, with a contribution of approximately 15 % to the total flux (Miles and Thorpe, 2015).

In terms of the objectives of the project, it was obvious that the deployment method needed to evolve so that the instrument frame could be carried in to position at spring low tide, in order that the measurements could be gathered from the centre of the rip channel. In practice this meant that the frame would need to be deployed by a large team wading into approximately 0.8 m of water.

3.4.3: Sediment Transport in Rip Currents 1 (*STIR 1*)

Perranporth, October 2011

The goals of *STIR 1* were the same as the previous experiment; that is to make new measurements of suspended sediment concentrations and bedform dynamics, with additional hydrodynamic measurements in a rip current. A change in the location of the site was considered, as there are places on the North Cornish Coast and South Devon Coast with topographic rip currents that are active at higher tidal elevations, allowing instrumentation to be deployed at low tide and become covered as the rip current becomes active. However, after careful consideration the decision was made to continue with Perranporth as a study site. This was because observations of ARGUS images and beach visits suggested the strong possibility of a well-defined rip system that would be accessible at spring low water. The experiment was once again timed to run parallel with the second round of field data collection of the DRIBS project. This meant that the large amount of infrastructure at the location was again available in addition to the strong possibility of a dynamic rip system.

Frame design

The instrument frame had to be light enough to be able to be carried into the rip channel and also stable enough not to move. The biggest challenges were the positioning of the SRP data logger and the SRPs themselves. At least part of the frame needed to be reasonably high to accommodate the SRP heads, potentially making it less stable. To address these issues the frame consisted of a triangle shaped base which sat on the bed on which the SRP data logger was mounted, therefore keeping its weight low, with one corner of the triangle having two vertical poles to support the SRPs and the other instrumentation (Figure 3.13). Each corner of the triangle had vertical poles of approximately 0.4 m in length that would sink into the sand and offer stability. SRPs were positioned far away from the logger as possible, in order to reduce the likelihood of measuring frame-induced scour and frame-induced bedforms. Observations by wading, and with swimming goggles at greater depths, identified that

the bedforms under the SRPs were a consistent shape and size with those elsewhere in the rip neck.

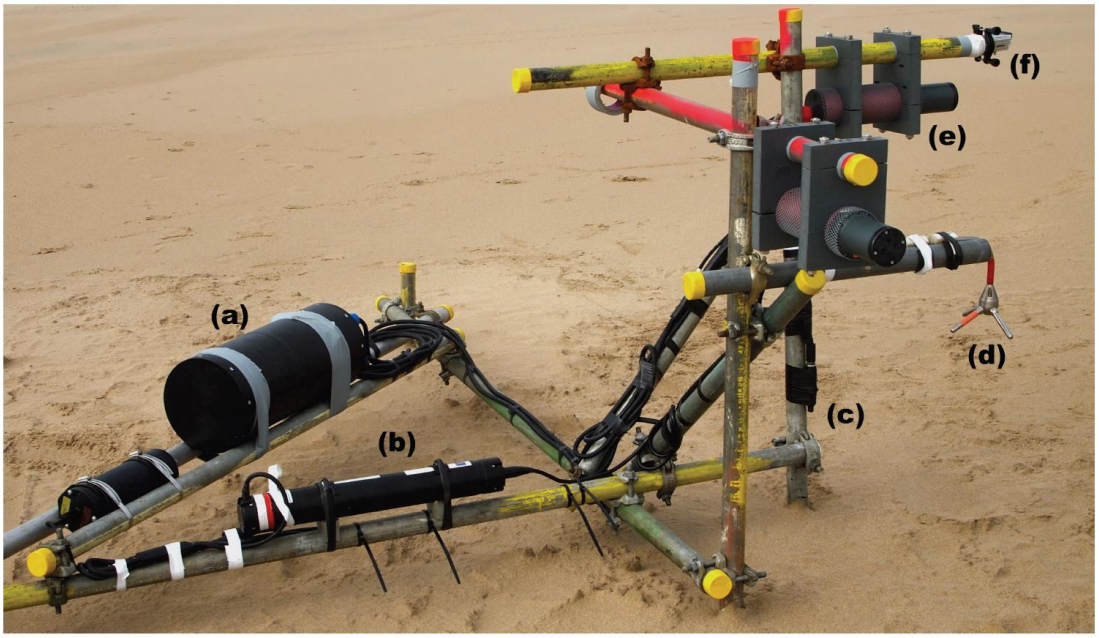

Figure 3.13: Photograph of instrument frame design and position of instruments; (a) SRP data logger and battery pack, (b) ADV data logger with internal PT (c) OBS (x 2), (d) ADV head, (e) SRP heads (x 2).

Instrument setup and deployment

Deployment of the instrument frame in the centre of the rip channel was only possible at spring low tide due to the sub-tidal nature of the rip morphology at Perranporth. The first deployment was for two complete tidal cycles over 14th and 15th October and the second was for four tidal cycles over the 26th, 27th and 28th October.

All instruments were programmed prior to being transported to the deployment site and secured to the instrument frame. The instruments were synchronized by carrying out the programming with the same computer. The ADV was programmed to record data at 8 Hz for the duration of each deployment. The channels that recorded data from both the pair of OBSs and the internal PT were activated. The SRPs were set to record bed scans sequentially every minute over a 120 degree swath arc, giving a theoretical scan footprint of approximately 3 m and a horizontal resolution immediately below the scanner of ~ 1.5 cm.

Table 3.2 shows the elevations of instruments relative to the bed level. An effort was made to co-locate all the sensors in the cross-shore orientation. The ADV head was positioned as close as possible to the cross-shore scan of the SRP without interfering with it, and with care taken that it was aligned in the cross-shore – longshore orientation. The OBSs were located in the same vertical plane and were aligned to be on the same cross-shore line as the sensing volume of the ADV.

Table 3.2: Instrument heights relative to the bed level at the beginning of the first deployment in *STIR 1.*

Instrument	Height (m)
SRP	0.9
ADV	0.45
PT	0.2
OBS 1	0.45
OBS 2	0.25

All instruments were monitored throughout daylight low tides and instrument heights relative to the bed level recorded. At the end of each deployment the frame was removed from the rip channel and data were then downloaded from the instruments.

Additional data consisted of topographic and bathymetric beach surveys, and GPS drifter deployments, all of which were undertaken as part of DRIBS project (Austin et al., 2012; Austin et al., 2014; Scott et al., 2014).

The resulting data set from *STIR 1* gave new measurements of bedform dynamics in a rip current with simultaneous sediment concentration and velocity measurements. The frame design worked well and the objectives of the experiment were fulfilled. Six tides of data were collected, that included 12 occurrences of rip currents, in wave heights ranging from 0.5 to 1.5 m.

3.4.4: Sediment Transport in Rip Currents 2 (*STIR 2*)

Perranporth, April 2013.

In *STIR* 1 continuous measurements of waves, currents and suspended sediment were collected, as were bed scans which consisted of approximately a 2 m foot print every minute from the centre of a rip channel. The requirement for further fieldwork was identified to increase the size of the data set and add diversity in terms of environmental conditions and the type of measurements made.

The theme of *STIR 2* was similar to that of *STIR 1*, in that a mobile frame would be deployed in the centre of a rip channel to measure waves, currents, bedform dynamics and suspended sediment dynamics. Various modifications were undertaken to improve the quality and resolution of the data:

- A second SRP was aligned in the same cross-shore transect to double the size of the scan footprint to approximately 4 m.
- A third OBS and a second ADV were used to allow vertically integrated suspended sediment transport to be calculated.

- A PT (TWR-2050) was deployed on the bar and in the feeder channel to investigate the hydrodynamic forcing in the rip current.
- A Trimble 5600 Total Station was used to measure bedform elevation in the rip, by walking high resolution cross-shore transects.

Frame design

The design of the instrument frame was adapted to allow the deployment of two SRPs, both in the same cross-shore plane. The frame was a cuboid shape with the two SRPs deployed at each end of the frame hanging over the bed (Figure 3.14). The frame had legs in each corner that extended 0.4 m below the bed and two longshore aligned horizontal bars that would rest on the bed. A diagonal bar was added to make the structure rigid. The ADV heads and OBSs were placed on vertical bars in the middle of the structure so that measurements would be made at the centre of the combined bed scans. The frame was trailed prior to the start of the field experiment at the field site and was found to have a minimum impact on the currents and the bed and was stable in a range of wave conditions. As previously, the SRP was positioned as far from the logger as possible in order to minimize the possibility if measuring scour or bedforms induced by the frame. Observations by wading and with swimming goggles at greater depths identified that the bedforms were aligned shore parallel under the SRPs and were a similar shape and size to those elsewhere in the rip neck and appeared unaffected by the frame.

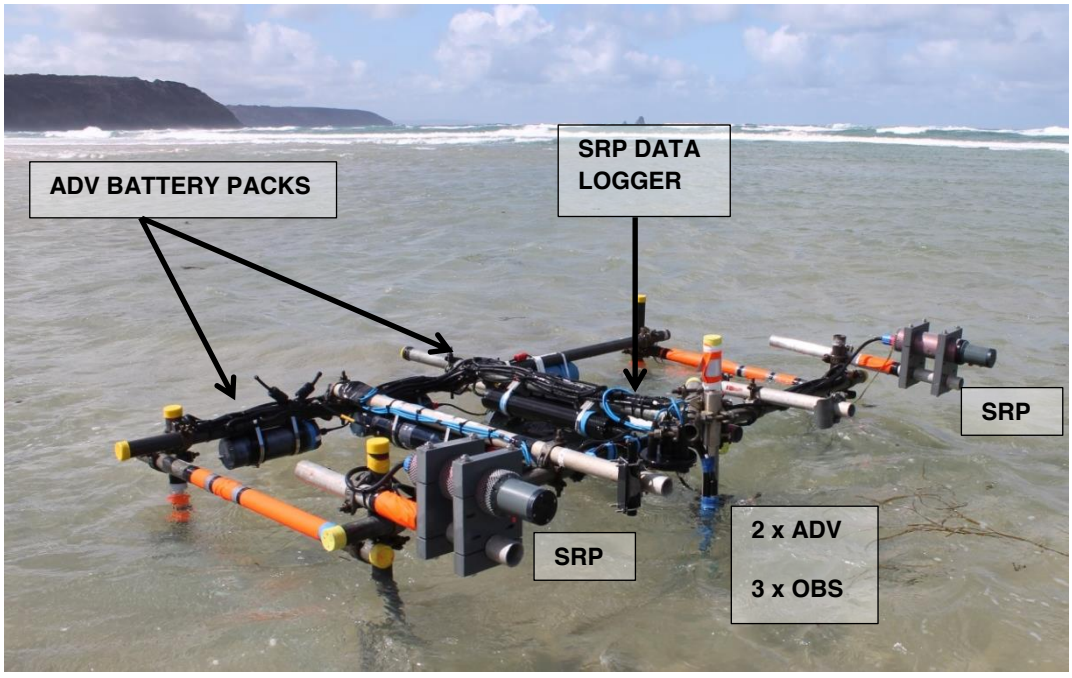

Figure 3.14: Photograph of instrument frame design and position of instruments; (*n.b.* ADV heads and OBSs are submerged and not visible).

Instrument setup and deployment details

As in *STIR 1*, all the instruments were programmed prior to being transported to the beach and where they were secured to the frame prior to deployment. The frame was deployed in the centre of a pre-determined rip channel for 6 days, encompassing 8 tidal cycles. The spring tide occurred on day 3.

The same instrument settings were used as in *STIR 1* for the ADVs and OBSs, with the exception that data were recorded at 4 Hz. This was done as the internal memory of the ADV housing units was not large enough to record at 8 Hz for 8 full tidal cycles. All instruments were synchronized by using the same computer for programming. The SRPs were positioned carefully so that the scans overlapped by approximately 0.5 m. They were programmed to scan the bed sequentially every minute with a swath arc of 120 degrees. Each scanner was positioned at heights of approximately 0.7 m above the bed, giving a theoretical scan footprint of 2.4 m, and a combined footprint of ~ 4.5 m, and a resolution of 1.1 cm directly below the scanner.

In Table 3.3 the deployment heights of all instruments are displayed. Instrument heights were recorded on all day time low tides, as were elevations and cross-shore and longshore position (using a total station).

Table 3.3: Instrument heights relative to the bed level at the beginning of the deployment in *STIR 2*.

Instrument	Height (m)
SRP 1	0.70
SRP 2	0.68
ADV 1	0.45
ADV 2	0.25
PT	0.20
OBS 1	0.45
OBS 2	0.25
OBS 3	0.05

Additional data collected consisted of topographic beach surveys, with data collected as part of a larger project on the beach morphology of Perranporth and adjacent beaches (Stokes et al., 2013). In addition, three TWR-2050 PTs were deployed, one on the instrument frame, one on the adjacent bar and one in the feeder. They were programmed to record 5 minutes 42 seconds of burst wave data every 17 minutes at 4 Hz. Two of three were secured to sand anchors with tape and cable ties which were twisted into the sand in on the top of the bar and in the centre of the feeder channel

(Figure 3.15). The third TWR-2050 was attached to a leg of the instrument frame. The position at which each TWR-2050 was deployed at was measured with the total station.

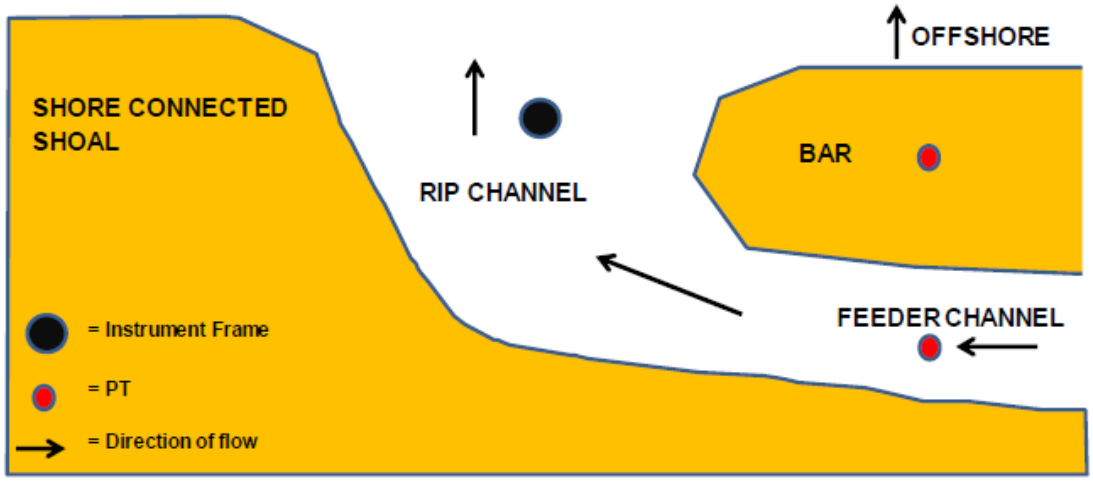

Figure 3.15: Schematic diagram showing a plan view of study area showing a simplified view of morphology and location of the instrument frame and PT during *STIR 2*. Instrument location and morphology in *STIR 1* was similar, although a PT was not present on the bar or feeder.

During *STIR 2,* 8 tides of data were collected, during which time the rip currents occurred on 15 occasions, in wave heights ranging from 0.9 m to 3 m.

3.5: Data Processing

In this section the methods used to process raw data into time series or into bed profiles used for further analysis are described.

3.5.1: De-spiking hydrodynamic data

Much of the hydrodynamic data was collected using an Acoustic Doppler Velocimeter (ADV) with external sensors (PTs and OBSs) attached. Recorded data were stored autonomously on different channels on the ADV's internal memory. The data was downloaded as a text file onto a PC and read into MATLAB, a numerical platform for data analysis and signal processing.

The first stage of the processing was to remove spikes from within the time series. As the ADV records the cross-shore, longshore and vertical velocity, the associated correlation of the signal strength for each 'ping' is also recorded. Spikes in the velocity data occurred when correlation values were low. Removing data points with a correlation of < 40% eradicated most spikes in the data (Martin et al., 2002; Nortek, 2010), and this cut off was therefore applied to the whole data set and the gaps interpolated (Goring and Nikora, 2002).

The data from the internal pressure transducer was de-spiked by removing all data points that were > 0.05 m in difference from adjacent data points and interpolating the gaps. Finally the pressure data was adjusted for the height the instrument was above the bed.

3.5.2 OBS calibration

The OBSs produced a voltage output in response to different sediment concentrations. An empirical relationship between voltage output and suspended sediment concentration was achieved by calibration of the instrument in known concentrations of sediment from the field site. It was important to source the sediment from the field site as grain size, distribution and the sediment composition can affect the voltage output (Downing et al., 1981).

To calibrate the OBS, the instrument was placed in a tank in a laboratory environment. Sediment (that has been dried and weighed) was added incrementally to the tank and the voltage output recorded (Campbell Cambell Scientific, 2013). One of the challenges of the calibration of quartz sand is the rate at which sediment falls out of suspension, particularly at high concentrations, which are prevalent in the surfzone. Studies using this instrument have used a recirculating tank, thus enabling concentrations of up to 100 g/l to be kept in continuous suspension (Downing and Beach, 1989). In this study a method developed by Butt et al. (2004a) in which sediment was mixed in glycerol was used for calibration. This allowed stable concentrations of up to 200 g/l. Glycerol is a clear fluid that has a higher viscosity than water, and therefore the settling velocity is reduced by three orders of magnitude compared to water. Glycerol has different optical properties to water, due to refraction and attenuation differences within the fluid; however errors introduced are accounted for in the calculation (Butt et al., 2004a).

To obtain the suspended sediment concentration (c) in units of kg/m^3 the following equation is used:

$$c = m\,(V_{output} - V_{offset}) \tag{3.2}$$

where m is the slope of the calibration curve and represents the gain, this is user controlled, V_{output} is the output voltage of the sensor and V_{offset} is the offset voltage.

A summary of the R^2 values for the calibration of each OBS is shown in Table 3.4. The average R^2 value is 0.97. For comparison Downing et al. (1981) obtained an average R^2 value of 0.99 for the calibration of the OBS. The calibration curves for each sensor used in *STIR 1* and *STIR 2* are shown in Figure 3.16.

Table 3.4: R^2 values for calibration of OBSs used in *STIR 1* and *STIR 2*.

Sensor	z (m)	Calibration Equation	R^2
STIR 1			
(a)	0.45	$c = 0.009 (V_{output} - 0.16)$	0.97
(b)	0.25	$c = 0.011 (V_{output} - 0.14)$	0.97
STIR 2			
(c)	0.45	$c = 0.019 (V_{output} - 0.19)$	0.99
(d)	0.25	$c = 0.019 (V_{output} - 0.19)$	0.97
(e)	0.05	$c = 0.036 (V_{output} - 0.42)$	0.97

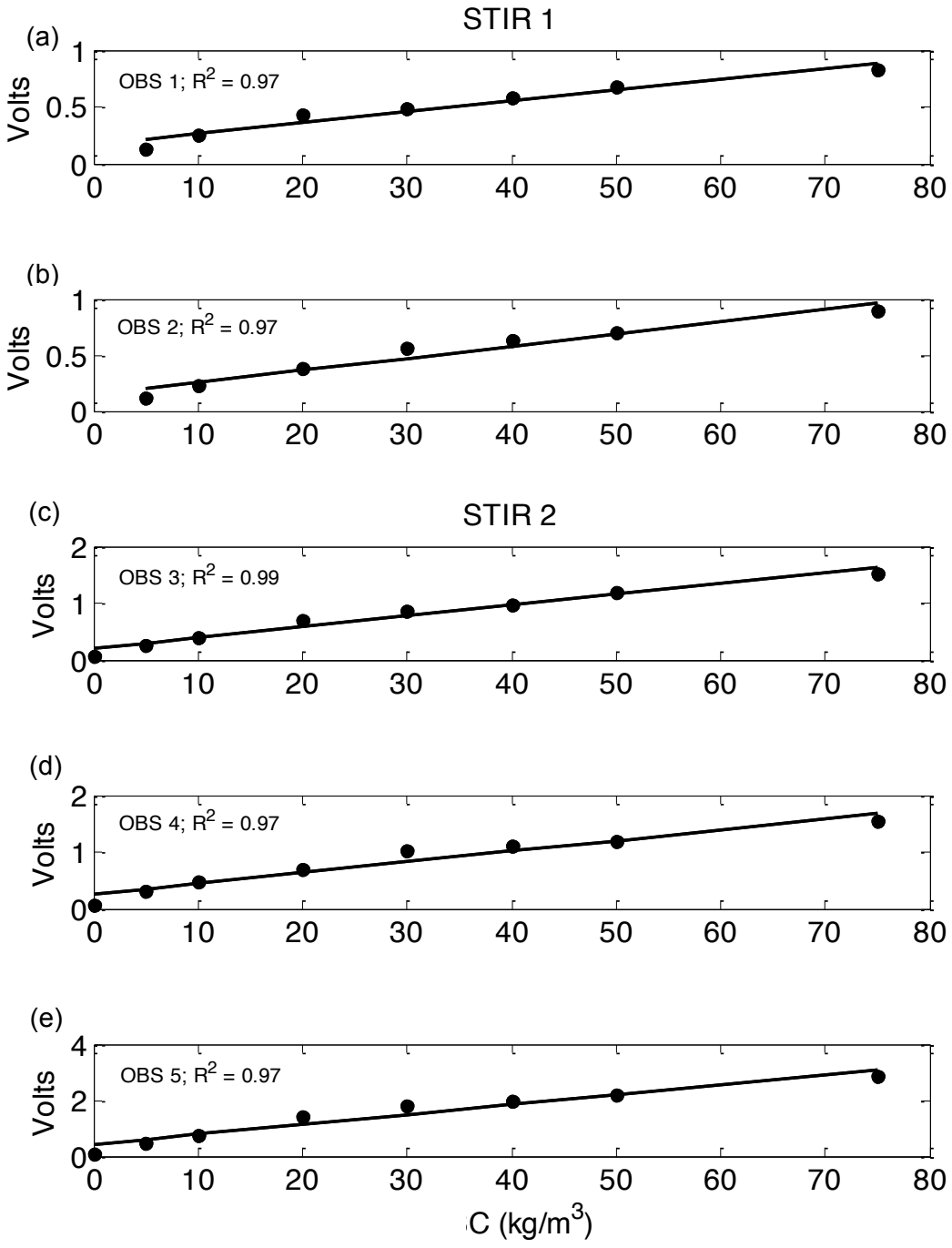

Figure 3.16: OBS calibration curves with R^2 value displayed for all sensors used in both *STIR 1* and *STIR 2.*

3.5.3: Processing SRP data

Data from the SRP were recorded in an ASCII (X, Y) co-ordinate system, with a text file written for every individual scan. All data were read into MATLAB with an associated time stamp.

Bed scans collected in the relatively shallow water of the rip current were occasionally subjected to breaking or passing waves, this had the effect of producing poor quality scans as acoustic pulses are reflected off other mediums than the sea bed. A common occurrence was that only parts of the scan would contain bad data, such as no returned pings or unrealistic returns. It is thought that this occurred as the scanner took approximately 20 seconds to complete a full scan so only part of the scan was affected by air bubbles or drying out of the scanner in the trough of a wave. To ensure as much data as possible was used, a 5 step averaging routine was applied by combining each scan with the two scans before and after following (Masselink et al., 2007). In most cases the combination of 5 scans allowed a complete bed profile of approximately 2 m for *STIR 1* and 4 m for *STIR 2* in length to be re-constructed. Following this, data points that were less than 500 mm below the SRP were removed (these points were deemed to be due to air bubbles or suspended sediment). A de-spiking routine was run to remove data points that were in excess of 50 mm from an adjacent data point. All the data were then interpolated on a regularly spaced transect, with data points 1 mm apart.

Prior to bedform statistics being calculated, the bedform data were filtered to remove small scale bed features and any noise within the data. All SRP scans were post processed to contain 2048 or 4096 (nearest 2^n) data points. Scans that contained less than 2048/4096 points were padded with zeros. Data was lowpass filtered at a length scale of 400 mm. A 1% Tukey window was applied to the data to remove the edges of the scan following filtering. Data points that fell outside this window were deemed to be unrealistic data and therefore removed (Figure 3.17).

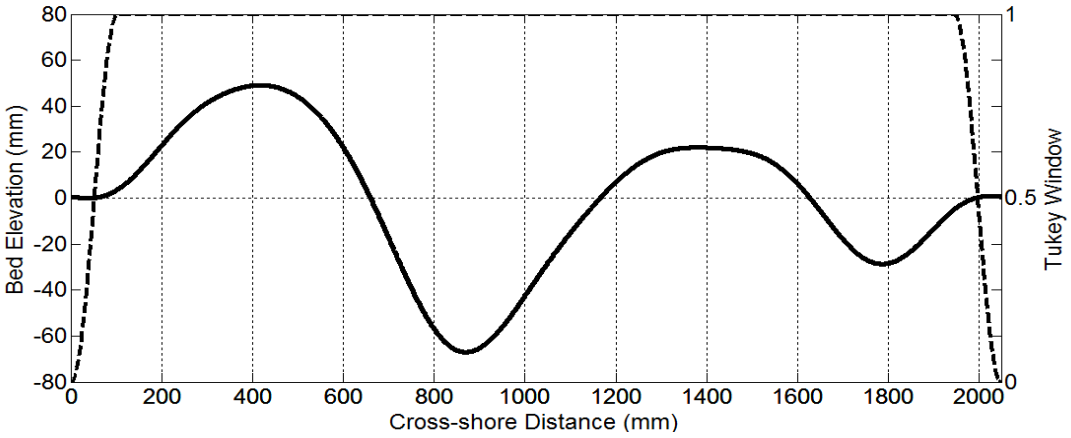

Figure 3.17: An example of a bed scan showing (solid line) with a 1 % Tukey window (dashed lines) applied.

Filtering at 400 mm frequency will remove wave ripples. Visual observations suggested that megaripples dominated the rip channel, and measurements made by Miles et al. (2014b) showed that wave ripples (i) only contributed to bed roughness in low energy conditions, and (ii) the contributed a relatively minor amount to total bed roughness in the presence of megaripples.

3.6: Data Analysis

3.6.1: Spectral analysis

To estimate different frequency fluctuations present in a time series it is necessary to shift the data from the time domain to the frequency domain (e.g. Huntley and Hanes, 1987). This is done in order to quantify the energy at different frequencies and thereby identify the relative importance of different processes. The conventional method for calculating spectral density estimates is by performing a Fast Fourier Transform (FFT) (Cooley and Tukey, 1965). The FFT method is most commonly used due to its computational efficiency (MathsWorks, 2014). It performs best when the original time series length is an integer power of 2 (Hegge and Masselink, 1996).

A useful spectral function is the power spectral density (PSD). The normalised PSD is proportional to the total variance in the original time series, as described by Parseval's theorem (Hegge and Masselink, 1996). It is calculated as the magnitude squared of the FFT of the original time series. The PSD is often visualised as a plot of frequency (Hz) against the spectral density. If the original time series was sampled in meters, at time intervals of seconds, the spectral density will have the units of meters squared seconds ($m^2 s^{-1}$) or meters squared per Hertz ($m^2 Hz^{-1}$). Producing only one estimate of PSD from the original time series introduces a large amount of variance. A method developed by Welch (1967) combines multiple spectral estimates from the same original time series, thus increasing confidence. The Welch method involves partitioning the time series into *m* segments of equal length and performing FFT on each segment and averaging the spectral estimates. It is also common to perform FFT on overlapping segments to further increase confidence (Hegge and Masselink, 1996), where typical overlaps are 50%. To prevent discontinuities arising in the data set, a windowing routine is used. A hanning window with a length the same as the data segment is applied to reduce 'ringing' (MathsWorks, 2014). The disadvantage of this method is that by separating the data into segments, the FFT is performed on fewer observations and therefore the frequency resolution (R_F) is reduced. This is a particular problem at very low frequencies. There is a balance to be obtained between variance and frequency resolution of the PSD. Resolution is calculated as;

$$R_F = \frac{2Ny}{S_w} \tag{3.3}$$

Where *Ny* is half the sampling frequency and S_w is the window size. To measure the confidence in the PSD estimate, the number of degrees of freedom (*ndf*) is assumed to be linearly related to the number of non-overlapping segments (Nuttal, 1971);

$$ndf = 3.82m - 3.24 \tag{3.4}$$

Using Figure 3.18 the upper and lower confidence limits can be identified by reading off the appropriate *ndf* from the *x* axis (Jenkins and Watts, 1968). Commonly, confidence limits are plotted as error bars alongside the PSD (e.g. Miles et al., 2002). It can clearly be seen that increasing the number of windows increases the *ndf* and therefore increases confidence in the PSD estimates.

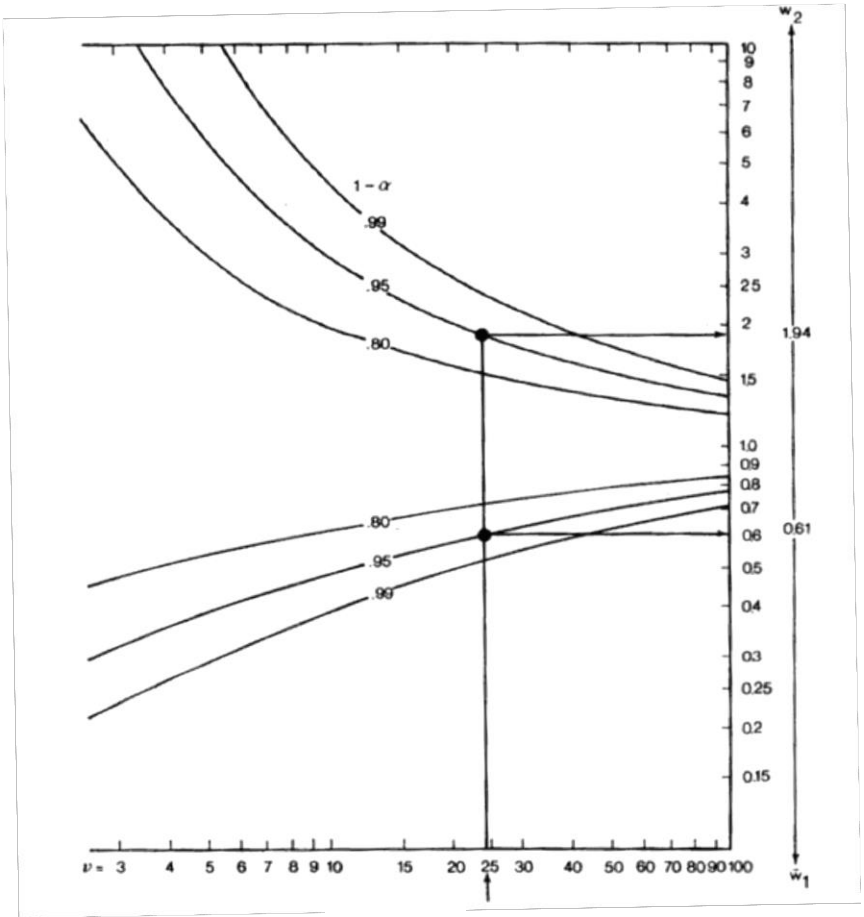

Figure 3.18: Relationship between *ndf* and multiplication factors to obtain upper and lower confidence limits at 80, 95 and 99% (Jenkins & Watts, 1968).

The co-spectrum quantifies the 'real' part of the cross spectral density of two time series. The output is the distribution of power per unit of frequency (MathsWorks, 2014). Huntley and Hanes (1987) used co-spectral analysis to identify the contribution of different fluctuations in the velocity time series and the suspended sediment time series to quantify sediment transport at different frequencies. They pointed out that if large

velocity fluctuations coincided with large suspended sediment concentrations at the same frequency, sediment would be transported. If they occurred at different frequencies or were out of phase with one another no transport would occur, therefore the co-spectrum quantifies the in phase oscillations. The units of the co-spectrum are the units of each times series multiplied by one another (*e.g. kg m^3 x m s^{-1} = kg/m^2/s*). The units can be normalised by dividing by the bandwidth (Butt and Russell, 1999) (*e.g. kg/m^2*).

The coherence squared represents how well the two time series are correlated as a function of frequency (Jenkins and Watts, 1968). A confidence limit (*CI*) for the coherence can be set using for the co-spectral estimates;

$$CI = 1 - sig^{\left(\frac{1}{0.5\,ndf-1}\right)} \tag{3.5}$$

where *sig* is the significance level (*i.e.* 0.05 = 95%). Values of coherence below the confidence limit would be deemed unreliable. For example, with 27 degrees of freedom, the 95% confidence limit would be 0.2 and co-spectral estimates with a coherence value less than this would not be reliable.

3.6.2: Filtering

Filtering is an operation that allows different frequency components to be separated out. This is done to investigate different frequency oscillations present in the time series, or to remove frequencies that are not of interest (Chatfield, 2013). Where low frequency variations are of most interest, short-period frequencies are removed from the original time series with a low-pass filter with a defined cut-off frequencies, above which all frequency variations are discarded. A high-pass filter removes the low frequency variations. A third type of filter is a band-pass filter; this removes both high and low frequency variations present in the original time series (Figure 3.19).

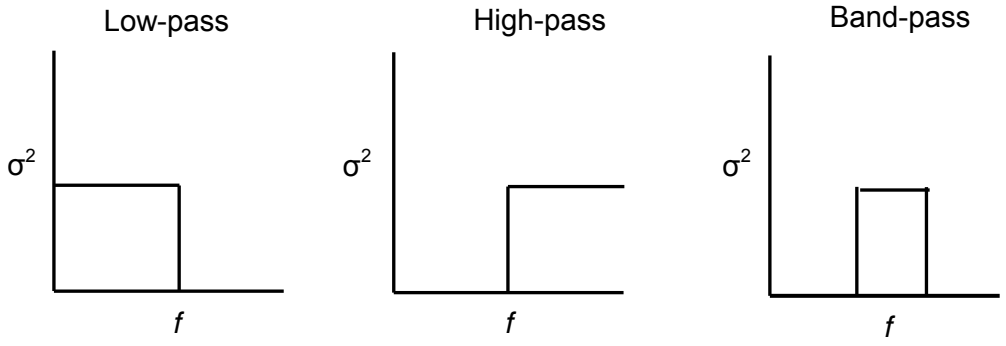

Figure 3.19: Schematic diagram of low-pass, high-pass and band-pass filters. The vertical lines represent the position of the cut-off frequency (Chatfield, 2013). It can be seen that the variance (σ^2) of the time scale changes as the frequency (*f*) increases.

3.6.3: Waves

Pressure records were corrected for pressure attenuation with depth prior to wave statistics being calculated (e.g. Miles et al., 2014b). Wave height and period were calculated from de-trended pressure data using a zero up-crossing method in which every data point immediately before the wave trace crosses zero is identified. Wave height is measured as the difference between the maximum and minimum elevation between consecutive up-crossings. Wave period is calculated by multiplying the number of data points between consecutive up-crossings by the sampling frequency in seconds. Wave height is given by the notation *H* for the mean wave height for the duration of the wave trace, or as H_s for the mean height of the largest 1/3 of the waves, termed the significant wave height. The mean wave period is represented by the notation *T*, the mean 1/3 of the largest wave periods is called the significant wave period (T_p) (Whitehouse and Sutherland, 2001).

Wave orbital velocity was calculated as;

$$U_m = 2\sqrt{\sigma_u} \tag{3.6}$$

where σ_u is the standard deviation of the velocity time series (Masselink et al., 2007). Wave skewness is a measure of wave shape. Skewed waves have larger peaks than troughs, positively skewed waves typically have a faster, albeit shorter, onshore than offshore stroke, and this can give rise to net onshore sediment transport and bedform migration (Gallagher, 2003). Un-normalised velocity skewness ($<u^3>$) is calculated from the oscillatory component of the cross-shore velocity, so this parameter includes information on both the velocity variance and the wave shape and is used in bedload transport models (e.g. Bailard, 1981). Normalised incident wave skewness (*S*) was calculated using velocity data high-pass filtered at 0.05 Hz following Elgar et al. (1988);

$$S = \frac{< u^3 >}{< u^2 >^{\frac{3}{2}}} \tag{3.7}$$

Wave asymmetry (*Asym*) can be defined as the skewness of the velocity acceleration (*accel*) and is used to quantify waves with a saw-tooth shape of the velocity time series (Miles et al., 2014b). Where the flow acceleration is:

$$accel(t) = \frac{\delta\, u(t)}{\delta\, t} \tag{3.8}$$

From this wave asymmetry is calculated following Elgar et al. (1988):

$$Asym = \frac{< accel(t)^3 >}{< accel(t)^2 >^{\frac{3}{2}}} \tag{3.9}$$

3.6.4: Currents

The notation u and v are given for the cross-shore and longshore flow respectively. The mean flow is calculated by time averaging the velocity time series and is denoted <*u*> and <*v*>. The resolved velocity is calculated following Austin et al. (2010);

$$r = \sqrt{< u >^2 + < v >^2} \tag{3.10}$$

The Froude number is a dimensionless expression of mean flow (u & v) and water depth. As rip currents are tidally modulated it has been used as a dimensionless representation of rip flow (Austin et al., 2010). Here it is calculated using the resolved velocity (*r*) and therefore it also accounts for the longshore component of the flow;

$$Fr = \frac{r}{\sqrt{gh}} \tag{3.11}$$

There are multiple forms of the mobility number. Here, the method of Gallagher (2003) was used as it includes both the mean and the oscillatory component of the velocity time series, where *s* is the specific gravity (a ratio of sediment to water density, 2.65 for quartz sand), *g* is acceleration due to gravity (9.81 m/s^2) and *D* is grain diameter.

$$\psi = \frac{(u^2 + v^2)}{(s-1)g\,D} \tag{3.12}$$

To define when the rip current was active, a simple model by Masselink and Black (1995), used to predict the expected cross-shore velocities (as a result of undertow), was compared to measured cross-shore velocities (Figure 3.20).

$$Expected < u >= \frac{\frac{1}{8}\sqrt{\frac{g}{h}\,H^2}}{h - \frac{H}{2}} \tag{3.13}$$

To consistently isolate the rip from non-rip conditions it was deemed that if 20 minutes of measured <*u*> (two consecutive observations at 10-minute averaging) exceeded expected <*u*>, then rip current conditions prevailed, but if in a 20-minute period the expected <*u*> exceeded measured <*u*> (after a period of rip conditions) this was defined as a return to non-rip conditions. The adoption of a 20-minute time window for the analysis gave results that were reasonably consistent with the expected rip dynamics. One tide of velocity data is displayed in Figure 3.20 with both the measured and expected <*u*> displayed. It can be seen they follow a similar trend at higher tidal elevations when <u> is weak. At lower tidal levels when the rip became active, measured <u> far exceeds the expected <*u*>, the point at which it is considered to be rip conditions is marked in red (Thorpe et al., 2014). The Argus images show wave breaking at the approximate period <*u*> was measured. It can be seen in rip conditions

that wave breaking patterns indicate three dimensional morphology and a cross-shore aligned rip channel. At high tide, in non-rip conditions there is no wave breaking.

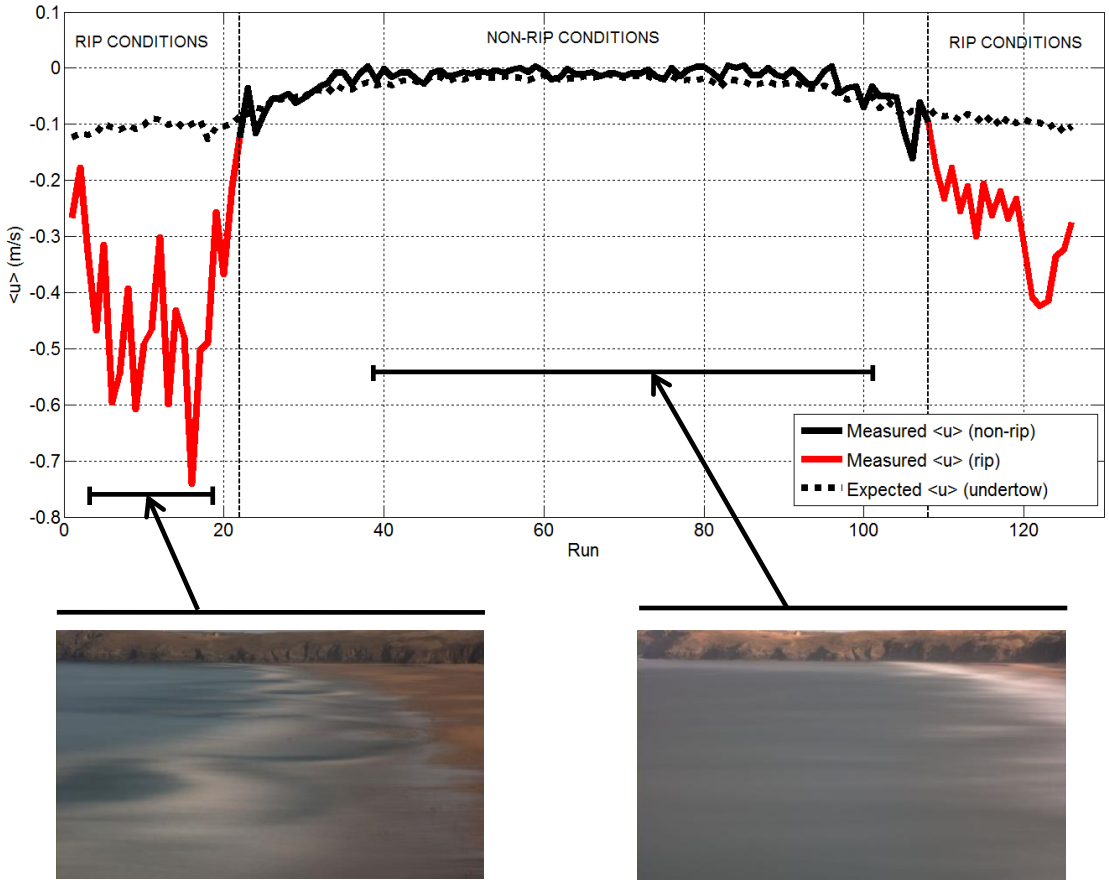

Figure 3.20: An example of rip identification. Measured <*u*> and expected <*u*> with rip and non-rip conditions marked (negative <*u*> is offshore). Argus images show wave breaking, and correspond to the approximate period when <u> measurements were made. There is no flood tide image as it occurred after dark.

3.6.5: Partitioning of suspended sediment flux

The suspended sediment flux was partitioned into the mean flux and wave driven flux following Jaffe et al. (1984). Both the time series of the cross-shore velocity (*u*) and the suspended sediment concentration (*c*) and are composed of a mean and fluctuating component where;

$$u = \langle u \rangle + u' \qquad c = \langle c \rangle + c' \qquad (3.14)$$

Where <> denotes time averaging and a prime denotes the fluctuating component (i.e. with the mean component removed). Therefore the mean sediment flux is the product of the time averaged velocity and time averaged concentration time series. The oscillatory sediment flux is the time averaged product of the de-trended velocity and de-trended concentration time series.

$$\langle uc \rangle = \langle u \rangle \times \langle c \rangle \qquad \langle u'c' \rangle = u' \times c' \qquad (3.14)$$

The oscillatory components of the velocity and concentration can be partitioned into frequency bands using filtering techniques, prior to the calculation of the oscillatory flux. This allows quantification of different processes of suspended sediment transport processes (Miles et al., 2002);

$$\langle u' c' \rangle = \langle u'c' \rangle_{VLF} + \langle u'c' \rangle_{IG} + \langle u'c' \rangle_{G} \quad (3.15)$$

where VLF, IG and G denote the very low frequency, infra-gravity and gravity frequency bands respectively.

3.6.6: Depth integrated suspended sediment flux

Depth integrated suspended transport were calculated so as to provide information on the total suspended load transport. When suspended sediment samples are collected as point measurements there are typically two methods to calculate depth integrated suspended sediment transport (Van Rijn, 1993).

Firstly, there is the partial method. This gives the total load suspended sediment transport from the lowest to highest sensors (Figure 3.21) by using a linear fit between the location of each sensor (Van Rijn, 1993). This method works best when multiple current and sediment concentrations measurements are made. The flux above and below the sensors may be ignored or extrapolated.

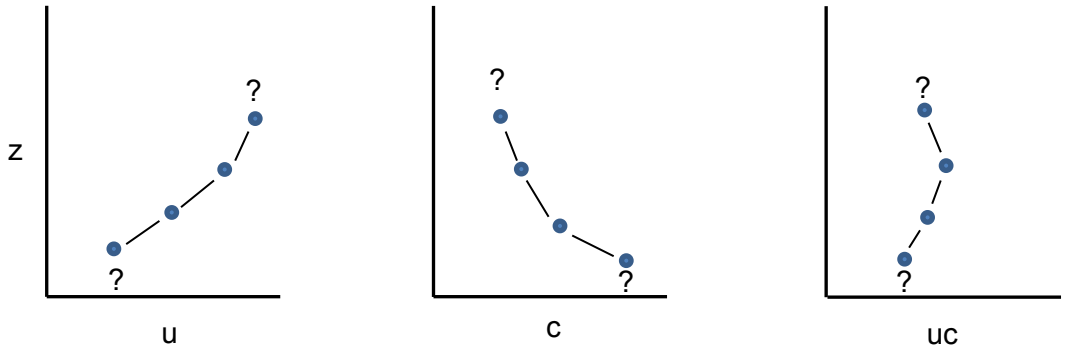

Figure 3.21: Partial method of processing depth integrated suspended sediment transport from point measurements.

The second method is the integrated method, which gives the suspended sediment transport between the bed and the water surface by fitting a theoretical distribution of velocity and concentration between the bed, the location of the point measurements and the water surface (Figure 3.22).

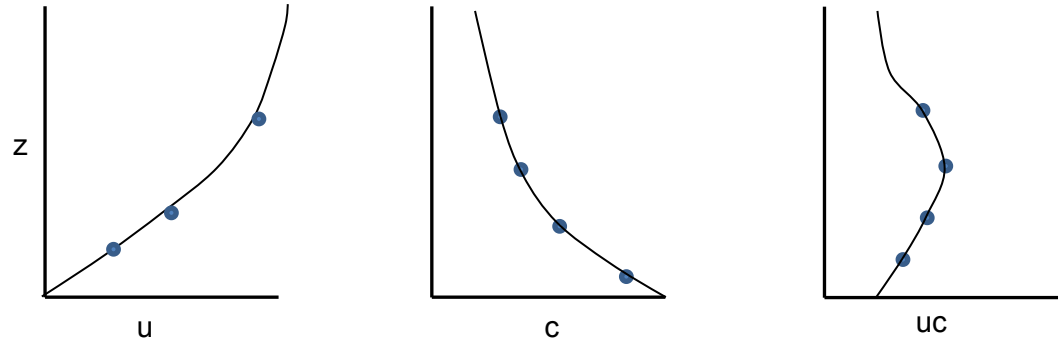

Figure 3.22: Integrated method of processing depth integrated suspended sediment transport from point measurements.

Given the number of sensors deployed in *STIR 1* (1 ADV and 2 OBS) and *STIR 2* (2 ADVs and 3 OBS sensors), an integrated approach was used to calculate depth integrated suspended transport. Velocity and concentration were calculated every centimetre for up to 9 m of water depth adhering to the following conditions as described by Miles and Thorpe (2015) and outlined in Figure 3.23:

Velocity

- From below the lowest sensor the formula of Van Rijn (1993) was used to construct a velocity profile.
- A linear fit was applied between the lower and upper ADV in *STIR 2*, in *STIR 1* data from only 1 ADV were used.
- Above the upper ADV a vertical profile was applied with a velocity equal to that of the upper ADV.
- Above the water surface the velocity is 0 m/s.

Concentration

- From below the lowest sensor the suspended sediment concentration was assumed to be depth uniform.
- The formula of Nielsen (1992) is used to fit a curve between the lower and upper OBS to the water surface.
- Above the water surface the sediment concentration is 0 kg/m^3.

It was not appropriate to extrapolate the concentration profiles below the position of the lowest OBS because this was likely to lead to an overestimation of the depth integrated flux. It is acknowledged that the technique used is likely to result in an underestimation of the total suspended load.

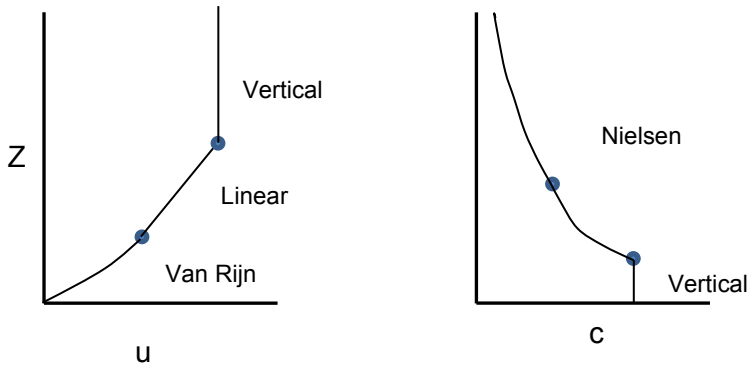

Figure 3.23: Schematic showing methods applied to calculate velocity and concentration profiles.

The formula of Van Rijn (1993) was used to calculate the velocity profile as it requires fewer assumptions than other methods that could have been used (Soulsby, 1997). The Van Rijn equation reduces the velocity to zero at the bed:

$$u_{(z)} = u \left(\frac{z}{z_1}\right)^{0.25} \tag{3.16}$$

Where z is the height above the bed, and the vertical velocity profile is fitted from the bed.

For rippled beds, Nielsen (1992) gives the variation in concentration (c) with distance from the bed (z) in terms of $c_{0,}$ a reference concentration at the bed, and $L_{s,}$ a length-scale representing the vertical diffusivity of the sediment.

$$c_z = c_o \, e^{-z/L_s} \tag{3.17}$$

Run-averaged values of concentration at the two heights measured were used to calculate run-averaged values of vertical diffusivity (L_s):

$$L_s = \frac{z_2 - z_1}{\log\langle c_1 \rangle - \log\langle c_2 \rangle} \tag{3.18}$$

Concentration at other heights (c_z), were calculated using OBS data from one height (z_1) and the vertical diffusivity (L_s) calculated from the two available OBSs:

$$c_z = c_1 \frac{e^{z_n/L_s}}{e^{z_1/L_s}} \tag{3.19}$$

where z_n is the height of the concentration prediction.

At each time step (t), a flux profile was obtained from the velocity and concentration profile. This was integrated to obtain a time series of the depth integrated sediment flux:

$$Q_s(t) = \sum_{z=0}^{z=h} \big(u(t,z)c(t,z)\big)\, dz \tag{3.20}$$

where dz is the depth interval between concentration and velocity predictions (0.01 m)

3.6.7: Bedform parameters

The bedform height was estimated as (Crawford and Hay, 2001);

$$\Delta = \sqrt{8\,\sigma} \tag{3.21}$$

where σ is the standard deviation of the bed scan. This is the equivalent of the root mean square equation often used for quantifying incident wave height (Masselink et al., 2007). Bedform wavelength was quantified by using the spatial lag corresponding to the largest negative auto-correlation of the bed scan (Masselink et al., 2007) (Figure 3.24b). The requirement for this method to work is that more than half a wavelength is present (Masselink et al., 2007) in the scan. Bedform length for the data collected in the total station transects was calculated by using a zero-up-crossing method (zero on the x-axis), similar to that used to calculate wave height.

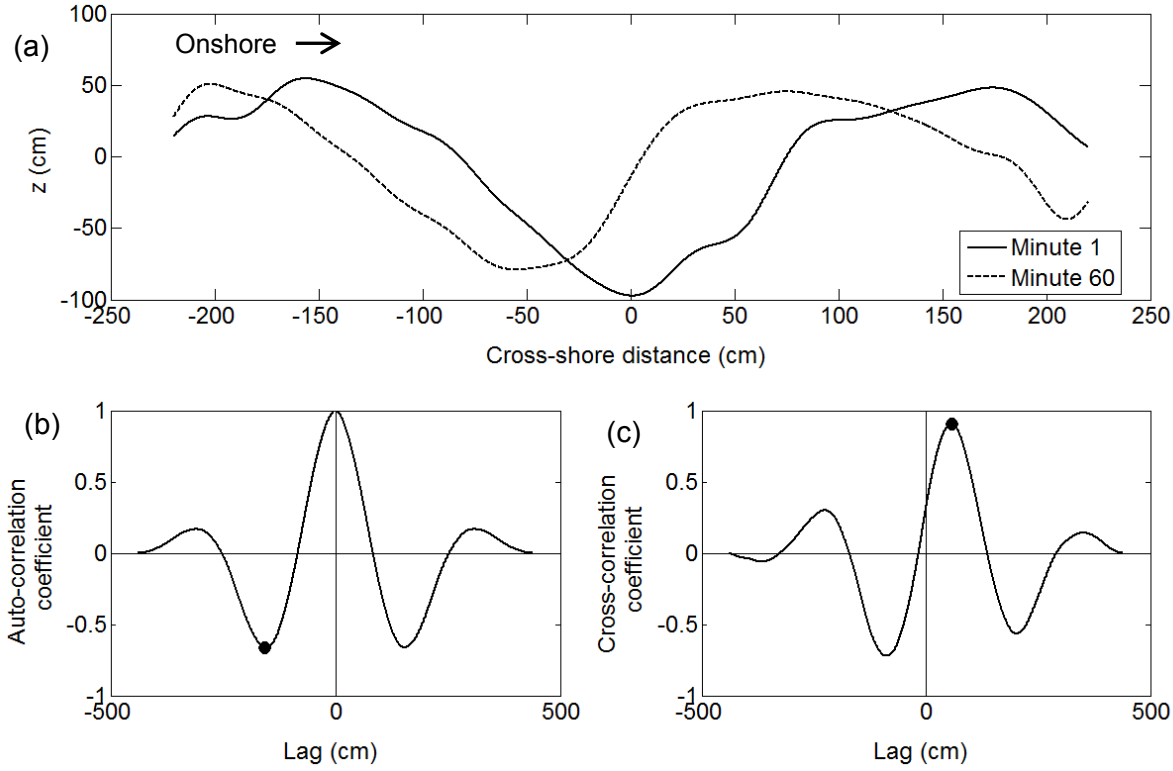

Figure 3.24: (a) Two processed SRP swaths 1 hour apart; (b) the strongest negative auto-correlation is a 156 cm for the scan at minute 1 representing a bedform wavelength of 304 cm and (c) the strongest positive cross-correlation between the two scans shows an offshore directed migration distance of 0.57 m in one hour.

Migration rate was determined by cross correlation of time separated bed scans, with the strongest positive correlation assumed to represent migration distance (Figure 3.24 a & c). This value was divided by the elapsed time to give migration rate as centimetres per minute (Masselink et al., 2007). A scan separation of 5-minutes was found to give results that were (i) of approximately similar magnitude to previous measurements and (ii) in keeping with visual observations of the images. Once the bedform statistics had

been calculated the time series of height, length and migration rate were bin averaged at 5-minute intervals.

Bedform migration rate can be used as a proxy for sediment transport, in some cases it has been referred to as bedload transport (Hoekstra et al., 2004), however in this case it will be termed the bedform sediment transport rate (Huntley et al., 1991; Masselink et al., 2007). It is assumed to be made up of bedload transport and an unquantified amount of saltation.

The bedform transport rate is based on the cross-sectional area of the bed feature and is calculated from its height and migration rate. The assumption is that the geometry stays constant within each run (5-minutes in this case). The equation is as follows (Kachel and Sternberg, 1971; Huntley et al., 1991; Masselink et al., 2007);

$$Q_b = 0.59\,\rho_s\,\Delta\,M_r \tag{3.22}$$

where 0.59 is a constant based on sand packing, ρ_s is sediment density (2650 kg/m^3), Δ is the mean height and M_r, the migration rate (m/s). Multiplying by the sediment density gives the final units in kg/m/s, this will allow for comparison with depth averaged suspended sediment fluxes.

CHAPTER 4: FIELD OBSERVATION OF RIP CURRENTS

4.1: Introduction

The aim of this chapter is to present results from both *STIR 1* and *STIR 2* that provide a spatial and temporal context for the results relating to suspended sediment transport and bedform dynamics presented later in this study.

An insight into the spatial scale and variability of the rip systems is achieved by presenting results from topographic and bathymetric surveys alongside data from ARGUS cameras and grain size analysis. The second part of this chapter examines the hydrodynamics of the rip systems on a range of time scales. This was achieved by quantifying offshore wave processes, *in-situ* velocity statistics and wave breaking on the adjacent bar. Morphological and environmental data were used to describe rip current forcing. Spectral analysis and filtering techniques were used to present evidence of rip current pulsing. Data used to create the plots showing the three dimensional morphology of the beach and drifter track data were collected during the DRIBS experiment in October, 2011 and kindly supplied by Scott and Austin (2012).

4.2: Beach Morphology

Perranporth is a 3.5 km long beach, that exhibits well defined rythmic low tide bar - rip morphology (Austin et al., 2010), as clearly seen in the time averaged ARGUS image in Figure 4.1, captured during *STIR 1*.

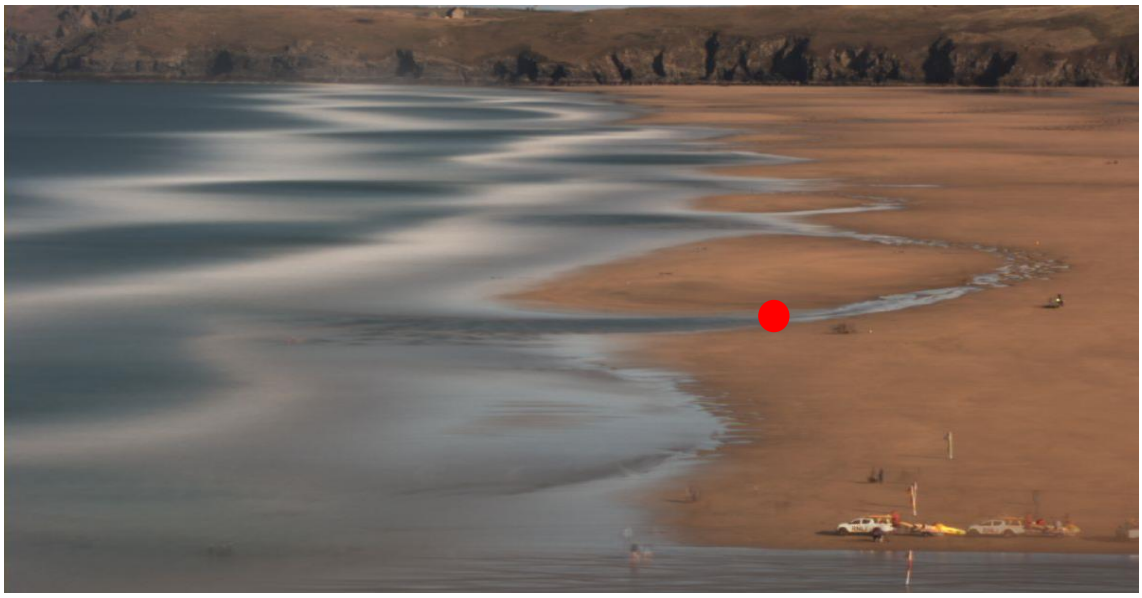

Figure 4.1: Time averaged ARGUS image of Perranporth Beach showing the quasi-regular bar - rip morphology at low tide. This image was captured on 28/10/11 during *STIR 1*. The instrument frame is marked.

4.2.1: Beach classification

To provide an estimate of beach slope in the study area, cross-shore profiles that pass through the instrument location were extracted from topographic data that were collected by an All-Terrain Vehicle (ATV). Figure 4.2 shows that the beach profile relative to mean sea level from the two field campaigns was very similar, with a beach slope (*tan β)* of 0.016 in both experiments.

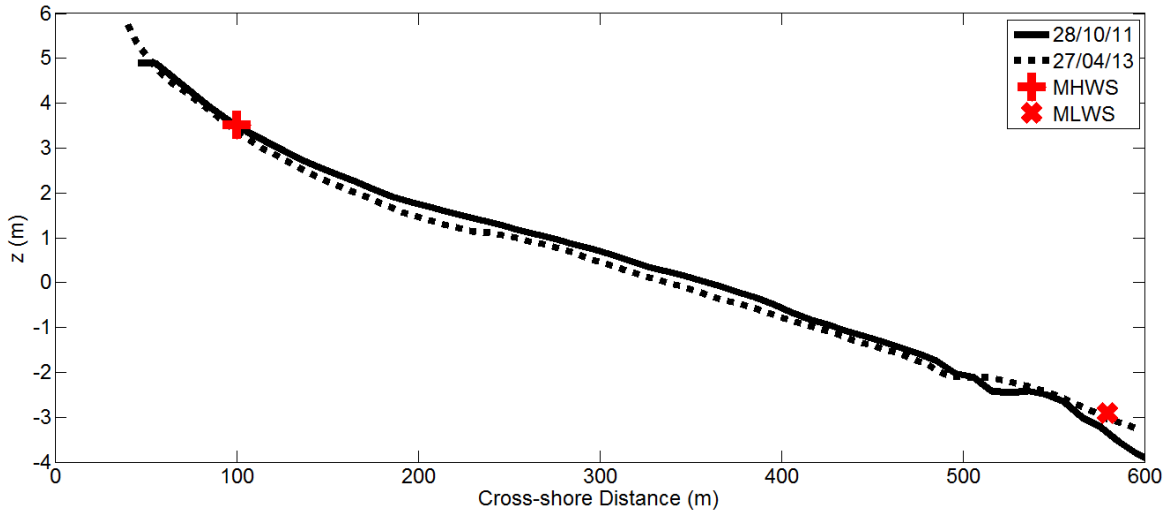

Figure 4.2: Cross-shore beach profiles taken during each of the two collection periods, in *STIR 1* and *STIR 2*. The profiles start from the bottom of the dunes (not shown) and all heights are given relative to mean sea level.

The beach is classified using three different conceptual models; the Dimensionless Fall Velocity (Wright and Short, 1984), the Surf Scaling Parameter (Guza and Bowen, 1976), and the Relative Tidal Range (Masselink and Short, 1993). Each model includes the breaker height parameter; this was defined as the highest 10% (H_{10}) of nearshore wave measurements for the duration of the experiment. This was found to correspond with the largest wave heights at the outer edge of the surfzone and with the wave conditions at the outer edge of the undertow.

The Dimensionless Fall Velocity (Ω) of Wright and Short (1984) predicts the beach classification based on the sediment fall velocity (w_s), breaker height (H_b) and period (T) following;

$$\Omega = \frac{H_b}{w_s T} \tag{4.1}$$

The Surf Scaling Parameter (ξ) predicts the beach as reflective, intermediate and dissipative (Guza and Bowen, 1976) based on the wave conditions and the beach slope (*tan β*).

$$\varepsilon = \frac{a_b w^2}{g \tan^2 \beta} \quad (4.2)$$

where a_b is the breaker amplitude ($H_b/2$) and w is the radian frequency.

These two approaches do not consider tidal effects on morphology, which may be significant in a macro-tidal environment. The model of Masselink and Short (1993) includes tidal range along with wave conditions and grain size by combining the Relative Tidal Range (RTR) with the Dimensionless Fall Velocity, where:

$$RTR = \frac{MSR}{H_b} \quad (4.3)$$

Table 4.1: Summary of beach classification models for *STIR 1* and *STIR 2*; Dimensionless Fall Velocity (Ω) (Wright and Short, 1984), Surf Scaling Parameter (ξ) (Guza and Bowen, 1976) and Relative Tidal Range (RTR) (Masselink and Short, 1993).

	H_{10} (m)	T (s)	Ω	ξ	RTR
STIR 1	1.0	9.6	3.3 Transverse Bar - Rip	86 Dissipative	6.3 Low Tide Bar - Rip
STIR 2	1.2	11.4	3.3 Transverse Bar - Rip	73 Dissipative	5.3 Low tide Bar - Rip

The conceptual models are sensitive to changes in wave height and period. In both *STIR 1* and *STIR 2* the beach is classified as Transverse Bar and Rip by the Dimensionless Fall Velocity, Dissipative by the Surf Scaling Parameter and as a Low Tide Bar - Rip beach by the Relative Tidal Range model. Visual observations of Perranporth identified a low tide bar punctuated by rip channels, and this was substantiated by surveys and ARGUS images, as shown in Figure 4.3.

(a) (b)

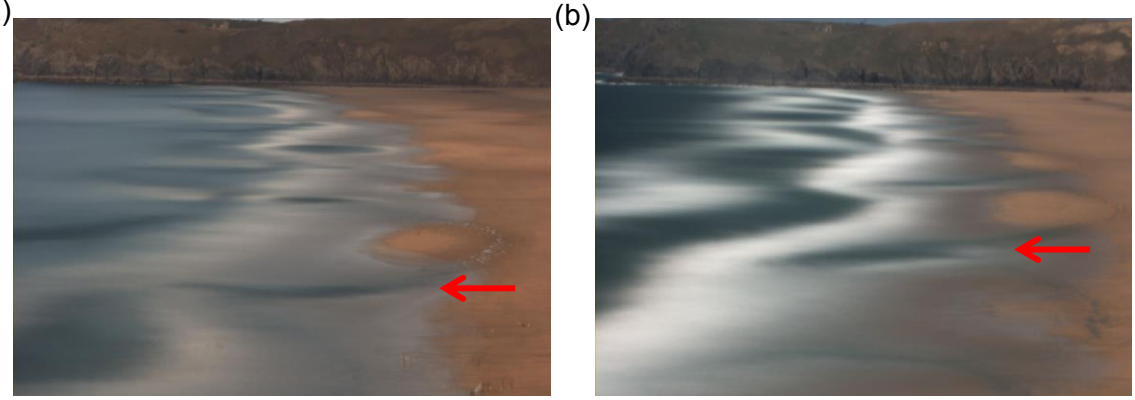

Figure 4.3: Time avergaed photos captured with an ARGUS camera during (a) *STIR 1* (28/10/11) and (b) *STIR 2* (26/04/13). The rip currents used in the study are marked.

4.2.2: Whole beach scale rip morphology

The three-dimensional morphology of the same section of Perranporth beach during both *STIR 1* and *STIR 2* is shown in the contour plots in Figure 4.4. The section of beach measures 1400 m in the longshore direction and 225 m in the cross-shore direction. In *STIR 1* (Figure 4.4a) there are three rip systems *(y* = -1100 m, -800 m and 400 m) with a small pertubation in the longshore morphology at approxtiamtley *y* = 100 m. During *STIR 2* (Figure 4.4b) there are two large, well defined rip systems (*y* = -1000 m and -600 m) as well as two smaller features (y = -250 and 50). All rip systems exist across the MLWS position (Figure 4.4), therefore they are features of both the sub-tidal and inter-tidal zones. The rip channels did not completely dry out in either *STIR 1* or *STIR 2* at spring low tide, although the adjacent sandbars did, suggesting the rip system is rarely fully exposed. The spacing between the largest rip systems was approximatley 400 m, with smaller systems showing reduced spacing of approximaltey 250 m in both *STIR 1* and *STIR 2*. The rips shown in Figure 4.3 appear in different locations, suggesting that rip formation does not favour a particular position on Perranporth Beach, or that if particular locations are favoured for rip formation, the rip channel is prone to longshore migration.

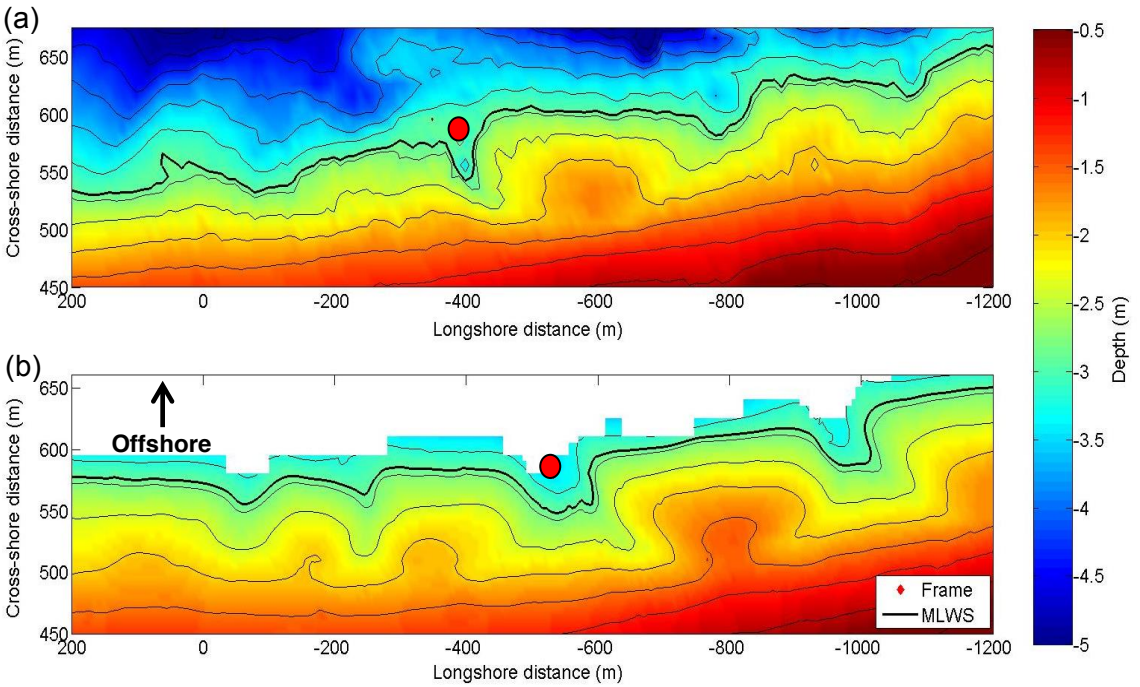

Figure 4.4: Contour plots showing morphology of Perranporth beach; (a) plot compromises of merged topographic and bathymetic data collected on 28/10/11 and (b) topographic data collected on 26/04/2013. Both data sets are rotated onto a local coordiante system. The instrument locations are marked. Elevations are realtive to Ordance Datum Newlyn (mODN).

Areas of wave breaking on rectifed ARGUS images (Figure 4.5) suggest that in both *STIR 1* and *STIR 2* the rip channels chosen for the study were the most pronounced on the beach. In both cases the rip channels are skewed towards the south and are fed

via a feeder channel that runs shore parallel, shoreward of a sand bar to the north. In *STIR 1* there is also a secondary smaller feeder system to the south of the rip neck, which is less evident in *STIR 2*. In both *STIR 1* and *STIR* 2 the instrument frame is situated in the centre of the rip channel. In *STIR 1* a rip head bar is present offshore of the rip neck. As there was no bathymetric data collected during *STIR 2* it is unclear from Figure 4.4 what the sub-tidal morphology is. However, wave breaking offshore of the rip system that is visible in Figure 4.5 indicates the presence of an offshore longshore bar across the whole longshore profile of the beach.

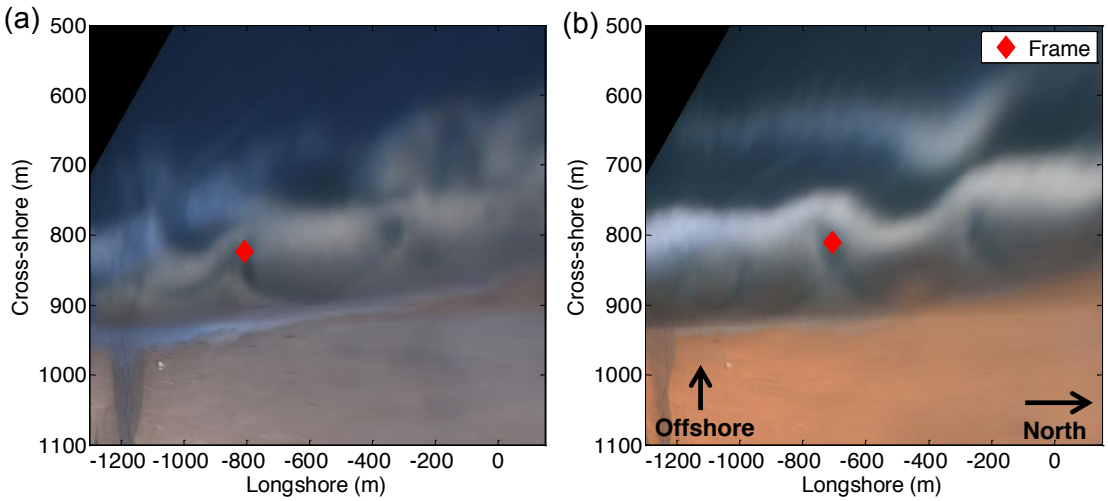

Figure 4.5: Rectified ARGUS images captured the same section of Perranporth Beach during (a) *STIR 1* on 28/11/11 and (b) *STIR 2* on 26/04/2013. The instrument frame position is marked.

4.2.3: Individual rip scale moprphology

In Figure 4.6 the three-dimensional morphology of the indiviual rip systems studied in *STIR 1* and *STIR 2* are presented, with the position of the instrument frame marked. The rip system in *STIR 2* is larger than the rip system in *STIR 1* in the cross-shore and longshore orientation as well as in depth. This can be seen visually in Figure 4.6. The difference in height between the top of the bar and the deepest part of the rip channel was approximaltey 1 m in *STIR 1* and 1.3 m in *STIR 2* (Figure 4.7). There is a longshore distance of 150 m and 260 m from the highest point of the bar to the deepest point in the channel (in the plane of the instrument frame) in *STIR 1* and *STIR 2* respectively. In *STIR 1,* 10 m of the width of channel was 1 m below the height of the bar crest (in the plane of the instrument frame). In contrast approximatley 70 m of the width of the channel was more than 1 m below the height of the bar crest in *STIR 2* (Figure 4.7).

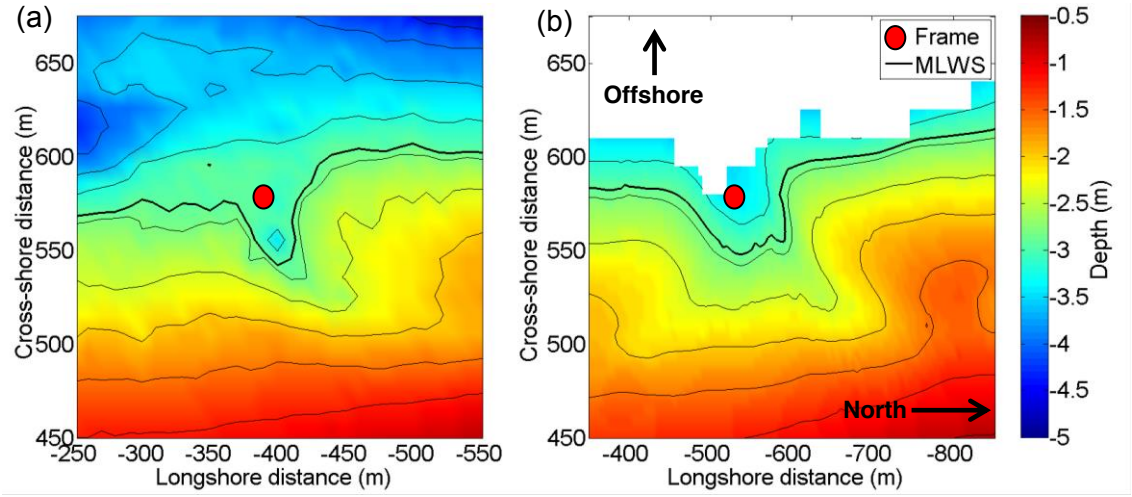

Figure 4.6: Morphology of Perranporth beach; (a) merged topographic and bathymetic data collected on 28/11/11 and (b) topographic data collected on 26/04/2013. Both data sets are rotated onto a local co-ordiante system. The instrument frame position ismarked. Elevations are realtive to Ordnance Datum Newlyn (mODN).

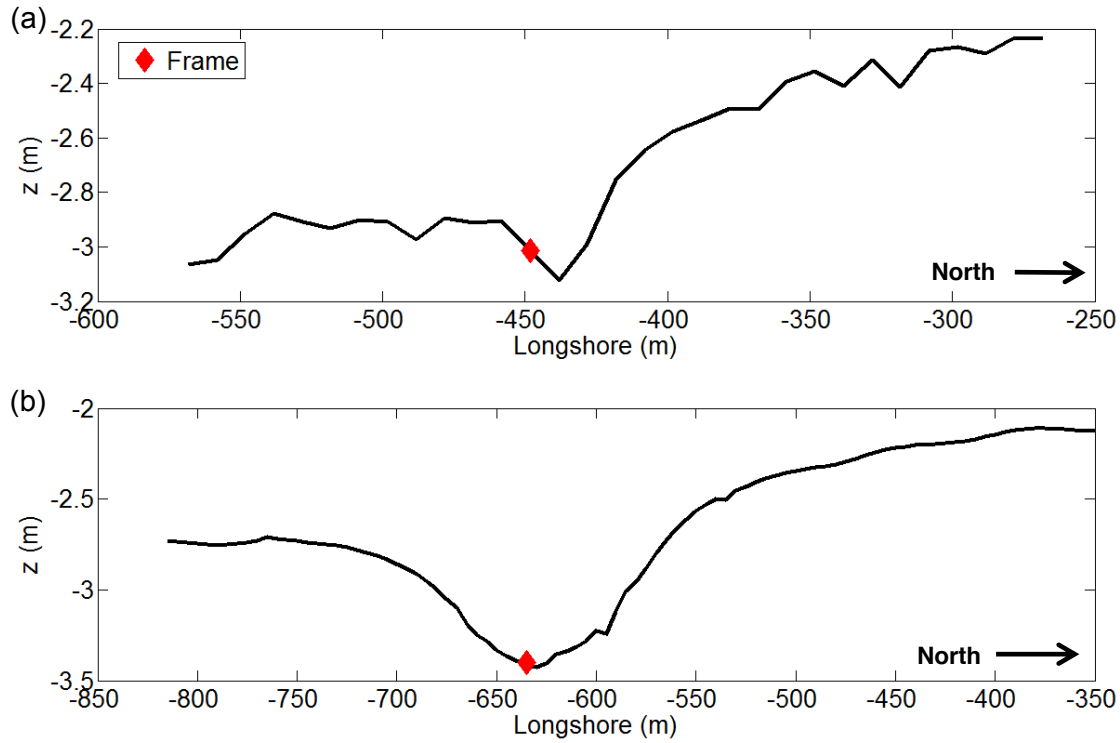

Figure 4.7: Longshore profiles through the instrument location during (a) *STIR 1* and (b) *STIR 2*. Elevations are realtive to Ordnance Datum Newlyn (mODN).

4.2.4: Spatial variability of rip current flow

Average drifter tracks from Lagrangian drifter measurements, made during *STIR 1* as part of the DRIBS project (Austin et al., 2012; Austin et al., 2014), are overlaid on to the corresponding contour plot of beach morphology collected on the previous day, (Figure 4.8). This allows the spatial variability of the rip flow to be visualised. Average drifter tracks were processed by dividing the surfzone into a 10 m x 10 m grid. The number of

individual passes per cell was calculated and cells with fewer than 3 drifter passes were discarded and the cells containing at least 3 drifter passes were averaged to find the mean velocity and track (Austin et al., 2012).

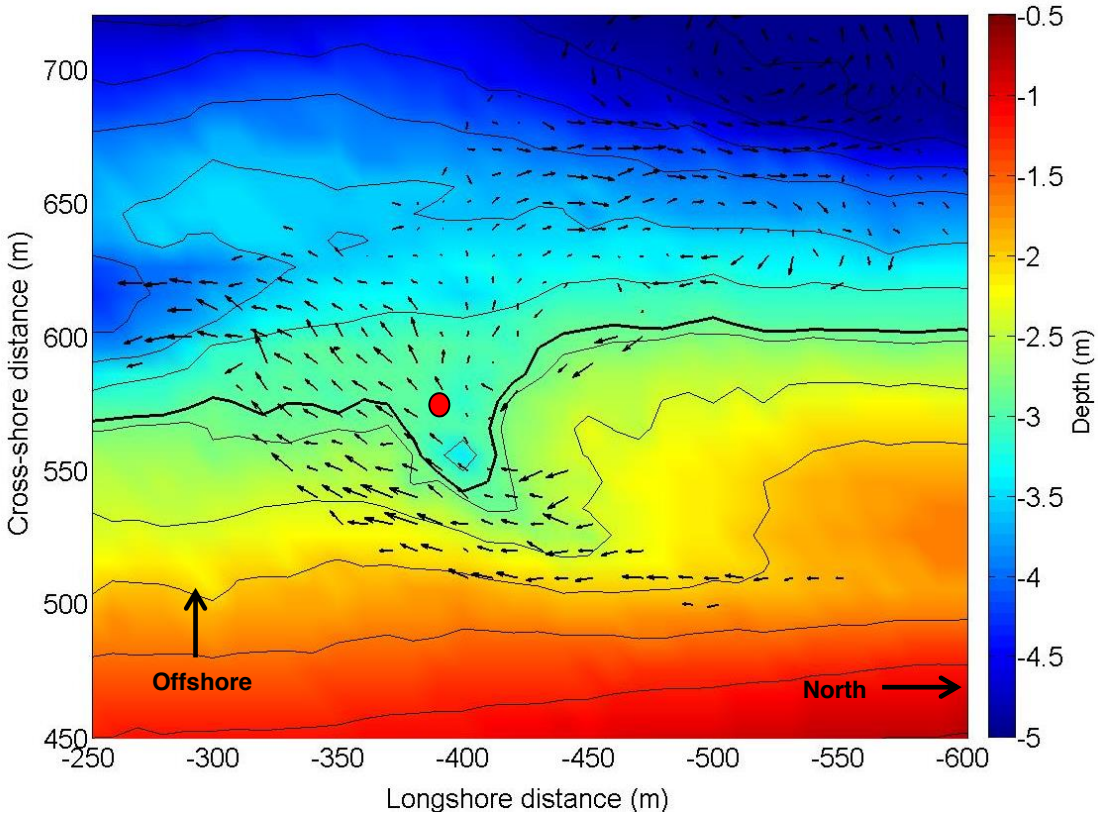

Figure 4.8: Contour plot showing beach morphology and averaged GPS drifter tracks for 2 hours either side of low tide at the rip studied in *STIR 1*. Arrow length is proportional to rip speed and angle indicates flow direction. The instrument frame and the MLSW position are marked. Elevations are realtive to Ordance Datum Newlyn (mODN). Data kindly supplied by Scott and Austin (2012), figure reproduced indepedntly.

Following the flow from its origin at the north end of the feeder channel, where the drifters were deployed, it can be seen that the dominant flow is initially towards the south in the feeder channel and then follows a more offshore track in the rip neck. Beyond the MLWS position the drifters exhibit three different behaviour patterns; (i) they move in a southerly direction, (ii) circulate on to the bar to the north of the rip system or (iii) become drawn into a secondary sub-tidal circulation system approximately 150 m to the north and 100 m offshore of the position of the instrumentation. As the data is averaged two hours either side of low tide, these three different types of behaviour are not necessarily occurring simultaneously. However, the data does provide an insight into the spatial variability of the rip flow, with the main offshore directed flow being limited to approximately 120 m offshore of the instrument frame.

4.3 Grain Size Analysis

Sediment samples were collected from five locations on the beach for grain size analysis during *STIR 2*. These locations were the upper beach, the mid beach, the bar, the feeder channel and the rip neck adjacent to the instrument frame and are identified in Figure 4.9.

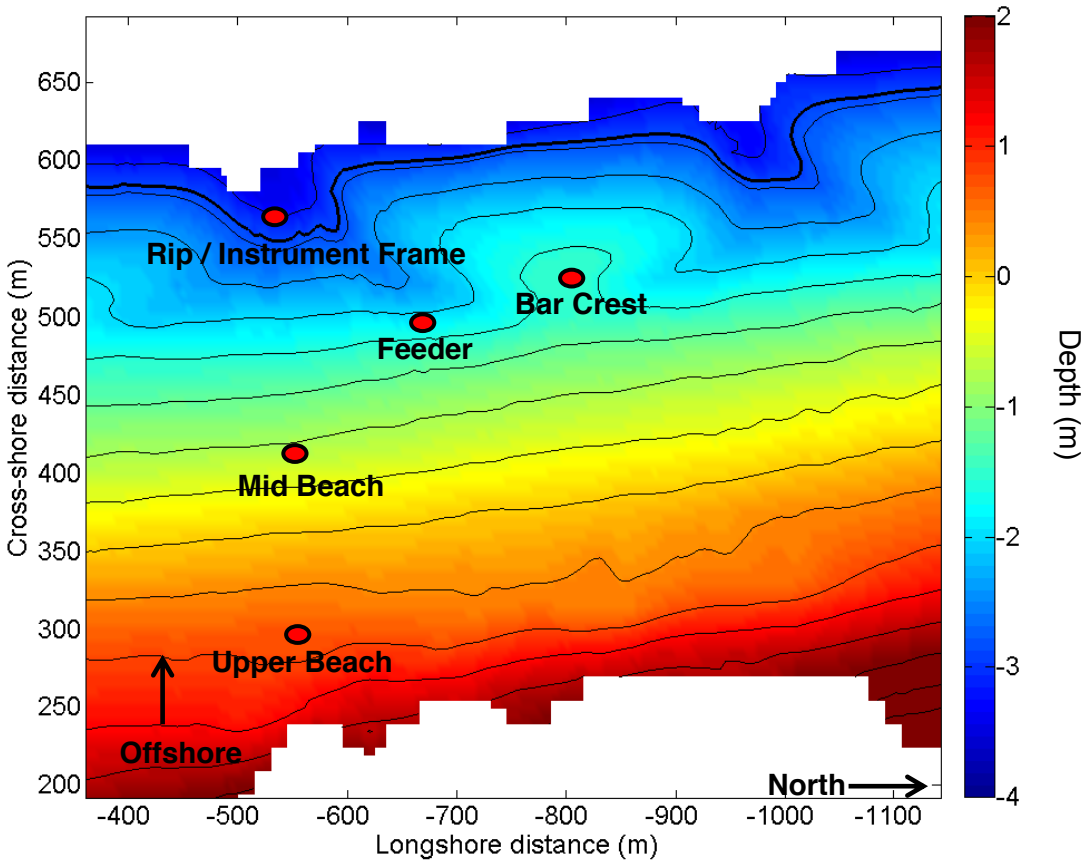

Figure 4.9: Contour plot showing the location of sediment samples.

Grain size analysis was performed in a settling column once sediment samples had been rinsed and dried. The median grain size (D_{50}) for each location is shown in Table 4.2. The grain size distribution suggests two distinctly different populations of sediment. The D_{50} (averaged over 3 sub-samples) in the rip neck was 0.66 mm, classifying the sediment as coarse sand based on the Wentworth scale (Dyer, 1986). The D_{50} for all other sample locations was between 0.39 mm and 0.40 mm, classifying it as medium grained sand, which is the grain size widely quoted to be present at Perranporth (Poate et al., 2009; Austin et al., 2010; Stokes et al., 2013). Figure 4.10 illustrates the difference in grain size between the rip neck and all other locations in which sediment was sampled. The figure is produced by plotting the percentage of each sample that falls between bands of the Wentworth scale. The similarity between each of the sub-samples (Figure 4.10b) for same locations shows the analysis was well replicated.

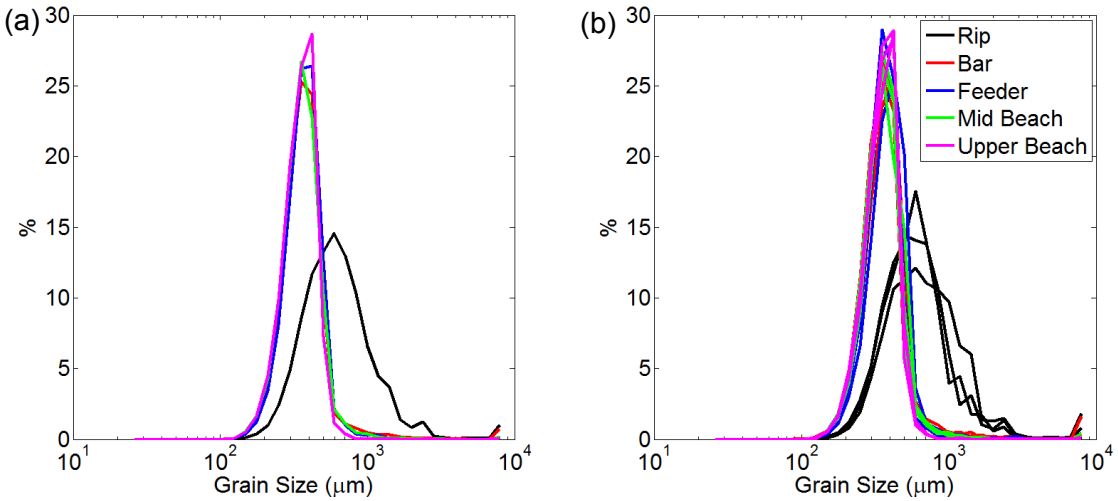

Figure 4.10: Percentage of each sediment sample that fall between bands of the Wentworth scale collected on three consecutive days; (a) mean (where 3 sub samples were averaged) and (b) individual sub-samples.

The standard deviation (σ) is used as measure of sediment sorting (Table 4.2). The standard deviation indicates that the sediment in the rip neck is the least well sorted, this is followed by the sediment from the bar and the feeder channel. The sediment collected at the mid and upper beach was comparatively well sorted with a standard deviation an order of magnitude less than the other sites.

Table 4.2: Grain size analysis results

	Rip	Feeder	Bar	Mid Beach	Upper Beach
D_{50} (mm)	0.66	0.39	0.40	0.39	0.39
σ (mm)	0.05	0.01	0.02	0.003	0.002

4.4: Quantification of Environmental Parameters

4.4.1: Offshore wave climate

Observations of offshore wave conditions were made with a Directional Wave Rider (DWR) buoy deployed by the Channel Coast Obsevatory (2015), 1 km offshore of the study site, in approximately 14 m of water. Observations were made for the entire duration of both *STIR 1* and *STIR 2* every 30 minutes in a wide range of offshore wave conditions, as shown in Figures 4.9 and 4.10. A summary of the tidal averages of offshore wave conditions are displayed in Tables 4.3 and 4.4.

In *STIR 1* significant offshore wave height (H_o) ranged from 0.5 m in Tides 1 and 2 to 1.9 m in Tides 5 and 6. Peak period was typically around 10 seconds with a maximum of 12 seconds recorded in Tide 4. There was evidence of a mixed wind and swell component in Tide 6, indicated by the period switching from between 5 to 10 seconds during the tidal cycle. The wave data suggests the wave angle of approach varied from 260° to 330° relative to the shore normal orientation of 293°. Tidally averaged wave directions indicate a general pattern of waves from the south, with the angle of incidence ranging from 273° to 291°.

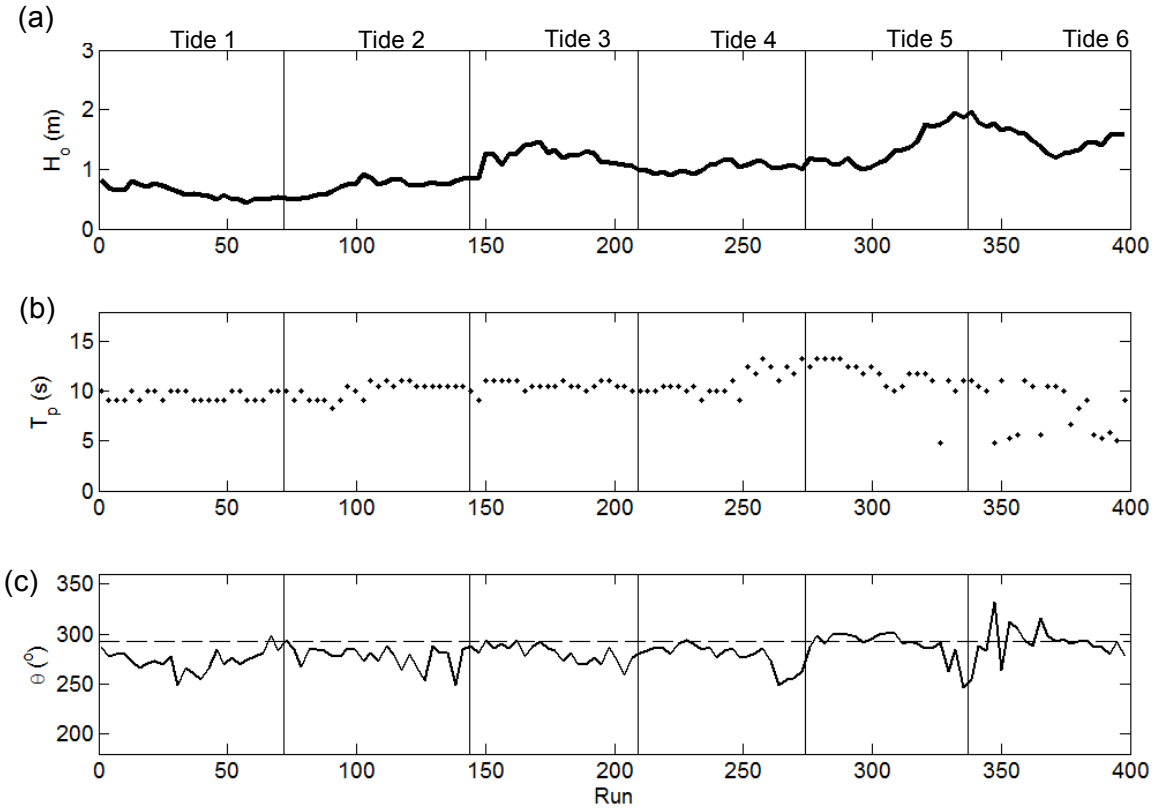

Figure 4.11: Offshore wave parameters collected from a DWR buoy during *STIR 1*; (a) significant offshore wave height (H_o), (b) peak offshore wave period (T_p) and (c) angle of wave incidence (θ), where shore normal is 293° (as indicated by the dashed line). Vertical lines represent the boundary between tides.

Table 4.3: Summary of offshore wave parameters during *STIR 1;* Average significant wave height over each tidal cycle (H_o), largest wave height during a tidal cycle (H_{Max}), average peak period (T_p) and average wave direction (θ).

Tide	H_o (m)	H_{max} (m)	T_p (s)	θ (°)
1	0.61	0.82	9.5	273
2	0.91	0.71	10.0	277
3	1.20	1.47	10.6	280
4	1.00	1.17	10.8	279
5	1.31	1.95	11.6	291
6	1.54	1.96	8.3	289

In *STIR 2,* H_o ranged from 0.9 m in Tide 1 to 3 m in Tide 4. The beginning and end of the experiment experienced swell conditions (T_p = 12 - 13 s), whereas in-between the two longer period swell events there were shorter period wind sea conditions (T_p = 6 to 8 s). The angle of wave incidence ranged from 282° to 300°, thus giving waves approaching from both south and north of shore-normal. Waves approaching from north of shore-normal were generally shorter period waves that were driven by a strong NW wind (10 – 28 knots), particularly in Tide 5 (28/04/2013). The longer period swells were generally from south of shore normal and were lower in height (e.g. Tide 1).

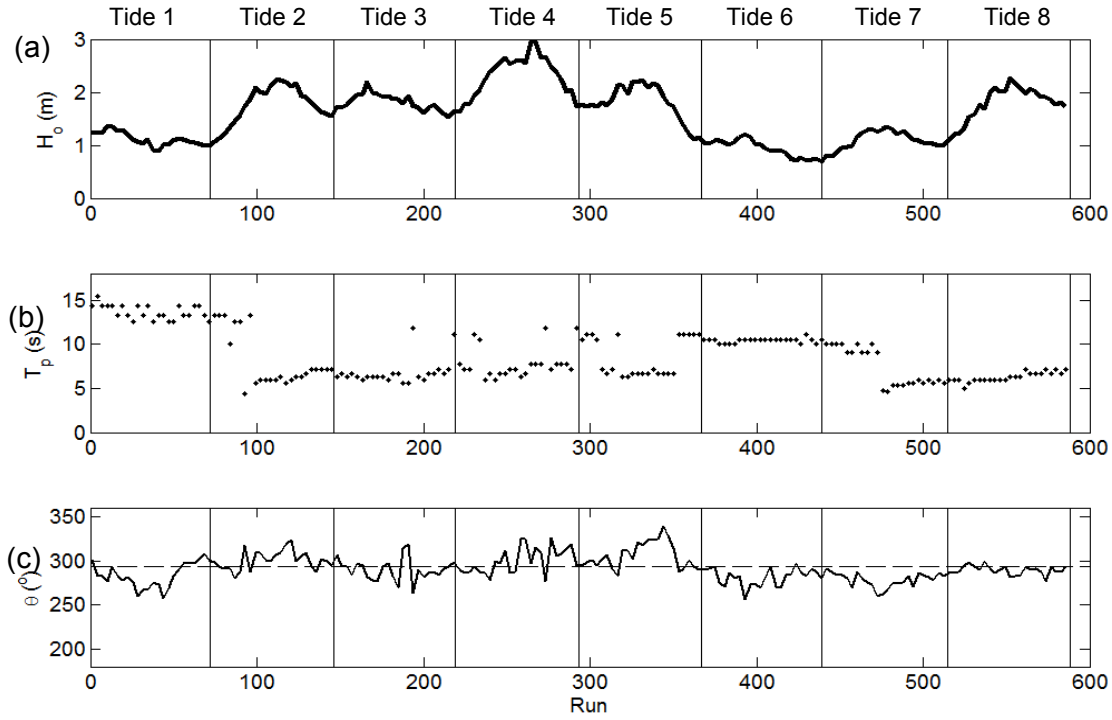

Figure 4.12: Offshore wave parameters collected from a DWR buoy during *STIR 2*; (a) significant offshore wave height (H_o), (b) peak offshore wave period (T_p) and (c) angle of wave incidence (θ), where shore normal is 293° (as indicated by the dashed line). Vertical lines represent the boundary between tides.

Table 4.4: Summary of offshore wave parameters during *STIR 2: A*verage significant wave height over each tidal cycle (H_o); largest wave height during a tidal cycle (H_{Max}); average peak period (T_p) and average wave direction (θ).

Tide	H_o (m)	H_{max} (m)	T_p (s)	θ (°)
1	1.12	1.38	13.6	283
2	1.77	2.23	8.02	300
3	1.81	2.19	6.8	289
4	2.3	2.96	8	300
5	1.72	2.7	8.5	305
6	0.91	1.22	10.3	280
7	1.16	1.36	6.8	279
8	1.86	2.27	7.3	291

4.4.2: *In-situ* velocity measurements

In-situ velocity statistics were calculated from 10-minute sections of instantaneous velocity data recorded at 0.45 m above the bed (Figures 4.13 and 4.14), at the instrument frame deployed in the rip channel.

Orbital velocity (U_m) maxima were found to occur just before and after low tide and ranged from 0.7 to 1.2 m/s in *STIR 1* (Figure 4.13b) and 0.5 to 1.4 m/s in *STIR 2* (Figure 4.14b). A decrease in U_m at the lowest tidal elevations is a result of wave dissipation offshore of the instrument frame. Minimum values of U_m were around 0.2 m/s and found at higher tidal elevations.

Maximum mean offshore directed velocity (<*u*>) during both *STIR 1* and *STIR 2* ranged from 0.3 to 0.7 m/s with velocities typically close to zero at high tide (Figures 4.13c and 4.14c). Overall the magnitude of rip flow was stronger and showed less variability in *STIR 2* than *STIR 1.* In *STIR 2,* <*u*> exceeded 0.5 m/s in all but 1 of 15 periods when the rip current was active (accounting for flood and ebb tides); whereas in *STIR 1,* <*u*> only exceeded 0.5 m/s in 1 of 12 periods when the rip current was active. The fastest instantaneous velocities were ~ 2 m/s and were recorded in *STIR 2.*

The method for identifying periods when the rip current was active (described in Section 3.6.4) appears to perform well. In *STIR 1* there were 12 occurrences of rip currents over 6 tidal cycles and in *STIR 2* there were 15 occurrences of rip currents over 8 tides. In Tide 7 of *STIR* 2 it can be seen that on the flood part of the tide the maximum <*u*> was 0.14 m/s (Figure 4.14c, run 453). During this period the rip current was deemed to not be active as it did not adhere to the rules identified in Section 3.6.4.

In *STIR 1* the longshore velocity (Figure 4.13d) was typically small in magnitude during the flood part of the tide (<*v*> = 0.18 to 0.27 m/s) and in the northerly direction (negative). On the ebb tide the velocity was greater (<*v*> = 0.37 to 0.52 m/s) and the flow was consistently in a southerly direction. This tidal asymmetry was not observed in the longshore flow during *STIR 2,* with flow being of similar magnitudes during the flood and ebb tides (<*v*> = 0.07 to 0.48 m/s) and also always being in the southerly direction. The dominance of the southerly flow in *STIR 2* is likely to result from strong North West wind and the associated North Westerly wave direction. The resultant velocity (<*r*>) represents the combined longshore and cross-shore components of the flow. Maxima were found at lower tides of up to 0.8 m/s (Figures 4.13e and 4.14e).

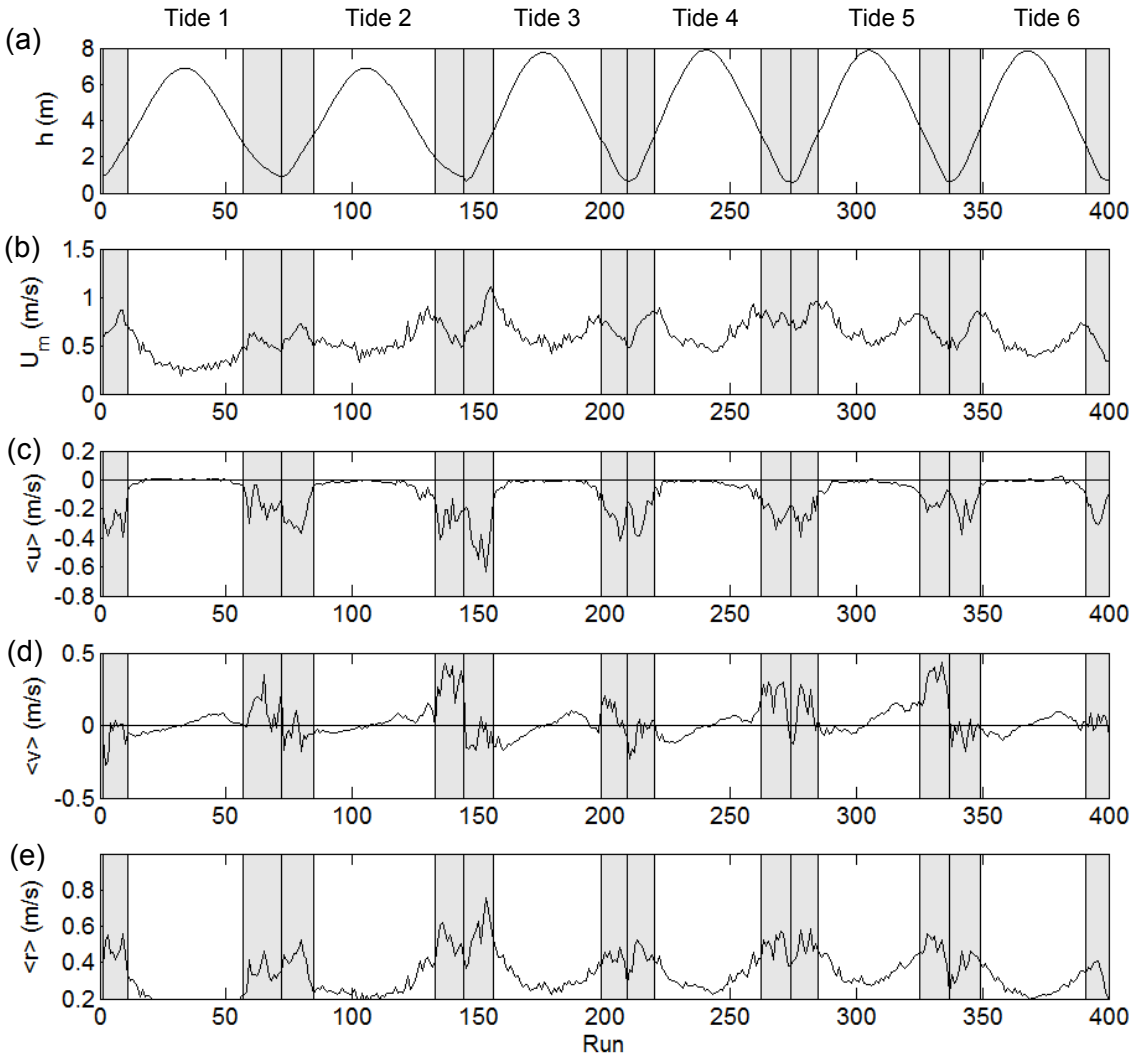

Figure 4.13: Summary of *In-situ* velocity parameters calculated from 10-minute sections of data collected during *STIR 1;* (a) water depth (h), (b) orbital velocity (U_m), (c) mean cross-shore flow (*<u>*), (d) mean longshore flow (*<v>*) and (e) mean resolved velocity (*<r>*). The shaded areas mark periods when the rip current was deemed to be active, the centre line in the shaded area represents the boundary between tides.

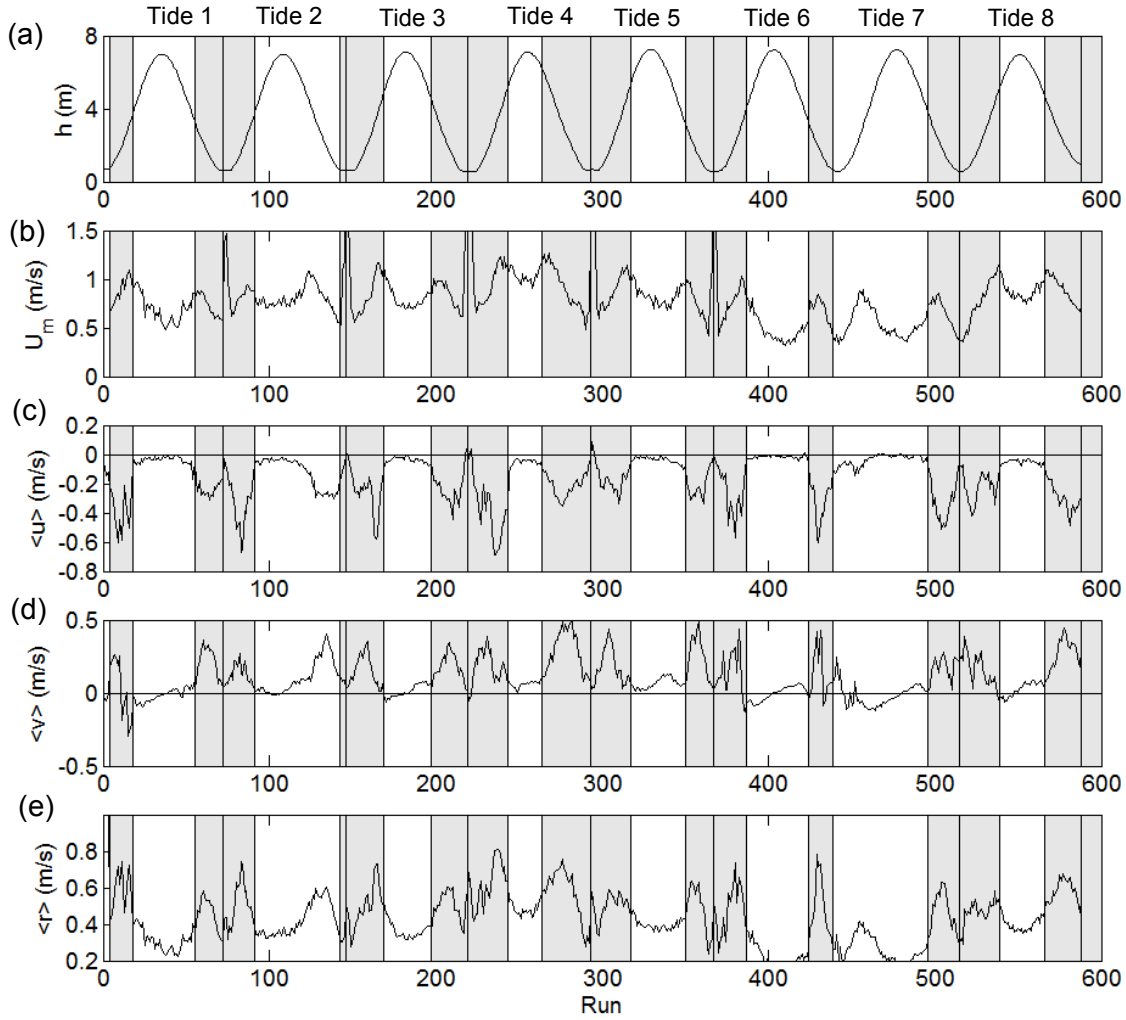

Figure 4.14: Summary of in-situ velocity parameters calculated from 10-minute sections of data collected during STIR 2 (a) water depth (h), (b) orbital velocity (U_m), (c) mean cross-shore flow (*<u>*), (d) mean longshore flow (*<v>*) and (e) mean resolved velocity (*<r>*). The shaded areas mark periods when the rip current was deemed to be active, the centre line in the shaded area represents the boundary between tides.

The resolved velocity is investigated further in Figures 4.15 (*STIR 1*) and 4.16 (*STIR 2*); the directionality of the flows over a whole tidal cycle for each tide is displayed in vector plots. In *STIR 1*, the flow direction exhibits a tidal asymmetry as observed in Figure 4.13d. On the flood tide the flow is either offshore directed or slightly north of offshore, as indicated by arrows pointing to the left or in an upward direction. On the ebb tide the flow is generally directed south of offshore. In the flood tides of *STIR 2* the observed trend is an initial southerly flow that becomes more offshore directed with greater depth. On the ebb tide the flow is predominantly in the southerly direction throughout, with the exception of Tide 6 (Figure 4.16f) where the flow direction fluctuates.

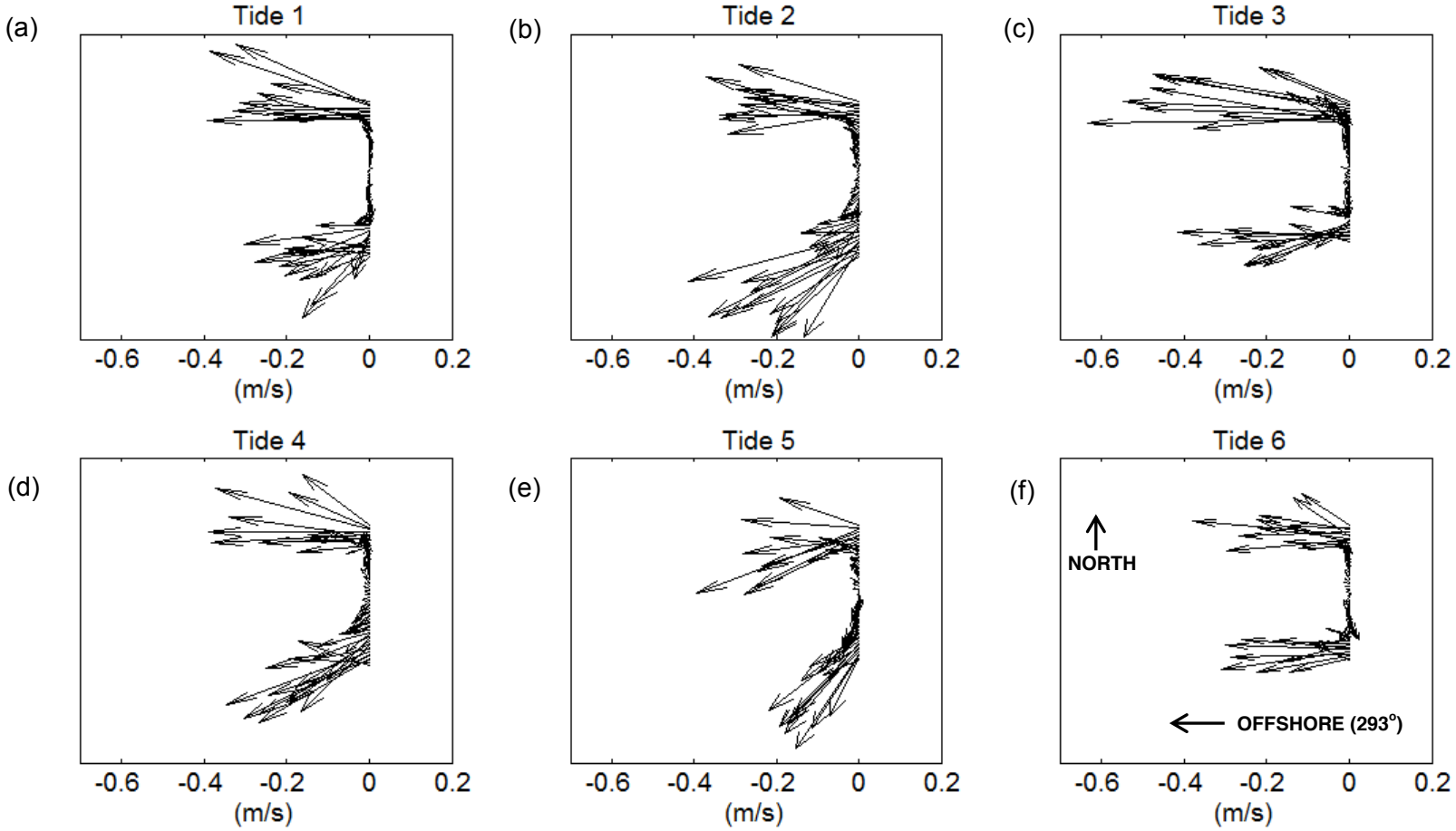

Figure 4.15: Vector plots showing the direction of the mean flows throughout each entire tidal cycle (a - f) during *STIR 1*. The beginning of each tidal cycle starts at the top of each panel, the arrows pointing towards the left indicate offshore directed flow.

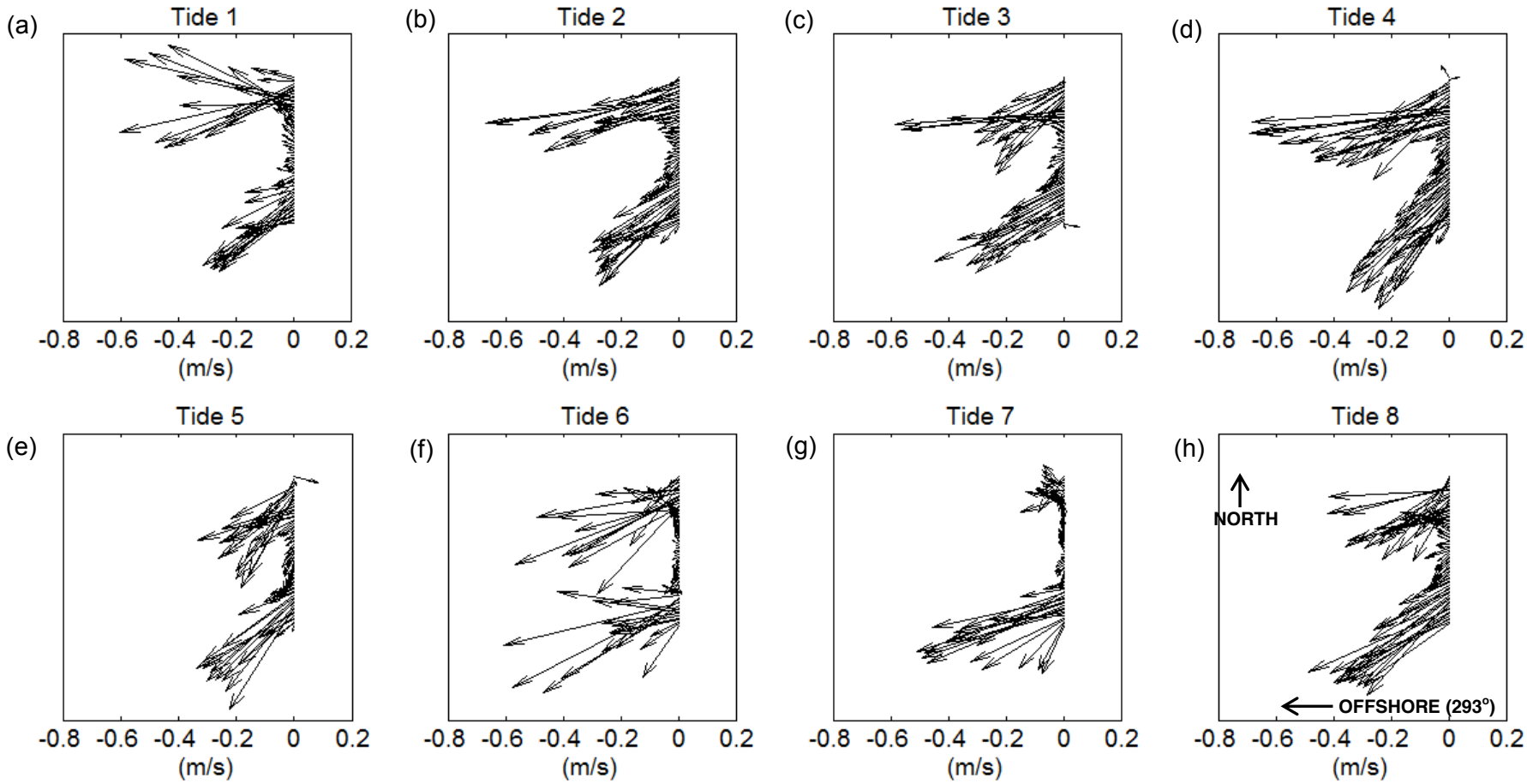

Figure 4.16: Vector plots showing the direction of the mean flows throughout each entire tidal cycle (a - h) during *STIR 2*. The beginning of each tidal cycle starts at the top of each panel, the arrows pointing towards the left indicate offshore directed flow.

4.4.3: Sensitivity of velocity measurements

In *STIR 1*, measurement of the velocity in the rip channel was performed with an ADV at z = 0.45 m above the bed. In *STIR 2* measurements of velocity were also made at z = 0.25 m in the same vertical plane. Figure 4.15 offers a comparison between the flow at these two heights. Visually the time series of velocity at z = 0.45 and z = 0.25 (Figure 4.17a & b) are very similar. This is tested using the cross-correlation function (Figure 4.17c & d), where it can be seen there is zero lag between the two time series, indicating that the current and wave processes are vertically uniform in the example presented. The mean current for the time series at z = 0.25 is -0.44 m/s, whereas the mean of the time series at z = 0.45 over the same period is -0.49 m/s, indicating that, as expected, there is a small amount of decay in velocity with decreasing distance above the bed. The slight difference in velocity is represented by R^2 values of 0.95 when correlating the two time series.

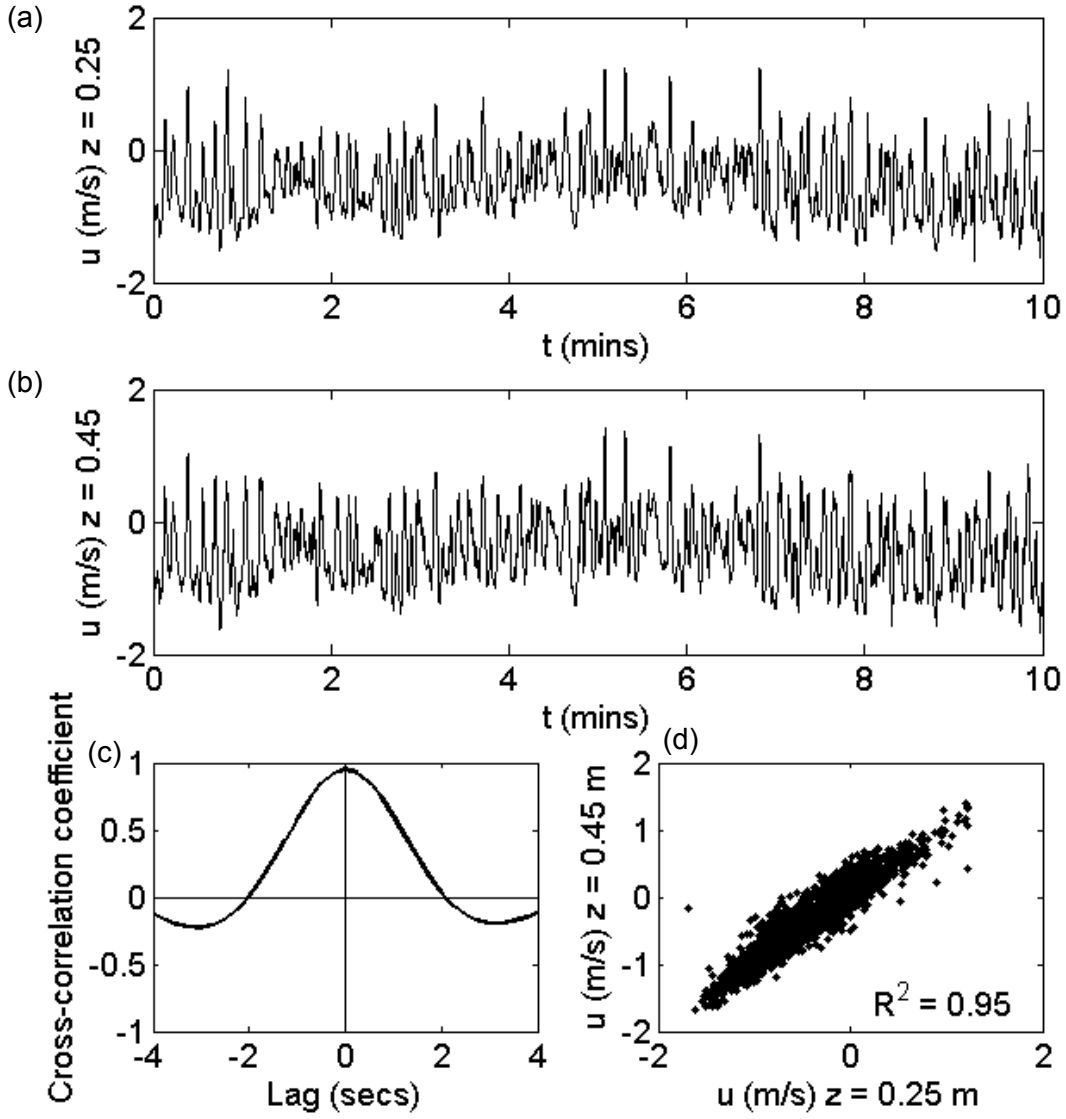

Figure 4.17: Example of a velocity time series at (a) z = 0.45 m and (b) z = 0.25 m and the (c) cross-correlation and (d) correlation of the velocity time series displayed in panels a & b.

4.4.4: Pressure gauge statistics (on the bar)

In addition to the measurements made in the rip channel during *STIR 2,* the wave height and water depth were measured on the bar crest to the north of the rip channel with a Pressure Transducer (Figure 4.18). Water depth reached a maximum of approximately 6 m. Wave height increased with water depth, possibly due to the effect of saturation. With the exception of Tides 6 and 7, wave height peaked at over 1 m in each tide with the largest wave height of 1.7 m recorded in Tide 4.

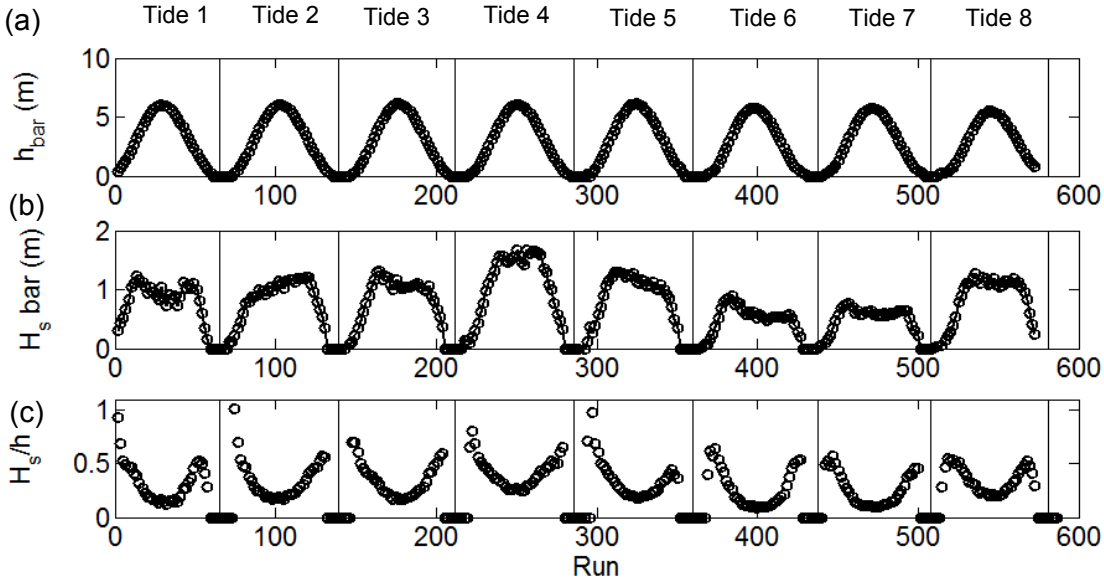

Figure 4.18: Summary of pressure statistics measured on the bar crest at 17-minute intervals; (a) Water depth (*h*), (b) significant wave height (H_s) and (c) local relative wave height (H_s/h).

Ruessink et al. (1998) and Masselink et al. (2007) used the ratio of wave height to water depth (H_s/h) to indicate surfzone position. H_s/h values are low in deep water and increase shoreward to a maximum at the breakpoint. Ruessink et al. (1998) found the breakpoint was defined where H_s/h = 0.4 on a barred intermediate beach in the Netherlands. Discounting periods when the bar crest was dry at the lowest tidal elevations (where *Hs/h* = 0), H_s/h in this data ranged from 0.15 to 2.

In data presented in Figure 4.19, the position of the breakpoint is identified from the variance in the pressure records. Variance was assumed to increase with increasing H_s/h until a maximum was reached at the position of the breakpoint. This was found to occur when H_s/h was between 0.3 and 0.4. Due to the large amounts of scatter, it is not possible to specify an exact value of H_s/h at which wave breaking occurs. This is likely to be a result of the wide range of conditions in which data were collected. However, this parameter does provide a useful indicator of when wave breaking occurs on the bar.

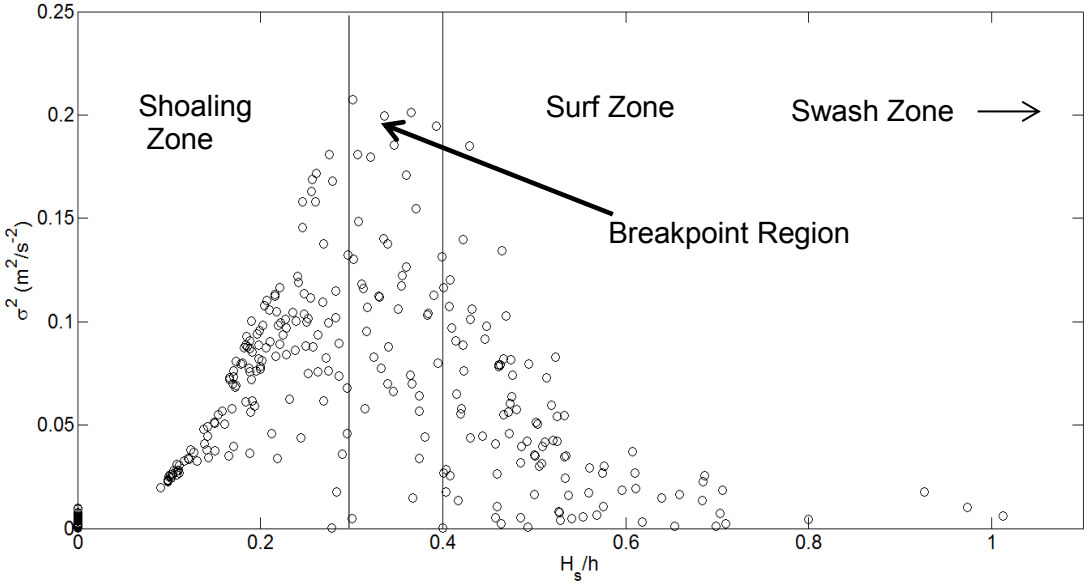

Figure 4.19: Local relative wave height (H_s/h) on bar crest as a function of variance (σ^2). The breakpoint, shoaling zone and swash zone are marked.

4.5: Rip Current Forcing

4.5.1: Tidal forcing

Cross-shore velocity in the rip channel was found to exhibit strong tidal modulation, with the fastest flows occurring at lower tidal elevations. In both *STIR 1* and *STIR 2* the fastest velocities were typically found when the water depth in the rip channel (h_{rip}) at the position of the instrument frame was approximately 2 m (Figure 4.20). Velocties in *STIR 1* showed a greater dependency on water depth than in *STIR 2*. In *SITR 1* when h_{rip} = 4 m, cross-shore velocity was < 0.1 m/s, whereas in *STIR 2* when h_{rip} = 4 m cross-shore velocites of > 0.4 m/s occured. This is likely to be a result of the greater amplitude of the bar-rip morphology in *STIR 2.*

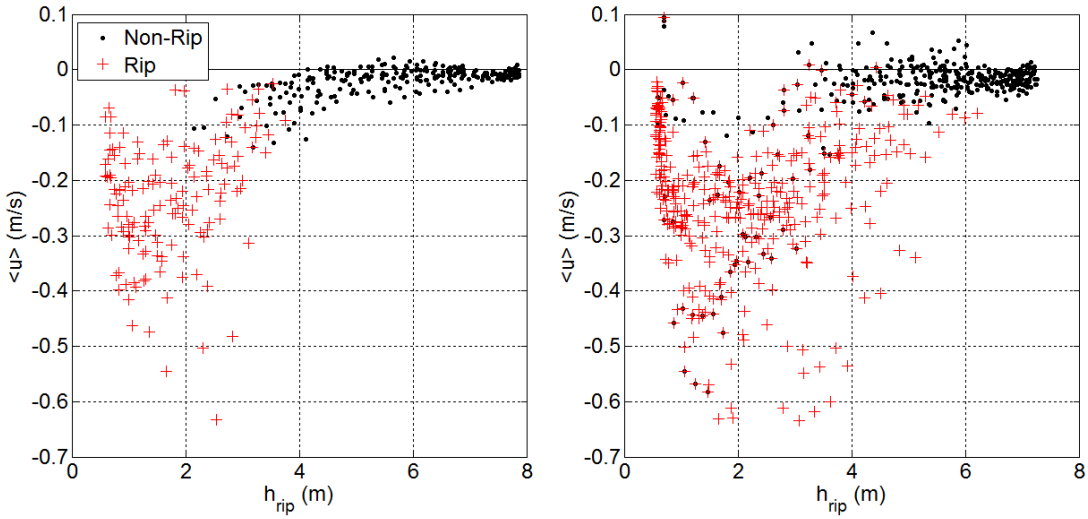

Figure 4.20: Mean cross-shore flow (*<u>*) as a function of water depth in the rip channel (h_{rip}) during (a) *STIR 1* and (b) *STIR 2*. Rip and non-rip conditions are marked.

4.5.2: Forcing by offshore wave climate

The siginifcance of the offshore wave climate on the mean cross-shore velocity is examined in Figure 4.21. This plot was produced by identifying all periods when the rip current was active on the flood and ebb tide (shaded areas in Figure 4.11 and 4.12). For all these periods the mean flow was calculated and plotted against wave height and period for the corresponding time. The isolated rip current velocity data was averaged in 10-minute sections and the maximum and miniumum velocity for each period when the rip current was active is displayed as error bars. It can be seen in both *STIR 1* and *STIR 2* that H_o (R^2 = 0.16 and 0.09) and T_p (R^2 = 0.16 and 0.27) show no relation to cross-shore velocity. The fastest velocities of over 0.5 m/s are recorded in wave heights ranging from 0.5 m to 2.5 m and periods ranging from 6 to 14 seconds. Therefore, rip flow appears to be independent of offshore wave conditions, though wave heights of < 0.5 m did not occur during either experiment, and this could potentially reduce the magnitude of rip flow.

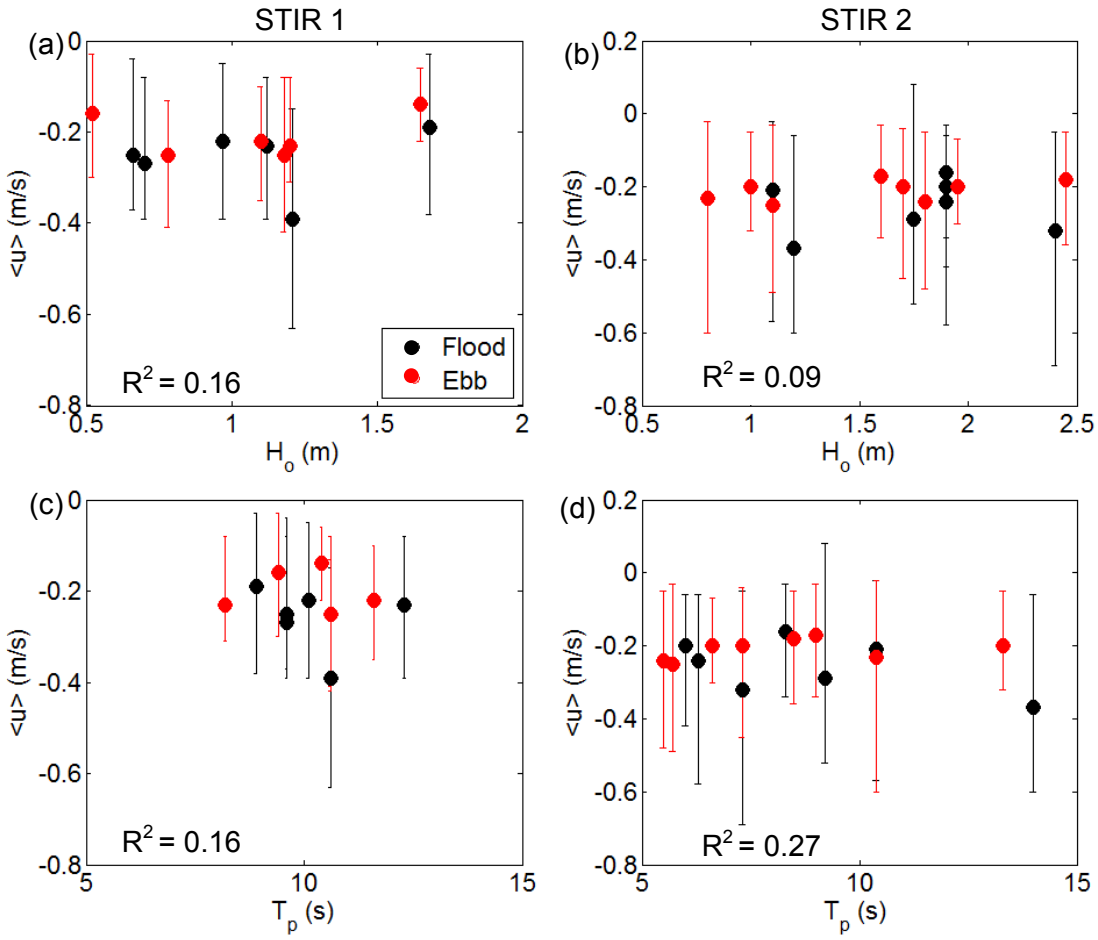

Figure 4.21: Mean cross-shore velocity (*<u>*) as a function of offshore signifcant wave height (H_o) (a & b) and T_p (c & d) during *STIR 1* (a & c) and *STIR 2* (b & d) for periods when the the rip was active. Maximum and minimum velocity (as a 10-minute mean) in each rip is also displayed as error bars.

4.5.3: Forcing by nearshore wave activity

The deployment of a Pressure Transducer on the adjacent bar crest in *STIR 2* allowed the effect of water depth, wave height and wave breaking on the adjacent bar on rip flow to be investigated (Figure 4.22). The PT on the bar crest sampled for 5 minutes, 42 seconds, every 17.1 minutes. The continuous 4 Hz velocity data for all of *STIR* 2 (rip and non-rip conditions) were re-sampled to match these bursts for the analysis.

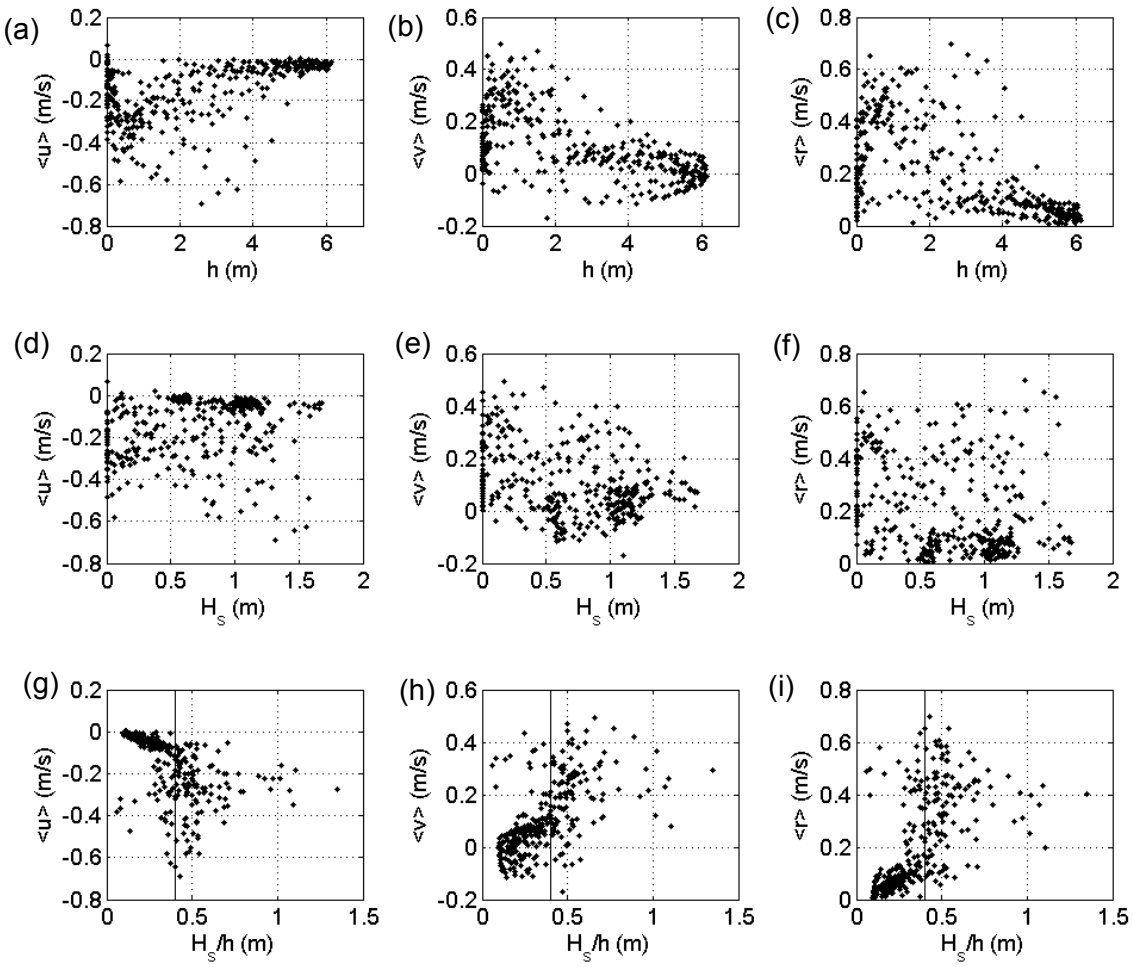

Figure 4.22: Mean cross-shore (a, d & g), longshore (b, e & h) and resolved (c, f & i) current velocities in the rip channel as a function of forcing on the bar crest from (a-c) water depth (*h*), (d-f) significant wave height (H_s) and (g-i) local relative wave height (H_s/h).

The mean current velocities have a dependence on tidal elevation over the bar, with maximum flow velocities generallty occuring when water depth on the bar crest was low (Figure 4.22a, b & c). The fastest offshore directed flow occur when water depth on the bar is between 1.5 and 4 m (Figure 4.22a), however there is significant offshore directed flow when h = 0 m on the bar. This is likely to be as a result of morphological constriction of the flow, as described by Austin et al. (2010). The fastest longshore flows (<*v*> = 0.5 m/s) are in a southerly direction (positive) when *h* is low. The preference of the rip to flow towards the south and not show any variability with the tidal flow (where a flooding tide flows towards the north) in *STIR* 2 suggests that either the presence of strong NW winds and swell drives longshore currents to the south or the morphology of the rip system, with a channel feeding the rip from the north has a greater effect than the tidal flow. The magnitude of the longshore flow appears to decrease as the cross-shore flow increases, suggesting that when water depth is shallow over the bar, flow is predominantly longshore and becomes more offshore as water depth increases. This was also observed in the vector plots presented in Figure

4.16. The resolved velocity shows a lot of scatter, with velocities of all magnitudes occuring at all depths. However there are more obsevations of strong velocites at the shallowest depths and of weaker velocities at the greatest depths.

There is a large degree of scatter between H_s on the bar and mean flows in the rip channel, though there is some evidence that the fastest cross-shore velocities occur when waves on the bar are at their largest. In the longshore directed component of the flow, the weakest flows appear to be associated with the largest waves, this may be a result of the largest waves occuring at high tide, when wave breaking and tidal forcing are low.

The strongest offshore directed flows are concentrated when H_s/h = 0.3 to 0.4, suggesting that wave breaking on the bar is an important factor in driving rip flow. The longshore velocity magnitude increases to a maximum when H_s/h > 0.5 suggesting that broken waves and potentially swash events are important in driving longshore flows. The fastest resolved velocities are also found at approximalry H_s/h = 0.3 to 0.4. However there is more scatter than the cross-shore flow and a slower decrease in velocity magnitude when H_s/h > 0.4.

4.5.4: Summmary of flow characteristics

In Figure 4.23 a summary of flow characteristics for the rip systems studied in *STIR1* and *STIR 2* are presented in a schematic diagram. The dynamics of the the rip is initally governed by the beach morphology, though this varies temporally depending on tidal state. At low tide, when the bar dries out, offshore directed flow in the rip neck exists as a result of morphological constriction. Visual observations suggest that the extent of the rip flow is potentially limited at low tide due to wave breaking across the outer bar. At mid tide, wave breaking on the bar adjacent to the rip channel results in mass transport of water over the bar and into the feeder channel. This water then escapes offshore through the rip neck. Visually, this appeared to be when cell circulation was most likley to occur. At high tide, water is of sufficient depth that waves pass over the morphology without interacting with it.

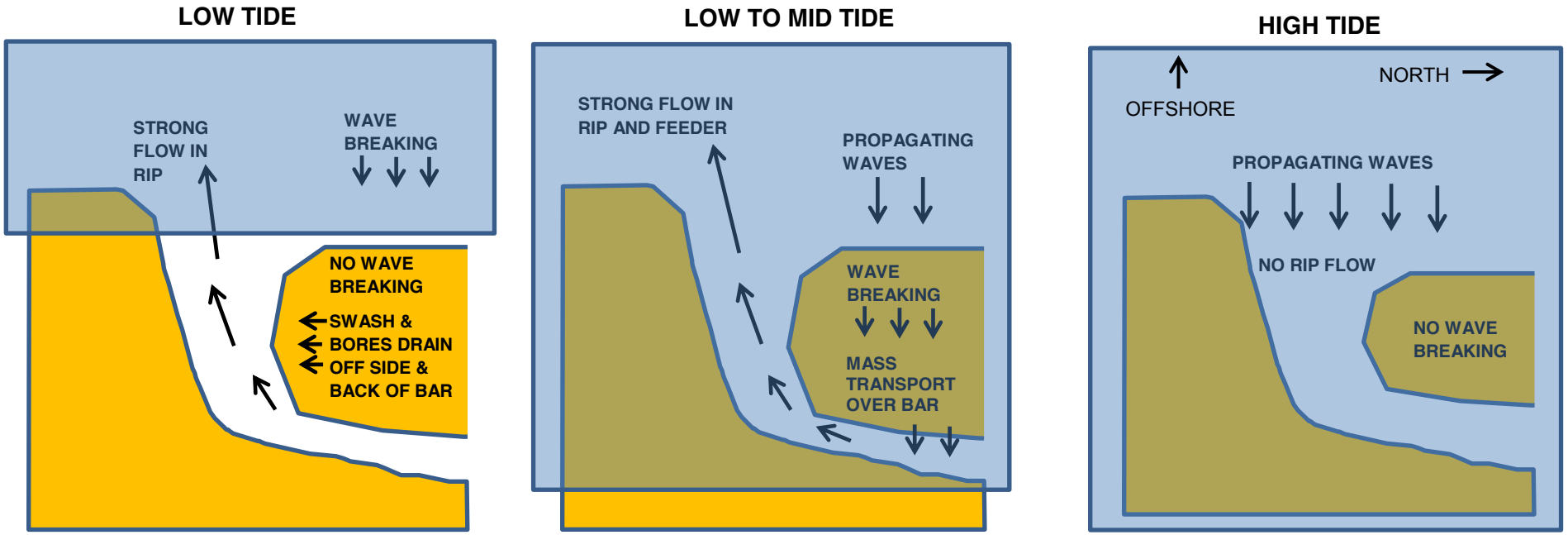

LOW TIDE

- No wave breaking on bar, flow maintained by morphological constriction
- Swash and bores may drain off side of bar
- Offshore extent of flow may be limited by wave breaking

LOW TO MID TIDE

- Wave breaking in bar drives onshore mass transport
- Water travels through feeder and offshore in rip neck
- Likely to drive cell circulation
- May be some bores in rip channel

HIGH TIDE

- Deep water prohibits wave breaking and interaction with beach morphology

Figure 4.23: A summary of the mechanisms that drive rip flow at different stages of the tide from observations and analysis of data from *STIR 1* and *2* during low tide, low to mid tide and high tide.

4.6: Rip Current Pulsing

4.6.1: Identification of VLF pulsing

Visual observations of instantaneous rip current velocity data show that both the cross-shore and longshore flows occasionally oscillated on time periods exceeding wave group scale. To investigate the phenomena of rip current pulsing on different time scales an example is presented that demonstrates a very low frequency (VLF) signal in the rip flow. The example consists of 68 minutes of rip data, illustrating VLF oscillations representative of the whole data set. The associated environmental conditions are presented in Table 4.5. Mean values are calculated over the entire 68-minute section of data and the range is the highest and lowest 10-minute mean within the 68-minute section.

Table 4.5: Environmental conditions for a 68-minute section of rip data exhibiting VLF pulsing. The range in conditions is the maximum and minimum 10-minute mean within the 68-minute section of data.

<u> (m/s)		<v> (m/s)		h (m)		H_o (m)	T_p (s)
Mean	**Range**	**Mean**	**Range**	**Mean**	**Range**	**Mean**	**Mean**
-0.25	-0.13 to -0.36	0.33	0.15 to -0.43	1.2	0.9 to 1.5	0.75	10.5

The presence of VLF pulses in the cross-shore and longshore flow is shown in the de-trended time series in Figure 4.24a & b and is presented with a 2-minute running mean overlaid to illustrate the oscillations. The instantaneous cross-shore velocity shows pulses at a period of 15 – 20 minutes and is responsible for velocity fluctuations of around 0.3 m/s, whilst the longshore velocity shows pulses at a period of 5 – 10 minutes causing fluctuations in the velocity of a similar magnitude. The cross-shore and longshore velocities appear out of phase with one another, though there is some indication that the beginning of the offshore directed pulses (negative flow) are accompanied by a pulse of northerly (negative) flow of a shorter period.

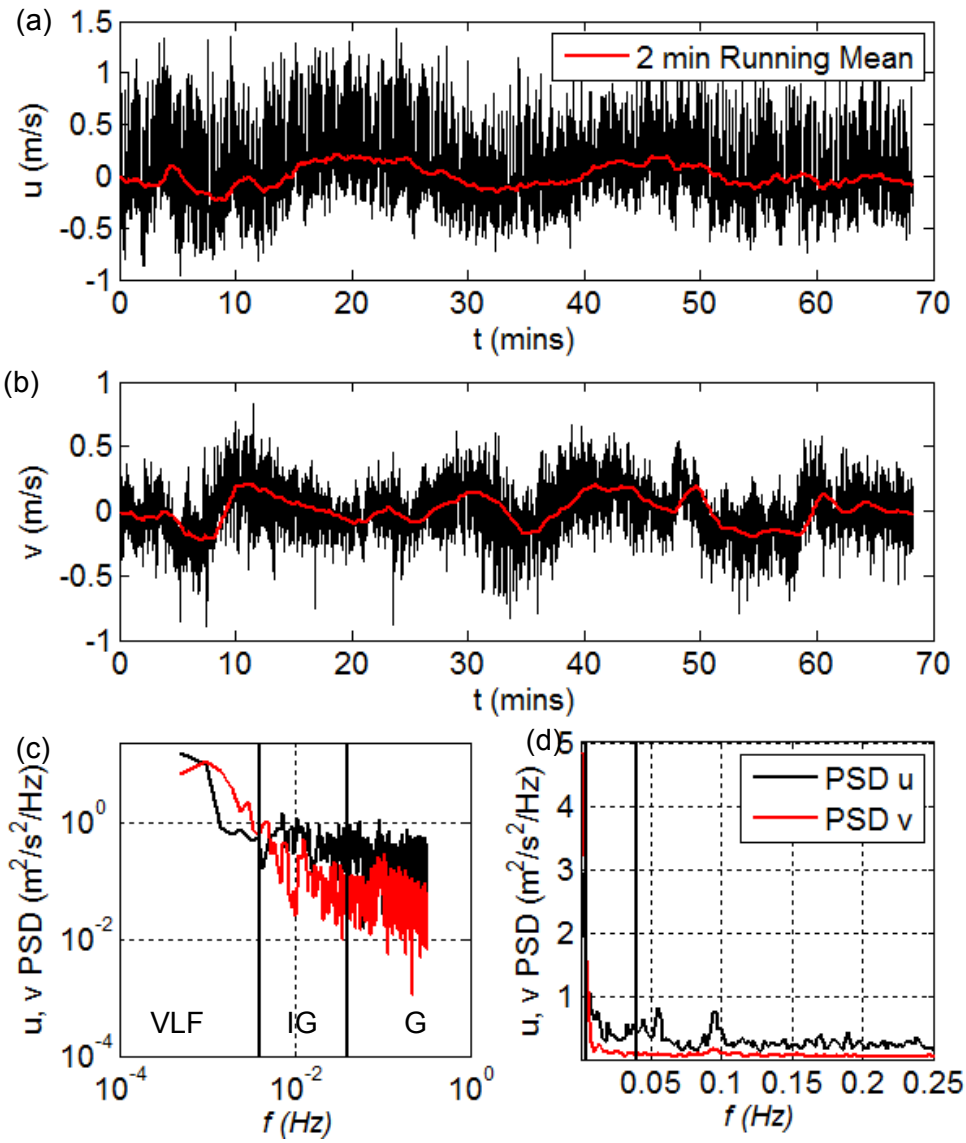

Figure 4.24: Time series of (a) u and (b) v velocity data showing VLF oscillations with a 2-minute running mean overlaid to aid visualisation. (c) Power spectral density (PSD) of u and v with 2 non-overlapping windows and 1 overlapping window and (d) with 8 non-overlapping and 4 overlapping windows, a linear axis is used so energy at high frequencies can be visualised.

The Power Spectral Density (PSD) of the velocity time series are shown (Figure 4.24c & d). A section of 68 minutes in length was chosen as it was considered a balance between sections of data sufficiently long to capture multiple VLF oscillations and short enough that environmental conditions did not change significantly. The PSD is presented twice (Figure 4.24c & d). In order to give maximum resolution in the VLF band the PSD was initially calculated using 2 non-overlapping sections and one overlapping section giving 4.4 degrees of freedom (Jenkins and Watts, 1968). This is followed by calculating the PSD of the velocity data using 8 non-overlapping and 4 overlapping windows, giving 27.3 degrees of freedom. The advantage of using more non-overlapping sections is that it increases confidence in the spectral estimates.

However this is at the cost of resolution in the VLF band, therefore the PSD is presented using both approaches.

Frequency bandwidths are identified from the spectral estimates as the positions where troughs were visible in the spectral energy that were reasonably consistent between the cross-shore and longshore velocity throughout all data. The frequency bandwidths are identified in Table 4.6, these frequencies are consistently used as boundaries between VLF, IG and G bandwidths within the literature when studying rip current pulsing (Smith and Largier, 1995; MacMahan et al., 2005; Bonneton et al., 2006; Reniers et al., 2007; Bruneau et al., 2009).

Table 4.6: Boundaries for frequency bands (in Hz and Seconds) used in spectral analysis.

Frequency Band	Hz	Seconds
VLF	< 0.004	> 250
IG	0.004 to 0.04	250 to 25
G	>0.04	< 25

The PSD (Figure 4.24c) show that peaks are present in the cross-shore and longshore flow indicating the presence of energy in the VLF band. The apparent difference in the frequency of the VLF oscillations between the cross-shore and longshore flow is represented in the maximum energy peaks in the spectra, with the longshore velocity showing a peak at a higher frequency. The cross-shore flow shows small peaks in the G band of 0.09 Hz (11 s) and IG band of 0.005 Hz (200 s) that can be observed more clearly in Figure 4.24d. The longshore component of the flow shows very little energy in either the IG or G bandwidths.

4.6.2: Occurrence of VLF pulsing

To assess how often the VLF oscillations were present in the rip flow, all of the data collected over the two field experiments were separated into sections of 68 minutes in length, every 10 minutes. The large overlap was used as it eliminated any bias of the selection of sections of data for further analysis and makes sure longer frequency oscillations are always captured in full. It also allows the whole tide to be analysed. In *STIR 1* data were recorded at 8 Hz with each section containing 32768 points and in *STIR 2* data were recorded at 4 Hz with each section containing 16384 points. A lowpass filter was applied to filter the velocity data at VLF frequencies, a bandpass filter was used to separate IG frequencies and a highpass filter was used to separate G frequencies in the velocity data. The cut-off frequencies of the filter routines are identified in Table 4.6. Velocity variance (σ^2) was calculated for each bandwidth of

interest to allow the temporal variability of the rip flow to be quantified. The results are presented as a continuous time series alongside measurements of h, u and v for *STIR 1* data (Figures 4.25) and *STIR 2* data (Figure 4.26).

It is apparent from Figure 4.25 and 4.26 that VLF motion is present to some extent in the cross-shore and longshore flow at lower tidal elevations during all tides, therefore indicating it occurs at similar times to rip flow. Cross-shore VLF variances (σ^2_{VLF}) range from 0 m^2s^{-2} at around high tide to maxima of between 0.005 to 0.025 m^2s^2 in *STIR 1* (Figure 4.25c) and 0.005 to 0.032 m^2s^{-2} in *STIR 2* (Figure 4.26c). In the longshore orientation, σ^2_{VLF} is of a similar magnitude to cross-shore σ^2_{VLF}. Typically σ^2_{VLF} maxima occurred shortly before and after the low tide.

The maximum cross-shore IG variance (σ^2_{IG}) peaks at different times to that the cross-shore σ^2_{VLF}, with the largest magnitudes occurring at the lowest tidal elevations. IG flows are known to be maximised at shoreline when incident waves have dissipated (Butt and Russell, 1999). The ebb of Tide 4 in *STIR 2* shows larger magnitudes of σ^2_{IG} compared to other tides. This was expected due to the large wave heights and accompanying wide surf zone that occurred on that day, similar to processes observed by Russell (1993). The cross-shore σ^2_{IG} is 0.06 m^2s^{-2} (Figure 4.25d and 4.26d). Generally the σ^2_{IG} is larger in *STIR 2*, which was characterised by generally larger waves than in *STIR 1*.

In the G band cross-shore velocity variance (σ^2_{G}) follows a similar trend to that of the σ^2_{VLF}, with maxima found at a similar stage of the tide, though it is approximately an order of magnitude greater than the σ^2_{VLF} with maximum magnitudes of between 0.1 and 0.35 m^2s^{-2} (Figure 4.25e and 4.26e).

The longshore variance tends to be much lower than the cross-shore variance in the IG and G bands because. This is likely to be because the waves propagate in an onshore direction.

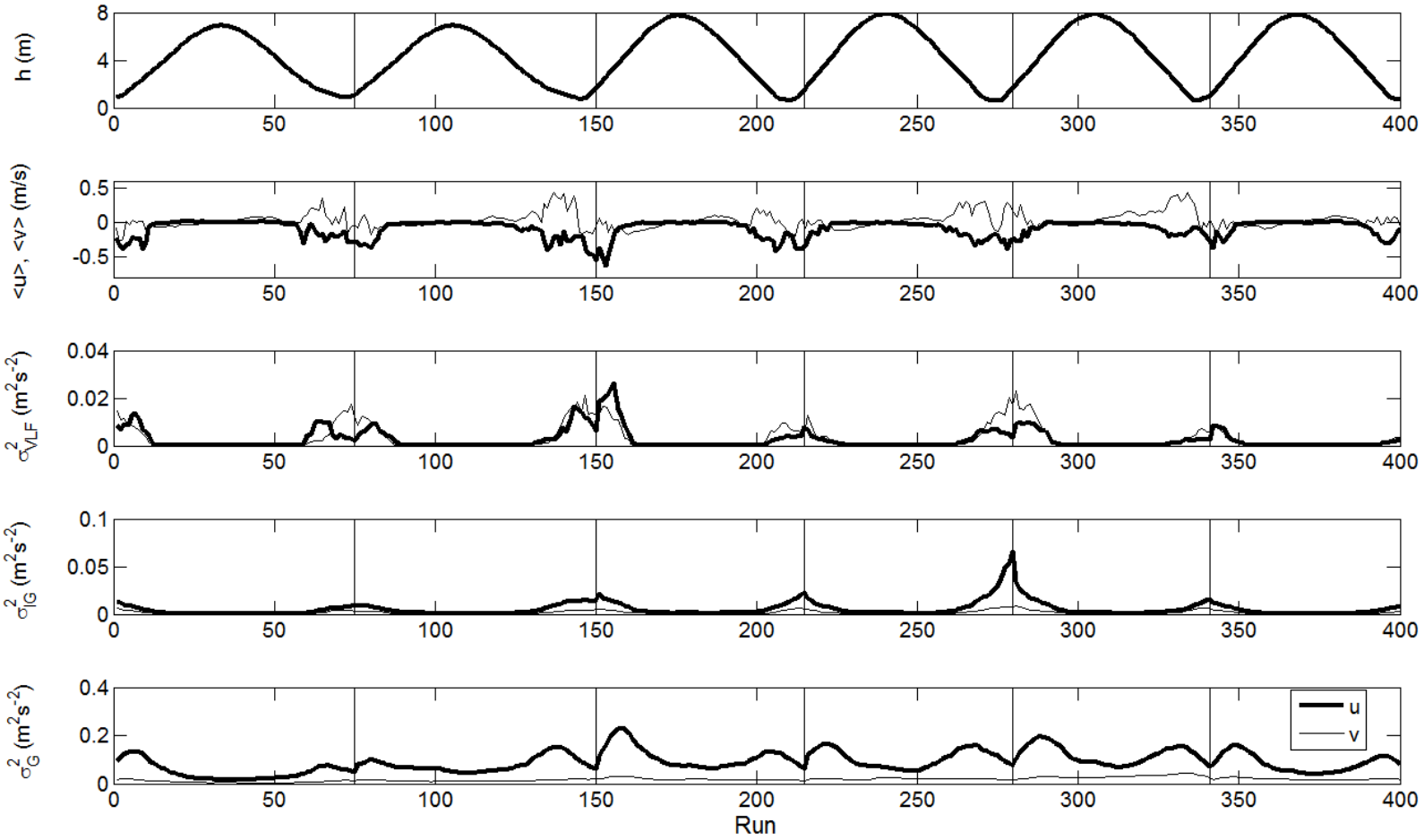

Figure 4.25: From top; Water depth (*h*), cross-shore (*<u>*) and longshore (*<v>*) mean velocity, cross-shore and longshore VLF variance (σ^2_{VLF}), cross-shore and longshore IG variance (σ^2_{IG}) and cross-shore and longshore G variance (σ^2_{G}) for all tides during *STIR 1*. Vertical lines represent the boundary between tides.

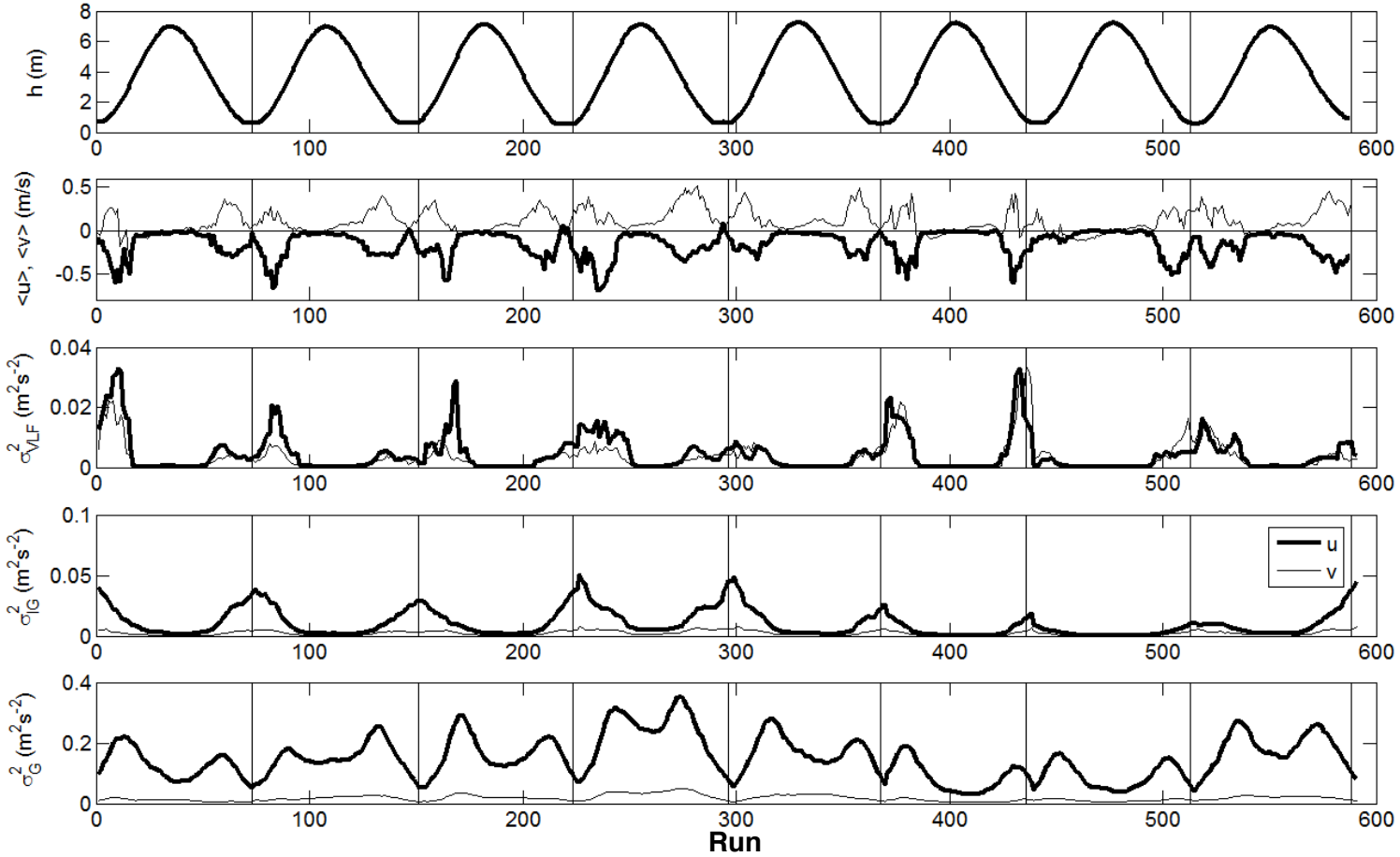

Figure 4.26: From top; Water depth (*h*), cross-shore (*<u>*) and longshore (*<v>*) mean velocity, cross-shore and longshore VLF variance (σ^2_{VLF}), cross-shore and longshore IG variance (σ^2_{IG}) and cross-shore and longshore G variance (σ^2_{G}) for all tides during *STIR 2.* Vertical lines represent the boundary between tides.

4.6.3: Processes controlling VLF motions

To investigate the controls of VLF oscillations within the velocity data, cross-shore VLF velocity variances were correlated with cross-shore mean flows for each tide of data. Mean flows were calculated as the mean velocity within each 68-minute section of data. The flood and ebb sections of the tides were plotted separately for both *STIR 1* (Figure 4.27) and *STIR 2* (Figure 4.28). During both *STIR 1* and *STIR 2* mean cross-shore flow shows a positive correlation with the cross-shore VLF velocity variance (it appears as a negative correlation because offshore flow is represented by a negative velocity). This suggests that the presence of rip flow is an important factor in the generation of VLF motion, and that stronger rip flow is likely to lead to a stronger VLF component in the rip. A similar trend exists with the resolved and longshore flow (plots not displayed), though it is slightly less pronounced.

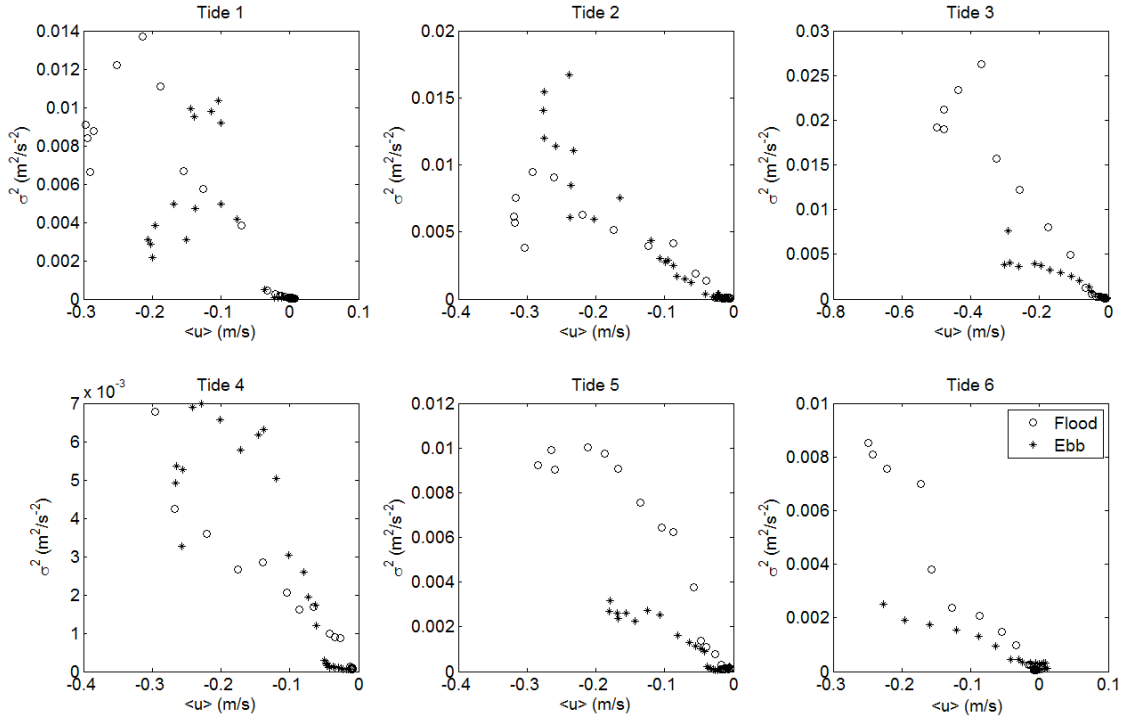

Figure 4.27: Cross-shore VLF velocity variance (σ^2) as a function of mean cross-shore flows (*<u>*) for 68-minute sections of data plotted throughout each tide in *STIR 1* (n.b. *y*-axis scales vary).

It is also appears in Figures 4.27 and 4.28 that the presence of a VLF signal is often more prevalent in the flood tide than the ebb tide. In some cases this may be due to velocities being lower in the ebb tide, however when mean velocities are similar in the flood and ebb tides (e.g. Tide 6, *STIR 1*), the VLF variance is larger on the flooding tide.

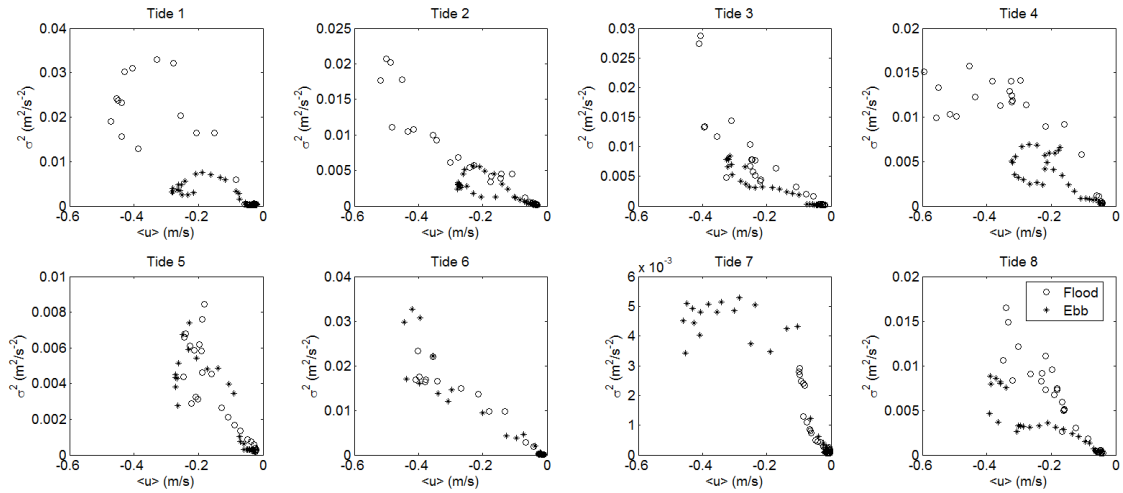

Figure 4.28: VLF variance as a function of mean cross-shore flows for 68-minute sections of data plotted throughout each tide in *STIR 2* (n.b. *y*-axis scales vary).

Offshore wave height, averaged over periods corresponding to 68-minute sections of data from which VLF variance was calculated, showed no relationship with VLF variance. The maximum VLF velocity variance from the flood and ebb tide is plotted against the offshore wave height in Figure 4.29. The largest VLF velocity variances (0.32 m^2/s^2) occur when H_o = 1.2 m, and when H_o = 2.4 m (the largest wave height) the velocity variance is relatively low at 0.016 m^2/s^2.

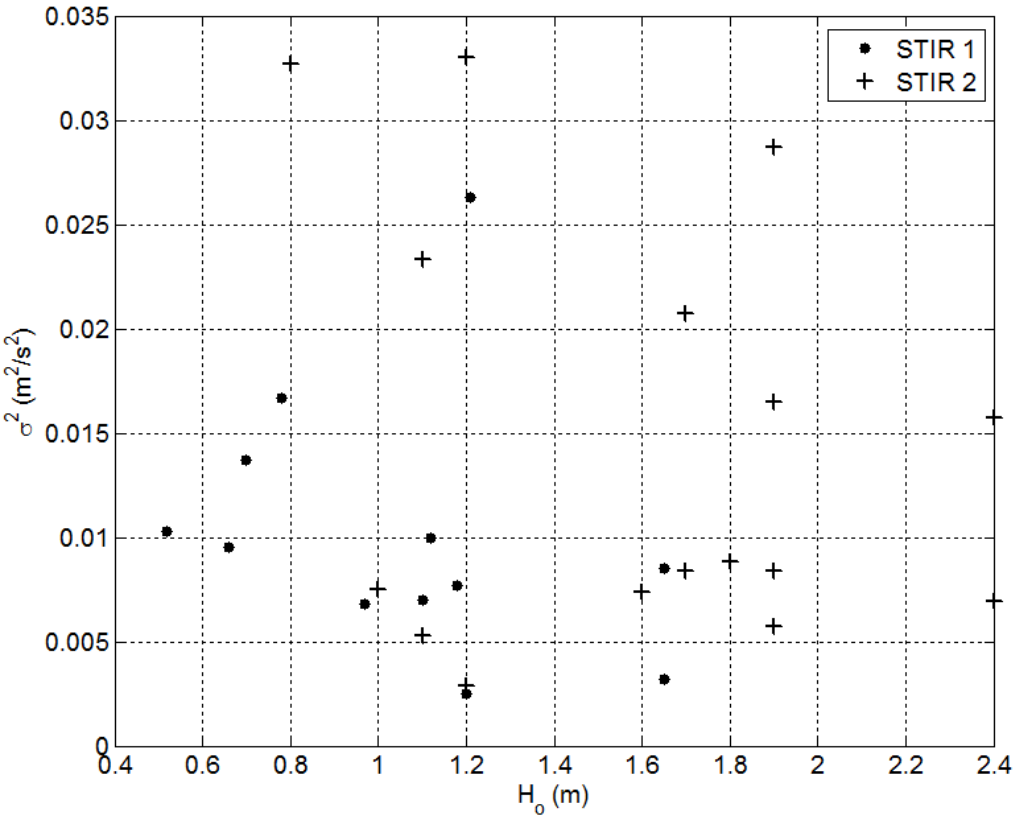

Figure 4.29: Maximum cross-shore VLF velocity variance (σ^2) as a function of offshore wave height (H_o) for every tide during *STIR 1* and *STIR 2*.

Following the evidence that VLF pulsing appears to be related to the magnitude of the rip flow, the cross-shore VLF variance is plotted against the local relative wave height (H_s/h) in Figure 4.30. Figure 4.19 indicated that wave breaking on the bar commenced at approximately $H_s/h > 0.3$. Although there is some scatter, it can be that the largest VLF variances are found when $H_s/h > 0.3$. This suggests that a requirement for VLF motion is that there is wave breaking on the bar. It appears VLF oscillations were less prevalent when the bar was dry and the rip was driven by the process of morphological constriction.

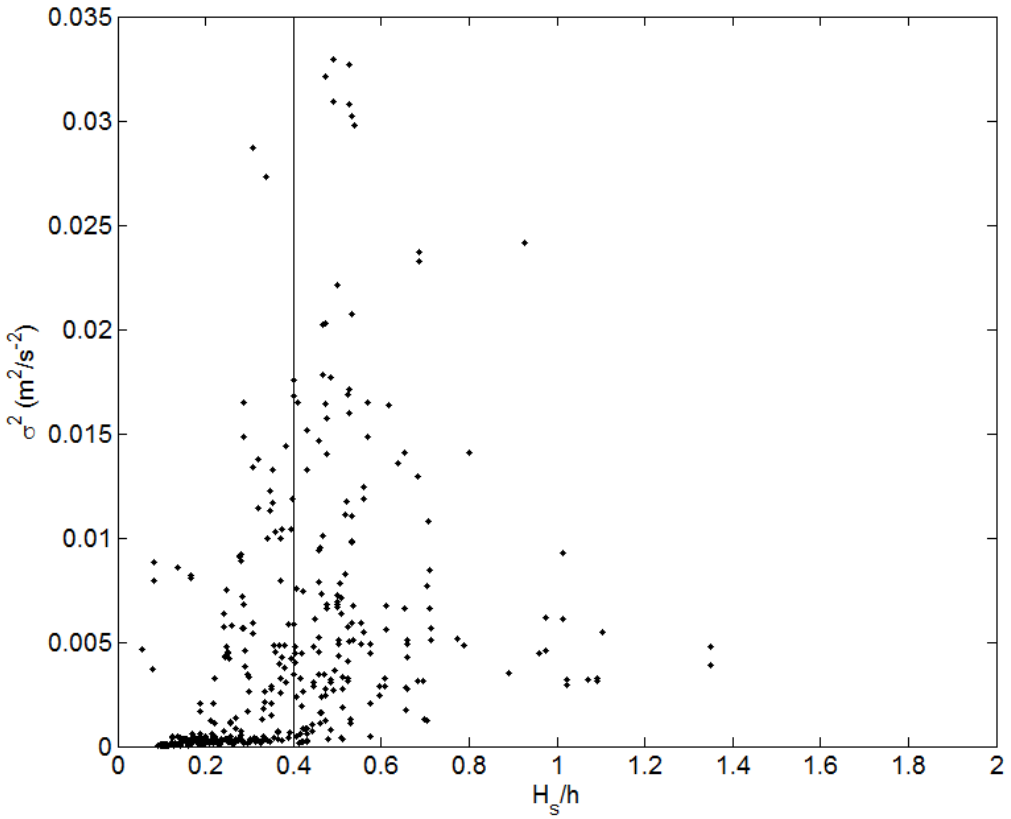

Figure 4.30: Local relative wave height (H_s/h) as a function of cross-shore VLF variance (σ^2). H_s/h = 0.3 is marked, the point at which wave broken was shown to commence.

4.7: Discussion of Results on Rip Current Dynamics

In this section, the data collected relevant to both the spatial and the temporal context of the rip systems at Perranporth is discussed. The spatial scale ranges from the morphology of the entire beach to individual rip scale morphology and includes grain size analysis at various locations on the beach. The temporal scale of the rip is examined between individual tidal cycles, during each period when the rip was active, and in 68 and 10-minute sections of data.

Contour plots of the inter-tidal morphology (and sub-tidal morphology in *STIR 1*) and rectified ARGUS images show that during both field campaigns Perranporth exhibited pronounced rhythmic low tide bar – rip morphology. ARGUS images also suggest wave – current interaction at the head of the rip currents, which can be seen as a longshore meandering of the broken waves. The pronounced morphology provides the conditions to drive a longshore variation in wave height required for rip activity as described by Bowen and Inman (1969). Perranporth was described to exhibit rhythmic low tide bar – rip morphology by Austin et al. (2010), and this agrees with the beach classification using the Relative Tidal Range conceptual model of Masselink and Short (1993). It is felt this model is the most applicable due to its inclusion of the effect of a macro-tidal range. Using the MLWS position as a guide it can be seen that the rip channels measured in this study span across the inter-tidal and sub-tidal zones. The majority of the inter-tidal zone, up to the high water mark is planar. Rip formation is favoured at low tide due to the tidal stationarity (Scott et al., 2009a). Rhythmic rip channel spacing has often been observed in the field (Short, 1985; MacMahan et al., 2005; Turner et al., 2007; Orzech et al., 2011) and also been subject of modelling studies (Reniers et al., 2007; Orzech et al., 2011). The spacing of the rip systems was similar in both *STIR 1* and *STIR 2*, with approximately 400 m between larger rip systems. Smaller systems were also present with a spacing of around 250 m. An increase rip spacing has often been attributed to increasing wave energy (McKenzie, 1958; Bowen and Inman, 1969; Short, 1985; Huntley and Short, 1992; Short and Brander, 1999). Variations of this observation appear in Hino (1974), who found rip spacing to scale with surfzone width and in Deigaard et al. (1999) who observed spacing in line with the width of the bar crest. However, Holman et al. (2006) and Turner et al. (2007) suggested that the antecedent morphology is the principal controlling factor and that there is little correlation between the spacing and the number of rip channels and offshore wave conditions. Turner et al. (2007) also showed that rhythmic rip spacing does not always occur. ARGUS images collected at Perranporth showed the morphology to be stable during each study and although the data were collected in a range of conditions the morphology showed no obvious short term response. Richardson (2011) found rip channel spacing to be between 450 – 600 m at Perranporth and that spacing reduced under low energy conditions when ephemeral features appeared. The development of smaller systems may explain the smaller spacing between what appear to be smaller rip systems. Austin et al. (2010) found rip spacing to be around 250 m at Perranporth suggesting there is a degree of variability in spacing at Perranporth.

The result of Richardson (2011), that larger rip channels persist for > 118 days at Perranporth suggests that the rips are stable on a seasonal time scale. Scott et al. (2011) observed that low tide bar-rip systems were more often present in low energy

summer conditions on the beaches of the North Cornish Coast (where Perranporth is located). In the winter these were modified due to high energy conditions, resulting in offshore directed sediment transport, creating a flat inter-tidal beach and a shore parallel sub-tidal bar. This is described as a reset of beach morphology by Thornton et al. (2007). The location of rip channels in *STIR 1* is approximately 150 – 200 m further south than in *STIR 2*, though the general shape of the morphology is similar throughout the length of the beach. Richardson (2011) found that rip channels at Perranporth favoured certain locations dependent on water outflow, headlands and geological variations. Results presented here suggest that if this is true there is some localised longshore migration of rip channels. Migration of rip channels has been observed in the field (Ruessink et al., 2000; Turner et al., 2007), and has been hypothesised to scale in a linear fashion with longshore transport (Orzech et al., 2010), due to increased angle of wave incidence.

The rip system in *STIR 2* is much larger than in *STIR 1.* The width of the channel that was ≥ 1 m below the adjacent sand bar was approximately 70 m in *STIR 2* compared to around 10 m in *STIR 1.* Both rip systems were of a similar shape, with the rip neck skewed to the south and both were fed by a feeder channel that ran longshore shoreward of a well pronounced bar to the north. To the south of the rip neck there was a shore connected shoal, though there was evidence of a small feeder channel in *STIR 1* at this position. Referring to the classification scheme of Brander (1999a), an adaption of the earlier model of Short (1985), the rip systems are visually best classified as Transverse Bar – Rip. The example of Langrangian drifter measurements presented here showed that the flow was constrained by the morphology of the rip system, with drifters travelling longshore in the pronounced feeder channel before heading offshore and either circulating, travelling longshore or exiting the surfzone. This is consistent with observations that well developed three dimensional morphology controls rip current spacing, cell circulation and flow (Sonu, 1972; Noda, 1974; Brander, 1999a; Short and Brander, 1999; Austin et al., 2010; MacMahan et al., 2010; Scott et al., 2014).

Eulerian measurements found the rip flow to exhibit strong tidal modulation, with the fastest flows being found at lower tidal elevations, consistent with findings of many other authors (Aagaard et al., 1997; Brander, 2001; MacMahan et al., 2005; Bruneau et al., 2009; Austin et al., 2010). At spring low tides the velocity was observed to show a slight reduction in magnitude as the receding tidal level resulted in wave breaking on the bars to ceased as the bars dried out. This has also been observed by Castelle and Bonneton (2006) and Bruneau et al. (2009) in the macro/meso tidal environment of the French Aquitaine coast (tidal range = 3.7 m). This highlights the importance of rip morphology in controlling rip flows. In contrast, in high energy conditions (H_s = 2.5 to 3

m) the rip currents have been observed to be active throughout the tidal cycle (Bruneau et al., 2009). Maximum mean cross-shore flows were between 0.34 and 0.54 m/s in *STIR 1* and between 0.14 and 0.72 m/s in *STIR 2*, with the largest instantaneous velocities of ~ 2 m/s occurring in *STIR 2*. Velocities of the order of 0.3 m/s to 0.8 m/s are typical for a low energy rip current (Bowman et al., 1989; Aagaard et al., 1997; Brander, 1999b; MacMahan et al., 2005; Austin et al., 2010; Austin et al., 2012; Austin et al., 2014), whereas in a high energy environment (H_s > 2.5 m; T_p = 10 – 15 s) Brander and Short (2000) measured mean velocities of the order of 1 m/s at the margin of the feeder and rip neck using flow meters. Around high tide mean flows were negligible in *STIR 1* and at times were in an onshore direction in *STIR 2* indicating the rip was completely inactive.

In *STIR 1*, longshore flow showed a large degree of tidal asymmetry, with longshore flows between 0 and 0.1 m/s in the northerly direction in rip conditions during the flood tide. When the rip became active on the ebbing tide the longshore flow strength was up to 0.5 m/s in a southerly direction. Vector plots show in *STIR 1* (Figure 4.16) the tidal asymmetry observed in the longshore velocity time series. In the flood tide, flows are almost straight offshore, indicated by arrows pointing towards the left. However, in the ebb tide the flow is skewed to the south. The preference for southerly flow on an ebb tide may be due to the combined effect of the channel being skewed towards the south and because the tide flows from north to south when ebbing. The asymmetry was not observed in *STIR 2* (Figure 4.17), with the flows being skewed to the south in both the flood and ebb parts of the tide. This may be a result of large volumes of water flowing off the side of the bar, which was larger than the bar in *STIR 1* and therefore more water had the potential to drain into the rip channel (Dronen et al., 2002) Longshore southerly flows were strongest when the water depth over the bar was lowest, providing supporting evidence for this theory. It is possible that longshore flow was driven by the strong NW wind or the angle of wave incidence.

Mean cross-shore, longshore and resolved velocity in *STIR 2* exceeds that measured in *STIR 1* and significant velocities are also present at greater depths, suggesting the rip was active for a larger part of the tidal cycle, which is likely to be linked to the size of the system and greater amplitude of the bar-rip morphology and therefore its ability to affect wave and current processes in deeper water due to the large gradient in size and shape (Brander, 1999a).

Grain size was found to vary spatially throughout the beach. As expected, the finest sediment was found in the higher and drier area of the beach. The coarsest sediment was found in the rip neck. Gallagher et al. (2011) observed similar results and attributed the coarser sediment in the rip neck to be a result of the finer sediment being

stripped out by the rip flow. Similarly, Cook (1970) stated that rips selectively remove fine sand with a low specific gravity from the beach to the inner continental shelf and that the remaining coarser material may be seen as a band in the sedimentary structures that can be used to reconstruct paleo-shorelines.

Larger offshore waves (Shepard et al., 1941; Ranasinghe et al., 2000; MacMahan et al., 2005; Austin et al., 2010) and increased peak period (Austin et al., 2012) have been attributed to forcing rip current flows. The relationship between incident waves and rip flow dynamics maybe be more complex than this though, with rip strength not always found to increase with wave energy (MacMahan et al., 2010). Indeed, Scott et al. (2014) found rip currents posed the most significant risk to beach safety at or below average wave conditions. Data presented here did not show increasing current strengths with increasing wave height, evidenced by the $R^2 \leq 0.16$, with maximum mean flows of > 0.6 m/s when wave heights ranged between 0.5 and 2.4 m. This may be due to the fact when wave height exceeds some threshold, wave breaking occurs across the outer bar (which is shown in the rectified ARGUS images), and the increased onshore mass transport in the rip channel limits offshore directed rip flow. MacMahan et al. (2010) observed that when larger waves broke further offshore more material was retained in the surfzone, indicating that the extent of offshore directed flow is limited in larger waves. In the case of Eulerian measurements, the relative position of the sensors becomes important. During the experiment, the study site received a mix of swell and wind sea, with wave periods ranging from 6.5 to 14 s, this also appeared to have no impact on rip flow ($R^2 = 0.26$). Generally, the angle of wave incidence did not deviate far from shore normal (20^o south and 12^o north of shore normal). Harris et al. (1964) and Komar (1998) suggested that in high angle of wave incidence longshore flows would dominate over offshore directed rip flow. Examining the time series of velocities, there is some evidence to show that when longshore flows were stronger, cross-shore flows were weaker. Although offshore wave height appeared to have little impact on rip flow, wave breaking on the bar was found to be important for cross-shore, longshore and resolved velocity measured in the rip channel. Longshore variability in incident wave heights has long been recognised as the driving force for rip currents (Bowen, 1969). Typically this occurs due to longshore variability in the morphology, with wave breaking focused on the bars and minimised in the rip channel (Sonu, 1972; Aagaard et al., 1997; Brander, 2001; MacMahan et al., 2005; Austin et al., 2010). This is well represented in data collected in *STIR 2.* Wave breaking on the bar was found to occur when H_s/h = 0.3 to 0.4. Cross-shore and resolved mean velocities were at a maximum at this point, similar to results obtained by MacMahan et al. (2005) and Austin et al. (2010). Longshore flow increased in magnitude until H_s/h >0.5, which is beyond the point that wave breaking is likely to have occurred. This suggests that shoreward

travelling bores and swash events were more important than wave breaking for driving longshore flows at the location of the instrument. This may be because onshore travelling bores and swash events drain off the side of the bar into the rip channel and flow past the instrument frame.

Of interest is that when the bar is dry, significant flows (<*u*> = 0.55 m/s; <v> = 0.48 m/s; <*r*> = 0.6 m/s) are recorded. This was also observed by Austin et al. (2010) who identified this as an effect of morphological constriction and side drainage from transverse bars, which is exaggerated on macro-tidal beaches where the bar completely dries out at spring low tide. The effect of increasing velocities in a narrowing channel was also observed by Brander (1999a) when carrying out a field study in an accretionary environment.

Oscillations of between 4 to 30 minutes were regularly observed in both the cross-shore and longshore flow at lower tidal elevations when the rip current was active. The pulsing had a significant effect on the rip flow, and can be attributed to velocity fluctuations of up to +/- 0.15 m/s. VLF pulses in the rip flow on this time scale have been observed in the field (Smith and Largier, 1995; Brander, 2001; Callaghan et al., 2005; MacMahan et al., 2005; Bonneton et al., 2006) and have also been subject to modelling studies (Fowler and Dalrymple, 1990; Reniers et al., 2007).

In this data, VLF oscillations increased with increasing rip strength and were therefore assumed to be directly linked to the nature of wave breaking on the adjacent bar. When H_s/h was ~ 0.3 to 0.4 the rip flow was strong and VLF variance was high. When the water was deeper over the bar and wave breaking stopped, the rip flow was reduced in strength and the VLF variance was reduced. This is similar to the results obtained by Bruneau et al. (2009); they measured rip current oscillations with a with a velocity of > 1 m/s and a period of 10 to 30 minutes, and found them to be most prevalent when wave breaking occurred over well-developed bars. Instabilities in the longshore flow (Smith and Largier, 1995) or instabilities in the rip flow itself (Haller, 1999; Haller and Dalrymple, 2001; Bruneau et al., 2009) are proposed as a mechanisms for observed VLF pulsing in the rip current.

Bowen and Holman (1989) proposed that a uniform wave driven longshore current was assumed to develop a small perturbation that was liable to grow causing the longshore current to become unstable, leading to observed oscillations, which they termed shear waves. Further research on shear waves within the surfzone (Reniers and Battjes, 1997) found that instabilities were more likely to occur on beaches that exhibited longshore bars, than beaches that where more planar, indicating that morphology can increase the chance of instabilities in a steady current. Therefore, the stronger the rip flow, the more likely instabilities are to form; this fits with the observation that they

occur with wave breaking on the bar, as this is when the fastest flows occur. Initially, wave breaking on the bar, which can be represented by the parameter Hs/h is well coupled with mean flows as wave depends on the water level over the bar reaching a critical depth. Results presented here indicate that wave breaking on the bar is also associated with VLF oscillations. Figure 4.31 summarises the processes that may have an influence on VLF oscillations in the rip current.

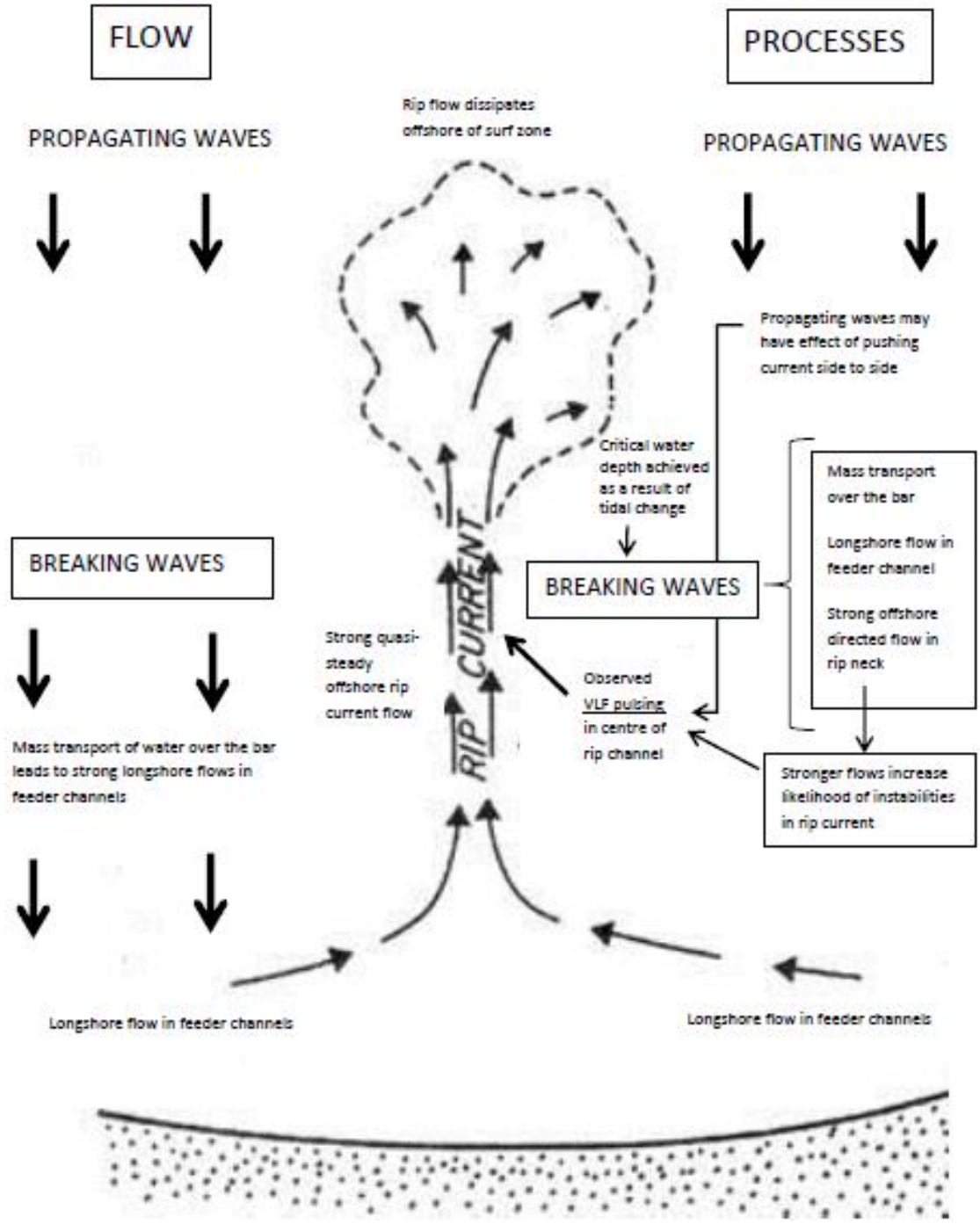

Figure 4.31: Schematic diagram illustrating the coupling of processes occurring in and around a rip system that may influence VLF rip current pulsing. Adapted from original diagram by Komar (1998).

The pronounced three-dimensional bar-rip morphology could also influence the generation of instabilities, as results of Reniers and Battjes (1997) suggest. This is likely to occur as an increase (decrease) in friction in shallower (deeper) water affects the flow. As the morphology of a bar rip system is often asymmetric, the dynamics of wave breaking either side of the rip current may be different, which could also promote the development of instabilities in the rip current flow.

Other mechanisms that may lead to VLF oscillations in rip currents have also been identified. Callaghan et al. (2005) and Bonneton et al. (2006) observed VLF motion to increase with increasing wave energy. It is likely that other characteristics of the swell such as period and groupiness could also affect the presence of a VLF signal. However, VLF motion measured here showed no relationship with offshore wave height and period. MacMahan et al. (2004b) found that VLF motions were driven by the underlying morphology. This was investigated further in a modelling study by Reniers et al. (2007) who found that that VLF velocity oscillations were the result of temporal and spatial variations in wave groups that developed pressure gradients in the surf zone. The rip system at Perranporth can be considered to be reasonably large (it is of a similar scale as rip systems measured by MacMahan et al. (2008), who refer to it as 'very broad') and is therefore likely to exhibit less coupling with wave groups, though this could manifest as multiple wave groups influencing the flow dynamics.

Spectral analysis found rip current pulses at infra-gravity scale (0.4 – 0.004 Hz) were present in the cross-shore flow, though the magnitudes of variance associated with infra-gravity motion were generally less than that in the VLF and gravity bands. The largest IG variance occurred at low tide, this is likely to be because the sensors were in shallow water and this when the IG energy is most significant on relatively flat beaches Butt and Russell (1999).The maximum magnitude of IG variance was found in Tide 4, *STIR 2*, this tide exhibited the largest waves and therefore a wide surf promoting the conditions for the presence infra-gravity energy, as observed on a dissipative beach in storm conditions by Russell (1993). Infra-gravity motion in rip currents has been observed in the rip current on numerous occasions (Sonu, 1972; Aagaard et al., 1997; Brander, 2001; MacMahan et al., 2004a). One accepted hypothesis for the forcing of infra-gravity pulses in the rip flow is that it is a result of significant volumes of water ponding close to the shore as a result of an incoming wave group, this ponded water then escapes seaward, resulting in a pulse in the rip flow on a wave group time scale (Munk, 1949; Shepard and Inman, 1950; Guza and Thornton, 1985). MacMahan et al. (2004a) also found large variability in the cross-shore component of the infra-gravity band to be associated with differences in bathymetry and proposed that cross-shore

standing waves gave rise to IG pulses, similar results were observed by Tang and Dalrymple (1989).

4.8: Summary of Results: Field Observations of Rip Currents

The aim of this chapter was to present data on the beach morphology, the environmental conditions during the experiments and the measured flow dynamics so that data collected on bedform and suspended sediment dynamics (Chapters 5 and 6) can be considered in context.

The results in this chapter may be summarised as follows;

- Over the two experiments, measurements were made in a wide range of hydrodynamic conditions. Offshore significant wave height varied from 0.5 to 3 m, peak period varied from 6.5 to 15 seconds, (where the annual averages for Perranporth are 1.6 m and 10.5 s respectively) and the wave direction varied from 273^{o} to 305^{o} (where shore normal = 293^{o}).
- Perranporth exhibited a large flat inter-tidal zone and well defined rhythmic low tide bar-rip morphology. Using the Dimensionless Fall Velocity (Wright and Short, 1984), Surf Scaling Parameter (Guza and Bowen, 1976) and Relative Tidal Range (Masselink and Short, 1993) the beach was classified as 'Transverse Bar and Rip', 'Dissipative' and 'Low Tide Bar-Rip' respectively. The Relative Tidal Range is the most appropriate classification as it considers the effect of the macro-tidal range (MSR = 6.3 m). The classification of Perranporth as a low tide bar- rip beach is consistent with the classification of Perranporth by Austin et al. (2010) and Scott et al. (2011).
- Rip currents are known to be forced by longshore variations in wave heights (MacMahan et al., 2006), which on open coast beaches is usually a result of the beach morphology (Short, 1985). The Lagrangian drifter data was collected as part of the DRIBS project to examine circulation in the rip system. Full drifter results are presented in Scott et al. (2014). Over 40 drifter deployments, they found in low energy conditions drifters often exited the surfzone, and as energy increased, drifter rotation in rip cells was identifiable. In higher energy conditions or at spring low tide drifters often travelled longshore. The vector plot of Lagrangian drifter data (Figure 4.8) indicated that the bar – rip morphology was a controlling factor in rip flow and cell circulation. The drifter tracks presented from *STIR 1* here showed three different behaviour patterns; the drifters (i) moved in a longshore direction, (ii) circulated onto the bar to the north of the rip system, or (iii) became drawn into a secondary sub-tidal circulation system.

- Grain size was shown to exhibit a spatial variability across the beach, with coarser sediment found in the rip current compared to the feeder channel, bar crest, mid beach and upper beach. This is likely to be because the finer grains are preferentially transported offshore by the rip current. Cook (1970) observed the same result and suggested that the remaining coarse band of sediment may be seen in sedimentary structures, and this feature can be used to reconstruct paleo shorelines.
- Tidal modulation of the rip current was observed to be an important factor in rip current dynamics, with rip current activity favouring lower tidal elevations. At high tide the rip current was completely inactive.
- The method for identifying rip flow and the point at which switches 'on' and 'off' by comparing measured flow with undertow velocities predicted by a simple model (Masselink and Black, 1995) appears to work well. 27 occurrences of rip currents were observed in total, this included 12 occurrences in *STIR 1* and 15 occurrences in *STIR 2.*
- Maximum 10-minute mean cross-shore flows were between 0.34 and 0.54 m/s in *STIR 1* and between 0.14 and 0.72 m/s in *STIR 2*. The largest cross-shore instantaneous velocities of ~ 2 m/s occurred in *STIR 2*. Mean longshore velocities were between -0.1 to 0.5 m/s (where negative is towards the North) at lower tides. The maximum mean resolved velocity was 0.8 m/s. Offshore velocities of the order of 0.3 m/s to 0.8 m/s are typical for measurements made in a rip current (Bowman et al., 1989; Aagaard et al., 1997; Brander, 1999b; MacMahan et al., 2005; Austin et al., 2010; Austin et al., 2012; Austin et al., 2014).
- The rip current flow showed no relationship with offshore wave height (R^2 < 0.16) or wave period (R^2 < 0.26). As expected, wave breaking on the adjacent bar was shown to be an important factor in driving rip flow, as also observed by MacMahan et al. (2005) and Austin et al. (2010). Offshore directed flow persisted at spring low tides once the adjacent bar had dried out. Austin et al. (2010) also observed this at Perranporth and attributed it to morphological constriction of the flow.
- VLF oscillations were present in the rip flow (in *u* and *v*) and their variance was found to increase with mean rip flow and when wave breaking occurred on the adjacent bar. This suggests that rip flow and the presence of VLF oscillations are linked. This supports the suggestions by Smith and Largier (1995); Haller et al. (1997); Haller (1999); Haller and Dalrymple (2001) that VLF oscillations in rip flow are a result of longshore instabilities.

CHAPTER 5: BEDFORM DYNAMICS IN RIP CURRENTS

5.1 Introduction

In this chapter bedform data collected from within a rip channel are presented and analysed alongside synchronous hydrodynamic data. Bedforms have seldom been quantified in a rip system (Sherman et al., 1993), and never before in the rip neck, though observations suggest they are ubiquitous features (Greenwood and Davidson-Arnott, 1979; Nielsen, 1992; Aagaard et al., 1997; Brander, 1999b). The aim of this chapter is to improve the understanding of bedform dynamics in rip currents, particularly with respect to sediment transport. Furthermore, bed roughness is a key parameter controlling the hydrodynamics of the rip system, and is necessary for accurate rip flow prediction. To achieve this, scans of the bed are analysed to provide information on bedform scale, the hydrodynamic conditions for the existence of bedforms in a rip channel and bedform migration. An attempt is also made to classify the bedforms. Finally the use of bedform migration as a proxy for bedload transport is investigated.

The data used in this chapter comprise six complete tidal cycles, collected during *STIR 1* and the flood tide of a seventh tidal cycle, collected at the beginning of *STIR 2*, in total this included 13 occurrences of rip currents.

5.2: Environmental Conditions

A brief summary of the environmental conditions is provided in this section (Figure 5.1). A more comprehensive analysis of the environmental conditions is provided in Chapter 4, however, much of that analysis was performed with a 10-minute averaging routines as opposed to the 5-minute averaging used for analysis of the bed profiles. In addition the hydrodynamics presented here are exclusively for periods when bedform data were collected, which was at a minimum water depth of ~ 0.8 m. A 5-minute averaging routine was chosen to analyse bedform dynamics as it highlighted rapid changes in the bed profile and migration dynamics that were not well represented when averaging over a longer period.

In-situ water depths ranged from 0.8 m (the depth at which the SRP was deployed) to a maximum of 7.4 m (Figure 5.1). *In-situ* wave heights (H_s) were corrected for depth attenuation and ranged from 0.5 m in Tide 1 to 2.1 m in Tide 5. Mean cross-shore flows ($<u>$) were close to zero at higher tidal elevations. In relatively shallower water the rip current became active, and offshore directed flows were typically in excess of 0.3 m/s

with a 5-minute mean maximum of 0.74 m/s in run number 294. Unless otherwise stated, cross-shore (<*u*>) velocity is used for much of the analysis as opposed to longshore (<*v*>) or resolved velocity (<*r*>) as visual observations found the bedforms to be aligned shore-normal at the location of the instrumentation. Periods when the rip current was deemed to be active were identified following the method outlined in Section 3.6.4 and are marked on the figures where relevant.

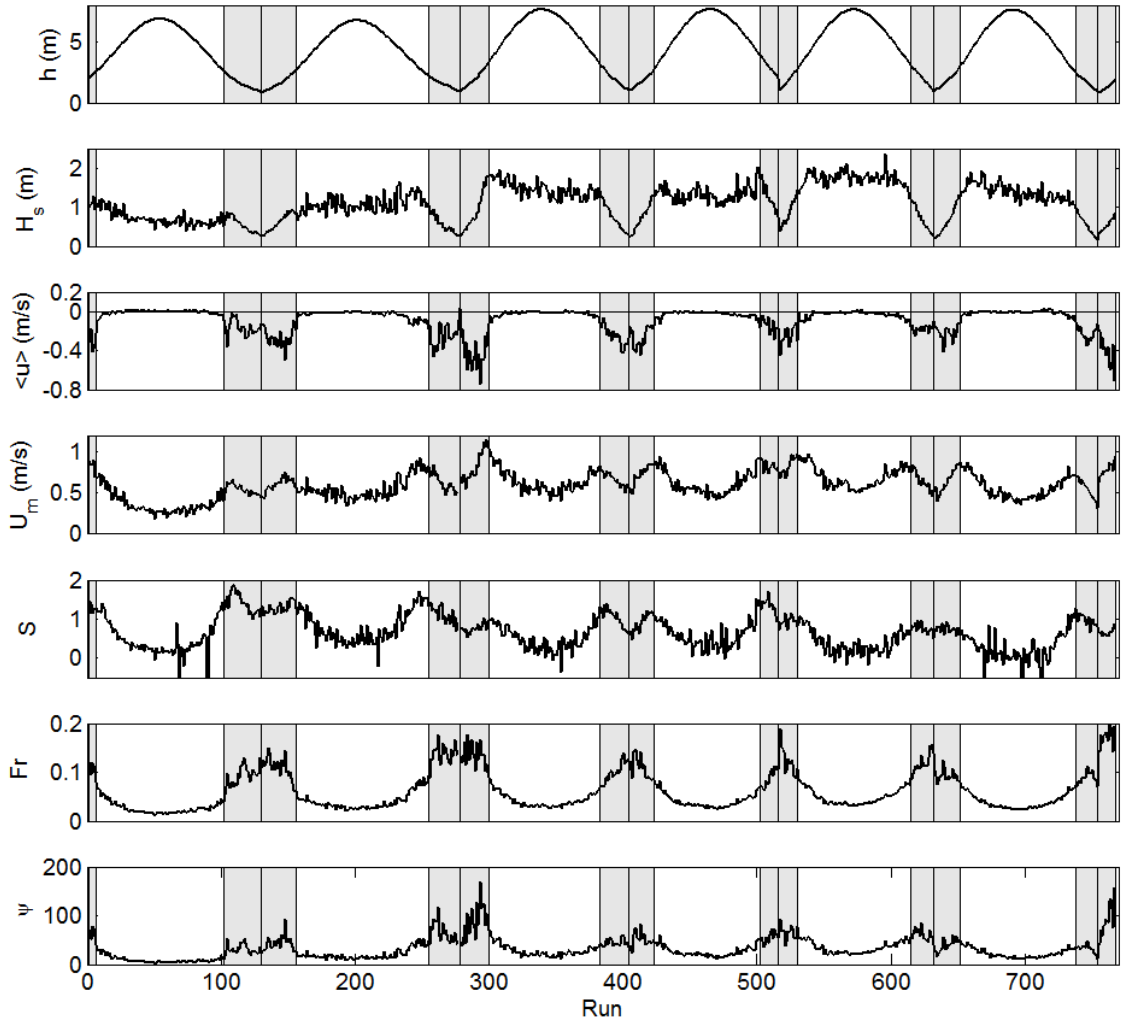

Figure 5.1: 5-minute averaged hydrodynamic parameters. From Top: water depth (h), significant wave height (H_s), mean cross-shore velocity (<*u*>), orbital velocity (U_m), incident wave skewness (*S*), Froude number (*Fr*) and mobility number (ψ). The shaded areas mark periods when the rip current was deemed to be active, the centre line in the shaded area represents the boundary between tides.

Wave orbital velocity (U_m) was calculated as the standard deviation of the velocity time series (Masselink et al., 2007). Wave skewness is a measure of wave shape. Positively skewed waves typically have a faster, albeit shorter, onshore than offshore stroke, and this can give rise to net onshore sediment transport and bedform migration (Gallagher, 2003). Un-normalised velocity skewness (<u^3>) (not shown here) is calculated from the oscillatory component of the cross-shore velocity, thus this parameter includes information on both the velocity variance and the wave shape and is used in bedload

transport models (e.g. Bailard, 1981). The equations for these parameters are displayed in Sections 3.6.3 and 3.6.4. The skewness parameter presented here is the 'normalised version (Equation 3.7). Both normalised and un-normalised wave skewness and orbital wave velocity exhibit a similar trend with the highest values found in larger waves and at lower tidal elevations (though not the lowest tidal elevations). The reason there is a decrease in the magnitude of all parameters describing wave action in the shallowest water depths is because that at low tide waves were likely to be dissipated before reaching the instrument frame.

The highest Froude numbers of between 0.1 and 0.15 were found in shallow water and in the fastest mean flows. The flow was always sub-critical and someway below the threshold for super-critical flows (of $Fr \geq 1$).

There are multiple forms of the mobility number. Here, the form of Gallagher (2003) was used as it includes both the mean and the oscillatory component of the velocity time series (Equation 3.12). The largest values of mobility number are found towards the ends of each tide in relatively shallow water when mean currents and wave action were most significant.

5.3: Bedform Dimensions

5.3.1: Bedform dimensions from SRP data

During periods when the rip current was deemed to be active, bedform length ranged from 0.56 to 3.11 m with a mean length of 1.45 m and a standard deviation of 0.57 m. Bedform heights in rip conditions were up to 0.19 m, with a mean of 0.06 m (Figure 5.2 and Table 5.1).

Bedforms in non-rip conditions had a mean length of 1.09 m with a range 0.61 to 1.87 m and a standard deviation of 0.22 m. Bedform heights in non-rip conditions were up to 0.12 m, with a mean of 0.06 m (Figure 5.2 and Table 5.1). The lowest bedform elevations were generally observed around the boundary of rip and non-rip conditions.

These results indicate that bedform length was larger in the rip current conditions compared to non-rip conditions, and bedform height was similar.

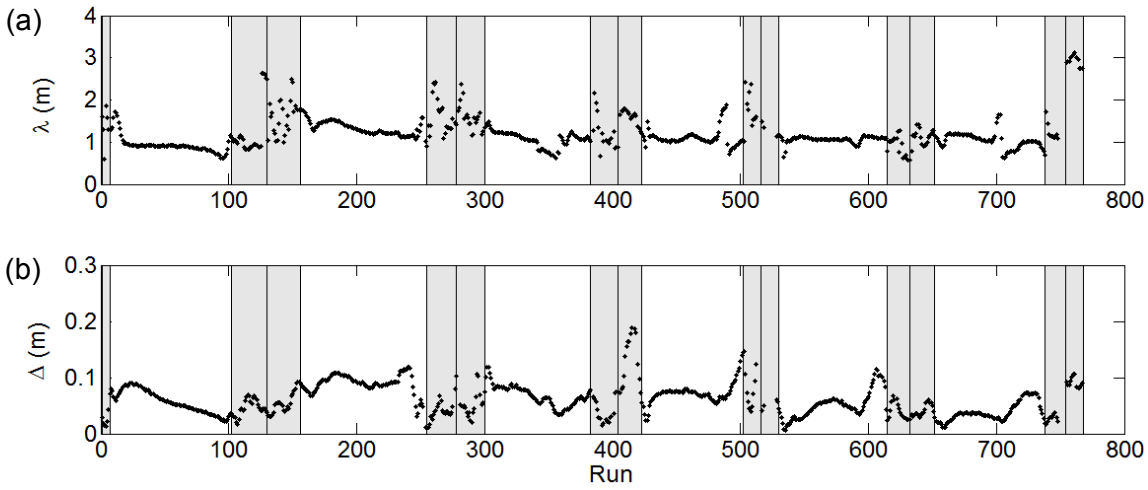

Figure 5.2: Bedform dimensions; (a) length (λ) and (b) height (Δ) for all SRP bedform data. The shaded areas mark periods when the rip current was deemed to be active, the centre line in the shaded area represents the boundary between tides.

Table 5.1: Bedform dimension statistics for rip and non-rip conditions.

	Mean (m)	Range (m)	90th percentile (m)	σ (m)
Rip				
λ	1.45	0.56 - 3.11	2.39	0.57
Δ	0.06	Up to 0.19	0.1	0.03
Non-Rip				
λ	1.09	0.61 - 1.87	1.39	0.22
Δ	0.06	Up to 0.12	0.09	0.03

5.3.2: Bedform dimensions from total station transect data

Further measurements of bedform dimensions were made by conducting relatively fine scale morphological surveys with a total station of cross-shore transects through the rip channel. The advantage of this method over measuring bed profiles with the SRP is that multiple bedforms are surveyed over a large cross-shore transect, compared to the 2 – 4 m footprint surveyed by the SRP. However, this data set only provides a snap shot in time and therefore bedform change relative to hydrodynamic conditions cannot be analysed. Five transects were measured within the rip system on consecutive daylight low tides, ranging from 8 to 23 m in length. The transects were measured in the rip neck as close as possible to instrument frame at a resolution of approximately 0.1 m in the cross-shore orientation (see Section 3.3.3 and Figure 3.7).

The bedforms measured in each transect were found to be of variable in size, with some being more than double the size of others measured only meters apart (Figure 5.3). Mean bedform length ranged from 2.5 m to 4.9 m, with a maximum and minimum

of 6.3 m and 0.9 m, respectively (Table 5.2). Mean bedform height ranged from 0.08 m to 0.21 m.

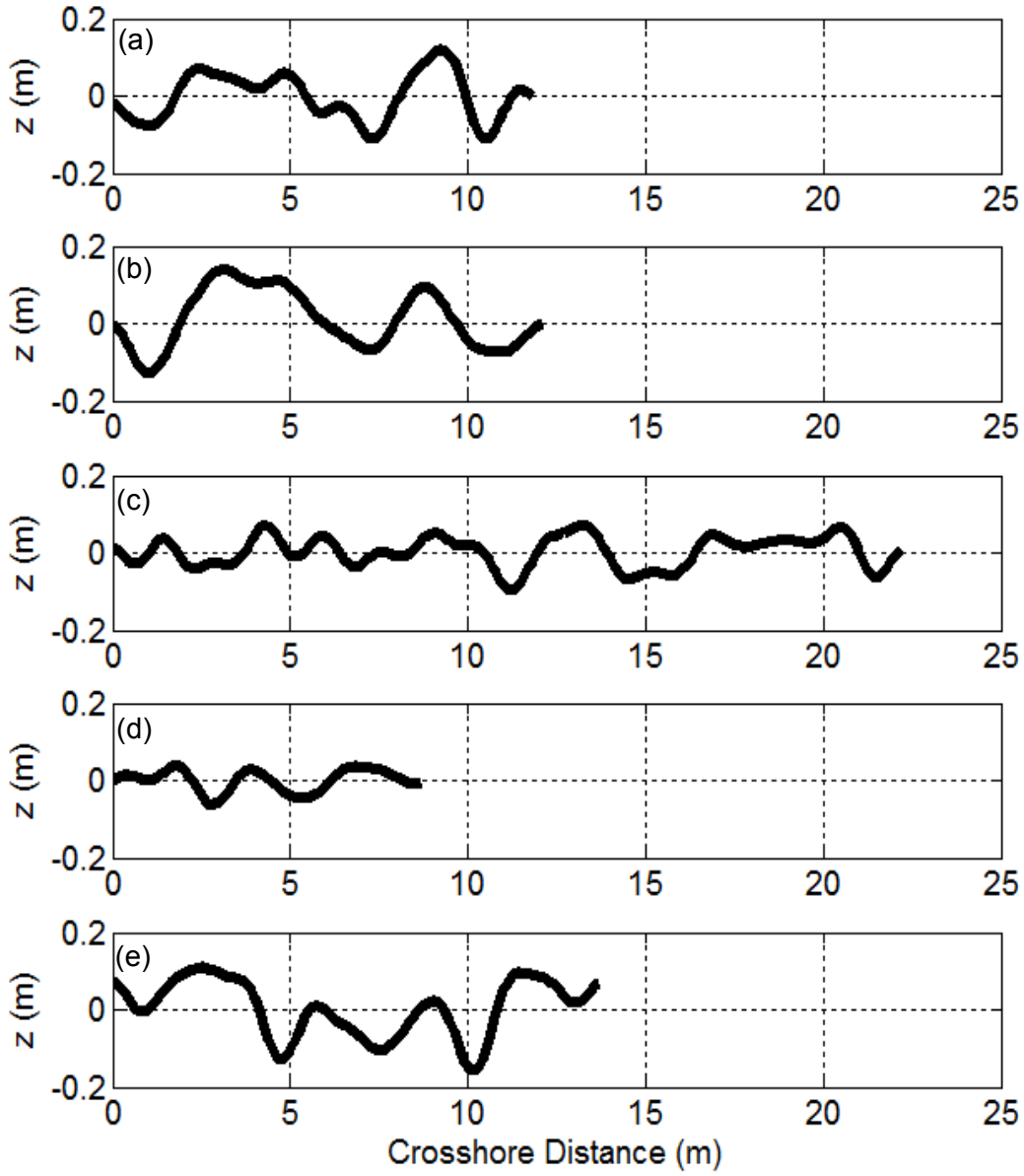

Figure 5.3: Cross-shore bed profiles (a – e) measured with a total station in the rip channel at low tide by walking cross-shore transects.

Table 5.2: Bedform lengths and heights from cross-shore total station survey.

Survey	Mean wavelength (m)	Range wavelength (m)	Mean height (m)
a	3.9	1.8 – 6.3	0.17
b	4.9	3.7 - 6.3	0.21
c	3.0	0.9 – 4.4	0.11
d	2.5	1.3 – 3.7	0.08
e	3.1	1.8 – 4.6	0.20

Although the mean dimensions of bedforms measured with the total station are at times larger than the majority of the bedforms measured with the SRP, bedforms of similar dimensions to those measured with the SRP during rip current conditions are present within all transects. This provides confidence in the results collected with the SRP.

5.4: Hydrodynamic Conditions for the Existence of Bedforms

The hydrodynamic conditions for the existence of bedforms are investigated by examining bedform length and height against a range of different hydrodynamic parameters. In many of the subsequent plots there is a large amount of scatter; however, it is possible to make some tentative observations of the hydrodynamic conditions that favour the existence of bedforms of certain dimensions.

5.4.1: Bedform dimensions as a function of water depth

Bedform lengths were greatest in water depths below 3 m and most of these observations were considered to be made when the rip current was active (Figure 5.4) and bedforms of shorter wavelengths (~ 0.6 m) are present at all water depths. Figure 5.4 indicates the existence of two different hydrodynamic regimes. It appears that bedform elevation shows no relationship with water depth. Bedform heights of ~ 0.01 m indicate that at times the section of bed measured is essentially flat, though bedforms of > 0.08 m are observed at all water depths (Figure 5.4).

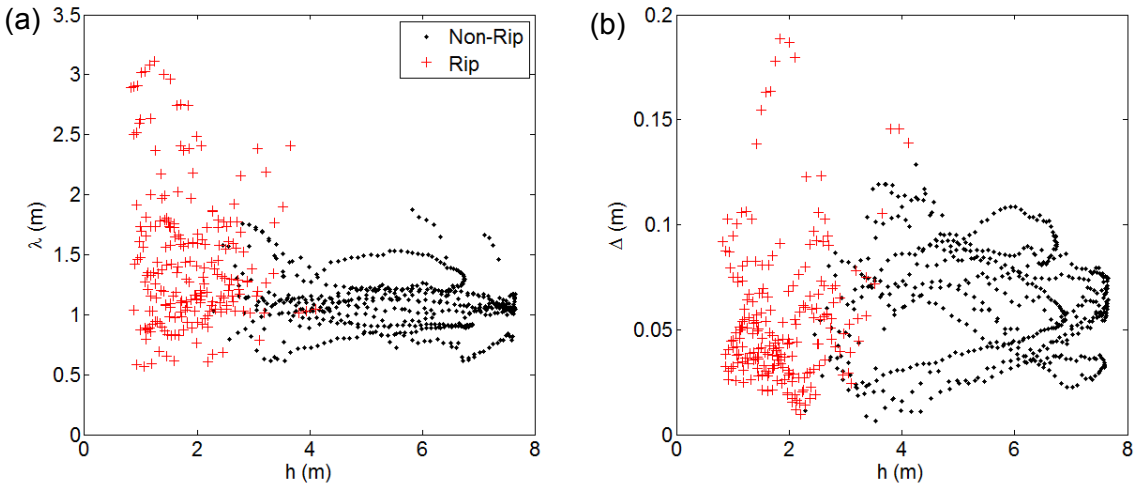

Figure 5.4: Bedform (a) length (λ) and (b) height (∆) as a function of water depth (*h*). Rip and non-rip observations marked.

5.4.2: Bedform dimensions as a function of mean cross-shore flows

The maximum bedform wavelength at weak velocities (< 0.1 m/s) is approximately 2.4 m, though the majority are < 1.5 m in length. Bedform length increases to a maximum of 3.1 m with increasing offshore directed mean flows (Figure 5.5) (R^2 = 0.51). The

largest wavelengths (> 3 m) were measured in offshore directed flows of > 0.3 m/s, while in faster flows there is no further increase in wavelength. This indicates that the bedforms may have reached an equilibrium state at which further increases in velocity have no effect. When the mean velocity is < 0.2 m/s the shortest bedform length is approximately 0.5 m. As mean flows increase beyond 0.2 m/s the minimum length of bedform increases in a linear fashion with minimum bedform lengths at velocities of 0.5 m/s of approximately 1.5 m. The increase in bedform length with increasing flows and decreasing water depth supports the earlier observations that bedform length is greater in rip than non-rip conditions. The largest bedform elevations are found in offshore directed flows between 0.2 m/s and 0.4 m/s, though in general, no relationship with mean flow strength is evident (R^2 = 0.04). Elevations ranging from 0.01 to 0.1 m occur at all flow velocities in both rip and non-rip conditions (Figure 5.5).

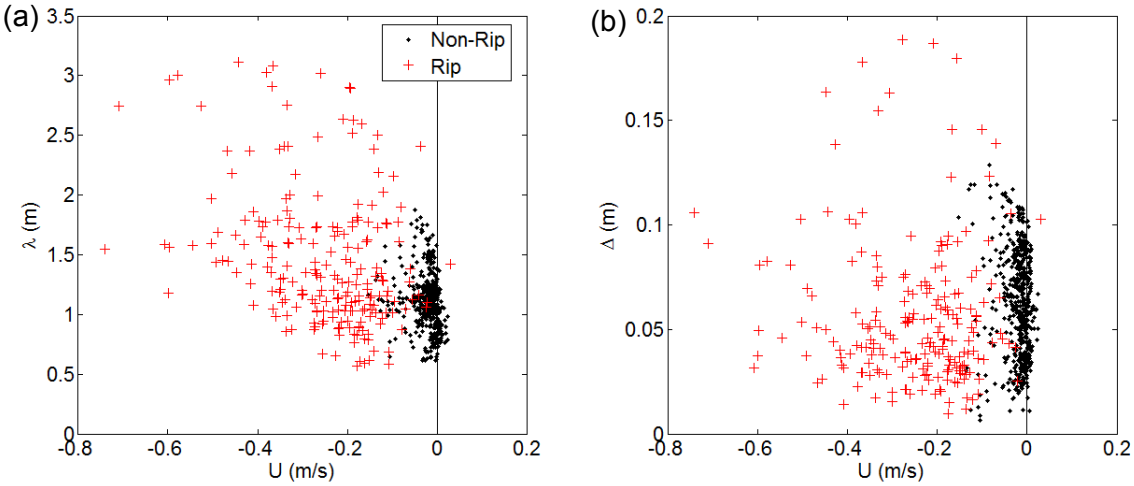

Figure 5.5: Bedform (a) length (λ) and (b) height (Δ) as a function of mean cross-shore velocity (<u>). Rip and non-rip observations marked.

5.4.3: Bedform dimensions as a function of orbital velocity

The effect of incident wave motion on bedforms was investigated by plotting bedform wavelength and height against orbital velocities (Figure 5.6). To avoid overlaying of data points rip and non-rip data are plotted separately. In non-rip conditions bedform length is < 1 m when U_m < 0.3 m/s. There is an increase in wavelength when U_m > 0.3 m/s, with the majority of the longest bedforms found in orbital velocities of between 0.4 and 0.8 m/s. Bedform height is around 0.05 m at low orbital velocities (~ 0.2 m/s). The range of bedform height increases with increasing orbital velocity. In rip conditions, there is no relationship between the bedform dimensions and U_m, suggesting that it is likely that the mean component of the rip flow has a greater influence on the bed.

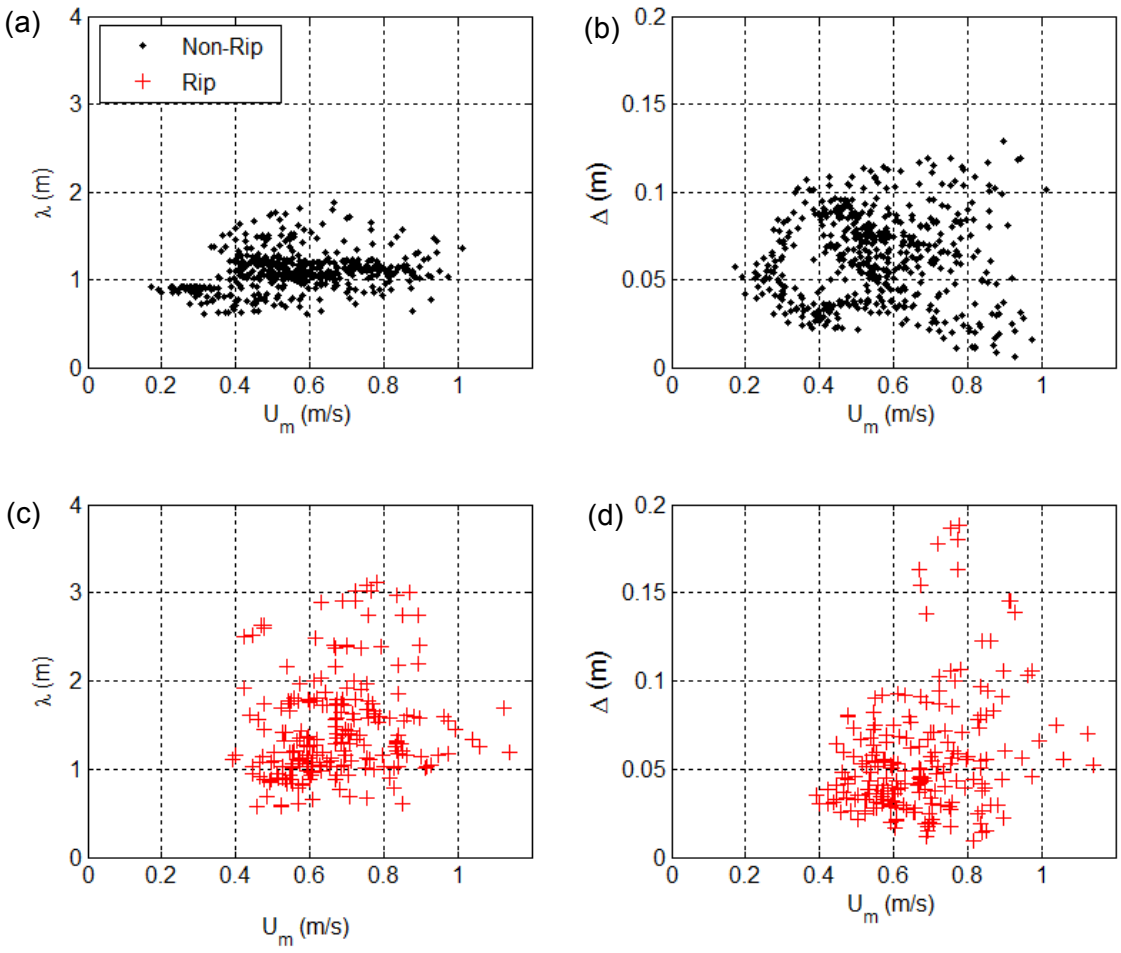

Figure 5.6: Bedform length (λ) (a & c) and height (∆) (b & d) as a function of orbital velocity (U_m). Data shows rip and non-rip conditions separately.

5.4.4: Bedform length as a function of Froude number and mobility number

Increasing the Froude number shows a weakly positive relationship with bedform length (Figure 5.7) (R^2 = 0.52) suggesting that water depth and mean currents are important factors in determining bedform length. As well as modulating rip circulation, a reduction of depth will result in the flow being constricted over the bed, thus increasing the Froude number.

The mobility number shows a positive correlation (R^2 = 0.47) with wavelength. There are no observations of bedform length < 1 m in mobility numbers > 80; however there are observations of bedform length of > 2.5 m in mobility numbers < 50. It is suggested that the strong mean flows maintain an influence on bedform length, while the weak oscillatory component reduces the mobility number. The stronger mean flow therefore appears to lead to the increase in wavelength.

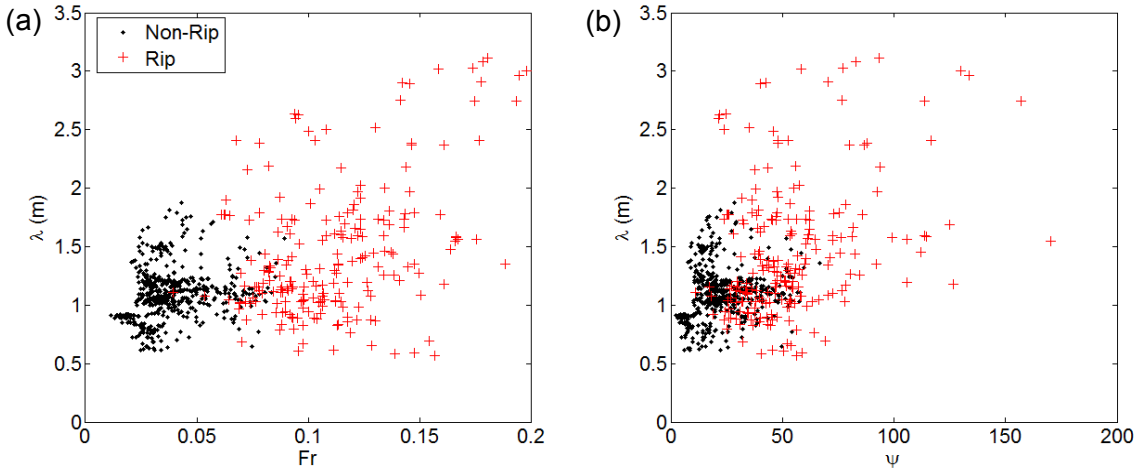

Figure 5.7: Bedform length (λ) as a function of (a) Froude number (Fr) and (b) mobility number (Ψ).

5.4.5: Rate of change of bedform dimensions

The rate of change of bedform height was calculated for all data as the change in bedform height divided by the change in time (δΔ/δt), where a 5-minute time step was used. This is plotted as a function of water depth (Figure 5.8). Bedform elevations were found to change (grow and decay) at rates of up to 0.8 cm/min, suggesting that at maximum rates a bedform feature with a height of 0.1 m could develop or disappear in a minimum of 12.5 minutes. The rate and the type of change (growth or decay) varied with water depth, though the most rapid changes all occurred in the relatively shallow water depth (h < 4 m). Figure 5.8 shows that bedforms generally grow when h < 2.5 m and when the bed is subject to rip current conditions. When h = 2.5 to 4 m, bedform elevation change is dominated by decay (Figure 5.8). This is well described by the partitioning of data into rip and non-rip conditions. When h is between 4 and 6 m, the bed height shows some growth, when h > 6 m and energy is insufficient to induce further change, the bedform becomes inactive, or they exist as relicts of the pervious hydrodynamic conditions.

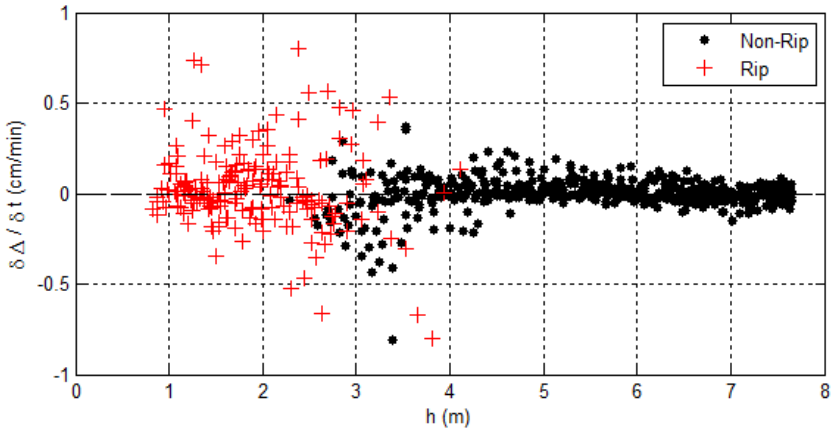

Figure 5.8: Rate of change of bed elevation (δΔ/δt) as a function of water depth

5.5: Bedform Classification

When considered in the classification scheme of Wiberg and Harris (1994), the bedforms in the rip current are most often sub-orbital (Figure 5.9a). An increase in d_o/Δ is observed towards the end of the tides and when rip is active. Orbital diameter (d_o) was calcaulated following Soulsby (1997) as:

$$d_0 = 2A_o \quad where \quad A_o = \frac{U_m T}{2\pi} \tag{5.1}$$

When classified using the O'Hara Murray et al. (2011) classification, the bedforms in the rip current tend towards a post-vortex state (Figure 5.9b).

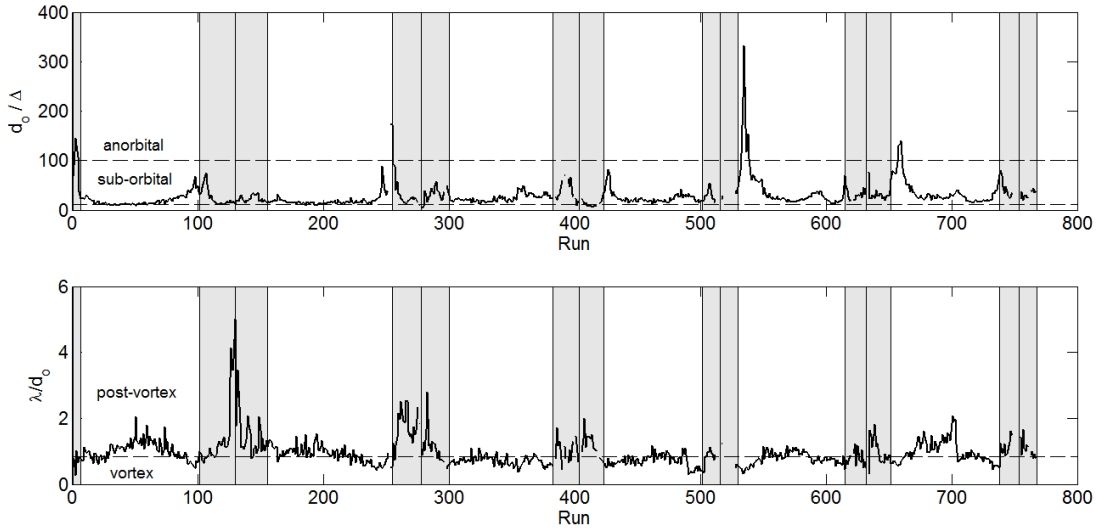

Figure 5.9: Bedform observations were classified as (a) anorbital, sub-orbital or orbital following Wiberg and Harris (1994) where anorbital = d_o/Δ >100; sub-orbital = d_o/Δ > 12 and < 100; orbital = d_o/Δ < 12 and as (b) vortex or post vortex following O'Hara Murray et al. (2011) where vortex λ/d_o < 0.83; post-vortex λ/d_o > 0.83.

In Tides 1 and 2 the bedforms were classified as post-vortex, indicating that high orbital velocities move the sediment from the bedform crest. During tides 3 to 6, λ/d_o is around 0.83, and therefore close to the boundary that separates vortex ripples from post vortex ripples. In rip conditions the threshold of λ/d_o = 0.83 is regularly exceeded. This is likely to be because the bedform wavelengths are larger when the rip current is flowing than when incident waves or surf zone conditions dominate.

The phase diagram of Boguchwal and Southard (1990) classifies the bed state as upper plane bed, dunes or ripples in current only conditions. The parameterisation classifies bedforms using the mean flow velocity and the grain size. For a grain size of 0.3 mm, the Boguchwal and Southard (1990) classification suggests a threshold of 0.5 m/s separates ripples and dunes. It was found that using the 5-minute mean velocity recorded in this study the majority of bedforms were classified as ripples. The 5-minute mean parameter possibly under-represents the influence of the stronger rip currents.

By using a, velocity parameter representing the upper 90th percentile of the absolute mean cross-shore velocity (U_{10}), instead of the mean, the observations made in the rip current often gave the bedforms a 'dune' classification. In the non-rip conditions (using U_{10}), when mean flows were relatively weak, the bedforms were often classified as 'ripples'.

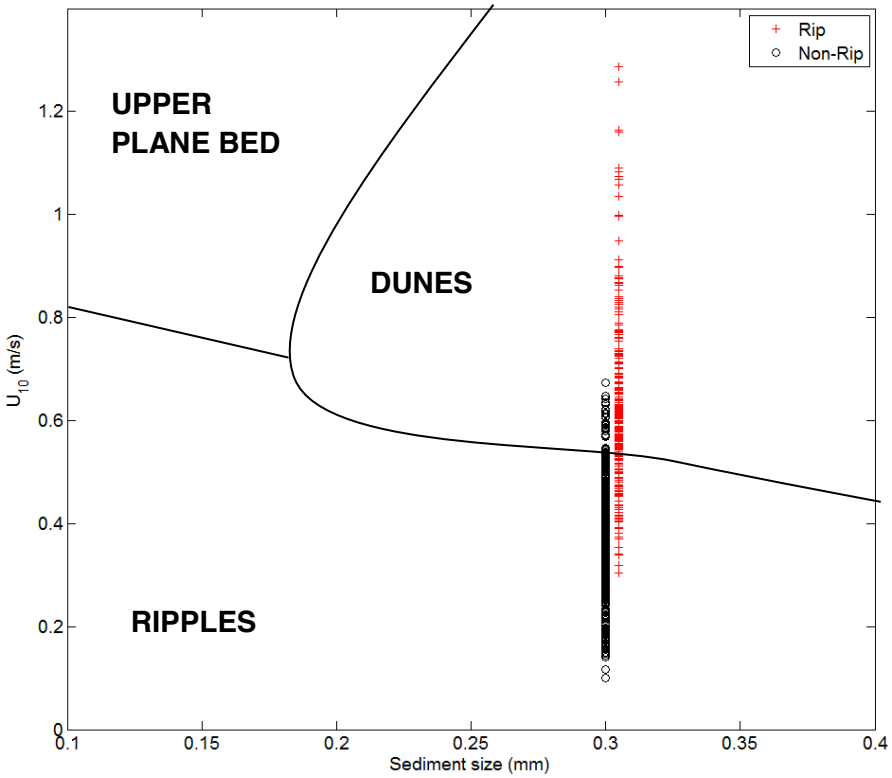

5.10: Bed state observations placed in the conceptual model of Boguchwal and Southard (1990), where bed state is a function of mean flows (U_{10}) and sediment size. Classification from rip and non-rip conditions are diaplyed seperatley and also seperated by a 0.05 mm grain size increment to aid visualisation.

The classification schemes above require that the ripples are *either* wave driven *or* current dominated. In fact, the conditions in the rip current include both high oscillatory velocities *and* strong currents. A broader classification may therefore be more appropriate. The majority of the ripples observed in the rip currents had wavelengths > 0.5 m. This suggests that the bedforms are of a similar classification to those observed by Gallagher et al. (1998a), who identified bedforms within the nearshore and surfzone with lengths and heights ranging from 1 – 5 m and 0.1 to 0.5 m respectively as 'megaripples'. This classification is appropriate here, as not only are the scale and location of the features similar to those identified by Gallagher et al. (1998a) but because the sediment sizes in which they are found in is similar, and like the observations of Gallagher et al. (1998a) these features are controlled both by waves and currents at different times. For the analysis in this study, it was therefore considered most appropriate to follow Gallagher et al. (1998a) and identify the bedform features as megaripples.

5.6: Bedform Migration

5.6.1: Quantification of bedform migration

Bedform migration was found to vary in both speed and direction over the tidal cycle (Figure 5.11). In rip current conditions mean bedform migration rate was 0.16 cm/min in the offshore direction with a maximum rate of 4.6 cm/min. In non-rip conditions the mean bedform migration rate was 0.09 cm/min in the onshore direction with maximum rates of 2.2 cm/min.

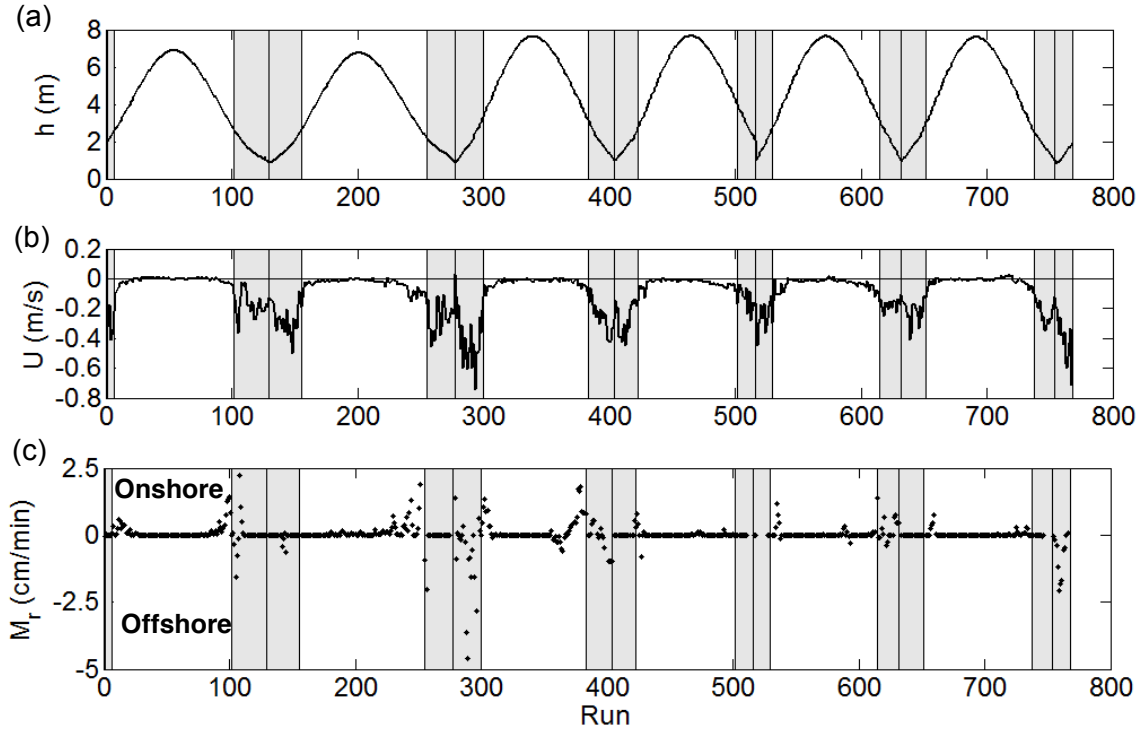

Figure 5.11: (a) Water depth (*h*), (b) mean cross-shore flows (<*u*>) and (c) migration rates (M_r) for all bedform data collected where negative migration is in the offshore direction. The shaded areas mark periods when the rip current was deemed to be active, the centre line in the shaded area represents the boundary between tides.

5.6.2: Bedform migration as a function of tidal elevation

In Figure 5.12 the dependence of bedform migration on water depth is investigated further. Figure 5.12a was produced by re-sampling the tidal data observations in 0.5 m bins for all tides and averaging the migration speed and direction within each depth-bin. Information on the water level is presented as a percentage of tidal cycle, with high tide equalling 50% of the tidal cycle. Migration is shown to vary with tidal state. The apparent asymmetry in migration rates is a result of large migration rates in the flood of Tides 3 and 7. Figure 5.12b shows migration speed and direction as a function of water depth. The majority of offshore migration occurs when $h < 2.5$ m, which is usually when the rip current is active. There is a clear change in migration dynamics between rip and

non-rip conditions. Bedforms showed two different forms of migration behaviour when the rip current was not active; when h = 2.5 to 5 m, the direction of migration was onshore, at a mean rate of 0.21 cm/min. When h > 5 m, the bedforms became static until the process was reversed on the flooding tide. Water depth itself provides a further mode of forcing of bedform dynamics by constricting the flow at shallower depths. The change in water depth throughout the tidal cycle modulates the wave breaking process and therefore affects the rip flow. At lower tidal elevations, wave breaking on the bar drives strong mean flows in the rip channel. At intermediate water depths (2.5 m to 5 m) water depth is too great for wave breaking on the bar to continue, however incident waves interact with the bed driving onshore migration. At water depths of > 5 m water depth bedform migration no longer occurs in this data.

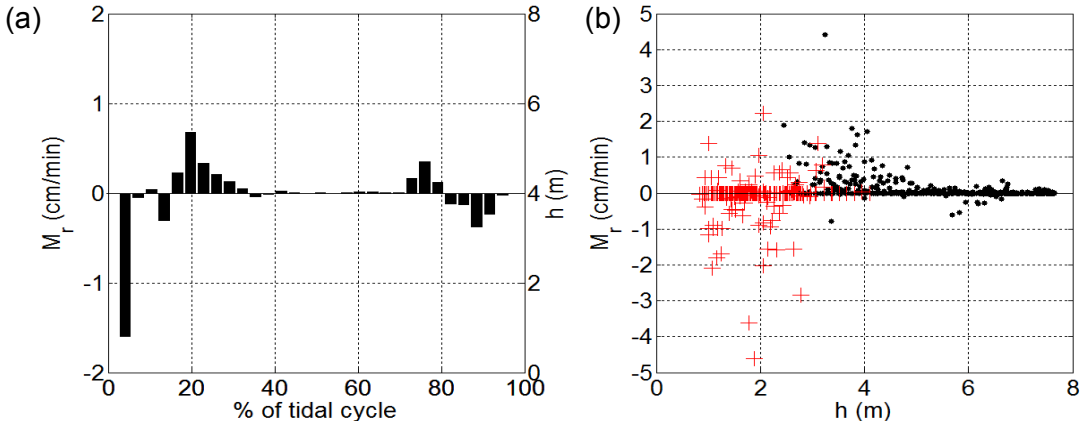

Figure 5.12: (a) Migration (M_r) data (bars) collapsed by re-sampling all data in 0.5 m increments as presented as percentage of tidal cycle, where 50% = high tide. (b) Migration (M_r) as a function of water depth (h) in the rip channel.

5.6.3: Bedform migration as a function of mean cross-shore flows

Offshore directed mean flows show a relationship with bedform migration speed and direction (R^2 = 0.26, R^2 = 0.39 when M_r = 0 is removed), with migration rates increasing with increasing current strength in the direction of flow (Figure 5.13). There is limited offshore directed migration occurring when offshore directed flow was < 0.3 m/s. All onshore directed migration was found to occur in offshore directed mean flows of < 0.2 m/s.

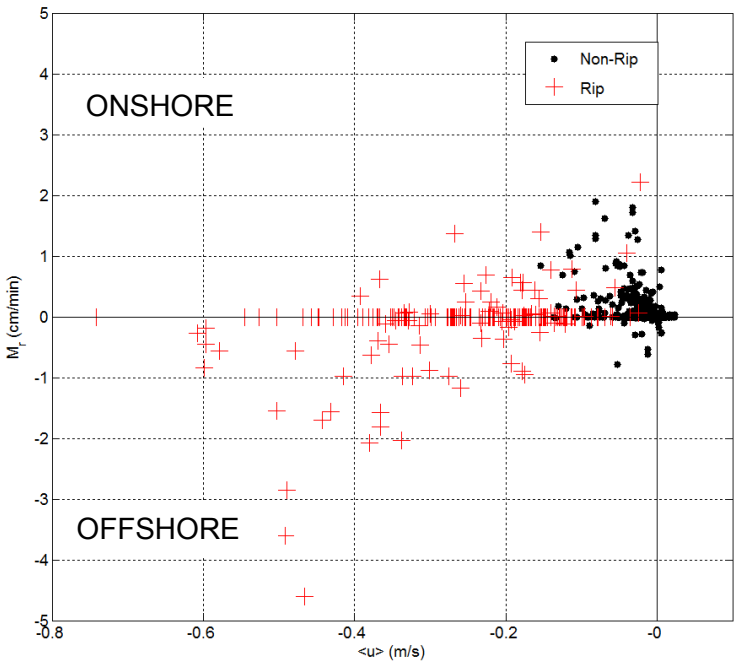

Figure 5.13: Bedform migration rate (M_r) as a function of mean cross-shore velocity ($<u>$).

5.6.4: Bedform migration as a function of incident wave processes

To examine the effects of different wave processes on migration, normalised incident wave skewness (S), un-normalised incident wave skewness ($<u'^3>$) and orbital velocity (U_m) were plotted against bedform migration rates (Figure 5.14). As earlier, observations from rip and non-rip conditions are plotted separately to avoid overlaying of data points. Generally in rip conditions there is no relationship between S, $<u'^3>$ and U_m (Figure 5.14b, d & f) and migration rate or direction.

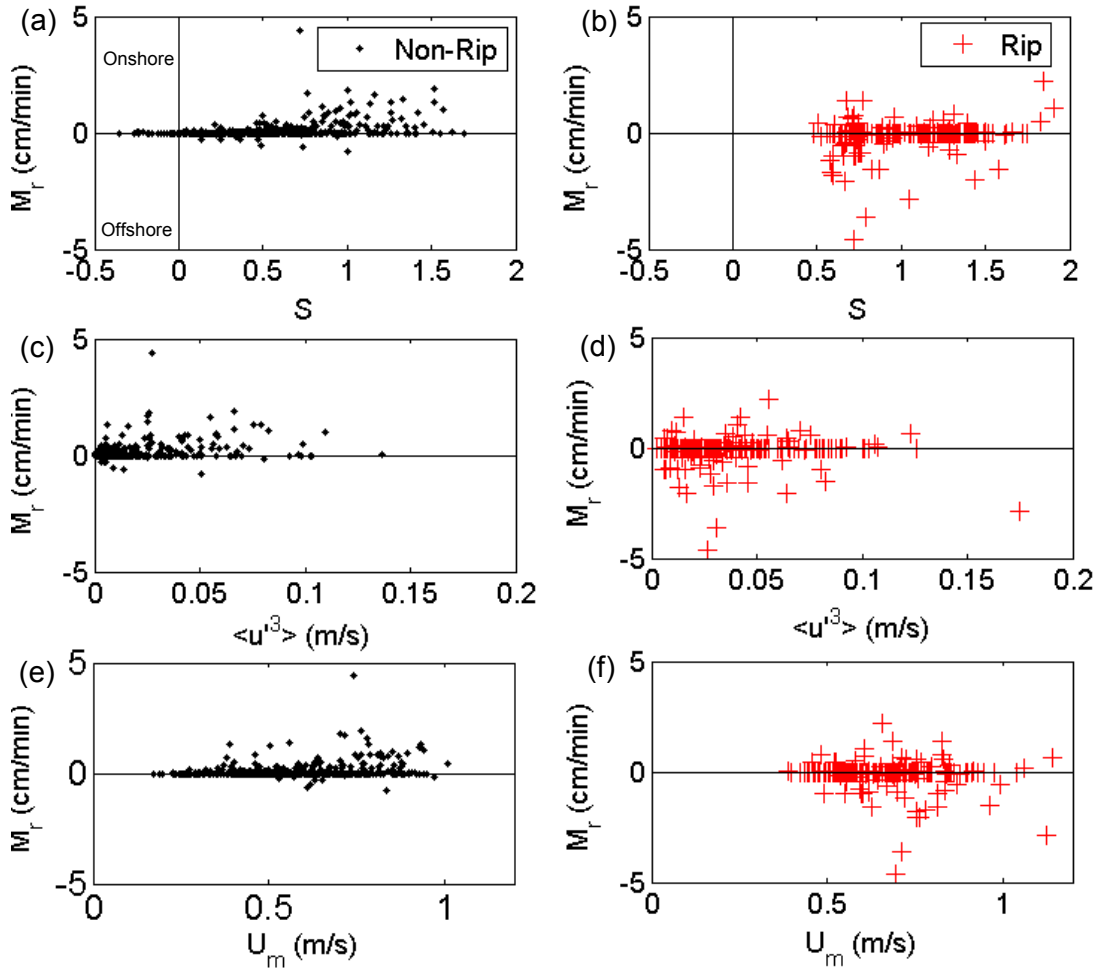

Figure 5.14: Bedform migration rate (M_r) as a function of (a & b) incident wave skewness (S), (c & d) velocity cubed (u^3) and (e & f) orbital velocity (U_m). Rip and non- rip conditions plotted separately.

When the rip is active, the majority of bedform migration is offshore directed. This is likely to be a result of the offshore directed mean flows of the rip current, and less to do with incident wave processes. In non-rip conditions there is no migration when $S < 0.5$ (Figure 5.14a). When $S > 0.5$ onshore migration increases with increasing S, although even at maximum values of S (~ 1.6) there are observations of the bed where no migration is occurring. The data for rip current conditions shows that in periods of reasonably high S that migration was still offshore directed. This suggests that if large $<u>$ and S occur simultaneously, the mean flows will dominate and the bedforms will migrate in the offshore direction. $<u^3>$ shows no relationship with migration in either rip or non-rip conditions. Migration as a function of U_m follows a similar, albeit less pronounced, trend as than with S.

5.6.5: Investigation of combined forcing of bedform migration

The combined forcing of bedform migration by mean offshore directed flows and normalised incident wave skewness is investigated further in Figure 5.15. The plot was produced by resampling the time series of Tides 3 to 7, (which are characterised by a

similar tidal range and therefore a similar time series length), allowing all observations of migration to be averaged within 5-minute bins. There are three well-defined parameter spaces within the figure: (1) when *S* and <*u*> are low the bedforms are relatively static; (2) when <*u*> is low and *S* is high bedforms migrate onshore; and (3) when negative values of <*u*> are large and *S* is low, bedforms migrate in the offshore direction.

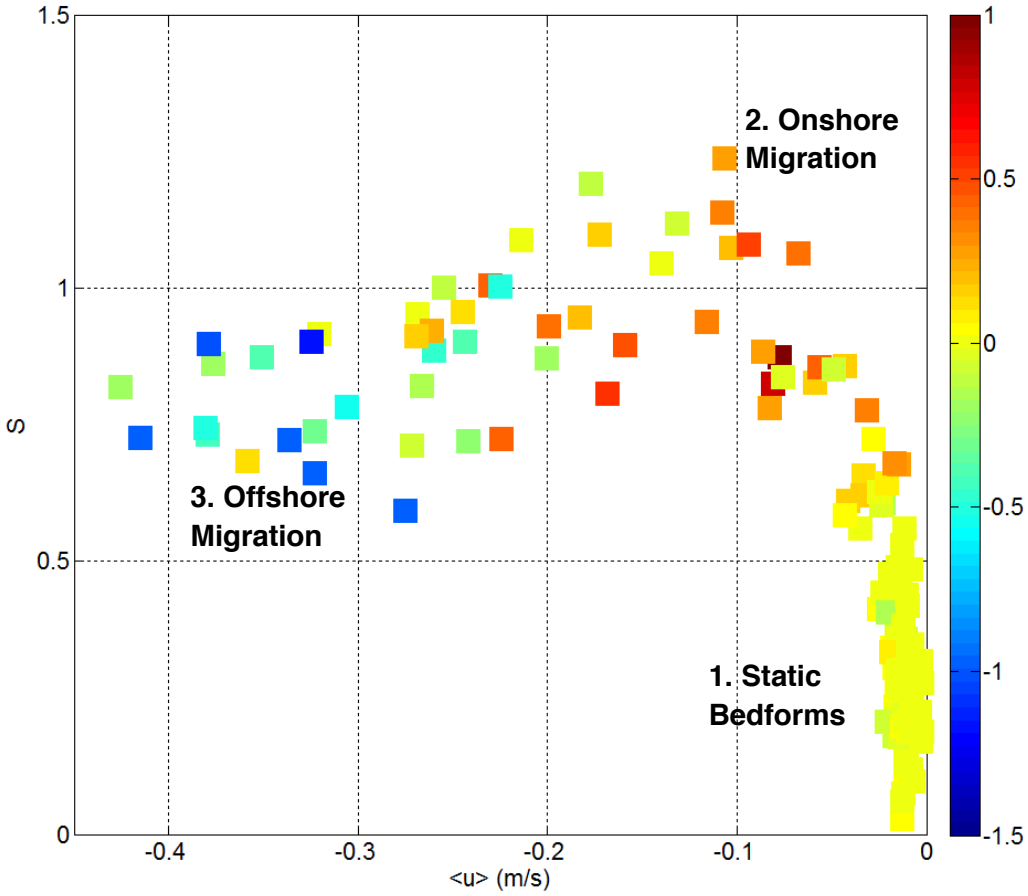

Figure 5.15: Migration rate (cm/min) represented by the colour bar; cool colours indicating offshore migration as a function of cross-shore velocity (<*u*>) and wave skewness (*S*). Data from Tides 3 to 7.

5.7: Bedform Transport Rate

Bedform migration rate can be used as a proxy for sediment transport (Huntley et al., 1991). The bedform transport rate (Q_b) is based on the cross-sectional area of the bed feature and is calculated from its height and migration rate. The method is described in Section 3.6.7 and the equation is also presented (Equation 3.22).

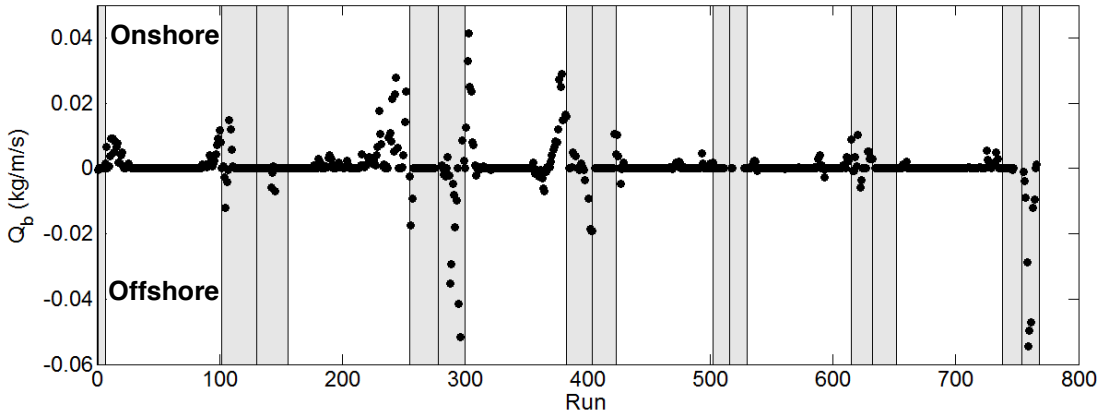

Figure 5.17: Bedform transport rate (kg/m/s) calculated from bedform data collected during *STIR 1* and *STIR 2.* The shaded areas mark periods when the rip current was deemed to be active, the centre line in the shaded area represents the boundary between tides.

Maximum mean bedform transport rates were 0.054 kg/m/s in the offshore direction, during periods when the rip current were active and 0.041 kg/m/s in the onshore direction when the rip was not active. The offshore directed mean bedform transport rate for all periods when the rip current was active was 0.0020 kg/m/s (Figure 5.17). The mean bedform sediment transport rate during periods when the rip current was not active was 0.0015 kg/m/s. Almost all offshore directed transport occurs in rip current conditions. It is worth noting that the rip current is still active when the water depth is too shallow for the SRP to collect data. Further bedform migration may take place in this shallower water, and therefore the extent of migration may be may be underestimated.

5.8: Discussion of Results on Bedform Dynamics

Instrumentation deployed in a rip channel measured bedform dynamics and hydrodynamics over six full tidal cycles and the flood of a seventh tide. At lower tidal elevations the rip current was active with strong offshore directed mean flows, often exceeding 0.3 m/s and with a maximum of 0.74 m/s. The tidal modulation of the rip current was very pronounced due to the macro-tidal setting. This allowed comparison to be made between bedform dynamics in rip current conditions and non-rip conditions at higher tidal elevations.

Bedforms were visually observed to be present throughout all channels within the rip system (rip neck and feeder channel) and absent from adjacent sand bars for the duration of all deployments. Thornton et al. (1998) and Swales et al. (2006) described a similar pattern, observing the rip system to consist of two distinctly different areas; the rip neck and feeder channel with large ripples and the bar with no bed features. Data

collected with the SRP shows that bedforms were ubiquitous in the rip channel throughout the tidal cycle, therefore encompassing periods when the rip current was both active and inactive.

In rip conditions mean bedform length was 1.45 m (with a range of 0.56 to 3.11 m) and mean height was 0.06 m (and up to 0.19 m). Measurements of bedforms made at low tide with a total station found that bedforms within the rip neck were not of uniform size, but had mean lengths ranging from 2.5 m to 4.9 m and height ranging from 0.08 m to 0.21 m. Although the mean length of bedforms measured with the total station are larger than that measured with the SRP, bedforms of similar dimensions were measured within each transect. Measurements in this study were similar to previous measurements of bedforms in rip currents reported in the literature. Sherman et al. (1993) measured bedforms of 1.6 m in length and 0.16 m in height in a feeder channel where water depth was 0.71 m and mean longshore flows were 0.4 to 0.6 m/s. Brander (1999b) observed bedforms in a rip current with lengths of 0.8 to 2 m and heights of 0.08 to 0.2 m. Thornton et al. (1998) observed bedforms of approximately 1 to 2 m in length in a rip current. Qualitative observations of bedforms in rip currents do not quote dimensions but refer to them as megaripples (Greenwood and Davidson-Arnott, 1979; Nielsen, 1992; Aagaard et al., 1997; Gallagher et al., 1998a). This puts them in the size range of 1 – 5 m in length and 0.1 to 0.5 m in height (Gallagher et al., 1998a).

In non-rip conditions bedforms were generally smaller, with mean lengths and heights of 1.09 m (with a range of 0.61 m to 1.87 m) and 0.06 m (and up to 0.12 m) respectively. Generally measurements of bedform dimensions here are of similar scale to those reported in the literature for rip currents, the surf zone and in uni-directional flows (as summarised in Table 5.3).

An attempt was made to classify the bedforms measured in this study based on the work of Wiberg and Harris (1994), O'Hara Murray et al. (2011), Boguchwal and Southard (1990) and Gallagher et al. (1998a). These classified the bedforms to be (i) sub-orbital (Wiberg and Harris, 1994), (ii) post vortex in Tides 1 and 2 and during Tides 3 to 6 they sit on the boundary (λ/d_o = 0.83) of the vortex / post vortex classification (O'Hara Murrary et al., 2011) and (iii) as dunes in the fastest 10% of the offshore directed mean flows (Boguchwal and Southard, 1990). Megaripple (Gallagher et al., 1998a) and dune (Boguchwal and Southard, 1990) dimensions compare well with measurements of bedform dimensions made in this study. Consistent with the nomenclature of bedforms of this scale measured in the surf zone and observed in rip currents, bedforms in this study are classified as megaripples.

Bedform migration underwent three distinct phases over an entire tidal cycle; (i) offshore migration in the rip current, (ii) onshore migration in intermediate water depths

(h = 2.5 to 5 m) when rip flow had ceased and (iii) stable in deeper water (h > 5 m) when mean currents were negligible and the influence of wave action on the bed had diminished. In the strong offshore directed flows of the rip, the mean migration rates were 0.16 cm/min, with a maximum of 4.6 cm/min. This was similar to observations by Sherman et al. (1993) of migration of 1.65 cm/min in a feeder channel in the direction of flow. However, this is a different environment as waves are likely to be propagating through the rip neck, whereas wave energy is dissipated on the bar before reaching the feeder channel. Mean onshore migration was 0.09 cm/min in non-rip conditions, with a maximum rate of 2.2 cm/min. In water depths of between 2.5 to 5 m (when the majority of onshore migration occurred), mean onshore bedform migration rate was 0.21 cm/min. Table 5.3 shows that this is comparable to previous observations of bedforms in the surfzone. Different authors use different units to express bedform migration; these have been carefully converted to cm/min for consistency in Table 5.3.

Dumas et al. (2005) observed that in increasing mean currents (<u> = 0.4 to 1 m/s) bedforms evolved into 'large asymmetric ripples' in an experiment conducted in a combined wave/current tank. The bedforms they observed (λ = 1.08 – 4.41 m; Δ = 0.09 – 0.41 m; M_r = 0.5 - 0.8 cm/min and a maximum M_r = 5 cm/min) behaved in a similar manner to bedforms measured in the rip current in this study. Further increases in mean flows in shallow water can lead to the formation of anti-dunes, bed features that migrate upstream in super-critical flows (Fr > 1), however in this experiment, flows were always sub-critical (Fr_{max} = ~ 0.15). Results of this study from an active rip current also compare favourably with bedform results from unidirectional flow in the South Saskatchewan River (Cant and Walker, 1978), where environmental conditions were similar (grain size = 0.3 mm, water depth = 1 m and current strength = 0.8 m/s).

Bedform length and height was generally observed to be greater in rip current conditions than in non-rip conditions. Rate of change analysis of bed elevations found that during periods when the rip currents were active the majority of change was growth (max = 0.8 cm/min), with the fastest growth occurring when offshore directed <u> > 0.3 m/s. Bedform length increased with increasing <*u*> until maximum lengths of approximately 3 m were achieved at velocities > 0.3 m/s. Hoekstra et al. (2004) observed an increase in length and height of bedforms in increasing velocity on a tidal shoal. Werner and Kocurek (1999) observed that the wavelengths of dunes in unidirectional flows increased with increasing age. In non-rip conditions bedform elevation initially shows a period of decay with increasing water depth (h = 2.5 – 5 m). Aagaard et al. (2000) noted that in some instances that megaripples disappeared in reduced mean currents. The reduction in height may eventually lead to a disappearance in megaripples, but did not occur fully due to rapid change in hydrodynamic conditions as a result of the macro-tidal cycle.

Table 5.3: Summary of field measurements of bedforms in the rip currents, the surf zone and for comparison uni-directional flow

Study	λ (m)	Δ (m)	M_r (cm/min)	Environmental Conditions
Rip Current				
Sherman et al. (1993)	1.6	0.16	1.65	Feeder channel; $<v>$ = 0.4-0.6 m/s
Brander (1999b)	0.8 - 2	0.08 - 0.2	-	$<u>$ = 0.3 -0.6 m/s
Thornton et al. (1998)	1-2 m	-	-	-
Surf Zone				
Gallagher et al. (1998a)	2 – 5	0.2 – 0.3	0.5 (max = 2.5)	h = 1.5 – 2 m; H_s = 0.5–4 m
Aagaard et al. (2000)	1.2 – 2.4	0.24	0. 75 – 1.5	Seaward slope of bar; H_s = ~ 1m
Swales et al. (2006)	≤2.9	0.2 – 0.3	-	Storm and fair weather
Vincent et al. (1999)	0.7-0.9	0.1- 0.15	-	H_s = 1 m
Ngusaru and Hay (2004)	-	0.05 – 0.5	0.17 – 0.67	H_s = 0.5 – 3.5 m
Clarke and Werner (2004)	0.5 - > 2	0.03 - > 0.15	-	H_s = ≥ 1.5 m
Uni-directional				
Hoekstra et al. (2004)	0.4 - 1	0.02 – 0.09	3 – 4 (max rates)	Tidal shoal; max - 0.35 – 0.5 m/s
Cant and Walker (1978)	-	0.3 (max)	-	River (minor channels); max = 1 m/s
Deep Water				
Traykovski et al. (1999)	1.0	0.15	0.05 (80 cm/day)	h = 11 m

Self-organisation models (e.g. Gallagher, 2011) predict that bedform spacing increases indefinitely in oscillatory conditions unless flow conditions change too rapidly (which may be induced by changes in tidal level) or the bed passes through the swash zone (Clarke and Werner, 2004). Miles et al. (2014a) observed both decay and growth of bedform length at rates of ~ 5 cm/min. Growth rates fitted the predictive curve of Clarke and Werner (2004) that suggests growth rates of 5 cm/min for ripple age of 21 minutes and 0.28 cm/min for ripple age of 0.5 days (720 minutes). Bedform lengths in this study

can be seen to both grow and decay, though this is likely to be a result of a shift from a current forced regime to a wave dominated regime as the tidal elevation exposes the low tide bar-rip morphology.

Whilst offshore directed migration can be attributed to the fast offshore flows of the rip, onshore migration was found to increase with incident wave skewness and to a lesser extent with orbital velocity. Bedforms have been observed on numerous occasions to migrate onshore in the surfzone (Table 5.3). There is some variation in the wave process other authors have found to be most efficient for driving onshore migration. Wave skewness (Crawford and Hay, 2003; Gallagher, 2003), orbital velocity (Ngusaru and Hay, 2004) and mobility number (Vincent and Osborne, 1993; Traykovski et al., 1999) are all attributed to the forcing of onshore bedform migration.

Gallagher et al. (1998a) suggested that as well as wave processes, a superimposed mean current may also induce megaripple migration. This was also observed by Crawford and Hay (2001) who found ripple scale (λ = 0.85; Δ = 0.03) features to migrate in an offshore direction, and by Ngusaru and Hay (2004) who identified possible offshore migration of megaripples when mean flows exceeded 0.2 m/s. As neither author mention rip currents, it is assumed the mean flows are a result of undertow. In the data presented here, onshore migration took place in the opposing direction of a weak offshore directed flow (< 0.2 m/s). In most cases these periods were considered non-rip conditions and are therefore assumed to be undertow. Dumas et al. (2005) made a similar observation in a combined flume tunnel, where bedforms (λ = 2 – 5; Δ = 0.3 – 0.4) migrated upstream when oscillatory flows were high (0.8 – 1.2 m/s) and opposing mean flows were low (0.15 m/s). They proposed a mechanism which is outline with the aid of Figure 5.18. When the offshore mean flow and the offshore stroke of the wave are in the same direction, sediment is suspended. When oscillatory flow reverses, the net flow is onshore and sediment is deposited on the shoreward face of the bedform. They termed these features reverse ripples.

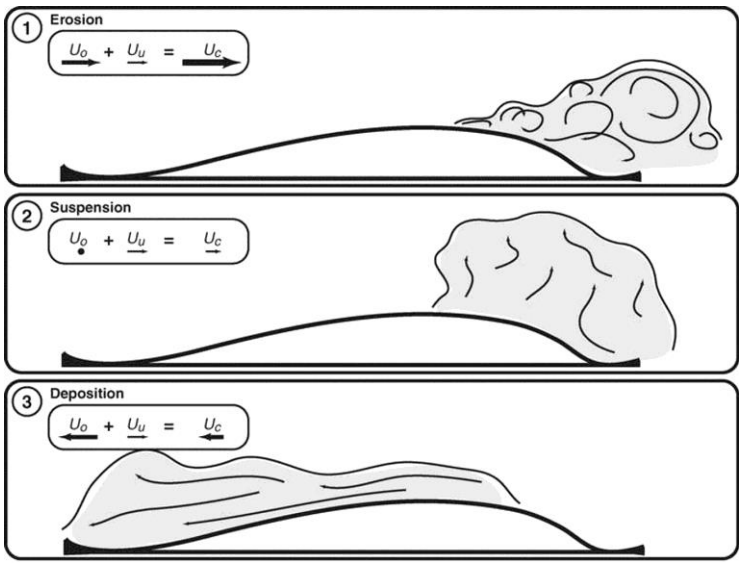

Figure 5.18: Schematic diagram showing the mechanism for which bedforms migrate upstream in weak unidirectional flows (U_u) and wave activity (U_o) from the opposing direction, where U_c is sediment transport (Dumas et al., 2005).

Results from a multivariate model presented in this study do a reasonably good job of predicting migration rates (R^2 = 0.53 and 0.59) and illustrates the balance between the strong offshore mean flows of the rip current against the increasing relative importance of wave skewness and orbital velocity as mean flows diminish.

Rip currents have been recognised to have the potential to transport significant volumes of sediment offshore (Aagaard et al., 1997). A potential mechanism for sediment transport is the offshore migration of bedforms (Kachel and Sternberg, 1971; Huntley et al., 1991; Masselink et al., 2007). In some cases bedform migration is considered as a direct proxy for bedload transport (Hoekstra et al., 2004). Work by Bagnold (1977) indicates that bedload transport scales with a higher power of mean velocity, however a poor relationship exists between $\langle u^{x3} \rangle$ and migration rates presented in this study. Therefore bedform migration is assumed to make up the bedload component and an unquantifiable amount of saltation also contributes (Masselink et al., 2007).

Mean bedform sediment transport in a rip conditions was offshore directed at 0.0020 kg/m/s with a maximum of 0.054 kg/m/s. Mean bedform sediment transport was onshore when the rip was not active at a rate 0.0015 kg/m/s with a maximum of 0.041 kg/m/s. The similar bedform transport rates in rip and non-rip conditions in opposing directions suggests that over a tidal cycle the net transport, due to bedform migration will be small. When the water level drops below the SRP it is important to note that the rip current may still be active and bedforms may still be migrating offshore and adding to the net bedform transport. As a comparison, bedform sediment transport rates have

been calculated from bedform migration rates published by other authors in Table 5.4. Q_b was identified using the quoted M_r and Δ data, and applied using equation 3.22.

Table 5.4: Bedform height (Δ), migration rate (M_r) and bedform transport rate (Q_b) compared to work by other authors (the median used where range reported).

Author	Environment	Δ (m)	M_r (cm/min)	Q_b (kg/m/s)
This study	Rip Non-rip	0.06 0.06	- 0.16 + 0.09	-0.0020, Max = - 0.054 +0.0015, Max = +0.041
Sherman et al. (1993)	Feeder Channel	0.16	1.65 (in direction of flow)	+ 0.07 (in direction of flow)
Gallagher et al. (1998a)	Surfzone	0.25	+ 0.5	+ 0.03
Aagaard et al. (2000)	Surfzone	0.24	+ 1.12	+ 0.07
Ngusaru and Hay (2004)	Surfzone	0.28	+ 0.37	+ 0.004
Hoekstra et al. (2004)	Tidal Shoal	0.06	+ 3.5 (max) (in direction of flow)	+ 0.05
Traykovski et al. (1999)	h = 11 m	0.15	+ 0.05	+ 0.002

In general onshore and offshore bedform transport calculated from data collected in this study compare well to bedform transport rates calculated from bedform dimensions reported by other authors within the nearshore (the environmental conditions are summarised in Table 5.3). The maximum offshore bedform transport rate (0.054 kg/m/s) in this study is similar in magnitude to the bedform transport rate calculated from data collected in a feeder channel by Sherman et al. (1993) of 0.07 kg/m/s. In non-rip conditions, the maximum bedform transport (0.041 kg/m/s) also compares well to the bedform transport rates calculated from the bedform results collected in the nearshore of other authors (Gallagher et al., 1998a; Aagaard et al., 2000; Hoekstra et al., 2004; Ngusaru and Hay, 2004) (Table 5.4).

5.9 Summary of Results: Bedform Dynamics

The aim of this chapter was to present data on bedform dynamics within a rip current. This is achieved largely by comparing bedform observations from when the rip current was active and when it was inactive.

The results in this chapter may be summarised as follows;

- Bedforms were found to be ubiquitous in the rip channel, occurring at all stages of the tidal cycle. This included periods when the rip current was and was not active. Bedform dynamics changed throughout the tidal cycle. This was attributed to changes in water level that modulated the effect of waves and the presence of rip flow, which in turn controlled the bedforms.
- Classification of the bedforms based on conceptual models of oscillatory bed features classifies them as sub-orbital (Wiberg and Harris, 1994) throughout each tidal cycle and most often as post-vortex when the rip current is active (O'Hara Murray et al., 2011). In a uni-directional flow classification system, the bedforms would be classified as dunes, following Boguchwal and Southard (1990). However, the bedforms in this study exist in a combined wave - current environment. The classification of megaripples is more appropriate in this case. Gallagher et al. (1998a) identified megaripples as bedform features with a length and height ranging from 1 to 5 m and 0.1 to 0.5 m respectively and these values are consistent with data presented here. Furthermore, this terminology is consistent with that used to describe bedforms in rip currents (Nielsen, 1992; Sherman et al., 1993; Brander, 1999b).
- There was evidence that bedforms were larger when the rip current was active. In an active rip current, length ranged from 0.56 to 3.11 m, with a mean length of 1.45 m. Bedform height was up to 0.19 m, with a mean height of 0.06 m. These dimensions compare favourably to measurements of Sherman et al. (1993) in a feeder channel and observations of bedforms in rip currents (Nielsen, 1992; Thornton et al., 1998; Brander, 1999b).
- In non-rip conditions bedform length ranged from 0.61 to 1.87 m, with a mean of 1.09 m. Bedform height was up to 0.12 m, with a mean of 0.06 m. These dimensions compare well to measurements made in the nearshore zone (Gallagher et al., 1998a; Aagaard et al., 2000; Clarke and Werner, 2004; Miles et al., 2014b).
- Bedform migration was often offshore directed when the rip current was active. This suggests migration is forced by the mean offshore directed flow of the rip. The mean migration rate in an active rip current was 0.16 cm/min in an offshore direction, with a maximum offshore directed migration rate of 4.6 cm/min. Sherman et al. (1993) measured bedform migration in the direction of flow, in a feeder channel at comparative rates (M_r = 1.65 cm/min).
- In non-rip conditions, bedform migration was generally onshore directed with a mean rate of 0.09 cm/min and a maximum rate of 2.2 cm/min. This correlated

well with incident wave skewness, as also observed by Crawford and Hay (2003); Gallagher (2003) and to a lesser extent, orbital velocity (Ngusaru and Hay, 2004). In non-rip conditions bedform migration exhibited two different types of behaviour; when h = 2.5 – 5 m mean bedform migration was onshore directed (mean M_r = 0.21 cm/min) and when h > 5 m the bedforms were generally stationary.

- Sediment flux associated with migrating bedforms was calculated following Kachel and Sternberg (1971), Huntley et al. (1991) and Masselink et al. (2007), and termed bedform sediment transport rate. During periods when the rip current was active, mean bedform sediment transport was offshore directed at a mean rate of 0.0020 kg/m/s, with a maximum rate of 0.054 kg/m/s (as a 5-minute mean). When the rip current was not active, bedform sediment transport was onshore directed, at a mean rate of 0.0015 kg/m/s with a maximum rate of 0.041 kg/m/s. This shows that over a tidal cycle, the net offshore bedform transport is, on average, relatively small due to the time the rip is active, compared to the time the conditions exist the onshore bedform migration.

CHAPTER 6: SUSPENDED SEDIMENT TRANSPORT IN RIP CURRENTS

6.1: Introduction

Previous studies have identified the importance of rip currents for offshore directed suspended sediment transport (Cook, 1970; Short, 1985; Aagaard et al., 1997; Brander, 1999b). This is due to the presence of fast flows and the interaction of waves with the bed (Brander, 1999b) in relatively shallow water, giving rise to the potential for sediment suspension and its subsequent offshore transport.

This chapter aims to identify the different processes responsible for suspended sediment transport in a rip current and to quantify the contribution of mean flows, incident waves, infra-gravity waves and VLF oscillations. Analysis is based on observations at one height above the bed. Additionally, the depth integrated total suspended sediment transport rate is estimated, so that comparison can be made with bedform transport rates.

Initially the processes responsible for sediment suspension in the rip channel are examined. The different processes responsible for sediment transport are investigated individually by use of examples. The total transport is composed of a mean (<*uc*>) and an oscillatory component (<*u*'*c*'>) (Jaffe et al., 1984). The oscillatory component is investigated using spectral analysis methods (Huntley and Hanes, 1987) to demonstrate the contribution that different frequency motions present within the rip flow have on suspended sediment transport.

The analysis is applied to all data, not just periods when the rip current was deemed to be active. This provides a comparison between rip and non-rip conditions and gives an insight into suspended sediment transport on a high energy macro-tidal beach. The suspended sediment flux is quantified using sections of data with a range of time scales. Initially 10-minute run lengths are used showing the relative contribution and magnitude of the mean, oscillatory and total flux throughout the entire data set. By using filtering techniques the flux at different frequencies is quantified and presented as a time series on a 68-minute time scale. The data is also presented on a *rip current time scale*. Using the method identified in Section 3.6.4**,** periods when the rip current was deemed active are isolated. From the runs of instantaneous measurements of velocity (*u*) and concentration (*c*) all modes of transport, including those at different frequencies, were quantified and presented in the form of time series and bar charts for each time the rip was active on the flood and ebb of the measured tides.

Depth integrated total suspended sediment flux (kg/m/s) is estimated using two point measurements of sediment concentration and one (*STIR 1*) or two (*STIR 2*) point

measurements of velocity. This value allows a comparison between bedform transport rate and suspended sediment transport rate and provides an insight into the total volume of suspended sediment transport in a rip current.

6.2: Sediment Suspension

6.2.1: An example of suspended sediment concentrations

Suspended sediment concentrations were found to be at a maximum in intermediate water depths (h = 2 to 5 m) when velocity variance and offshore flows were largest. The lowest concentrations were found when the water level over the instrument frame was at its greatest.

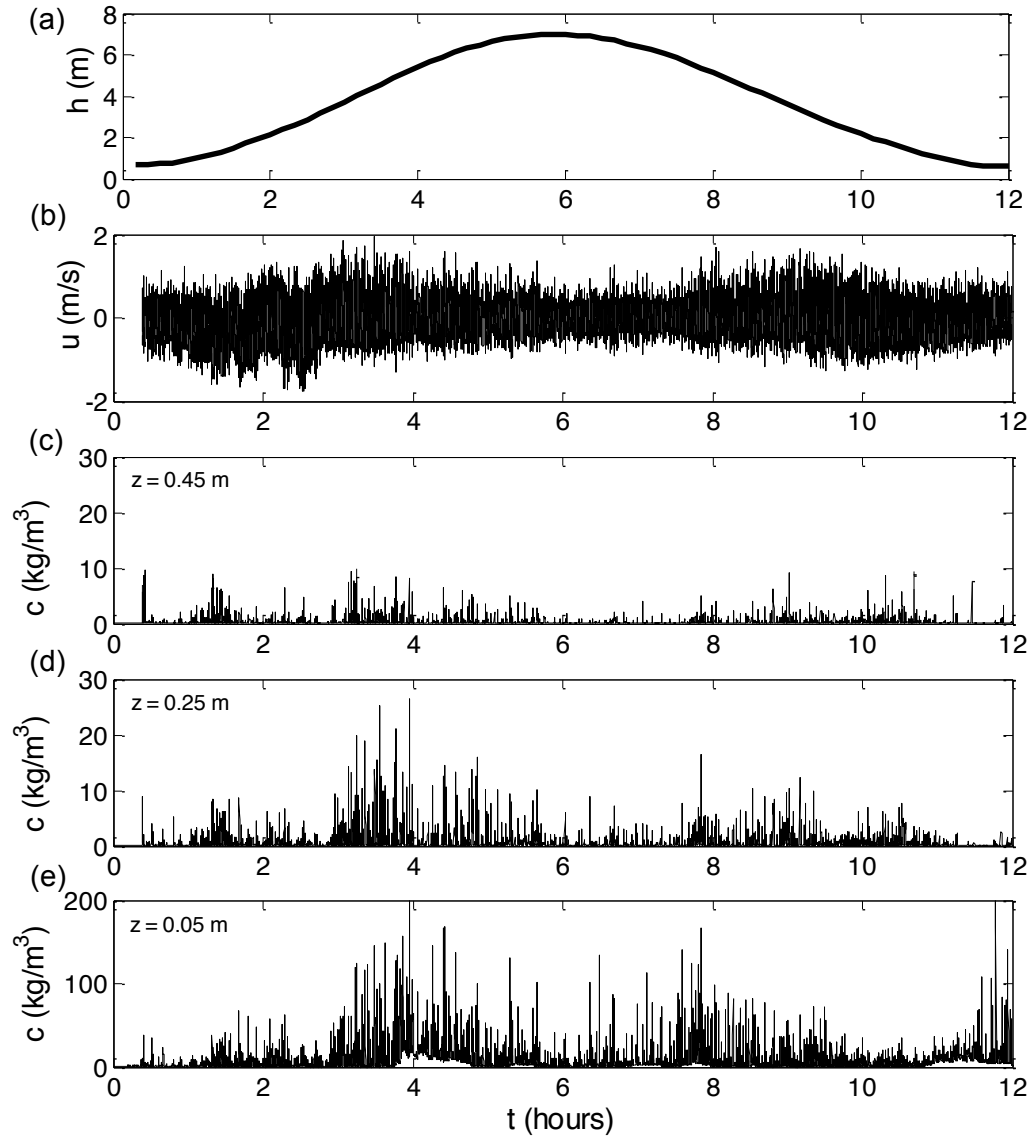

Figure 6.1: An example of instantaneous velocity and concentration data over a tidal cycle (H_o = 1.12 m, T_p = 13 s); (a) water depth (h), (b) instantaneous velocity (u) and instantaneous concentration at (c) z = 0.45 m, (d) 0.25 m and (e) 0.05 m. (n.b. y-axis scales differ between panels).

Suspended sediment concentration also appears to show a reduction in the shallowest water depths in Figure 6.1 (data from *STIR 2*, Tide 1). As expected, there is decay in suspended sediment concentration moving vertically away from the bed (Figure 6.1c-e). The concentration does not decay in a uniform manner, with concentrations at z = 0.05 m an order of magnitude larger than at z = 0. 25 m and z = 0.45 m.

6.2.2: Sensitivity of suspended concentration measurements

Much of the subsequent analysis is undertaken from a single fixed point measurement. The OBS at z = 0.25 m was chosen for this as it was present at this height during both *STIR 1* and *STIR 2* and as it recorded more data than the OBS positioned at z = 0.45 m. The sensitivity of measurements made at different elevations above the bed is investigated in Figure 6.2.

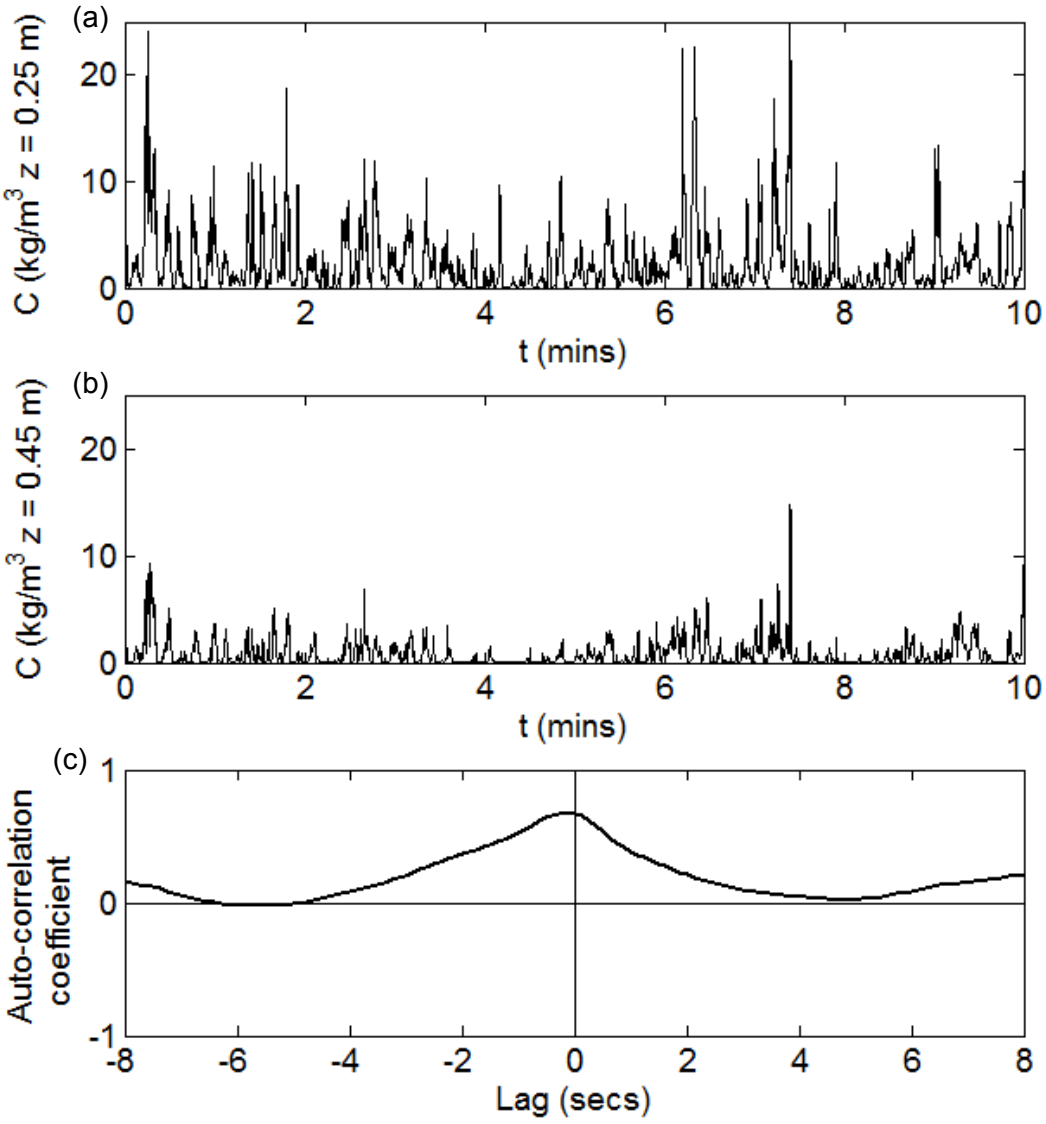

Figure 6.2: Instantaneous suspended sediment concentration from OBSs at (a) z = 0.25 m, (b) z = 0.45 m and (c) auto-correlation of the two concentration time series.

One assumption of the analysis is that, although the magnitude of concentration is greater closer to the bed, the timing and therefore the processes at z = 0.25 m are representative of other heights. This was investigated by performing cross-correlation analysis on vertically separated OBSs on a 10 minute section of data when the rip was active following the method of Hanes and Huntley (1986). An example of a cross-correlation between suspended sediment concentrations records at 0.45 m and 0.25 m is displayed in Figure 6.2c. It was found that there was no time lag between sensors during suspension events and there was a high correlation between the vertically separated sensors.

6.2.3: Investigation into sediment suspension processes

Investigation into the processes responsible for the suspension of sediment (Figure 6.3) found that the largest (10-minute) mean concentrations at z = 0.25m of > 1 kg/m^3 were found in water depths of between 2 and 5 m. A reduction in concentration was observed in the greatest water depths and also there was an indication of a reduction in concentration in the shallowest water depths in *STIR 2.* Maximum instantaneous concentrations were > 20kg/m^3 (Figure 6.1). The partitioning of observations into rip and non-rip conditions shows that in *STIR 2* the largest concentrations occurred when the rip was active, though in *STIR 1* there was little difference in the magnitude of concentration between periods when the rip was and was not active. The contribution of waves to the suspended sediment concentration is investigated by use of the orbital velocity (U_m) parameter from velocity measurements made at z = 0.45 m, following the wave stirring principle indicated by (Bailard, 1981). There is a clear increase in concentration with U_m, which is particularly evident in *STIR 1* and it can be seen in both experiments that maximum suspension occurred when U_m = ~ 1 m/s. Offshore mean flows appear to have a lesser effect on sediment concentration. Sediment concentrations observed in the fastest offshore flows were of equal magnitude to those observed in negligible flow. There is some evidence of an increase in concentration with mean flows in *STIR 1,* though the relationship is not as clear as that with U_m. The poor relationship between mean flows and concentration, and the fact that suspension appears to be reduced when the rip is active, particularly in *STIR 1,* suggests that some condition that leads to rip activity may prohibit sediment suspension (e.g. wave filtering by shallow bars).

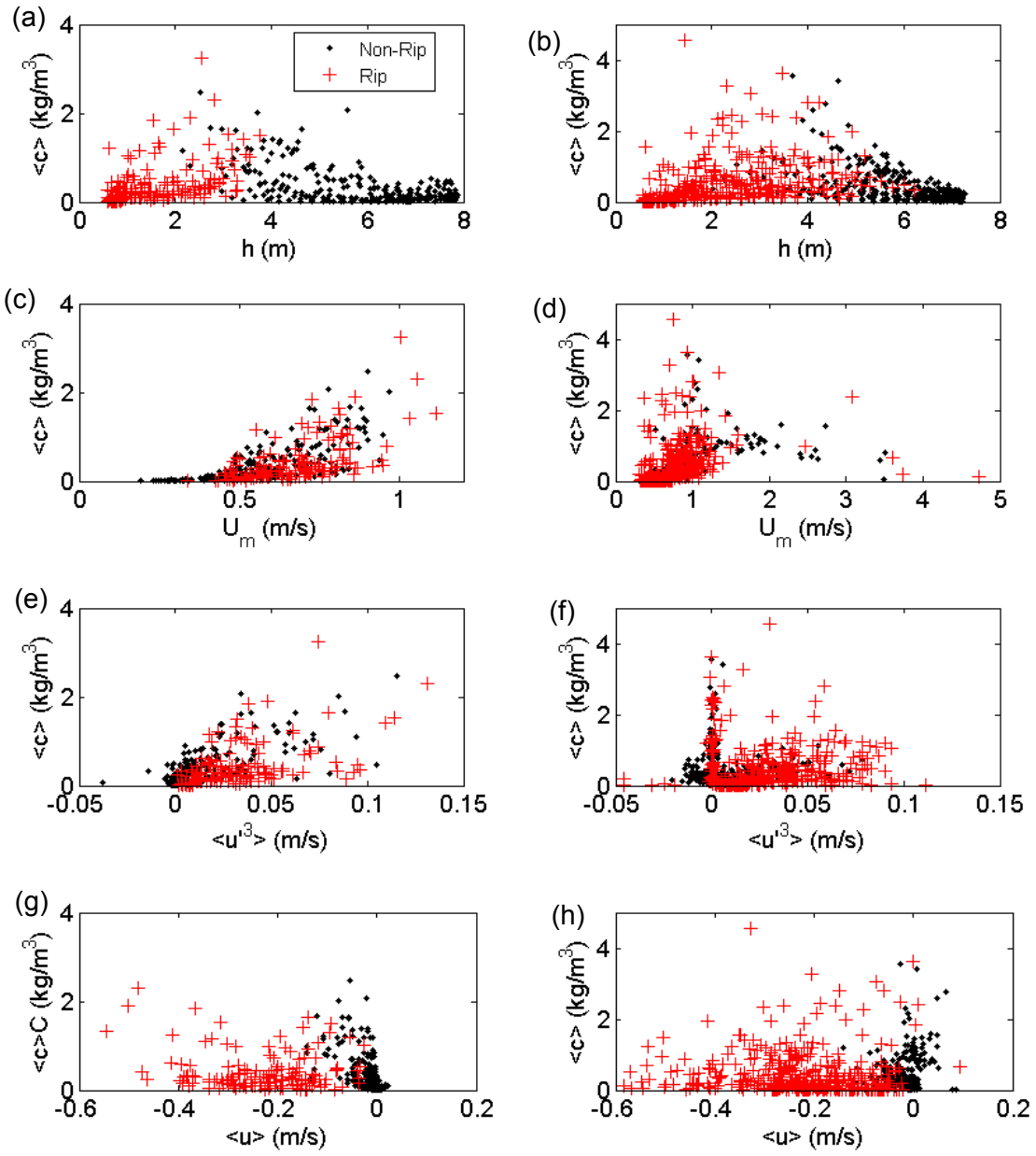

Figure 6.3: Factors contributing to mean suspended sediment concentration (z = 0.25 m) in the rip channel in *STIR 1* (left column) and *STIR 2* (right column); (a & b) water depth (*h*), (c & d) orbital velocity (U_m), (e & f) un-normalised velocity skewness ($\langle u'^3 \rangle$) and (g & h) mean cross-shore flows ($\langle u \rangle$).

6.3: Mean Flux

6.3.1: An example of mean suspended sediment flux

The suspended sediment transport is composed of a mean and a fluctuating component in response to mean and oscillatory flows (Jaffe et al., 1984). In a rip current, the contribution from the mean component is likely to be significant, due to the nature of the quasi-steady, strong offshore mean flow of the rip. An example of this is shown in Figure 6.4, where one tide of instantaneous data is averaged into 10-minute runs. It can be seen that at lower tidal elevations, when the rip is active, on both the

flood and ebb cycle, that the fastest offshore flows of 0.6 m/s and 0.3 m/s respectively occur simultaneously with the largest suspended sediment concentration of > 1 kg/m^3. Subsequently the mean flux is offshore directed at a maximum of > 0.5 kg/m^2/s. This example is representative of the mean sediment flux in a rip in both *STIR 1* and *STIR 2*.

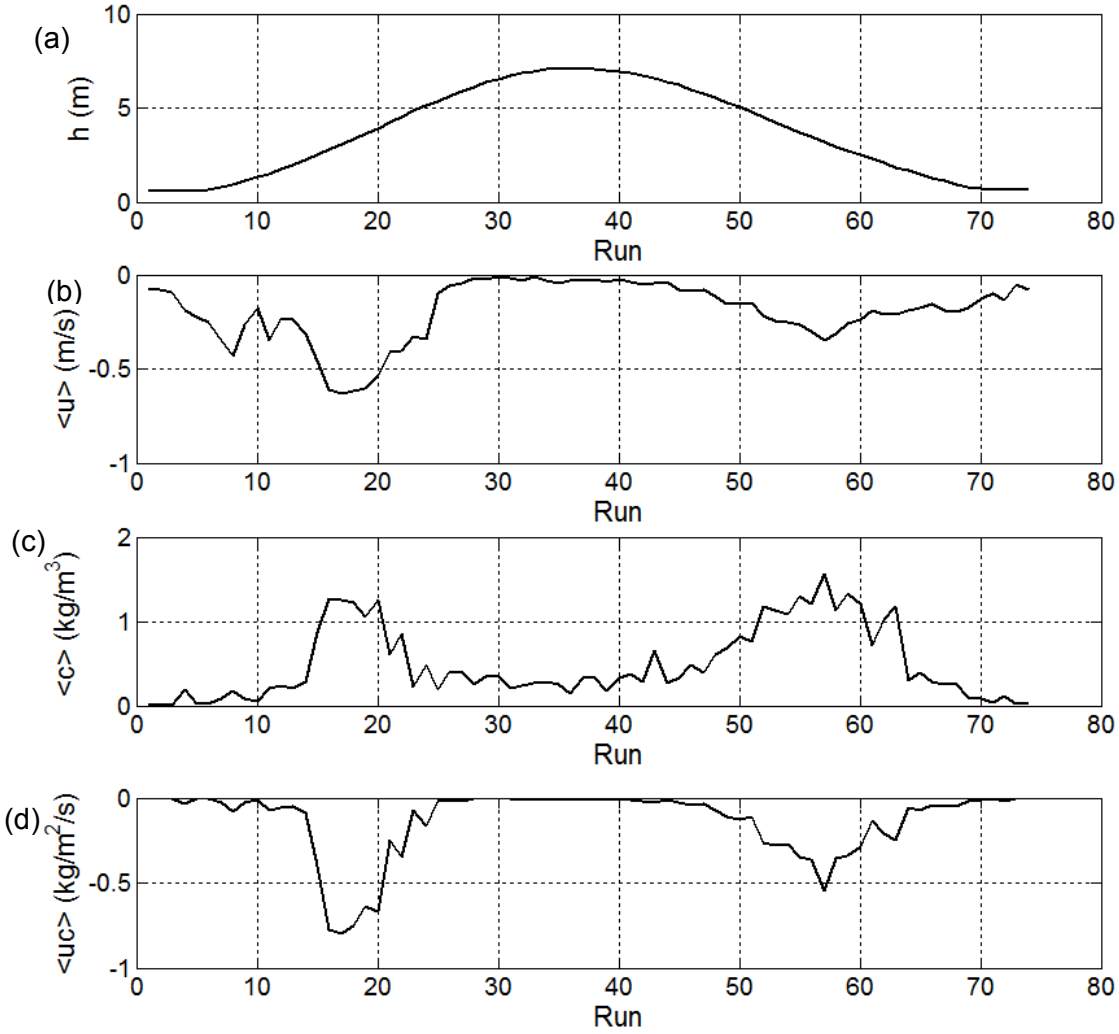

Figure 6.4: An example of the contribution of (b) mean flows (<u>) and (c) sediment concentrations (<c>) to (d) mean suspended sediment transport (<uc>), using 10-minute averaging.

6.3.2: Mean cross-shore flux as a fucntion of mean cross-shore flow

As indicated in Figure 6.4, the mean sediment flux generally increases with offshore directed mean flows. Figure 6.5 shows that although there is a degree of scatter when <u> and <uc> are correlated, generally the largest fluxes (> 0.8 kg/m^2/s) are found at the fastest offshore flows (~ 0.6 m/s). The reason for the scatter present in the correlation between <*u*> and <*uc*> is likley to be because other processes are required to effectively suspend sediment, as observed in Figure 6.3. In both *STIR 1* and *2* the flux is always offshore directed in offshore directed rip flows > 0.4 m/s.

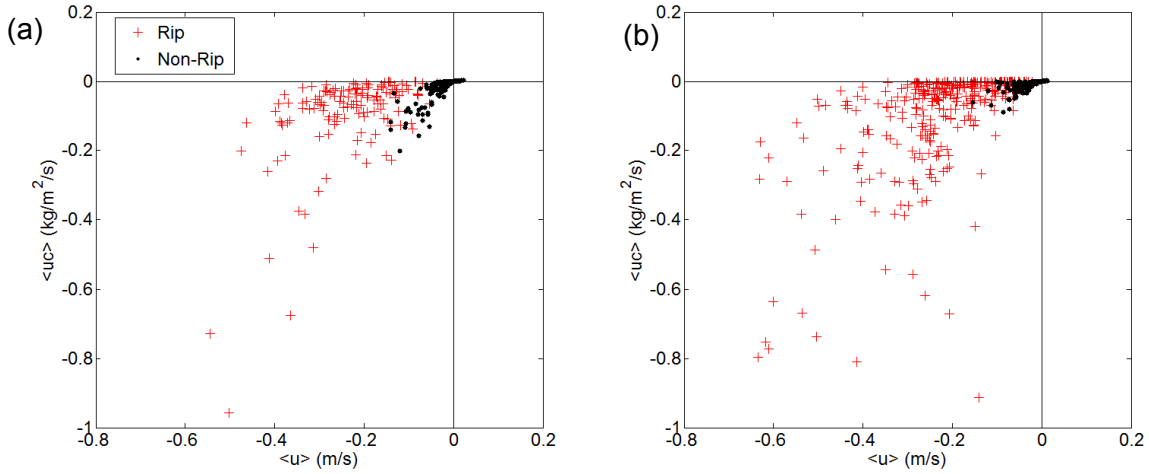

Figure 6.5: Mean sediment transport (<*uc*>) as a function of cross-shore mean flows (<*u*>) in (a) *STIR 1* and (b) *STIR 2.* Rip and non-rip conditions are marked.

6.3.3: Quantification of mean and oscillatory flux

The mean flux in both *STIR 1* (Figure 6.6a) and *STIR 2* (Figure 6.7a) exhibit a similar trend to one another with maximum offshore transport occurring just before (ebb) and after (flood) low tide when the rip was active (marked by the shaded area). At higher tidal elevations fluxes are negligible. In *STIR 2* maximum fluxes exceeded 0.2 kg/m^2/s on 11 of 15 occurrences of rip currents, compared to 4 of 12 occurrences of rip currents in *STIR 1*. However, the largest fluxes recorded over the two experiments were in *STIR 1*, with a maximum of 0.68 kg/m^2/s recorded in the ebb of Tide 2 and 2.1 kg/m^2/s recorded in the flood of Tide 3.

The oscillatory fluxes (Figures 6.6b and 6.7b) in both *STIR 1* and *STIR 2* exhibit more variability in direction and much smaller magnitudes than that of the mean flux, though they generally follow the same trend of greater transport at lower tidal elevations. In *STIR 1,* the direction of oscillatory transport when the rip is active varies considerably, though the largest fluxes occur in the onshore direction. In non-rip conditions the fluxes are generally smaller and though the direction varies, the largest fluxes are in the offshore direction. The trends present in the oscillatory flux in *STIR 2* are clearer than in *STIR 1*. In rip conditions the oscillatory flux is often onshore directed at rates of between 0.01 to 0.26 kg/m^2/s. In non-rip conditions, oscillatory fluxes were generally offshore directed and of lower magnitude than in the rip, where the maximums were between of 0.1 to 0.16 kg/m^2/s.

The total flux (<*uc*> + <*u'c'*>) appears to be very similar to the mean flux. This is due to the dominance of the mean flux for suspended sediment transport in the rip and the relatively small fluxes at high tide.

In Figure 6.8 the percentage contribution to total gross sediment transport from the mean and oscillatory flux is calculated for the entire duration the rip current was active for all 27 occurrences of rip currents. The periods when the rip current was active were isolated following the method described in Section 3.6.4. The mean flux is clearly the dominant component of transport over the oscillatory flux and it is always directed offshore in the rip current. This is well represented in the bar plot (Figures 6.8). Of the 27 occurrences of rip currents in this data set (12 in *STIR 1* and 15 in *STIR 2)*, the mean flux accounted for > 90% of the total suspended flux (<*uc*> + <*u'c'*>) on 10 occasions, > 70% of the total suspended flux on 19 occasions and accounted for < 60% of the total suspended flux on only 4 occasions.

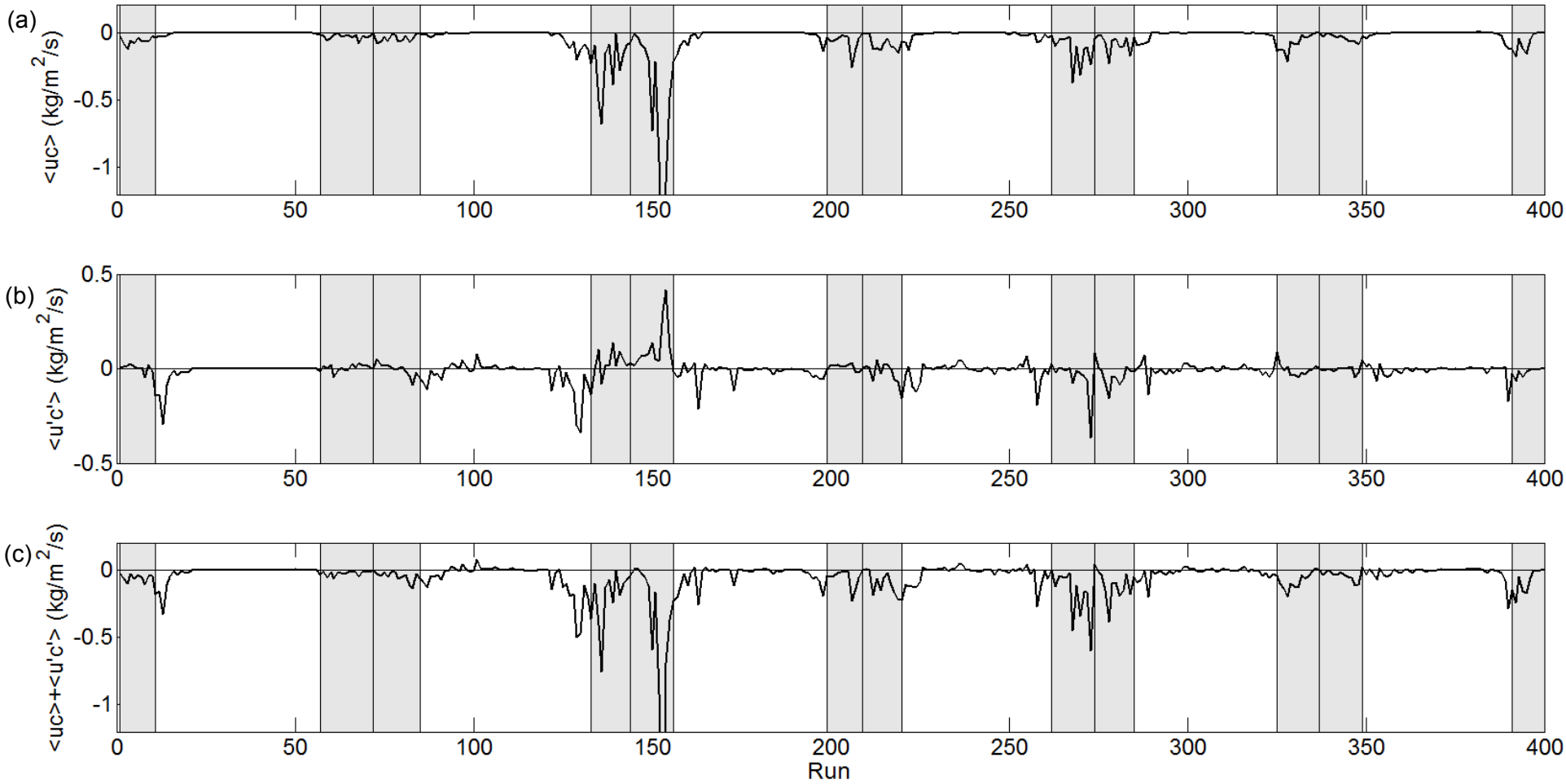

Figure 6.6: (a) Mean flux (<*uc*>), (b) oscillatory flux (<*u'c'*>) and (c) total flux (<*uc*> + <*u'c'*>) during *STIR 1*. Vertical lines represent boundaries of different tides. The shaded areas mark periods when the rip current was deemed to be active, the centre line in the shaded area represents the boundary between tides. n.b. run 153 = 1.74 kg/m/s.

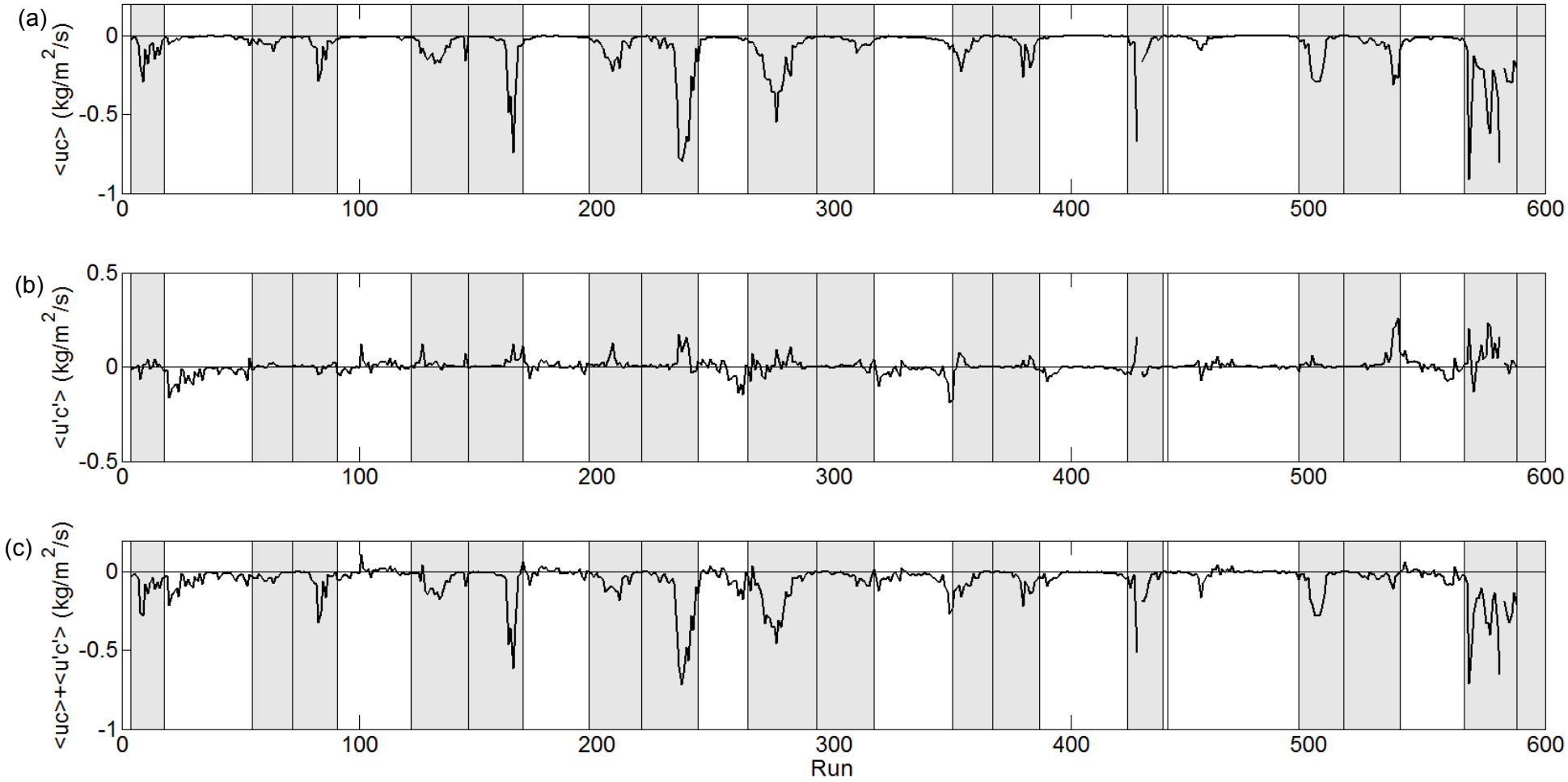

Figure 6.7: (a) Mean flux (<*uc*>), (b) oscillatory flux (<*u'c'*>) and (c) total flux (<*uc*> + <*u'c'*>) during *STIR 2*. Vertical lines represent boundaries of different tides. The shaded areas mark periods when the rip current was deemed to be active, the centre line in the shaded area represents the boundary between tides.

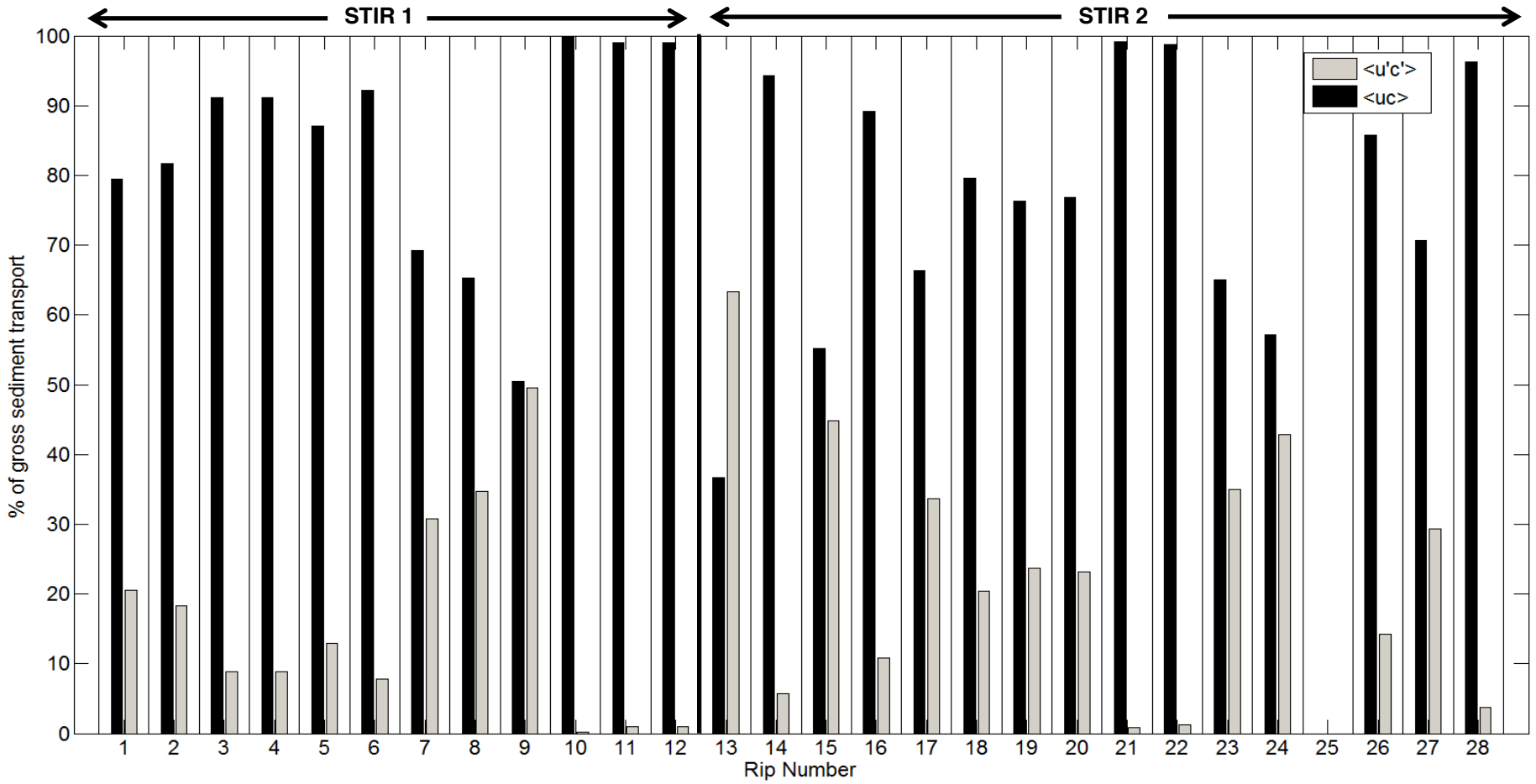

Figure 6.8: Percentage contribution to the total suspended sediment flux from the mean flux (<*uc*>) and oscillatory flux <*u'c'*> for all 27 occurrences of rip currents. Percentages are calculated over the entire duration the rip was active on the flood and ebb tide during *STIR* 1 and *STIR 2*. The thick vertical line marks the divide of *STIR 1* and *STIR 2* (n.b. Rip current was not deemed to be during 'rip 25').

6.3.4: Total flux as a function of mobility number

In Figure 6.3 it can be seen that, as expected, suspended sediment concentration increases with increasing orbital velocity, and therefore transport may be limited in smaller waves with lower orbital velocities, and Figure 6.5 shows that the sediment transport is likely to be limited by the absence of a strong mean flow. This is investigated further in Figure 6. 9, where the mobility number (Equation 3.12), which includes information on both the oscillatory and mean parts of the flow is correlated with total transport (<*uc*> + <*u'c'*>). In rip current conditions, total suspended transport generally increases with increasing mobility number (*STIR 1,* R^2 = 0.69 *STIR 2,* R^2 = 0.67). In non-rip conditions the relationship is weaker (*STIR 1,* R^2 = 0.51 *STIR 2,* R^2 = 0.31), this may be due to the absence of strong mean flows of the rip required to transport sediment.

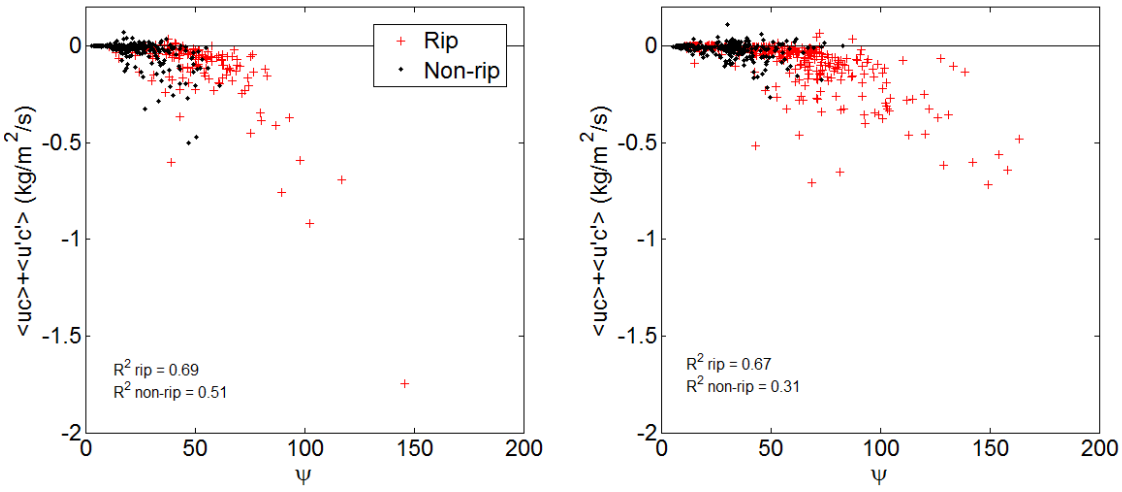

Figure 6.9: Total transport (<*uc*> + <*u'c'*>) as a function of the mobility number, rip and non-rip indicated.

6.4: Temporal Variability in Suspended Sediment Transport Dynamics

In this section the effects of oscillations present in the rip flow on suspended sediment transport are investigated using example time series and spectral analysis. Very low frequency (VLF), infra-gravity (IG) and gravity (G) motions are investigated individually.

6.4.1: Very low frequency (VLF) effects on suspended sediment dynamics

In Section 4.6 the presence of very low frequency (VLF) motions were identified in the rip flow. In this section the effect of VLF motion on suspended sediment transport dynamics in a rip current is investigated. This is achieved by examining an example

section of data taken from low tide when the rip current was active, and clear VLF oscillations were present.

In the example a 68-minute time series of instantaneous velocity and concentration data is presented. The data was investigated further with spectral analysis. The hydrodynamic conditions for the example are presented in Table 6.1. At low tide, when the rip was active, there is significant offshore directed mean flow of 0.28 m/s in waves of 0.85 m.

Table 6.1: The hydrodynamic parameters for an example that highlights the effect of VLF motions on suspended sediment concentration from low tide (LT) when the rip was active.

	h (m)	H_s (m)	U_m (m/s)	T_p (s)	<u> (m/s)	<c> (kg/m^3)
LT and VLF	1.6	0.85	1.6	9.5	-0.28	0.8

The boundaries of each frequency band were identified as consistent valleys in the spectra during analysis of the rip flow dynamics in Section 4.6 and are the same as those used in the literature when studying the time scale of rip motion (Smith and Largier, 1995; MacMahan et al., 2004b; MacMahan et al., 2005; Bonneton et al., 2006; Reniers et al., 2007), these are presented in Table 4.6. These boundaries are marked on the spectral plots to aid interpretation

The VLF oscillations in the velocity record are of the order of 20 minutes and are graphically indicated by a 2-minute running mean (Figure 6.10). A 2-minute mean was chosen because it highlighted the oscillations in the data that is picked out by eye. Maximum suspended sediment concentrations visually appear well correlated with offshore pulses in the velocity record, indicating that the pulses are likely to be important for sediment transport. It is probable that the sediment is not mobilised at the location of the sensors, and that the sediment is passing the sensor by means of advection as the pulsing of the flow is likely to be initiated shoreward of the instrument position in the centre of the rip channel.

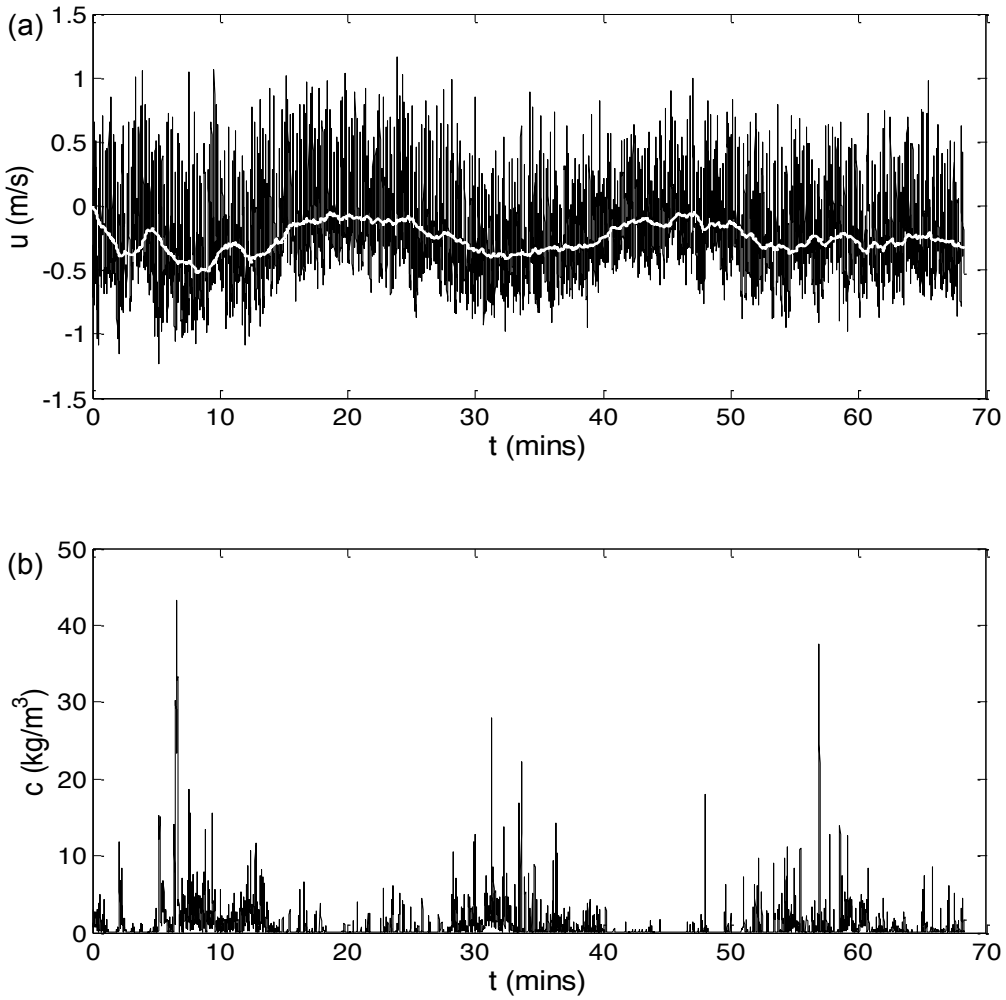

Figure 6.10: An example of VLF pulsing in the (a) cross-shore velocity time series featuring an overlaid 2-minute running mean and (b) suspended synchronous suspended sediment time series concentrations (z = 0.25 m).

The impact of an offshore VLF pulse on sediment concentration is investigated further in Figure 6.11. This figure comprises of data taken from between minute 29 and 31 in Figure 6.10 at the onset of an offshore directed VLF pulse. At the beginning of the time series (Figure 6.11a) (t = 0 to 25 seconds) the fastest offshore velocities are relatively low compared to the rest of the velocity time series. This is reflected in the concentration which is at a minimum at this stage.

The velocity begins to increase with the onset of an offshore pulse when t > 25 seconds. At this point the maximum offshore directed flow increased to ~ 1 m/s in the offshore direction, and simultaneously the concentration showed a noticeable increase from ~ 1 kg/m^3 to > 5 kg/m^3, thus indicating that an increase in offshore directed velocity is important for sediment suspension. However, incident waves were also well correlated with concentration maxima, indicating that incident waves are important for suspension when modulated by the VLF pulses. Although increasing the velocity increases the chance of suspension, and incident waves appear to correlate with

suspension events, no consistent threshold velocity or relationship with acceleration was observed. Flow acceleration was determined as the change in instantaneous velocity, following Equation 3.8. In spite of the visual observations from the time series of *u* and *c*, the correlation of *u* and *c* does not appear to show an increase in sediment concentration with increasing velocity (Figure 6.11c) or acceleration/deceleration (Figure 6.11d). This is likely to be a result of a time lag of re-suspension and the settling time of sediment already in suspension. It is also likely that sediment is transported by a advection process, in which the original suspension may occur further shoreward and therefore localised suspension processes are obscured.

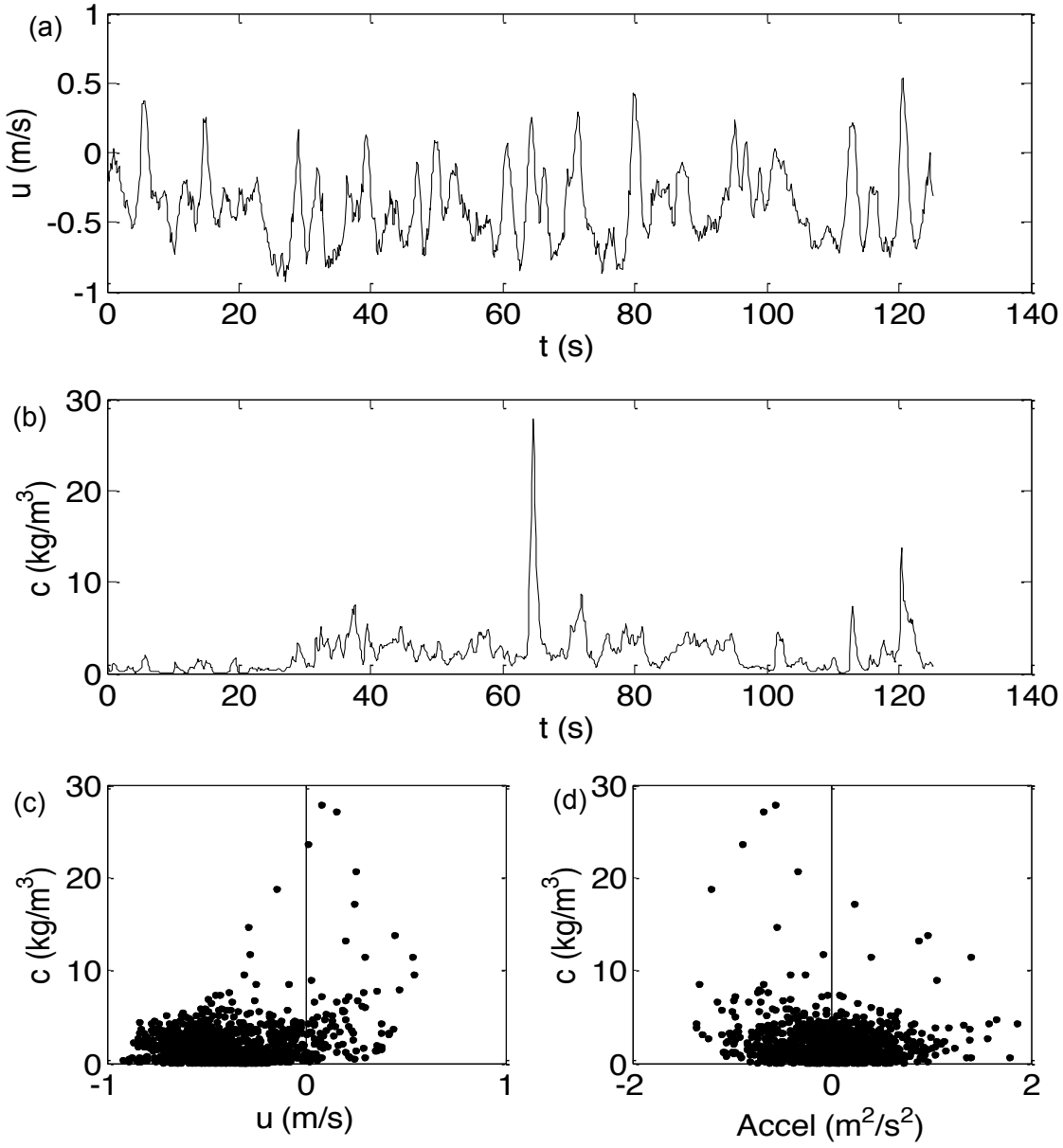

Figure 6.11: Closer examination of (a) instantaneous velocity (*u*) and (b) concentration (*c*) from between minutes 29 to 31 from Figure 6.10. Concentration as a function of (c) velocity and concentration as a function of (d) acceleration.

The spectra of both the *u* and *c* time series (Figure 6.10) are displayed in Figure 6.12 where 68 minutes of data collected at 8 Hz (32768 data points) were used for the analysis. Sections of 68 minutes in length were chosen as it is sufficiently long enough to capture multiple VLF oscillations whilst being as short a time as possible so to maintain tidal stationarity in order that changes in water depth would not change the general hydrodynamic conditions. The spectra were calculated using two non-overlapping windows and one window with a 50% overlap, giving 4.4 degrees of freedom (Jenkins and Watts, 1968). Two windows were chosen as it provided maximum resolution in the VLF band. It can be seen that spectra of both *u* and *c* contain significant energy in the VLF band, supporting the visual observations made from the time series of suspension maxima occurring simultaneously with low frequency pulses in the velocity record. The vertical lines on the spectral plots mark the boundaries of the different frequency bands.

The co-spectrum of the cross-shore velocity and concentration provided an estimate of the different frequencies that contribute to cross-shore sediment transport (Huntley and Hanes, 1987). The co-spectrum of *u* and *c* (Figure 6.12b) shows very small amounts transport in the infra-gravity (IG) and gravity (G) bands. However, in the VLF band the co-spectrum becomes negative, indicating that at VLF offshore transport occurs at a maximum rate of 0.025 $kg/m^2/s$ in an offshore direction. The coherence spectrum (Figure 6.12c) shows significance at the 95% confidence level in the VLF band, following Equation 3.5, thus giving confidence in the relationship between *u* and *c* and the suspended sediment transport estimates at these frequencies.

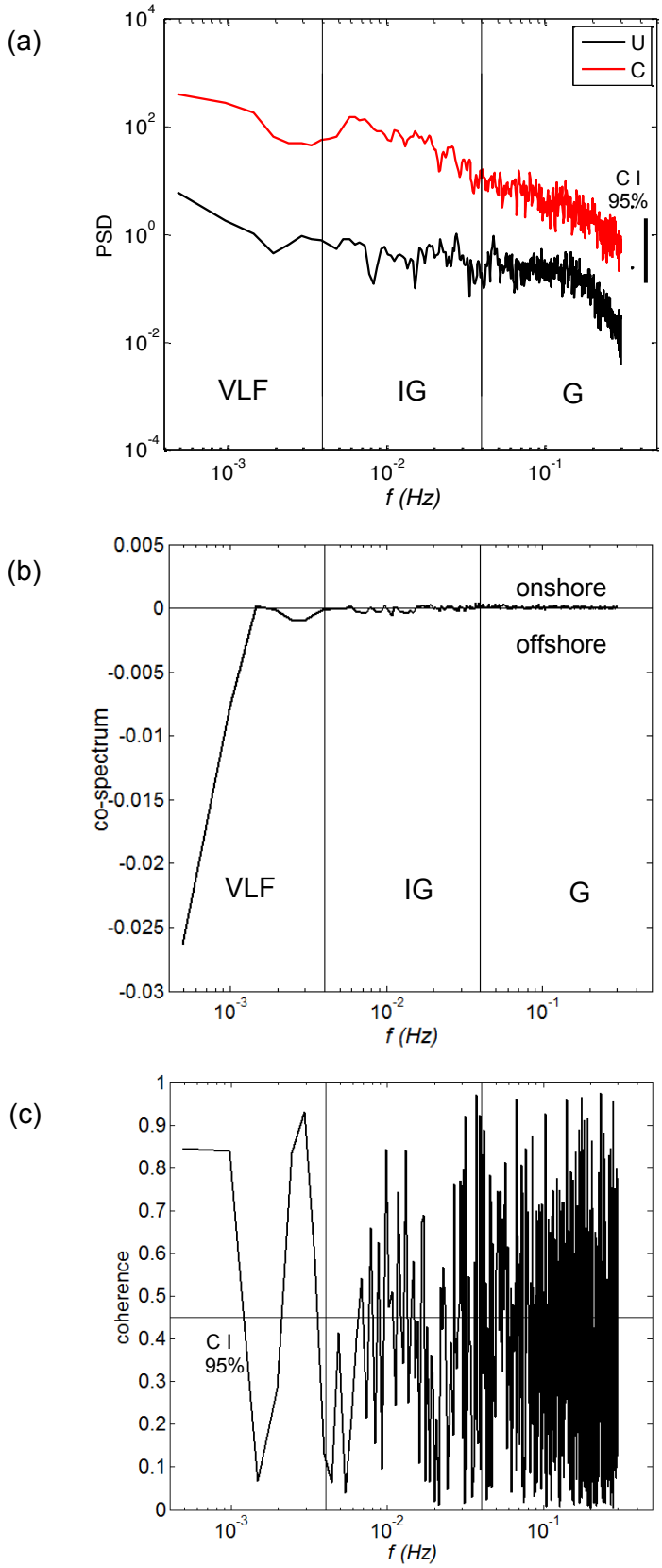

Figure 6.12: (a) Power Spectra Density (PSD) of cross-shore velocity ($m^2/s^2/Hz$) and suspended concentration ($(kg/m^3)^2/Hz$) of 68 minutes of 8 Hz data with 95% confidence interval marked. Spectral analysis performed with 2 non-overlapping windows and 1 overlapping window giving 4.4 degrees of freedom. (b) Co-spectrum, showing direction and magnitude of sediment transport at different frequencies ($kg/m^2/s/Hz$). (c) Coherence spectrum with 95% confidence level marked. The vertical lines separate VLF, IG and G frequency bands.

VLF motion was found to occur only at lower tidal elevations when mean flows were strong. As a comparison, 68 minutes of *u* and *c* data is presented for data collected around high tide when the rip current is inactive (Figure 6.13). The absence of the VLF pulsing in the example velocity time series during high tide is clear. At high tide the velocity record shows a similar degree of variance that can be attributed to the onshore-offshore stroke of passing waves.

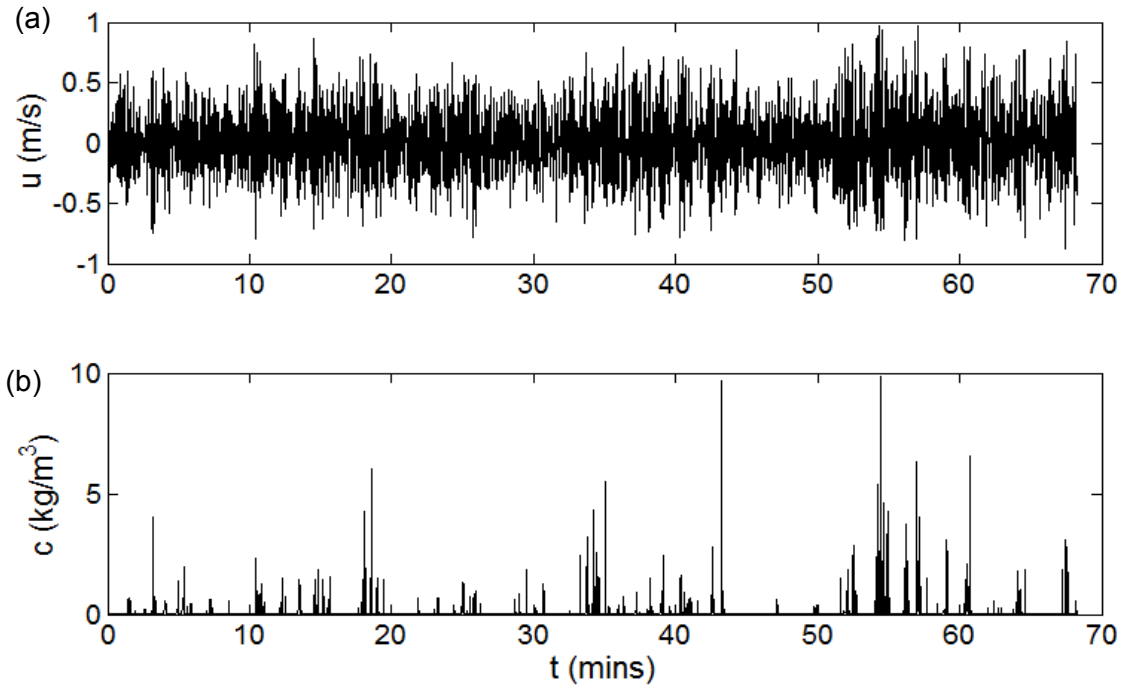

Figure 6.13: Example of 68 minute of instantaneous (a) velocity (*u*) and (b) concentration (*c*) data collected during a rip current in which VLF pulsing is absent and of *u* and *c* data collected at high tide when the rip current was inactive.

The suspended sediment flux from both examples (Figure 6.10 and 6.13) is quantified in Table 6.2. The mean and oscillatory flux was partitioned following Jaffe et al. (1984). A lowpass filter was applied to the de-trended instantaneous time series to filter the VLF component, a bandpass filter was used to separate IG frequencies and a highpass filter was used to separate the G frequencies. The cut-off frequencies are as identified in Table 4.6.

Table 6.2: Suspended sediment transport fluxes from all modes of transport from the low tide (LT) example time series exhibiting strong rip flow and VLF pulsing (Figure 6.10) and the high tide (HT) (Figure 6.13) example with weak flows and no VLF pulsing ; Mean flux (<*uc*>), oscillatory flux (<*u'c'*>), VLF band flux (<*u'c'*>$_{VLF}$), IG band flux (<*u'c'*>$_{IG}$) and gravity band flux (<*u'c'*>$_{G}$).

	<u> (m/s)	<uc> (kg/m^2/s)	<u'c'> (kg/m^2/s)	<u'c'> $_{VLF}$ (kg/m^2/s)	<u'c'> $_{IG}$ (kg/m^2/s)	<u'c'>$_{G}$ (kg/m^2/s)
LT	-0.28	-0.21	-0.02	-0.08	- 0.005	0.07
HT	0.009	-7×10^{-4}	-0.005	2×10^{-8}	-3×10^{-6}	-2×10^{-5}

The smallest fluxes for all modes of transport were found at high tide when the rip current is inactive, with fluxes for all modes of transport several orders of magnitude less than in rip conditions. The largest component of suspended sediment transport was the mean flux, found in the rip at low tide when a VLF signal was present. The flux associated with the VLF was offshore directed, and the G frequency flux was onshore directed, both accounted for approximately one third of the mean flux.

6.4.2: Infra-gravity (IG) frequency effects on suspended sediment dynamics

The rip flow was also found to exhibit pulsing on a wave group time scale (Section 4.6). Its contribution to sediment dynamics is investigated in Figures 6.14 and 6.15.

17.1 minutes of velocity data collected at 8 Hz was chosen to illustrate IG frequency motion and its effect on suspended sediment dynamics. The basic hydrodynamic parameters for this example are presented in Table 6.3. The offshore directed flow was 0.2 m/s, indicating a rip current. Wave groups occurred at intervals of 3 to 4 minutes and lasted for durations of between 1 and 2 minutes. The wave groups are synchronous with sediment concentration maxima and are sustained for a similar time scale.

Table 6.3: Hydrodynamic parameters for example time series presented in Figure 6.9.

	h (m)	H_s (m)	T_p (s)	<u> (m/s)	<c>(kg/m^3)
IG Example	2.3	1.1	10.1	-0.20	0.8

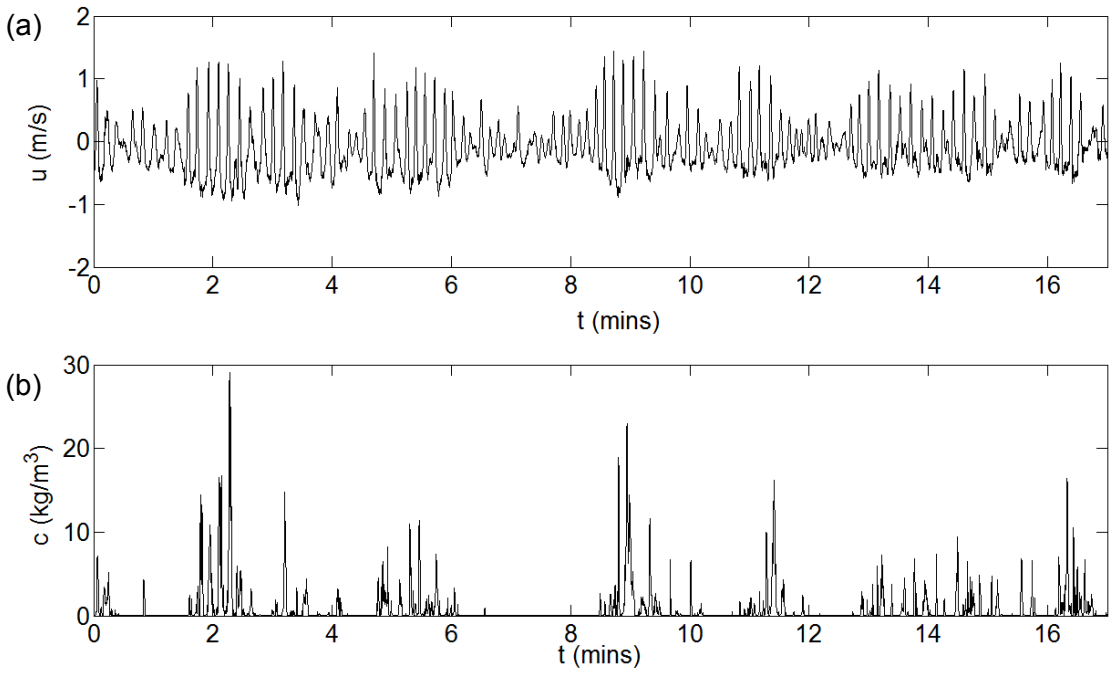

Figure 6.14: An example of wave groups present in the instantaneous (a) velocity (*u*) and associated (b) suspended sediment concentrations (*c*).

Spectral analysis was undertaken on the time series of *u* and *c*. 4 non-overlapping windows and 3 windows with a 50% overlap were used, giving 11.8 degrees of freedom (Jenkins and Watts, 1968). The spectra of both *u* and *c* show that there is significant energy found in the gravity band at a frequency of approximately 0.1 Hz (10 s). There is also energy present in the infra-gravity band. Using the co-spectrum of *u* and *c* to estimate sediment flux it can be seen that in the gravity band the direction of the flux fluctuates, with the largest magnitude of transport occurring in the offshore direction at a frequency of 0.1 Hz, coinciding with the largest peak in the spectra of *u* and *c* (Figure 6.15). However, the coherence spectrum gives poor confidence in this result. The largest magnitudes of sediment transport, as indicated by the co-spectrum, were found in the infra-gravity band, with a maximum flux of 0.0014 $kg/m^2/s$ in an offshore direction. The coherence spectrum indicates that this result is significant at the 95% confidence level for frequencies below 0.01 Hz (100 seconds).

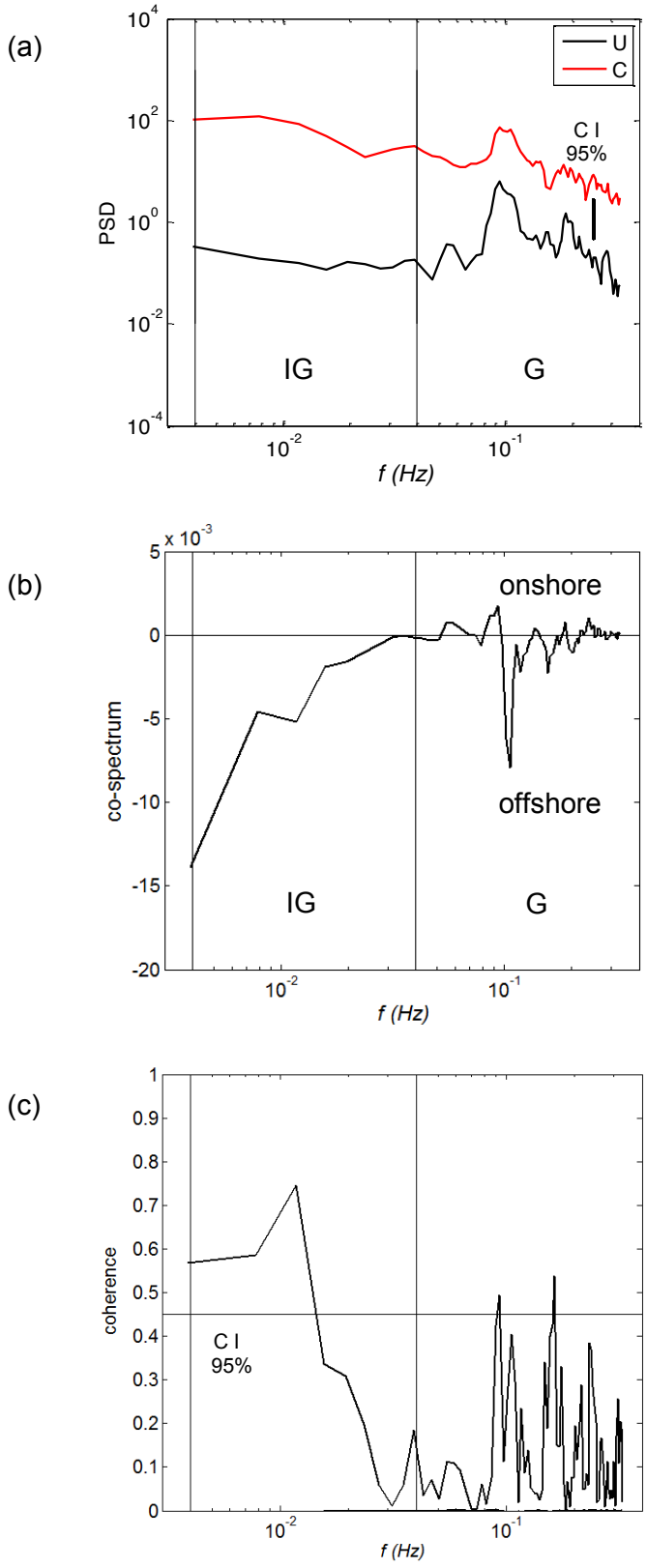

Figure 6.15: (a) Power Spectra Density (PSD) of cross-shore velocity ($m^2/s^2/Hz$) and suspended concentration ($(kg/m^3)^2/Hz$) of 68 minutes of 8 Hz data with 95% confidence interval marked. Spectral analysis performed with 4 non-overlapping windows and 3 overlapping window giving 11.8 degrees of freedom. (b) Co-spectrum, showing direction and magnitude of sediment transport at different frequencies ($kg/m^2/s/Hz$). (c) Coherence spectrum with 95% confidence level marked. The vertical lines separate VLF, IG and G frequency bands.

6.4.3: Gravity (G) frequency effects on suspended sediment dynamics

The effect of incident waves on sediment dynamics in a rip current is investigated in Figure 6.16, showing a 1.3-minute time series of *u* and *c*, collected at 8 Hz. The basic hydrodynamic parameters for this example are presented in Table 6.4 as 10-minute run averages (for 5 minutes either side of the middle of this time series).

Table 6.4: Hydrodynamic parameters for example time series presented in Figure 6.12.

	h (m)	H_s (m)	T_p (s)	<u> (m/s)	<c>(kg/m^3)
G Example	2.8	1.02	8.2	-0.48	0.007

In the 1.3 minutes of sample data shown, there were 8 wave events, therefore giving an average wave period of 11.3 seconds, with each wave event appearing to induce a suspension event. This is analysed further by spectral analysis in Figure 6.16.

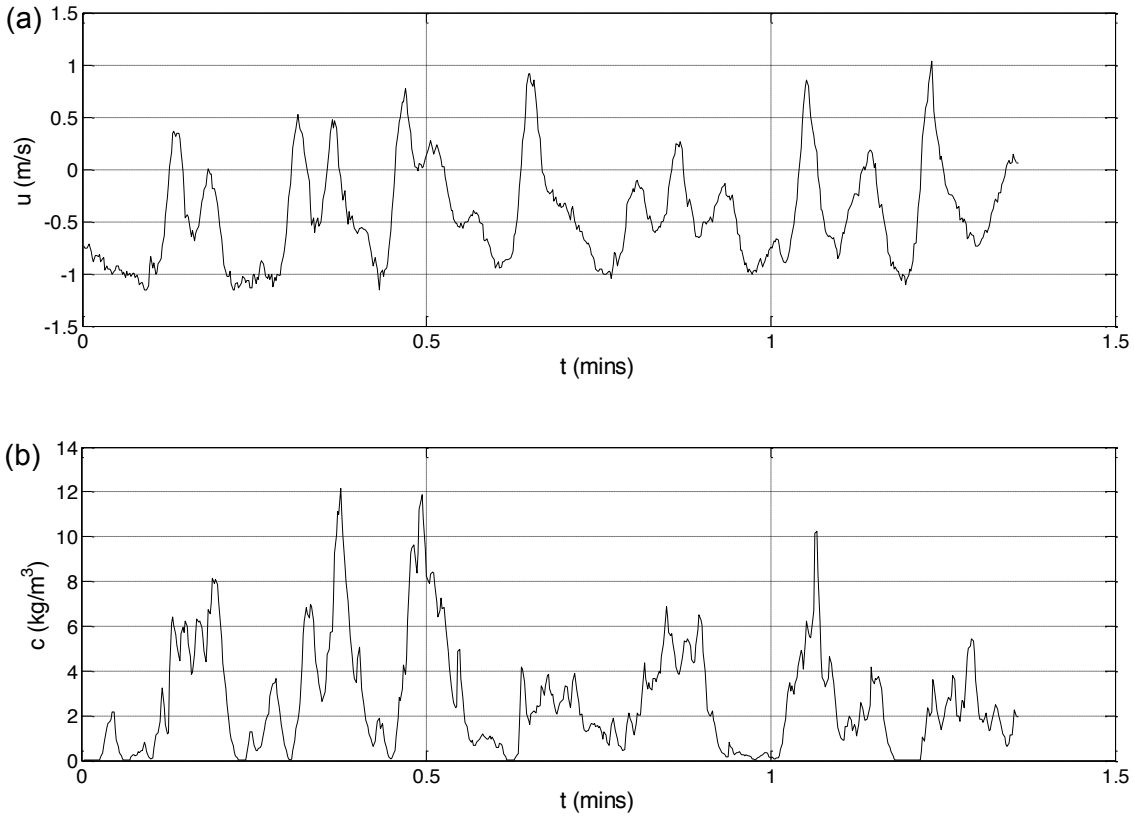

Figure 6.16: An example of individual waves present in the (a) instantaneous velocity (*u*) and associated (b) suspended sediment concentrations (*c*).

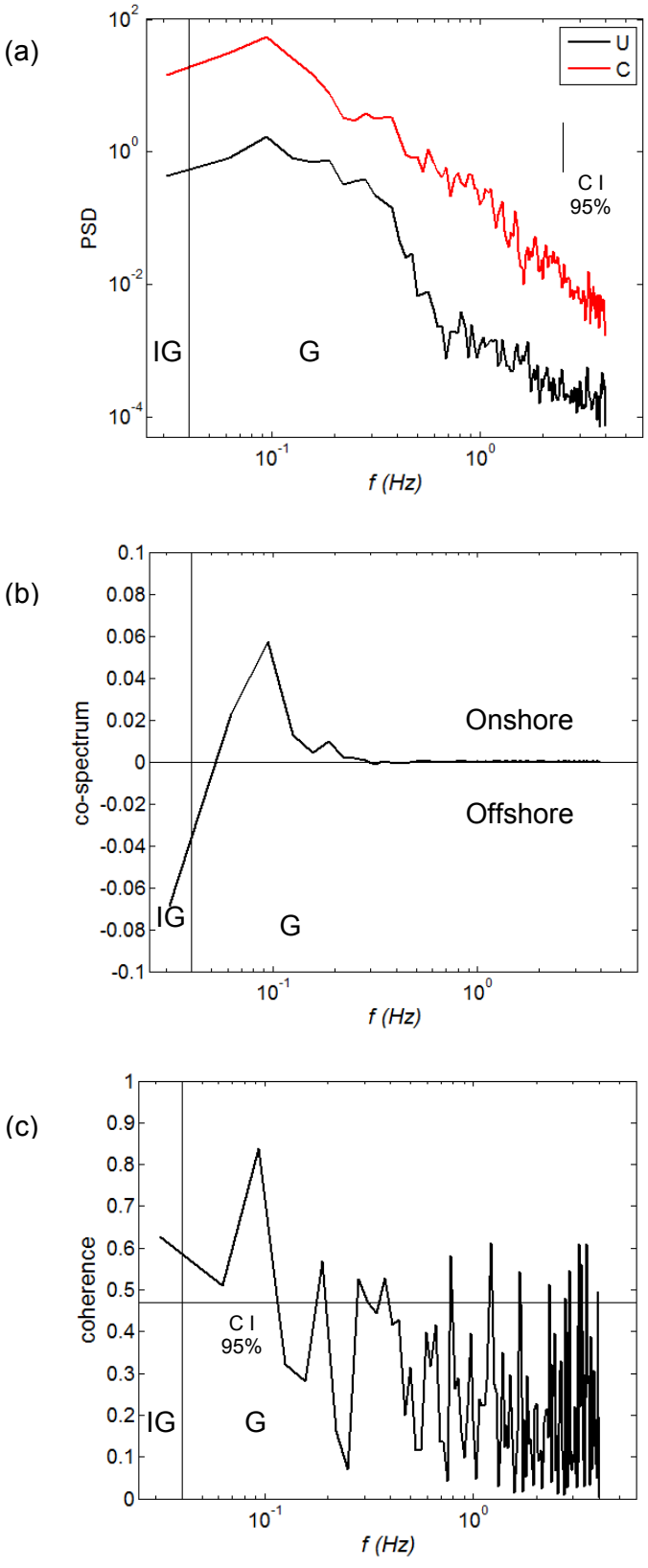

Figure 6.17: (a) Power Spectra Density (PSD) of cross-shore velocity ($m^2/s^2/Hz$) and suspended concentration ($((kg/m^3)^2/Hz$) of 68 minutes of 8 Hz data with 95% confidence interval marked. Spectral analysis performed with 4 non-overlapping windows and 2 overlapping window giving 12 degrees of freedom. (b) Co-spectrum, showing direction and magnitude of sediment transport at different frequencies ($kg/m^2/s/Hz$). (c) Coherence spectrum with 95% confidence level marked.

The spectra of *u* and *c* show the most significant peak at a frequency of 0.09 Hz (11.1 seconds), therefore in agreement with visual observations of wave period (Figure 6.17c). The co-spectrum shows that suspended sediment flux was at a maximum (0.06 kg/m^2/s) at this frequency and the transport was in an onshore direction. The coherence spectrum gives confidence in this result at the 95% interval.

During the time interval, the mean flux was offshore directed at a rate of 1.16 kg/m^2/s and the oscillatory flux was onshore directed at a rate of 0.65 kg/m^2/s for the duration of the example time series, giving a net offshore directed flux of 0.52 kg/m^2/s. Given the strong offshore directed mean flows, the oscillatory component makes a significant contribution (36%) to total gross suspended sediment transport (<*uc*> + <*u'c'*>). The reason for this comes apparent when examining the time series which shows minimal concentrations of suspended sediment transport in fast offshore directed flows (> 1 m/s), though large peaks in suspended sediment concentration occur during the onshore stroke of waves (with maximum onshore directed flows of 0.2 to 1.0 m/s). To investigate this observation the auto-correlation of *u* and *c* was calculated and is displayed in Figure 6.18. It can be seen that although there is a lag of 0.7 seconds (marked with a dashed line) between the maximum onshore flow and the maximum suspended sediment concentration, the cross-shore velocity peaks first, then the maximum sediment concentration occurs in, what is still relatively strong offshore flows. This gives rise to significant onshore sediment transport; however it is still secondary to the mean flux, additionally the contribution of advected sediment is unknown, but likely significant

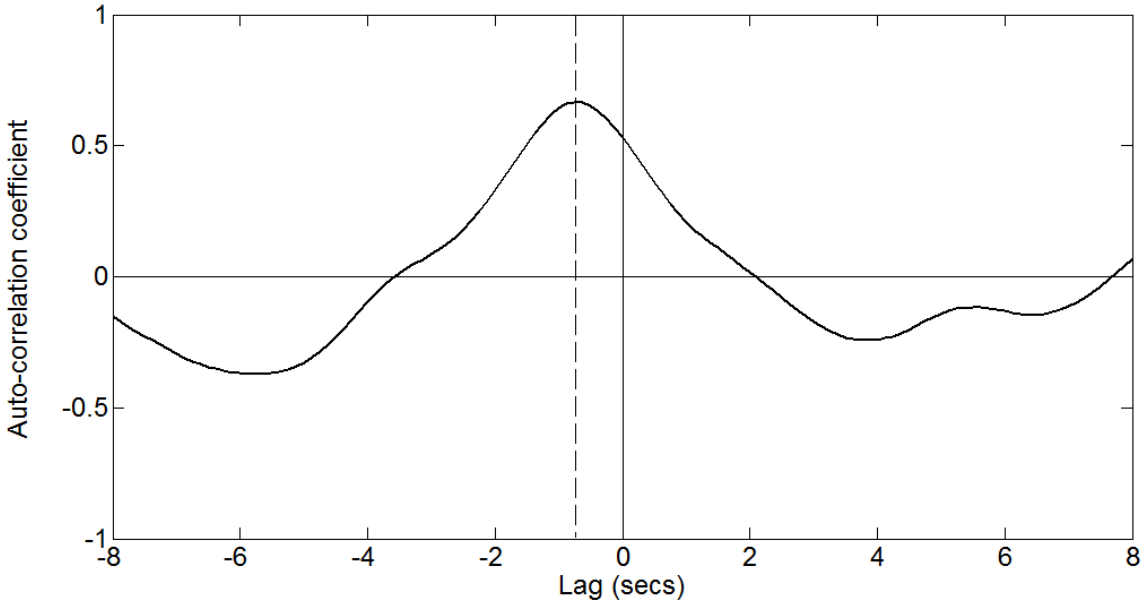

Figure 6.18: Auto-correlation between instantaneous velocity (*u*) and concentration (*c*) for data from time series in Figure 6.11. The solid vertical line marks zero lag and the dashed line marks the strongest lag of 0.7.

The velocity time series (Figure 6.16) appears to show waves that are both skewed (larger peaks than troughs) and asymmetric (steeper leading edge than trailing edge). Figure 6.19 shows scatter plots of oscillatory transport as a function of asymmetry and skewness (normalised (*S*) and un-normalised (<u'^3>)) during *STIR 1* and *STIR 2*. In all cases the partitioning of observations into rip and non-rip conditions appears to indicate that the presence of rip flow, co-incidental with modified asymmetry and skewness affects the oscillatory transport. In *STIR 1* and *STIR 2* when the rip is not active, asymmetry is low and suspended sediment transport is generally offshore, likely due to mean flow of undertow. Asymmetry increases in rip conditions, with the majority of wave driven suspended sediment transport in an onshore direction. In *STIR 1* and *STIR 2* the magnitude of transport increases with increasing normalised skewness, but the direction is variable.

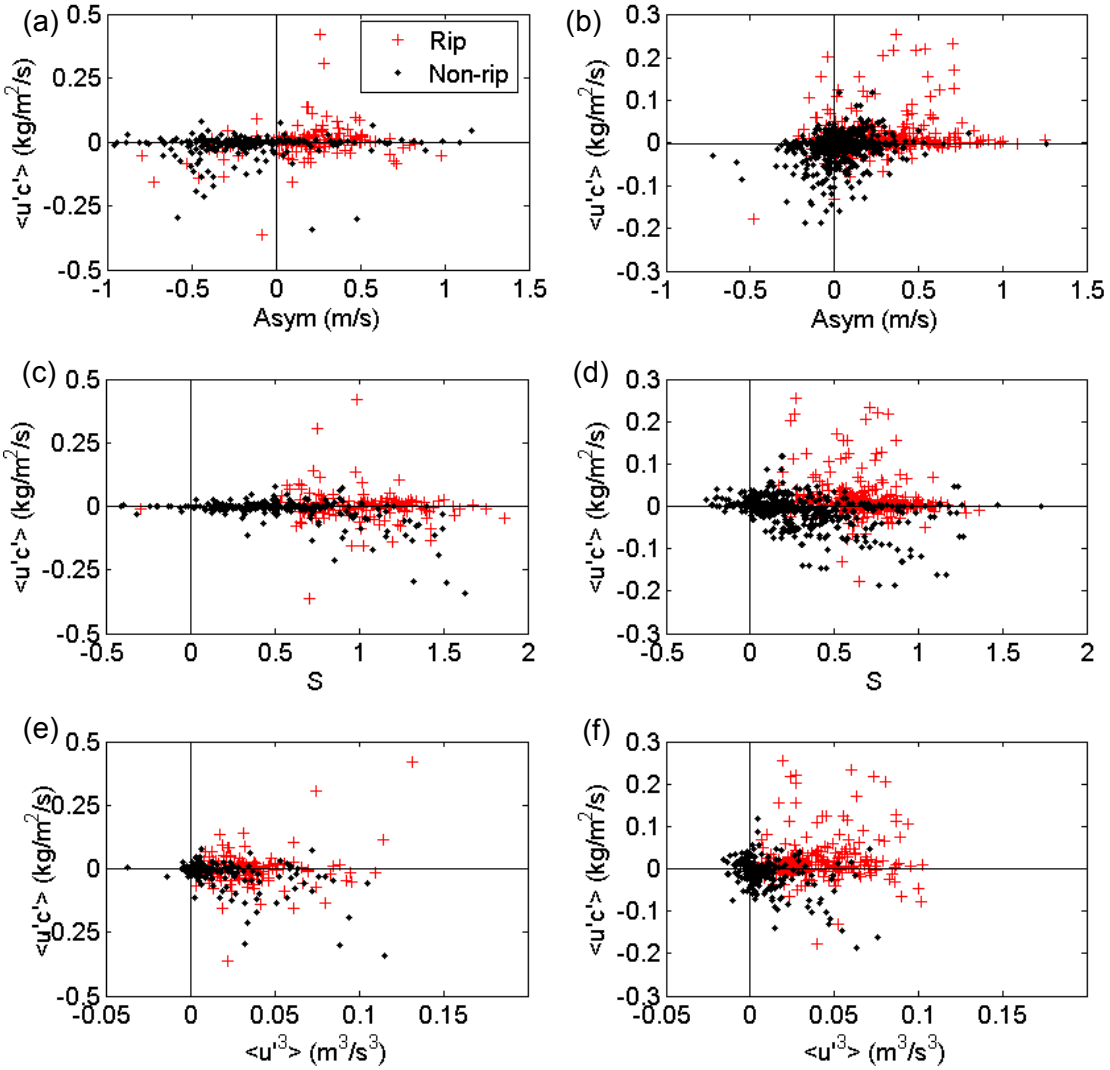

Figure 6.19: Oscillatory suspended transport (<*u'c'*>) in STIR 1 (a, c & e) and STIR 2 (b, d, & e) as a function of (a & b) asymmetry (*Asym*), (c & d) normalised skewness (*S*) and (e & f) un-normalised skewness (<u'^3>). Rip and non-rip conditions marked.

Un-normalised skewness is often used in suspended sediment transport models (Bagnold, 1963). Here it is shown to affect oscillatory suspended sediment transport in a similar way as the normalised skewness, with low magnitudes of transport increasing with increasing un-normalised skewness, though exhibiting a variation in direction.

6.5 Quantification of all Suspended Sediment Transport Processes

Suspended sediment transport is comprised of contributions from the mean flux and transport at VLF, IG and G frequencies. In this section point measurements of cross-shore suspended sediment fluxes are quantified. This is done in two stages;

- Following the identification of the influence of VLF, IG and G oscillations on suspended sediment dynamics the continuous time series were resampled into 68-minute sections, starting every 10 minutes for *u* and *c* data for the duration of every tide from data collected in both *STIR 1* and *STIR 2.* This was done to ensure that windows were of sufficient size to capture entire VLF oscillations and also so that no bias was introduced in the selection of sections for further analysis and quantification of sediment transport components. The continuous *u* and *c* data were filtered at the frequencies identified in Table 4.6 to isolate the VLF, IG and G component of the cross-shore and longshore flow and the suspended sediment concentration. The flux within each frequency band was then calculated. This is plotted as a time series in Figure 6.19 (*STIR 1*) and Figure 6.20 (*STIR 2*) alongside the mean flux.
- There were 27 occurrences of rip currents in this data set. For each of the 27 occurrences of rips, concentration and velocity data were isolated for entire time the rip current was deemed to be active. For these periods the mean flux, VLF flux, IG flux and G flux were calculated. The fluxes are displayed as bar charts showing; (i) the magnitude of flux of each transport component and (ii) the percentage contribution to total gross (and therefore the directionality is not considered) suspended sediment transport flux.

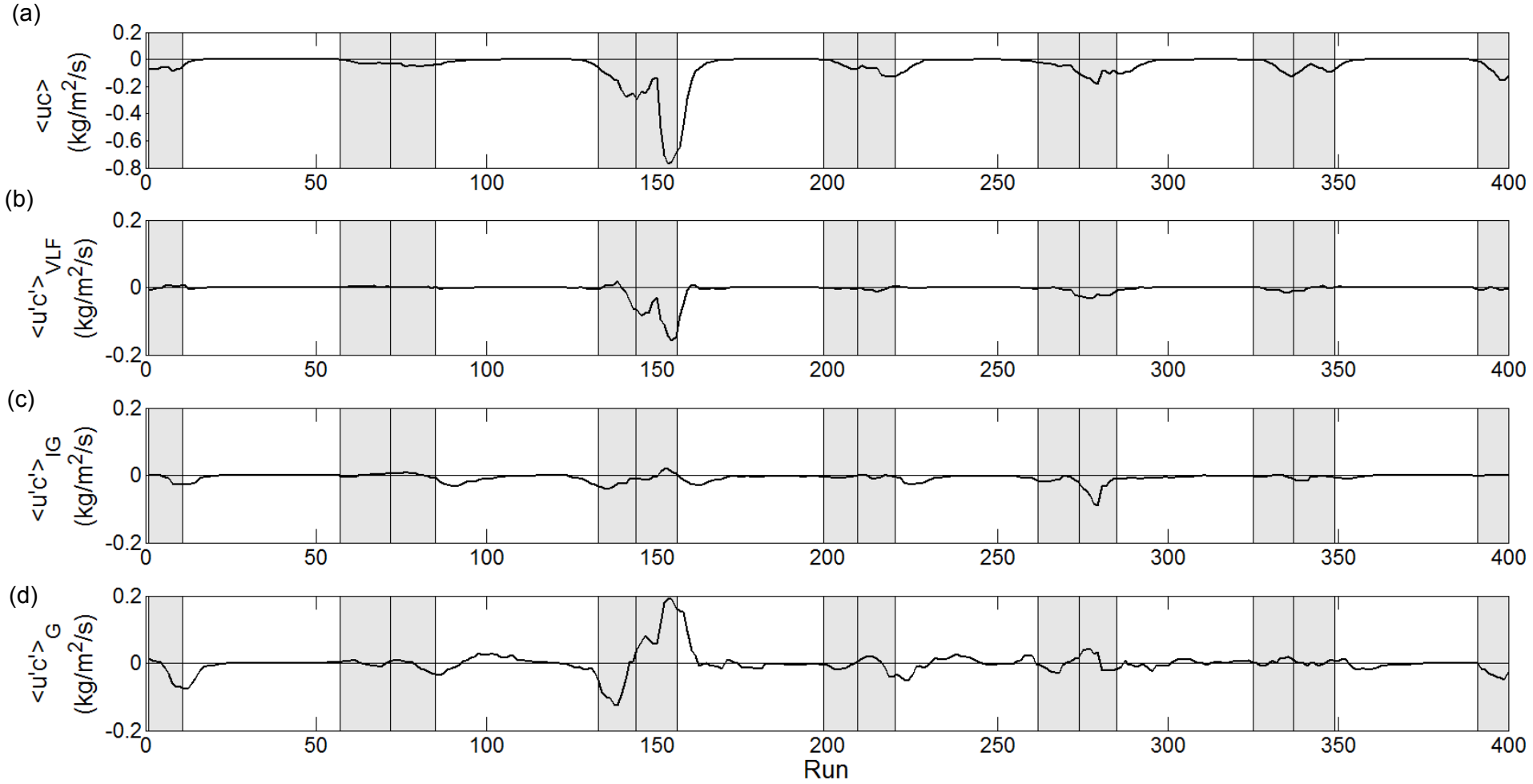

Figure 6.20: (a) Mean flux (<*uc*>) (n.b. y-axis scale is different to other panels) (b) VLF flux (<*u'c'*>$_{VLF}$), (c) IG flux (<*u'c'*>$_{IG}$) and (d) G (<*u'c'*>$_{G}$) flux for 68 minute runs for *STIR 2*; vertical lines mark boundaries between tides. The shaded areas mark periods when the rip current was deemed to be active, the centre line in the shaded area represents the boundary between tides.

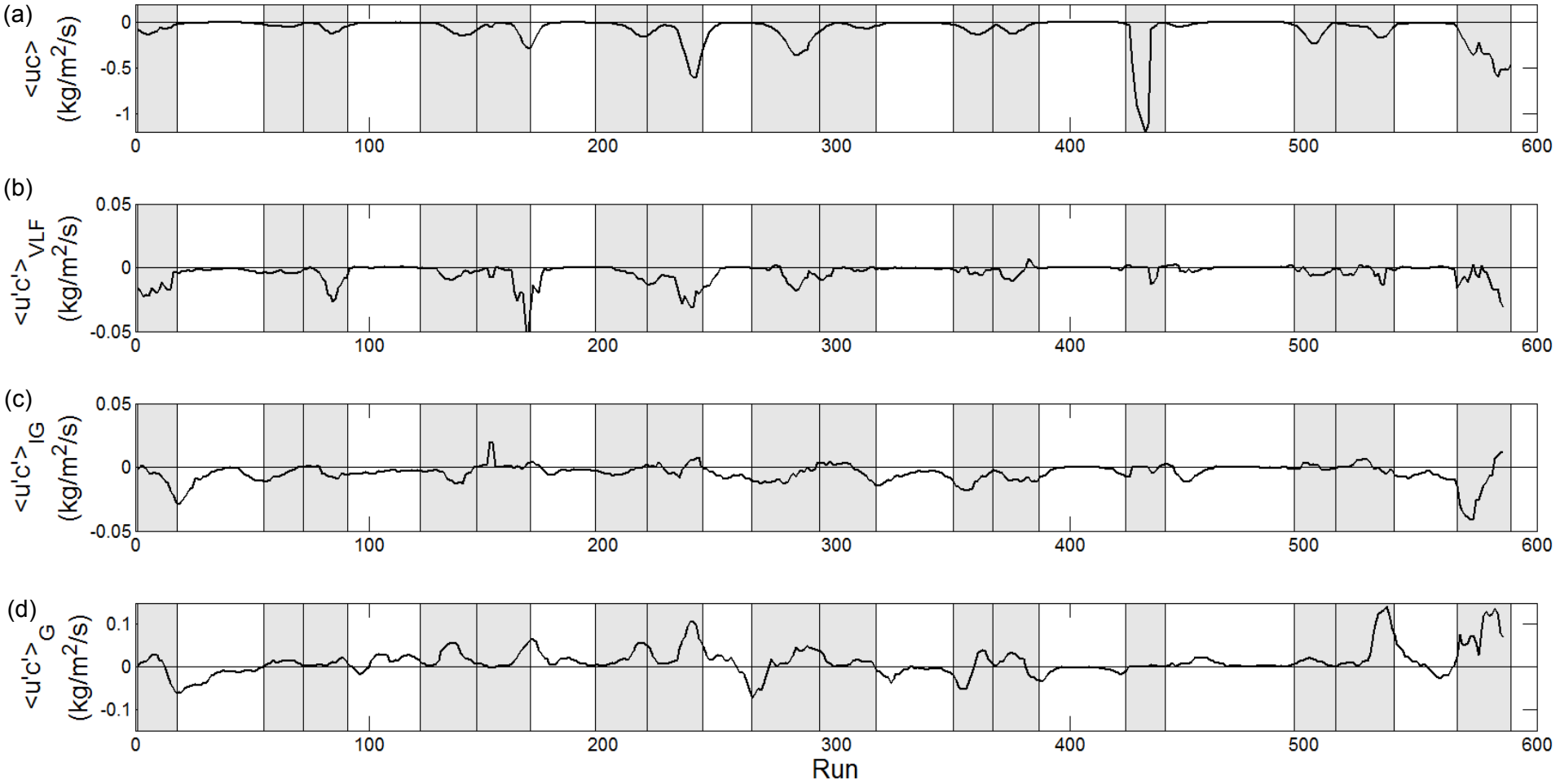

Figure 6.21: (a) Mean flux (<*uc*>) (n.b. y-axis scale is different to other panels) (b) VLF flux (<*u'c'*>$_{VLF}$), (c) IG flux (<*u'c'*>$_{IG}$) and (d) G (<*u'c'*>$_{G}$) flux for 68 minute runs for *STIR 2*; vertical lines mark boundaries between tides. The shaded areas mark periods when the rip current was deemed to be active, the centre line in the shaded area represents the boundary between tides.

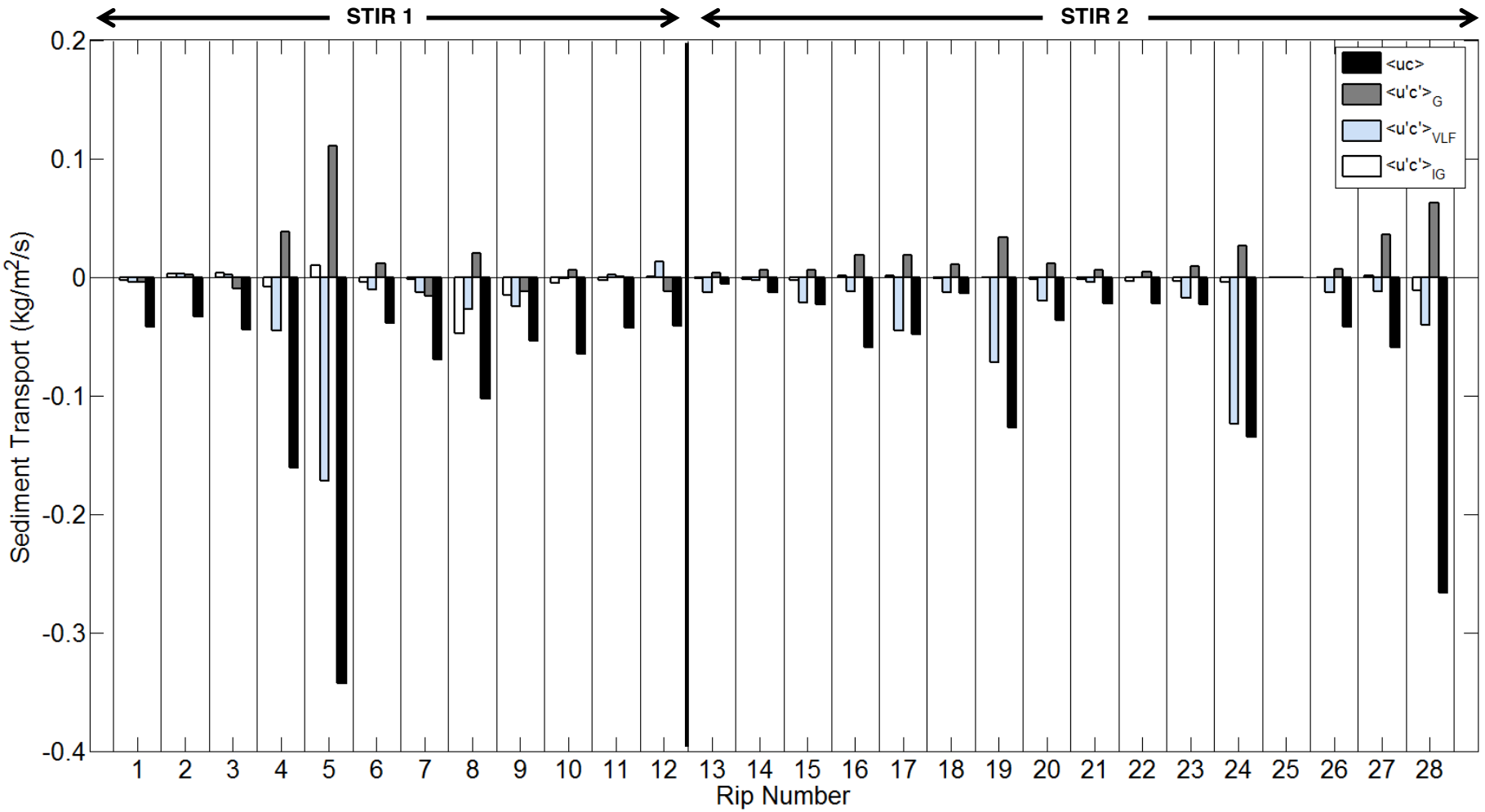

Figure 6.22: Quantification of suspended sediment transport from the mean flux (<*uc*>), the VLF flux (<*u'c'*>$_{VLF}$), IG flux (<*u'c'*>$_{IG}$) and G flux (<*u'c'*>$_{G}$) for all 27 occurrences of rip currents for the entire period the rip current was active on the flood and ebb tide during *STIR 1* and *STIR 2*. The thick vertical line marks the divide of *STIR 1* and *STIR 2* (n.b. Rip current was not deemed to be during 'rip 25').

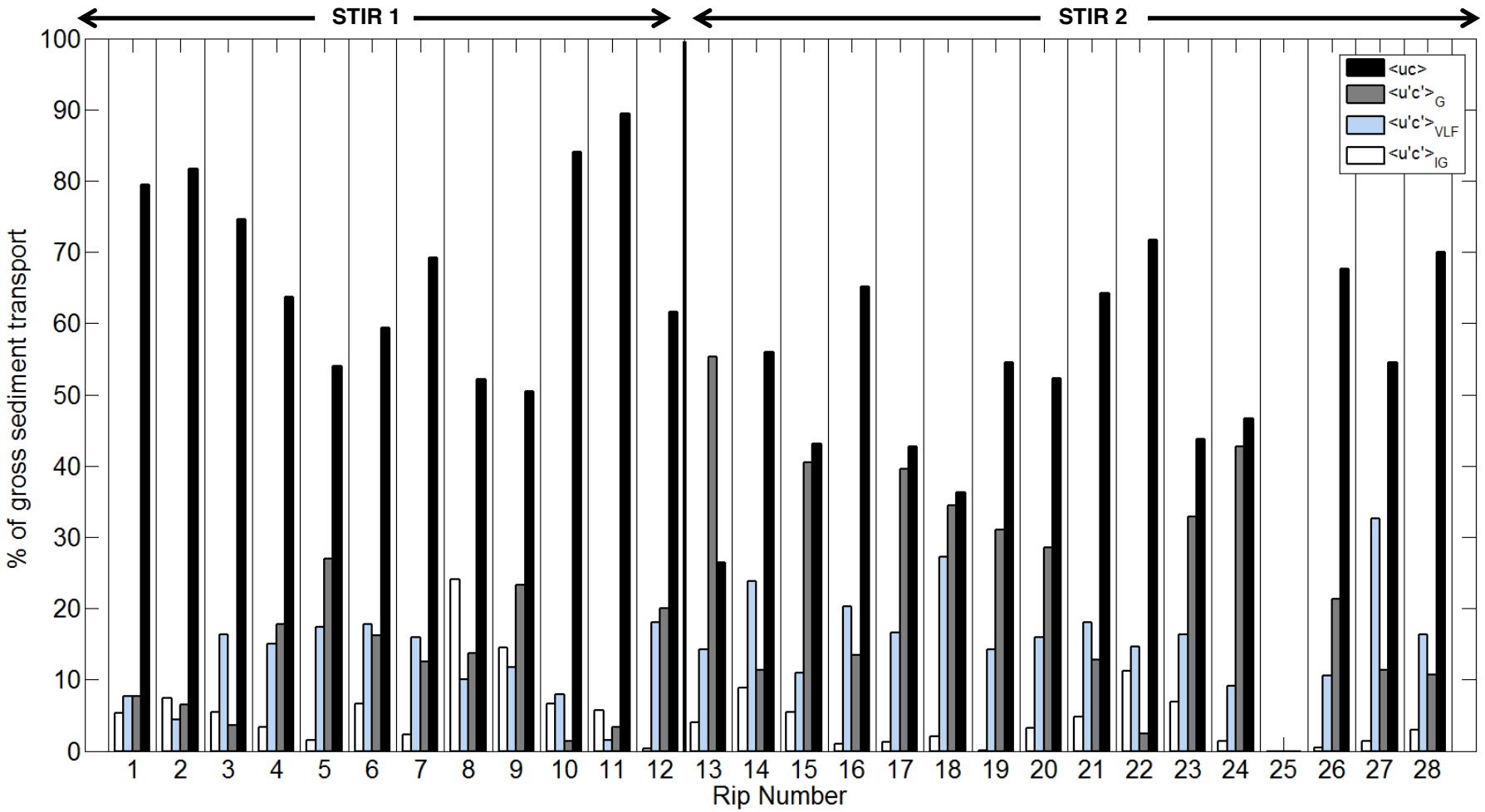

Figure 6.23: Percentage contribution to total sediment transport from the mean flux (<*uc*>), the VLF flux (<*u'c'*>$_{VLF}$), IG flux (<*u'c'*>$_{IG}$) and G flux (<*u'c'*>$_{G}$) for all 27 occurrences of rip currents for the entire period the rip current was active on the flood and ebb tide during *STIR 1* and *STIR 2*. The thick vertical line marks the divide of *STIR 1* and *STIR 2* (N.b. Rip current was not deemed to be during 'rip 25').

The results presented in Figures 6.19 to 6.23 illustrate the dominance of the mean flux as the most important mode of suspended sediment transport. In both *STIR 1* and *STIR 2* the mean flux, in most cases, was greater than all other modes of suspended transport and it was always directed offshore. These results also show the relative contribution of transport by the VLF, IG and G bandwidths.

Transport was offshore directed in the VLF band for 23 out of 27 occurrences of rip currents and was always offshore in *STIR 2* (Figure 6.20b and 6.21b). In *STIR 1* VLF fluxes exceed 0.01 kg/m^2/s on 5 of the 12 occurrences of rip currents. In *STIR 2* VLF fluxes were > 0.01 kg/m^2/s on 8 of the 15 occurrences of rip currents. Overall the maximum VLF flux was 0.12 kg/m^2/s. The percentage contribution to total gross transport by VLF motions ranges from 1.5% to 27% in *STIR 1* and 2.4% to 80% in *STIR 2.* VLF transport accounted was > 10% of the total suspended flux on 22 of the 27 occurrences of rip currents.

The IG flux was offshore directed in 20 of the 27 occurrences of rip currents, with the maxima in shallow water. The flux becomes negligible at higher tidal elevations. Maximum magnitudes of IG flux were up to 0.1 kg/m^2/s, though typically values were below 0.05 kg/m^2/s. Infra-gravity transport is often less than that of VLF and G bands, with a percentage contribution ranging from 0.5 to 24%, though a contribution to total gross transport of 10% is only exceeded 3 out of 27 times in total.

The G flux was onshore directed on 22 of the 27 occurrences of rip currents and was always onshore in *STIR 2* and accounted for > 10% of the total suspended flux during 21 of the 27 occurrences of rip currents. The G band flux varied in direction and magnitude from up to 0.05 kg/m^2/s in the onshore direction to 0.1 kg/m^2/s in the offshore direction. The trend of the G band transport rates generally followed that of the VLF band. It can also be seen that the largest onshore fluxes in the G band coincide with the largest offshore fluxes in the VLF band. This is likely to result in low net oscillatory transport as the opposing directions of transport cancel one another out.

On occasion the magnitude of VLF and G flux was comparable to that of the mean flux (STIR 2, Flood tides 1 to 3 and the ebb of tide 6). However, during these periods the VLF flux was directed offshore and was balanced by the G flux in an onshore direction, thus resulting in the oscillatory flux being relatively small. This is investigated further in Figure 6.24. It can be seen that there is a linear relationship between $\langle u'c' \rangle_{VLF}$ and $\langle u'c' \rangle_{G}$ ($R^2 = 0.64$). The G band flux makes a minimum contribution of 19% to the total oscillatory flux and a maximum of 72%. This is likely to be due to the continuous presence of incident waves.

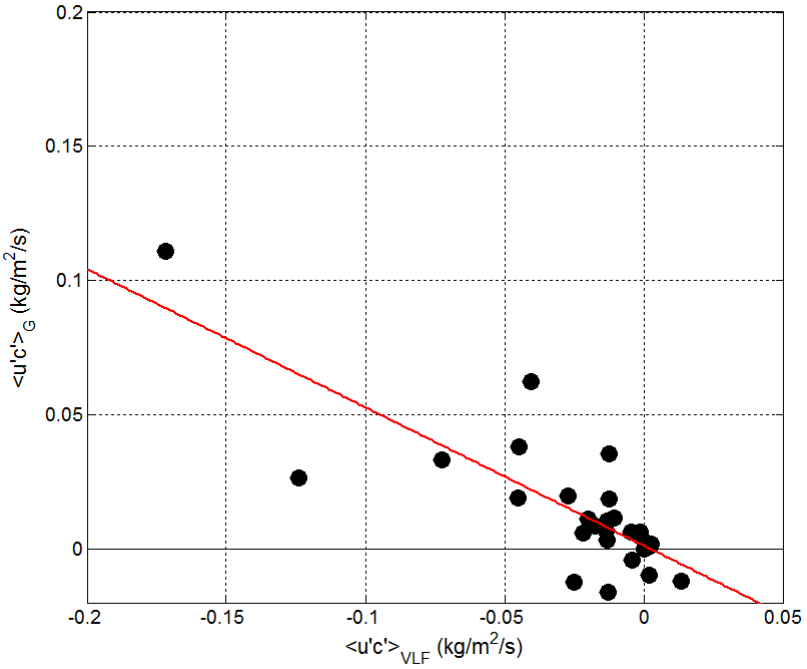

Figure 6.24: Correlation of VLF flux (<*u'c'*>$_{VLF}$) and G frequency flux (<*u'c'*>$_{G}$) transport. (R^2 = 0.64).

Generally the VLF transport is marginally larger than the G transport. Although these two modes of transport appear to make a significant contribution to sediment transport in a rip current individually, their contribution to the total transport is effectively cancelled out because they are in opposing directions and at a similar time.

The magnitudes of all modes of suspended transport are plotted against the mean cross-shore velocity to investigate the effect of increasing rip strength on sediment transport (Figure 6.25). The mean, VLF, and G component all show some increase with velocity. The greatest increase in suspended sediment transport is in the mean component in an offshore direction due to the strong mean rip flow. This is followed by the VLF flux which also increases in an offshore direction with <*u*>. The G frequency flux exhibits a similar trend and magnitude, however, the transport increases in an onshore direction. The IG flux shows no relationship with current strength, IG fluxes are generally much smaller than any other mode of transport, with the largest fluxes (0.05 kg/m^2/s) occurring at velocities of around 0.2 m/s.

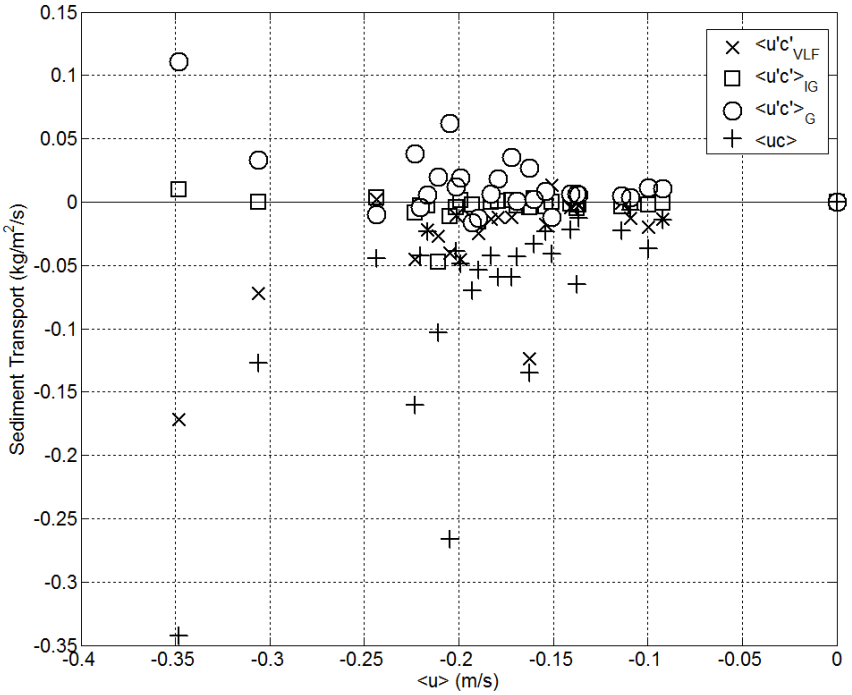

Figure 6.25: Oscillatory suspended sediment flux from different modes of transport (<*uc*>, <*u'c'*>$_{VLF}$ <*u'c'*>$_{IG}$ <*u'c'*>$_{G}$) as a function of mean flows for periods when the rip current was active.

6.6: Depth Integrated Suspended Sediment Transport

6.6.1: Justification of depth integration method

A best estimate of total suspended sediment flux was calculated to facilitate comparison with the bedform transport rate. The method follows that recommended by Van Rijn (1993) and Miles and Thorpe (2015), and provides a single value of sediment flux representing the total (mean and oscillatory) flux. The units are in kg/m/s, which is the equivalent to those given by the bedform transport formula of Huntley et al. (1991) calculated in Chapter 5. More detail on the method is provided in Section 3.6.6.

The results for depth integration in *STIR 1* are likely to be less accurate than those in *STIR 2* as the velocity profile is calculated from measurements made from one ADV, not two, as were used in *STIR 2.* However, the point measurements of velocities at z = 0.25 m and z = 0.45 m in *STIR 2* were found to be very similar (Figure 4.17), giving confidence in the method used.

The results obtained from depth integration of data in both experiments are considered to be conservative estimates (Miles and Thorpe, 2015). The suspended sediment concentration from the lowest OBS (positioned at z = 0.25 m) is assumed to be vertically uniform from the sensor to the bed, this fixes a concentration value which is

likely to be an under-estimate, but more importantly, it avoids generating an over-estimate.

The method involves calculating the vertical diffusivity (L_s) from two vertically separated OBSs which is used to fit a Nielsen (1992) concentration profile from the lowest sensor to the water surface (Figure 3.22). In *STIR 1* the mean L_s value was 0.08, when the rip was active it was 0.09, compared to 0.07 when the rip was not active. L_s values were larger in *STIR 2*, the mean L_s was 0.3, when the rip was active it was 0.45, compared to 0.15 when the rip was not active (Figure 6.26). The reason L_s values are much larger in *STIR 2* is likely to be because increased suspension occurs as a result of larger waves. Figures 6.26 ad 6.27 highlight the variability of L_s over a tidal cycle.

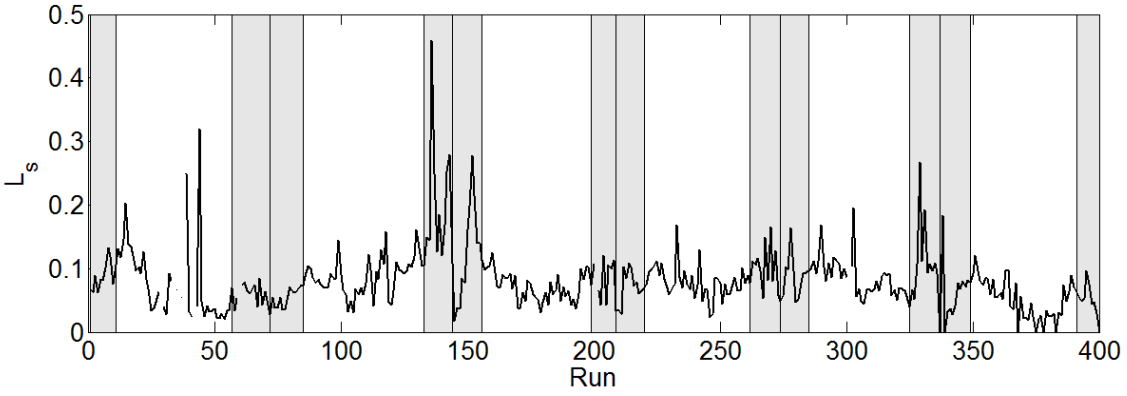

Figure 6.26: Time series of vertical diffusivity (L_s) calculated from sediment concentrations at z = 0.25 m and 0.45 m in *STIR 1*. The shaded areas mark periods when the rip current was deemed to be active, the centre line in the shaded area represents the boundary between tides.

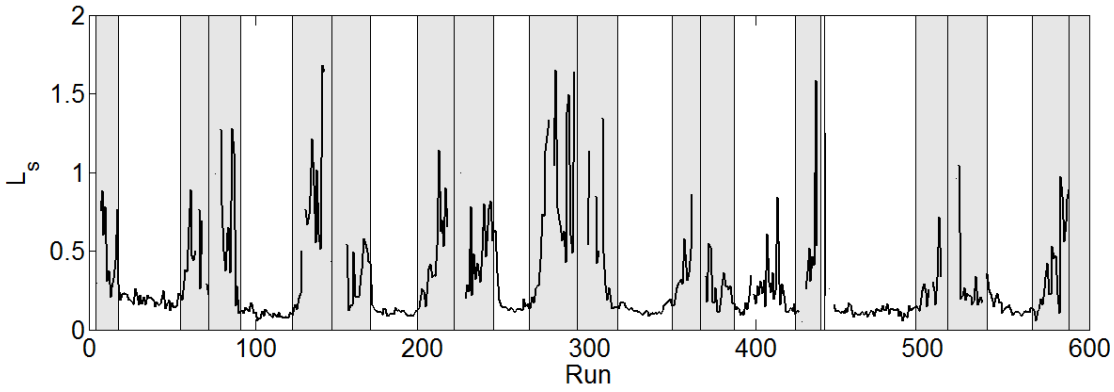

Figure 6.27: Time series of vertical diffusivity (L_s) calculated from sediment concentrations at z = 0.25 m and 0.45 m in *STIR 2*. The shaded areas mark periods when the rip current was deemed to be active, the centre line in the shaded area represents the boundary between tides.

6.6.2: Quantification of depth integrated suspended sediment flux

The depth integrated suspended sediment flux (Q_s) was always offshore in both *STIR 1* and offshore for the majority of the time in *STIR 2*, with the largest magnitudes generally found when the rip current was active (marked by the shaded area) (Figures 6.28 and 6.29). For all periods when the rip was active the mean flux was offshore directed at a rate of 0.03 kg/m/s compared to a mean of 0.005 kg/m/s when the rip was not active. Typically the largest fluxes were found to be around 0.1 kg/m/s, though the largest flux was 0.76 kg/m/s (run 153), also in the offshore direction.

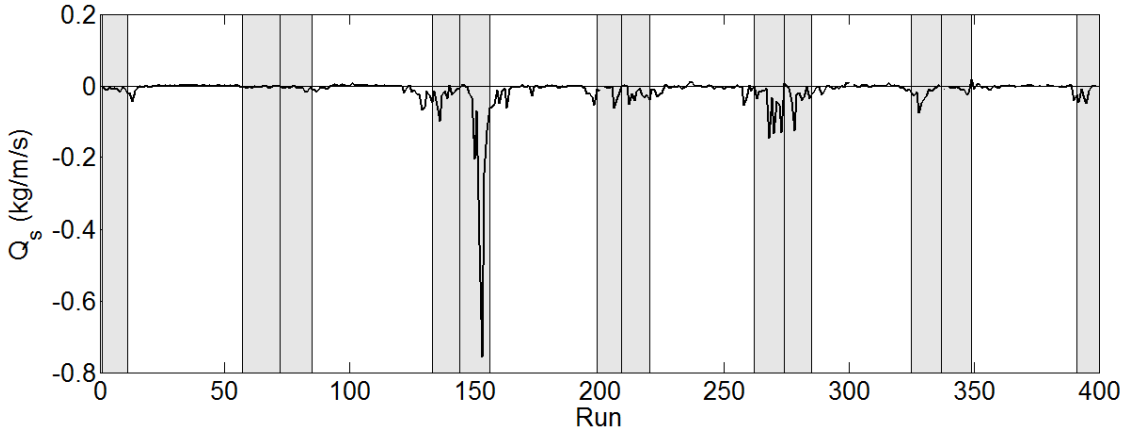

Figure 6.28: Time series of depth integrated suspended sediment transport (Q_s) during *STIR 1*. The shaded areas mark periods when the rip current was deemed to be active, the centre line in the shaded area represents the boundary between tides.

In *STIR 2* the mean depth integrated flux for all periods when the rip was active was offshore directed at a mean rate of 0.08 kg/m/s compared to 0.005 kg/m/s when the rip was not active, also offshore directed. Typically the largest fluxes were between 0.1 and 0.2 kg/m/s, though the flux was greater than 0.5 kg/m/s on four occasions.

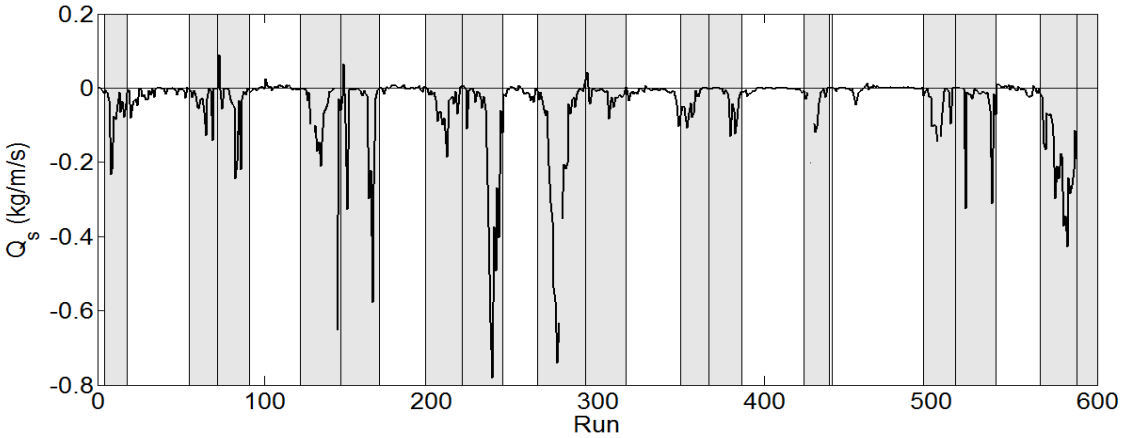

Figure 6.29: Time series of depth integrated suspended sediment transport (Q_s) during *STIR 2*. The shaded areas mark periods when the rip current was deemed to be active, the centre line in the shaded area represents the boundary between tides.

6.6.3: Validity of depth integration method

The time series of depth integrated flux shows a strong resemblance to the point measurements of the total flux in Figures 6.6 and 6.7. To test this, the results from the point measurements of total flux (<*uc*> + <*u'c'*>) made at z = 0.25 and z = 0.45 are correlated with the depth integrated flux in Figures 6.30 and 6.31.

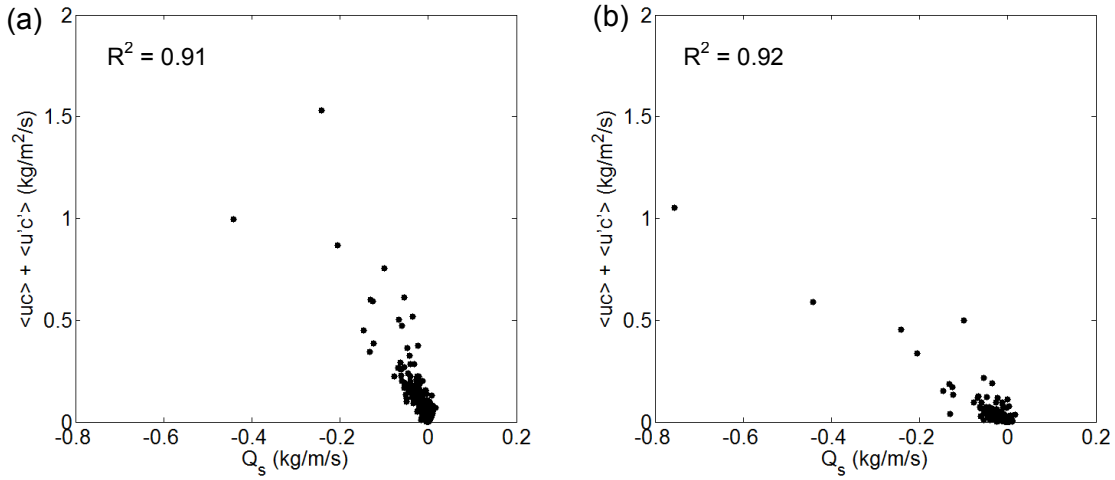

Figure 6.30: Correlation of point measurments of total suspended sediment transport (<*uc*> + <*u'c'*>) at (a) z = 0.45 and (b) z = 0.25 with depth integrated flux (Qs) in *STIR 1*.

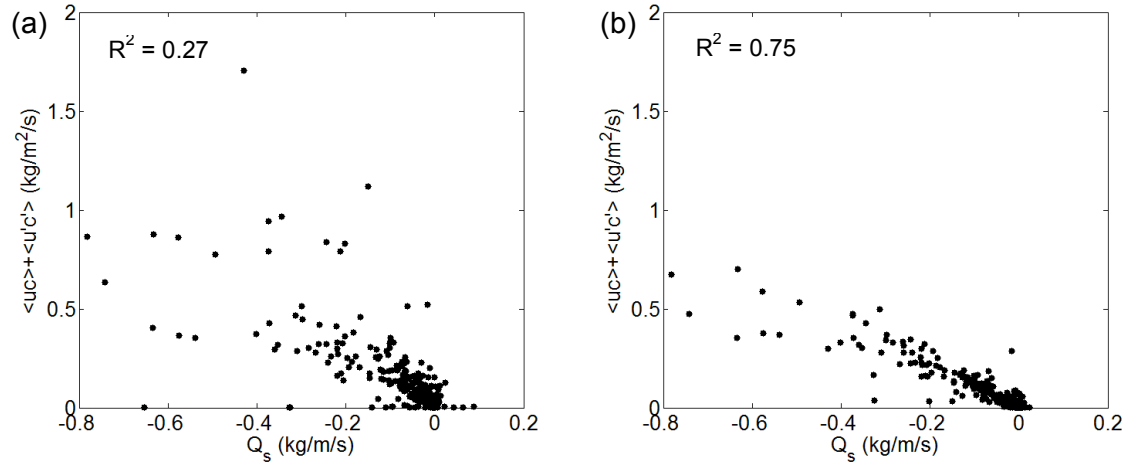

Figure 6.31: Correlation of point measurments of total suspended sediment transport (<*uc*> + <*u'c'*>) at (a) z = 0.45 and (b) z = 0.25 with depth integrated flux (Qs) in *STIR 2*.

Generally there is a good correlation between point measurements of total suspended flux and depth integrated flux. In *STIR 1* the R^2 exceeds 0.9 for measurements made at z = 0.25 m and z = 0.45 m (Table 6.5). In *STIR 2,* the correlation is quite weak for point measurements made at z = 0.45 m (R^2 = 0.27), though visually the correlation appears to be stronger at lower fluxes, with the correlation becoming weaker as transport rates increase. The correlation between point measurements at z = 0.25 m is clearer with an R^2 of 0.75.

Table 6.5: R^2 values for the correlation of point measurements of suspended sediment and depth integrated flux

z (m)	STIR 1	STIR 2
z = 0.25	0.91	0.27
z = 0.45	0.92	0.75

6.6.4: Forcing of depth integrated sediment transport

Suspended sediment flux has a positive relationship with the mean rip flow (Figure 6.5), though there is a significant amount of scatter. This suggests that in addition to current strength another factor is important for suspended sediment transport. Following Figure 6.3, it can be seen that sediment concentrations increase with orbital velocity. Repeating the analysis used on 10-minute sections of data in Figure 6.9, the mean depth integrated suspended sediment (Q_s) is averaged for the every entire period in which the rip current was active, on all 27 occurrences of rip currents, and is plotted against the mobility number for the corresponding periods. The form of the mobility number of Gallagher (2003) is used, following Equation 3.12. This is because it incorporates information on both the oscillatory and therefore accounts for wave stirring and the mean component of the flow. It can be seen that Q_s and Ψ when correlated give an R^2 of 0.77 indicating that suspended sediment transport is potentially dependent on both wave stirring to suspend sediment, and strong mean flows to transport the sediment once suspended. This suggests that in small waves suspended sediment transport may be limited by a lack of suspension, despite the presence of a strong rip current and that the mobility number is a useful parameter to describe this observation.

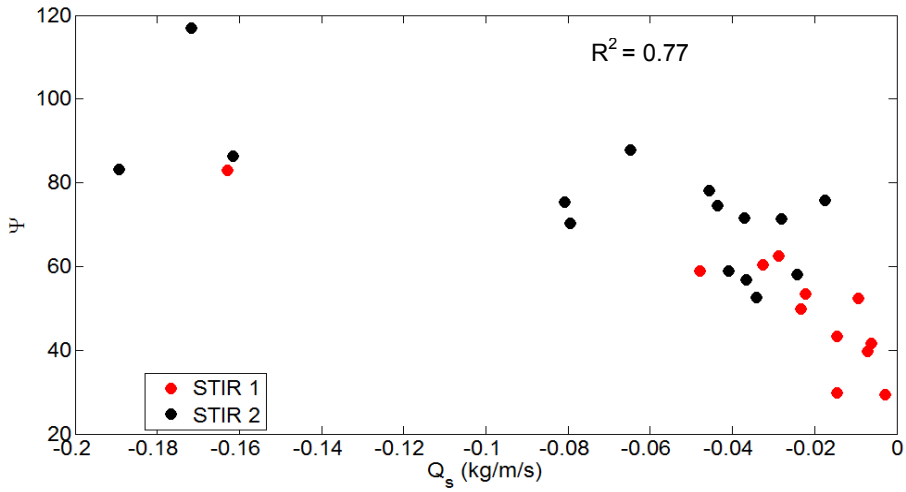

Figure 6.32: (a) Depth integrated suspended sediment flux (Q_s) as a function of mobility number (Ψ) averaged over every period the rip current was active. *STIR 1* and *STIR 2* plotted separately.

6.7: Discussion on Rip Current Suspended Sediment Transport Dynamics

Suspended sediment was found to be ubiquitous in the rip channel throughout all stages of the tidal cycle, and therefore includes times when the rip current was both active and inactive. However, the magnitude of sediment concentration varied considerably over the tidal cycle, with maxima found at lower tidal elevations, and particularly at the rip/non-rip boundary as rip flow commenced/ceased. This may be a result of the bed (forms) adjusting to a change in flow dynamics or because this is when wave orbital velocities were greatest.

Suspended sediment transport was found to be tidally modulated, with the largest fluxes occurring in an offshore direction at low tide when the rip current was active (Aagaard et al., 1997; Brander, 1999b). At higher tidal elevations suspended sediment transport was minimal.

Suspended sediment concentrations were found to decay vertically away from the bed, with concentrations at z = 0.05 m found to be an order of magnitude larger than concentrations found at both z = 0.25 m and z = 0.45 m, therefore indicating an exponential decay away from the bed, as indicated by Nielsen (1992). In spite of this decay, (10-minute) mean concentrations of > 1 kg/m^3 and instantaneous concentrations of > 20 kg/m^3 are found at z = 0.25 m, which can be considered relatively high for that elevation above the bed (*c.f.* Russell, 1990; Miles et al., 2002; Masselink et al., 2007; Aagaard and Hughes, 2010). A possible explanation for the enhanced sediment suspension is that the presence of bedforms increases roughness and enhances vorticity and therefore leads to greater sediment mixing within the water column (Vincent and Osborne 1996). Wave stirring can also lead to sediment being suspended relatively high up in the water column (Russell and Huntley, 1999; Reniers et al., 2004b) and in the presence of mean currents is susceptible to advection.

Evidence presented in this study suggests that incident wave orbital motion is required to suspend sediment in order for the mean flow of the rip current to give rise to offshore directed suspended sediment transport. The first deployment (Tides 1 and 2 in *STIR 1*) experienced the smallest wave conditions of all data collection periods (H_s = 0.76 m, T_p = 9.8 s) and also some of the lowest sediment concentrations measured. Though, during these periods the cross-shore velocity was similar to other occasions the rip current was active (<u> ~ 0.4 m/s, where the maximum in the study was ~ 0.7 m/s), where much higher sediment concentrations were measured. Increasing mean cross-shore currents up to 0.6 m/s appeared to have little effect on suspended sediment concentrations, particularly in *STIR 1* (Figure 6.3). However, increasing orbital velocity

was shown to lead to an increase in suspended sediment concentration and this is particularly clear in *STIR 1* (Figure 6.3). The high orbital velocities in the rip channel led to the continual presence of large volumes of suspended sediment, obscuring the clarity of the phase of suspension by the waves at the location of the instrument frame. Brander (1999b) observed the requirement for wave activity to initiate suspension in a rip current even when significant mean flows were present (<*u*> = 0.5 m/s). He found that the critical threshold for the entrainment of beach sand in a rip current was always exceeded by the combined contribution of waves and currents, and also by the contribution of waves alone. However, Brander (1999b) also found that the contribution from currents alone was not always sufficient to initiate entrainment, particularly in the feeder channels. The implication of this observation is that in smaller waves or in feeder channels, where wave energy has already been dissipated on the bar, sediment transport is likely to be limited by a lack of wave driven suspension. This is a potentially significant result as it would suggest in a low energy accretionary environment, the rip and feeder channel could undergo net infilling due to small limited offshore sediment transport being unable to maintain the channel.

When VLF oscillations were present (Section 4.6 & Section 6.1.3), the offshore part of VLF flow was observed to be synchronous with maximum suspended sediment concentrations. During the example time series presented in Figure 6.10, the mean concentration was 0.8 kg/m^3. This increased to between 5 to 40 kg/m^3 during the offshore pulse of the rip flow. VLF motion has been observed to correlate well with suspended sediment concentration in other studies (Aagaard and Greenwood, 1995a; Miles et al., 2002), though transport at these frequencies has not been observed in a rip current before. Miles et al. (2002) found suspension occurred at incident wave frequency, but was modulated at shear wave frequency (VLF). A threshold velocity of 0.5 m/s in the offshore direction was identified for suspension, and this velocity was a combination of undertow and the offshore VLF component of a shear wave. Similarly, a closer investigation of the *u* and *c* time series presented during an offshore (VLF) pulse (Figure 6.11) shows that whilst the concentration increases with increased offshore directed velocity during an offshore directed pulse, individual peaks in concentration correlate with incident wave events, suggesting that the total instantaneous velocity is the key driver in suspending sediment.

Aagaard et al. (1997) found infra-gravity pulses within rip current flow to be important for sediment suspension, with concentrations increasing from 3.9 kg/m^3 to between 10 and 50 kg/m^3 during offshore pulses (at z = 0.05 m). Similarly results presented here also highlight the importance of infra-gravity motion for sediment suspension, with mean concentrations of 0.8 kg/m^3 increasing to maximums of around 10 kg/m^3 during

offshore pulses. As a comparison, in storm conditions in the surfzone Russell (1993) found concentrations associated with IG motion at z = 0.04 m peaked at 70 kg/m^3 and lasted for 30 to 40 seconds. Though these concentrations are higher than measured in this study, they were made lower in the water column, and in the inner surf zone of a planar, high energy, dissipative beach.

All calculations of suspended sediment flux were made from point measurements of suspended sediment concentration at *z* = 0.25 m and velocity measurements made at *z* = 0.45 m in *STIR 1,* and at z = 0.25 m in *STIR 2*. Aagaard et al. (1997) calculated point measurements of suspended sediment flux from ADVs and OBSs at different heights, and although they recognised the potential for an over estimate of the mean flux (due to the logarithmic nature of the mean velocity profile) the method was still applicable for computing bulk characteristics (i.e. directions, processes and relative magnitudes). With respect to the concerns of Aagaard et al. (1997) a comparison between velocity measurements made at both *z* = 0.25 m and z = 0.45 m in *STIR 2* found that they were very similar (Figure 4.17), both when the rip current was active and not active. Data collected form the OBS deployed at z = 0.05 m was not used for the analysis, as apart from only being deployed in *STIR 2,* the sensor was intermittently buried, probably by migrating bedforms. The OBSs deployed at z = 0.45 m were not used for calculation of flux from point measurements due to a reduction in data length close to low tide.

The mean component of the flux was found to be the dominant mode of transport when the rip was active and thus agreeing with results of Aagaard et al. (1997) and Brander (1999b). This was consistent throughout the whole data set and is due to the strong mean flow of the rip current. Oscillatory flows are shown to have an important, but secondary role, as noted by Aagaard et al. (1997). When the rip current was active, the mean flux was largest and was always offshore directed at an average of 0.12 kg/m^{2}s in *STIR 1* and 0.10 kg/m^{2}s in STIR 2, with a maximum offshore transport rates of 2.1 kg/m^2/s and 0.68 kg/m^2/s respectively. Of the 27 occurrences of rip currents, the mean flux accounted for > 90% the gross total flux on 10 occasions and for > 70% on 19 occasions. Oscillatory fluxes for periods when the rip were active were close to zero in *STIR 1* and averaged 0.015 kg/m^2/s in the onshore direction in *STIR 2*.

At higher tidal elevations, when the rip was not active, the mean flux was still directed offshore, this was likely to be due to bed return flow (Miles et al., 2014a). The flux in non-rip conditions was an order of magnitude less than when the rip current was active (0.014 kg/m^{2}s in *STIR 1* and 0.015 kg/m^{2}s in *STIR 2*). The oscillatory flux in non-rip conditions was negligible in magnitude in *STIR 1* and offshore directed at an average of 0.01 kg/m^{2}s in *STIR 2*.

Aagaard et al. (1997) presented sediment fluxes from a rip current as total transport (<*uc*> + <*u'c'*>). Their measurements of total suspended sediment transport in a rip current are between 0 and 1.6 kg/m^2/s (max <u> = 0.6 m/s, measured at z = 0.05 m). The larger magnitude of flux measurements made by Aagaard et al. (1997) are likely to be because they made measurements lower in the water column. The sediment trap method used by Brander (1999b) did not allow the mean and oscillatory components to be separated. He found transport to be offshore directed, and calculated the total suspended sediment transport giving average fluxes of 0.13 kg/m^2/s and maximum fluxes of up to 0.73 kg/m^2/s. In this study the total transport (<*uc*> + <*u'c'*>) rates in the rip current are very similar to those of Brander (1999b). Due to the dominance of the mean flux (of 0.12 kg/m^{2}s in *STIR 1* and 0.10 kg/m^{2}s in *STIR 2*), total transport rates are also similar to the mean transport rates. Therefore results presented in this study support the mechanisms observed by Aagaard et al. (1997) and Brander (1999b). Brander (1999b) found transport rates to be directly related to <u'^{3}> and subsequently suggested that a Bagnold (1963) type approach might be appropriate for the modelling of transport in rip currents, however, this would only apply to suspended load transport, as Brander's (1999b) analysis does not include any consideration of bedload transport. The same analysis was carried out in this study, and although there is a general increase in total transport with <*u'*^{3}>, there is a large amount of scatter.

Skewness (in the shoaling zone) and asymmetry (immediately offshore of the breakpoint) are widely recognised as important mechanisms for the onshore directed transport of suspended sediment (Elgar et al., 1988). Shoreward of the breakpoint the effect of these mechanisms are balanced by mean offshore transport in the surf zone due to bed return flow (Russell and Huntley, 1999). Data presented here shows onshore gravity frequency transport increases with increasing asymmetry and skewness in rip conditions (Figure 6.15), although there is a large amount of scatter. As wave breaking is observed to be restricted in the rip channel (MacMahan et al., 2006) it is possible that the presence of the deeper water in a rip current affects the incoming waves by increasing their skewness and asymmetry, allowing waves to remain unbroken for longer than they may do without the presence of a rip channel. Gravity frequency transport was usually onshore (on 22 of the 27 occurrences of rip currents) when the rip was active and accounted for > 10% of the total suspended flux on 21 of the 27 occurrences of rip currents. Maximum transport rates were 0.1 kg/m^2/s, which is comparable to mean fluxes. When the rip was not active at higher tidal elevations, incident wave frequency transport was often directed offshore. Inman and Bowen (1963) described a mechanism of offshore directed sediment transport in onshore propagating waves over bedforms. During the onshore stroke of the wave sediment is carried a small distance onshore close to the bed and becomes trapped in a vortex in

the lee of the ripples. As the flow reverses the sediment is ejected into the water column and transported then offshore. The gravity frequency transport may have been onshore during rip conditions, as large volumes of sediment were continuously in suspension through much of the lower part of the water column and therefore not trapped in the vortex of bedforms. The onshore stroke of the wave could therefore preferentially transport sediment onshore.

Co-spectral analysis techniques (Hanes and Huntley, 1986) and filtering techniques (Miles et al., 2002) were used to investigate the contribution of motion at frequencies exceeding incident wave time scale. Infra-gravity frequency transport was found to often be offshore (on 20 of the 27 occurrences of rip currents) whilst the rip current was active. Transport rates in the rip at IG frequencies were generally much less than that transported of the VLF and G bands. The largest fluxes were around 0.05 kg/m^2/s and it accounted for > 10% of the total suspended flux on only 3 of the 27 occurrences of rip currents. Aagaard et al. (1997) observed that whilst infra-gravity motions were important for sediment suspension in the rip current, they have a secondary role in sediment transport. In the surfzone (with no rips), infra-gravity motions have been found to have an important role in beach erosion during storms (Russell, 1993). Offshore transport will occur as a result of undertow and infra-gravity motion and net transport will likely to be offshore directed in high energy conditions (Beach and Sternberg, 1991; Russell, 1993; Aagaard and Greenwood, 1995a). Rips therefore provide an extra mechanism in addition to the IG waves and bed return flow that have the potential to contribute to beach erosion and offshore sediment transport.

VLF motions were found to be efficient in transporting suspended sediment offshore and when VLF pulsing was present it lead to a secondary (to mean flux) but significant contribution to offshore transport. The contribution of VLF motions was quantified by filtering the velocity and concentration time series (Miles et al., 2002). VLF transport was found to account for > 10% of the total suspended flux on 22 of the 27 occurrences of rip currents and was offshore directed on 23 of the 27 occurrences of rip currents. The maximum flux in the VLF band was 0.12 kg/m^2/s, which is comparable to mean fluxes, though often the VLF flux was one order of magnitude less than this. Miles et al. (2002) observed offshore directed sediment transport by shear waves in the VLF band on the inter-tidal bar of a macro-tidal beach to be an important offshore transport mechanism and accounted for up to 37% of oscillatory transport. Whilst the mean flux dominated the transport (69% of total transport), transport in the VLF band accounted for 16% of the total transport, similar to results presented in this study. Aagaard and Greenwood (1995a) also identified the importance of VLF motion for the transport of sediment (65% of total flux). Sediment transport in the VLF band has not

been measured before in a rip current, though the model results of Orzech et al. (2011) indicated that while the mean flux is likely to be the dominant mode of transport, VLF transport may be an important component of the total load transport in a rip current. In addition to cross-shore rip pulsing, pulsing at VLF timescales was also observed in the longshore flow. The effect of this has not been investigated as the aim of the study is to assess cross-shore sediment transport, though given the importance of cross-shore VLF transport, it is feasible large quantities are transported in the longshore flow (Aagaard and Greenwood, 1995a).

The sediment transport in the VLF band was found to increase with an increase in sediment transport in the gravity band (Figure 6.25). The result of this is that when VLF motion is present and contributing to offshore directed sediment transport, a similar contribution occurs from incident waves in the gravity band in an onshore direction and thus results in a small overall net oscillatory flux (Figure 6.6 & 6.7).

Depth integrated suspended sediment transport is a measure of total suspended sediment transport (throughout the water column). It was calculated primarily to provide a comparison between total suspended sediment transport and bedform transport, but also to offer a comparison with literature data of total transport from other near shore work. It is acknowledged that a higher resolution in the vertical velocity profile and suspended sediment concentration profile would improve the accuracy of the depth integrated suspended sediment calculations. A pragmatic approach, as used by Miles and Thorpe (2015) has been applied based on the available instruments. It is likely the estimates of depth integrated flux applied here are conservative, this is because concentration is assumed to be uniform below the height of the reference concentration ($z = 0.25$ m). In this study, mean depth integrated fluxes were found to be 0.03 kg/m/s in *STIR 1* and 0.08 kg/m/s in *STIR 2* (when averaged over all periods the rip was active) in an offshore direction. The flux maxima were found to be 0.76 kg/m/s and fluxes of between 0.1 to 0.2 kg/m/s occurred regularly. A comprehensive comparison is made between bedform transport and depth integrated flux in the following chapter. The contribution by depth integrated suspended sediment transport was approximately an order of magnitude larger than the bedform transport rate. The mean bedform transport rate during all periods the rip was active was offshore directed at a magnitude 0.0020 kg/m/s and maximum bedform transport rate in the rip was 0.05 kg/m/s.

Confidence in the results presented here is achieved with a comparison to other measurements of depth integrated flux made within the nearshore using various other methods. A comprehensive comparison is provided in Table 6.13, giving depth integrated fluxes in a range of environments. Work by Brander (1999b), Aagaard et al. (2012) and Aagaard et al. (2013) and Masselink et al. (2007) is discussed in more

detail as these three studies used different methods to calculate the depth integrated flux.

Brander (1999b) used a vertical array of sediment traps deployed in a rip current, where the maximum velocity was 0.52 m/s. He recorded average depth integrated fluxes of 0.05 kg/m/s and a maximum of 0.17 kg/m/s. These measurements are very similar to measurements from this study and with the exception they were made in a feeder channel as opposed to the rip neck, are from a similar type of environment ($<v>$ = 0.4 – 0.6 m/s, h = 0.71, H = 0.4 – 1 m)

In Aagaard et al. (2012) and Aagaard et al. (2013) an Acoustic Doppler Profiler (ADP) was used to measure vertically integrated transport rates on a reflective beach. The ADP used by Aagaard et al. (2012) had a vertical resolution of 1.6 cm, and measurements were made in storm conditions (H = 0.9 m) and in post-storm (H = 0.45 m) conditions over medium sand (D_{50} = 0.25 mm to 0.3 mm). Vertically integrated suspended sediment transport rates were an order of magnitude less than results presented from a rip current, with transport rates of -0.02 kg/m/s in the storm conditions, and 0.0048 kg/m/s in the post storm conditions. Compared to measurements made in this study, Aagaard et al. (2012) made measurements in a lower energy environment and therefore the fluxes may be expected to be lower.

In contrast Masselink et al. (2007) used a vertical array of closely spaced (0.03 m) OBSs sensors to create a concentration profile on an intermediate beach with a D_{50} of 0.6 mm. They found depth integrated transport rates of around 0.01 to 0.03 kg/m/s and maximums of 0.15 kg/m/s in the onshore direction in calm conditions near the breakpoint and up to 0.6 kg/m/s in storm conditions (H = 2 m). Aagaard et al. (2012) suggested the measurements of Masselink et al. (2007) were larger due to the larger waves and because measurements were made in shallower water depths. On a dissipative beach (Perranporth, D_{50} = 0.3 mm) Miles and Thorpe (2015) measured depth integrated flux of between 0 and 0.01 kg/m/s with maximum rates of 0.16 kg/m/s when the H = 0.5 to 2.2 m and h = 0.9 to 6 m.

Table 6.13: Comparison of depth integrated suspended sediment transport at different locations within the nearshore zone from multiple studies. Max or mean total suspended sediment transport displayed. Negative values indicate offshore transport. D = grain size; H = wave height.

Study	Environment	Conditions	Transport Rate (kg/m/s)
This Study	Rip Current	• H = 0.5 – 3.1 m • Macro-tidal • D = 0.3 mm • Intermediate /dissipative	**Mean:** -0.03 (*STIR 1*), -0.08 (*STIR 2*). **Max:** -0.8, often between -0.1 and -0.2
This Study	In a rip channel when h > 3 m	• H = 0.5 – 3.1 m • Macro-tidal (h > 3 m) • D = 0.3 mm • Intermediate/dissipative	**Mean:** -0.005 (*STIR 1* & *STIR 2*). **Max:** -0.06.
Brander (1999b)	Rip Current	• Low energy • Micro-tidal • D = 0.35 mm • Intermediate	**Mean:** -0.05 **Max:** -0.17
Miles et al. (2006)	Swash zone	• H = 1.5 m, T = 7s • Macro-tidal • D = 0.24 mm • Intermediate/dissipative	**Max:** 0.07
Masselink et al. (2007)	Surfzone (shoal, break point and surf zone)	• Macro-tidal • D = 0.7 mm • Intermediate	**Mean:** 0.01 - 0.03 **Max** 0.15 **Max** ~ -0.6 (High Waves)
Aagaard et al. (2006)	Surfzone	• H = 0.5-0.6 m; (max H = 2 m) • Micro-tidal • D = 0.24 mm • Dissipative	0.08 Bar crest / seaward slope of bar -0.02 (generally an order of mag less) Shoaling zone,
Grasmeijer and Van Rijn (2001)	Surfzone	• 0.5 to 1.5 m • Meso-tidal • D = 0.2 - 0.3 mm • Barred dissipative	**Range:** 0.0005 to 0.1

Beach and Sternberg (1996)	Surfzone	• H = 0.47 to 0.67 • Micro-tidal • D = 0.17 mm • Intermediate	**Max** = 0.03
Tinker et al. (2009)	Surfzone	• H = 0.6 (low energy) to 1.9 m (high energy) • Macro-tidal • D = 0.7 mm • Intermediate	**Max:** -0.02 to -0.03 in surfzone **Max:** 0.025 kg/m/s in shoaling zone
Aagaard et al. (2012)	Surfzone	• H = 0.9 m (storm) & H = 0.45 (post storm) • Micro-tidal • D = 0.25 – 0.3 mm • Reflective 0	-0.02 (storm conditions) 0.0048 (post storm)
Miles and Thorpe (2015)	Mid Surfzone	• H = 0.5 – 2.2 m, T =7 – 11 s • Macro-tidal • D = 0.28 mm • Intermediate/dissipative	**Max:** -0.16 (in mid surf zone). Weak onshore transport further seaward

The measurements made in the surfzone by Masselink et al. (2007) and Aagaard et al. (2012) are similar to those made at higher tidal elevations when the rip current was not active in this study. The mean depth integrated transport in non-rip conditions was found to be offshore directed at 0.005 kg/m/s averaged over all periods the rip was not active). In *STIR 1* and *STIR 2* the mean offshore directed transport rates when the rip current was active were 0.03 in *STIR 1* and 0.08 in *STIR 2*. The comparison between results collected in this study in rip and non-rip conditions and other studies (Table 6.13) indicate that significant quantities of sediment is transported in suspension in a rip current.

6.8: Summary of Results: Suspended Sediment Transport in Rip Currents

The aim of this chapter was to investigate the processes responsible for suspended sediment transport in rip currents and to quantify the magnitudes and relative importance of the processes.

The findings in this chapter may be summarised as follows:

- Suspended sediment transport was modulated by tidal elevation. This was attributed to changes in water level that modulated the effect of waves and the presence of rip flow. At lower tidal elevations (when the rip is active), wave

stirring and the strong offshore directed flows of the rip lead to relatively large rates of offshore sediment transport. At higher tidal elevations (when the rip is not active), suspended sediment transport is relatively small and occasionally directed onshore, consistent with observations of Aagaard et al. (1997).

- Wave stirring appears to an important factor in suspending sediment, prior to its subsequent offshore transport by the rip current. In smaller waves, suspended sediment transport was less than in larger waves, even though rip current strengths were similar. Brander (1999b) found that at times in a rip current, currents alone were not always sufficient to suspend sediment. In data presented in this study, the requirement for wave stirring is well described with the mobility number. The form of mobility number identified by Gallagher (2003), which includes both the mean and oscillatory components of the flow, showed a good correlation with total suspended sediment transport in a rip current (R^2 = 0.67 to 0.77). This indicates the importance of waves as a mechanism for suspension, and currents as a key mechanism to transport sediment once suspended.

- Very low frequency (VLF) and infra-gravity (IG) motion present in the rip flow correlated well with suspension events. Figure 6.10 shows that the mean concentration increased from 0.8 kg/m^3, to during 5 to 40 kg/m^3 an offshore directed VLF pulse in the velocity. This has not been observed before in a rip current, however, Miles et al. (2002) showed that the offshore directed part of a VLF shear wave had a similar effect on suspended sediment concentration. When IG motion was present in the rip flow, mean concentrations were observed to increase from a mean concentration of 0.8 kg/m^3 to maximums of around 10 kg/m^3. Aagaard et al. (1997) also found that IG motion was efficient at suspending sediment in a rip current.

- Quantification of suspended sediment fluxes confirmed that during rip conditions, offshore directed mean transport is the dominant mode of transport in the rip current due to the strong mean flows. The mean component accounted for > 70% of the total suspended flux (<uc> + <u'c'>) on 19 of the 27 occurrences of rip currents.

- Suspended sediment transport at VLF was an important contributor to offshore suspended sediment transport in the rip current, but was less important than the mean component. VLF transport was offshore on 23 of the 27 occurrences of rip currents. It accounted for > 10% of the total suspended flux on 22 of the 27 occurrences of rip currents. VLF transport has never been measured in a rip current before, however, a modelling study by Orzech et al. (2011) suggested

that VLF motions in rip currents had the potential to have an effect of sediment transport dynamics.

- Suspended sediment transport at IG frequencies was generally small, accounting for < 10 % of the total suspended flux 24 of 27 occurrences of rip currents, similar to results presented by Aagaard et al. (1997). The transport associated with infra-gravity frequencies was directed offshore for 20 of the 27 occurrences of rip currents.
- Suspended sediment transport at incident wave frequencies was onshore directed on 22 of 27 occurrences of rip currents and accounted for > 10% of the total suspended flux for 21 of 27 occurrences of rip currents. Wave asymmetry and skewness correlated with onshore sediment transport. Onshore suspended sediment at incident wave frequencies was correlated with offshore directed VLF transport. Therefore, although incident wave and VLF contributions were of significant magnitudes, they were in opposing directions and had the net effect of cancelling one another out.
- The mean depth integrated transport (averaged over all occasions when the rip was active) was calculated as 0.03 kg/m/s and 0.08 kg/m/s in *STIR 1* and *STIR 2* respectively, both in an offshore direction. Maximum transport rates were of 0.76 kg/m/s and 0.6 kg/m/s in *STIR 1* and *STIR 2* respectively, both in an offshore direction. At higher tidal elevations, when the rip current was not active mean depth integrated flux was 0.005 kg/m/s in both *STIR 1* and *STIR 2,* in an offshore direction. Therefore on average, depth integrated suspended sediment transport was 6 to 16 times larger when the rip was active compared to when it was not active. Results presented here for depth integrated suspended transport are comparable to results collected in a rip current with a vertical array of sediment transport by Brander (1999b).

CHAPTER 7: INTERPRETATION AND SYNTHESIS

7.1: Introduction

In this chapter the data collected and discussed in the previous three results chapters are drawn together and discussed as a whole. The purpose of this is to address the research questions proposed in the introduction and assess evidence relating to the original hypotheses, which may be summarised as:

- **Rip currents transport a significant quantity of sediment in 'normal' conditions.**
- **Due to the strong mean flows the mean suspended flux is the dominant mode of suspended transport in a rip current.**
- **Offshore migrating bedforms make a significant contribution to total offshore transport of sediment in a rip current.**

Also, included in this chapter is a discussion on the applicability of this study and some suggestions for further work.

7.2: Summary of Results

7.2.1: Summary of rip current sediment transport results

Data presented in this study provides a comprehensive overview of sediment transport processes in a rip current and their relative importance. Depth integration of suspended sediment transport and the calculation of the transport associated with migrating bedforms allows quantification of total sediment transport rate in a rip current

Table 7.1 provides a summary of the direction and relative importance of suspended sediment transport in a rip current. The frequency of the direction of different modes of transport and their relative contribution is given relative to the number of rip current occurrences.

Offshore migrating bedforms made a small contribution to offshore sediment transport in a rip current, accounting for ~6% of the total suspended sediment transport (Q_s), indicating that while bedform transport does contribute to the offshore sediment transport in a rip current, suspended sediment transport is much more important.

The mean flux is the dominant mode of suspended sediment transport (Table 7.1) Considering the relatively small contribution from migrating bedforms, the mean component is also the most important mode of offshore transport in a rip current

generally. The mean flux accounts for > 70% of the total suspended sediment transport (<uc> + <u'c'>) on 19 of the 27 occurrences of rip currents.

An unexpected result from this study was the offshore transport of suspended sediment at VLF. VLF transport was offshore directed on 23 of the 27 occurrences of rip currents. Its importance as a mode of transport is demonstrated by the fact it accounted for > 10% of the total transport on 22 of the 27 occurrences of rip currents. Rates of VLF transport were approximately an order of magnitude smaller than that of the mean flux.

IG transport was the smallest of all modes of suspended sediment transport and varied in direction. It was offshore directed on 20 of the 27 occurrences of rip currents. The largest infra-gravity fluxes were associated with the largest waves.

The incident wave frequency flux compares closely to VLF flux in magnitude, however, the dominant direction of transport is onshore and therefore they often have the effect of balancing each other out, resulting in a small net oscillatory flux.

Table 7.1: Direction and relative contribution to sediment transport in a rip current from all modes of transport.

Mode of Transport	Direction of transport and frequency of dominant transport direction	Relative contribution to transport and associated frequency
<uc>	Offshore (27/27 of the occurrences of rip currents)	> 70% of total suspended sediment transport (when compared to <u'c'>) in 19/27 occurrences of rip currents
$\langle u'c' \rangle_{VLF}$	Offshore (23/27 of the occurrences of rip currents)	> 10 % of total suspended sediment transport (when compared to all modes of suspended transport) in 22/27 occurrences of rip currents
$\langle u'c' \rangle_{IG}$	Offshore (20/27 of the occurrences of rip currents)	< 10 % of total suspended sediment transport (when compared to all modes of suspended transport) in 24/27 occurrences of rip currents
$\langle u'c' \rangle_{G}$	Onshore (22/27 of the occurrences of rip currents)	> 10 % of total suspended sediment transport (when compared to all modes of suspended transport) in 21/27 occurrences of rip currents
Q_b	Offshore	~6% of suspended sediment flux (Q_s) when the rip current was active

7.2.2: A comparison of results collected in rip and non-rip conditions

In *STIR 1* and *STIR 2* the depth integrated flux was directed offshore at rates of 0.03 kg/m/s and 0.08 kg/m/s respectively. When the rip current was not active depth integrated flux was 0.005 kg/m/s (in *STIR 1* and *STIR 2*) in an offshore direction, therefore indicating that suspended sediment transport in a rip current is 6 to 16 greater than in non-rip conditions. Examining Figures 6.6, 6.7, 6.20 and 6.27 it can be seen that all modes of suspended transport in non-rip conditions are generally relatively small compared to transport rates in the rip current.

In non-rip conditions, bedforms were observed to migrate onshore at a similar rate to their offshore migration in rip conditions. Therefore the mean offshore bedform transport rate (0.0020 kg/m/s) in a rip current was similar to the mean onshore bedform transport (0.0015 kg/m/s) in non-rip conditions. Additionally, in non-rip conditions the bedform transport was a more important mode of transport than suspended load transport.

On a flat dissipative section of Perranporth Beach, in non-rip conditions, Miles and Thorpe (2015) showed that net sediment transport was often offshore, with the bulk of the transport occurring in suspension via the mean and infra-gravity components ($<uc> > <u'c'>_{IG}$) with onshore migrating bedforms contributing up to 15% of the total suspended sediment transport (Miles and Thorpe, 2015). The reason that the results of Miles and Thorpe (2015) show offshore transport more clearly may be due to the fact that measurements were made in shallower water, where wave stirring, undertow, infra-gravity transport were likely to be more significant than in the deeper water of a rip channel.

The results from non-rip conditions in this study and those of Miles and Thorpe (2015) from a planar section of the beach at Perranporth probably differ from the sediment dynamics on the bar of a bar-rip system. By definition a rip current is a mass balance response to wave induced onshore mass transport. Rips offer a mechanism for the seaward return of water (MacMahan et al., 2006) that has travelled over the bar. The onshore mass transport of water over the bar that leads to cell circulation (Aagaard and Vinther, 2008) can result in a mean onshore directed current over the bar crest (Aagaard et al., 1998; Kroon and De Boer, 2001; MacMahan et al., 2005). This onshore directed flow is generally vertically uniform (Haller et al., 2002; MacMahan et al., 2006), as opposed to elsewhere in the surfzone where a mean offshore directed component may be present only close to the bed (Masselink and Black, 1995) as undertow.

The variation in processes in the longshore direction spanning a bar-rip system has the potential to have a significant effect on the sediment dynamics. Bars between rip

channels generally migrate onshore (Wright and Short, 1984; Short, 1985; Aagaard et al., 1998), indicating that mean onshore directed flows over the bar drive onshore sediment transport.

Aagaard and Vinther (2008) found that when mass transport across the bar from wave dissipation exceeded a threshold, the feeder and rip no longer had the ability to drain the excess water, and undertow on the bar was initiated. Conversely, when wave dissipation was lower, cell circulation was initiated. This work highlights the importance of environmental conditions in sediment transport dynamics in a bar – rip system. It also demonstrates that the dynamics of a bar – rip system on a bar crest may differ from a section of beach that does not exhibit cell circulation.

7.3: Context of Results

To put the results collected in this study in context and to facilitate discussion of their applicability, further attention is paid to the wave climate and morphology of Perranporth. This is achieved by examining the offshore wave climate and the predicted beach morphology (using the Dimensionless Fall Velocity parameter) during each deployment, for one month prior to each deployment and the historical average for the time of year (using data from 2006 to 2014). This approach will allow conclusions to be drawn on the state of the beach in terms of wave energy and morphology and whether it is typical of Perranporth. Comparison of the three deployments will also aid discussion of the results in terms of their wider context and relevance.

7.3.1: Wave climate

Data from the DWR Wave Buoy, 1 km offshore of Perranporth was used for this investigation (Channel Coast Obsevatory, 2015). Perranporth is described as a high energy environment (Austin et al., 2014). The annual significant wave height and peak period at Perranporth is 1.6 m and 10.5 s respectively. The wave climate of the Cornish coast exhibits significant variability on a seasonal time scale. Scott et al. (2014) found wave height measured at the Seven Stones wave buoy (located approximately 18 miles off the west coast of Cornwall) varied from 2.4 m to 1.2 m between winter and summer in the period between 2003 to 2008. The 10% exceedance wave heights during winter and summer were 4.8 m and 2.2 m, respectively.

A time series of the significant wave height and peak period during, and for one month prior to the each deployment (two deployments during *STIR 1,* one in *STIR 2*) are displayed in Figure 7.1. A summary of the results is provided in Table 7.2. It can be

seen that there is a significant variability in the wave climate in the month preceding each deployment. In each one month period, Perranporth experiences at least one occasion where H_o > 4 m and multiple occasions where H_o < 1 m. The variability is also evident in the peak wave period, which ranged from 6 to 18 seconds.

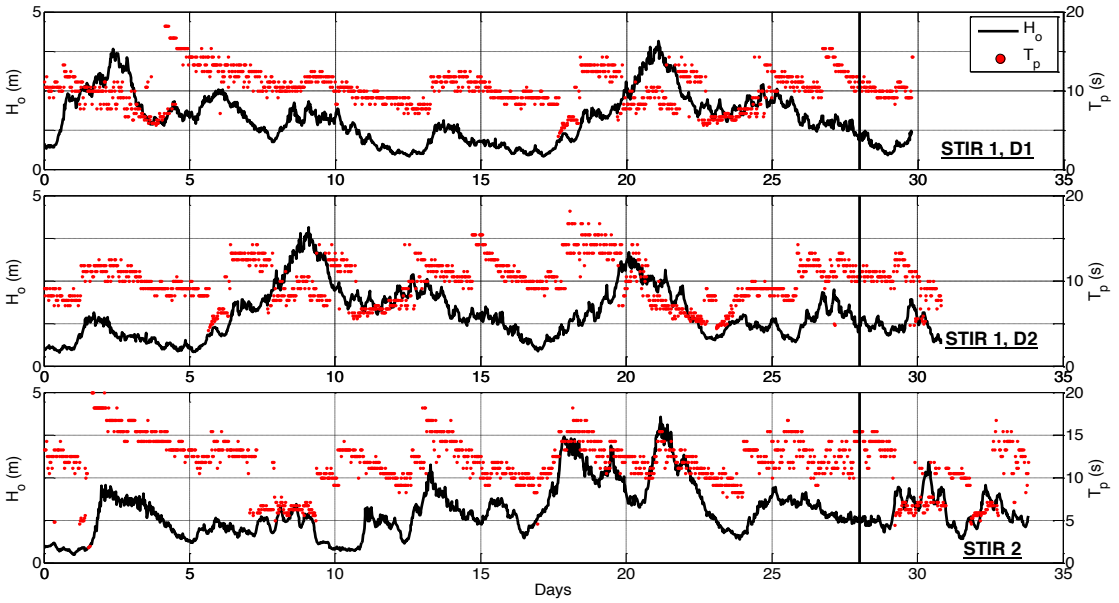

Figure 7.1: Wave height (H_o) and peak period (T_p) for the month preceding and during (a) *STIR 1*, deployment 1, (b) *STIR 1,* deployment 2 and (c) *STIR 2*. The beginning of each deployment is marked by the solid vertical line (Channel Coast Obsevatory, 2015).

Table 7.2: A comparison of offshore wave height (H_o) and peak period (T_p) during and prior to the experiment, and the historical average for the month of the deployment (Channel Coast Obsevatory, 2015).

Experiment	During		Month pre		Historical Month	
	H_o (m)	T_p (s)	H_o (m)	T_p (s)	H_o (m)	T_p (s)
Deployment 1 Oct 14-15	0.76	9.8	1.64	10.2	1.5	10.5
Deployment 2 Oct 26 to 28	1.26	10.3	1.56	10.0	1.5	10.5
Deployment 3 April 25 – 30	1.59	9.1	1.54	12.1	1.3	10.7

Although there is significant variability in the wave climate for the month preceding each deployment, mean H_o and T_p are similar (Table 7.2) to the historical monthly average (from data spanning the period 2006 to 2014) and to the wave conditions during each deployment. The exception is during the first deployment (Tides 1 and 2 in *STIR 1*) where wave height (H_o = 0.76 m) is approximately half of the average wave

height for the month preceding the experiment (H_o = 1.64 m) and the historical monthly average (H_o = 1.5 m). This suggests that during the first experiment the beach was in a particularly low energy phase. This is of interest as this period was identified as having low suspended sediment concentrations which resulted in low suspended sediment transport. However, during this period rip flow velocities were similar to occasions when suspended sediment concentration was much higher. This indicates that a certain amount of wave stirring is required to suspend sediment prior to it being transported.

During the second deployment (Tides 3 to 6 of *STIR 1*) the wave height and period (H_o = 1.26 m and T_p = 10.3 s) are similar to the average values from the preceding month (H_o = 1.56 m and T_p = 10.0 s) and the historical monthly average (H_o = 1.5 m and T_p = 10.5 s), suggesting the wave climate during this period of data collection could be classified as normal for Perranporth. During this period suspended sediment transport was greater than in the first deployment.

The final deployment (*STIR 2*) was characterised by a combination large waves and short period swell and smaller waves and long period swell. The mean wave height during the deployment (H_o = 1.59 m) was very similar to the preceding month (H_o = 1.54 m) and slightly larger than the historical average for this month (H_o = 1.3 m). The wave period for this deployment varied from 5 to 15 seconds and the mean (T_p = 9.1 s) was less than that of the preceding month (T_p = 12.1 s) and the historical monthly average (T_p = 10.7 s). However, examination of the spectral data collected by the wave buoy showed that for periods when the dominant peak period was of wind wave frequencies, a swell component was also always present. Figure 7.2 shows an example of the spectra of the wave energy collected over 30 minutes during *STIR 2*. During this period the peak period was 6.7 s and significant wave height of 1.8 m. An iterative routine was used to define sea and swell components as used by the Channel Coast Obsevatory (2015), and this indicated a spectral valley at 8 seconds. The wave spectra shows there is clearly defined peak at 11.1 s, accounting for 12.8% of the total energy and responsible for waves of 0.65 m. During *STIR 2,* the consistently large waves appear to lead to greater suspended sediment concentration than in the previous deployments, and therefore greater sediment transport.

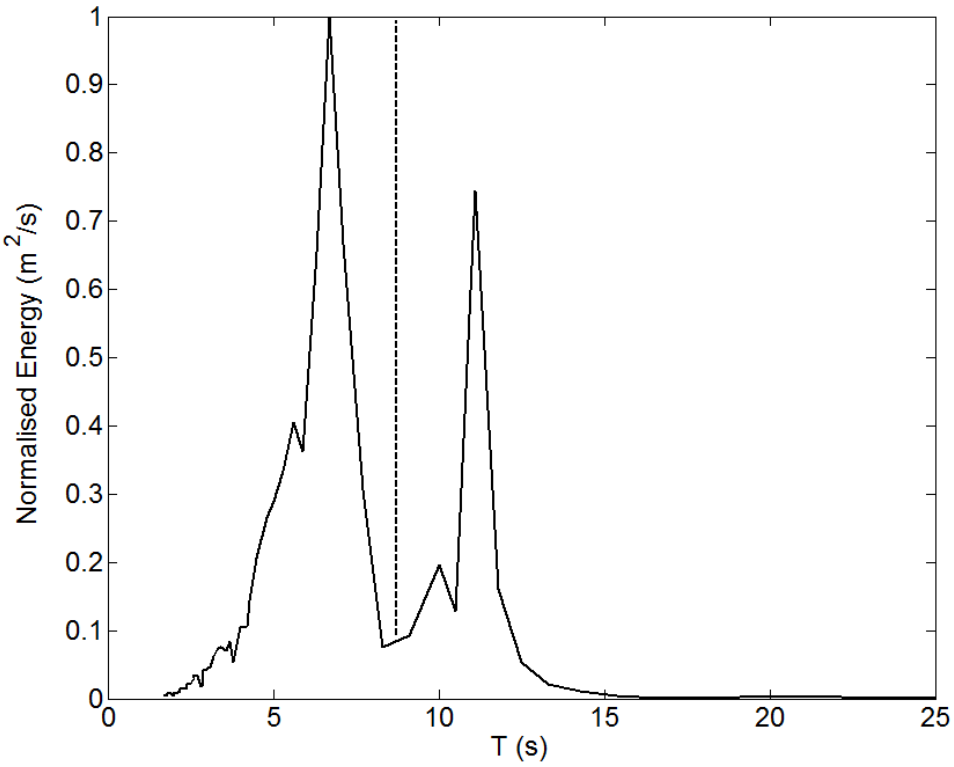

Figure 7.2: Offshore wave spectra during *STIR 2* (third deployment), demonstrating the presence of wind-sea (6.7 s) and swell component (11.1 s). The spectral valley of 8 seconds is marked by the dashed line.

7.3.2: Morphology

The morphology of Perranporth has been described as occupying the boundary between intermediate and dissipative beach classifications (Austin et al., 2010; Stokes et al., 2013). This is because it exhibits strong characteristics representative of both these beach states. It has a large flat featureless inter-tidal zone (Poate et al., 2009), typical of a dissipative beach and also highly variable and pronounced low tide bar rip system (Davidson et al., 2008; Poate et al., 2009; Stokes et al., 2013; Scott et al., 2014), and regularly exhibits transverse rips (Austin et al., 2010). Both these features are evident in spatial data presented in this study (Figure 4.1 to 4.4) and therefore suggest that the morphology during the study was typical of Perranporth, as a low tide bar-rip beach with a wide, flat inter-tidal zone.

To investigate the theoretical beach state of Perranporth during each deployment and to be able to assess whether the beach was in a stable, accretionary or erosional phase the dimensionless fall velocity (Ω) (Wright and Short, 1984) was calculated using wave data measured at the DWR wave buoy. Calculating Ω (Equation 2.4) based on the annual average wave height and period at Perranporth gives a value of 4.76, therefore classifying the beach as intermediate and of the sub category of rhythmic bar-beach or longshore bar – trough beach. The beach was classified using various

conceptual models in Chapter 4, Section 4.1, for the duration of each experiment using wave data measured *in-situ*. The beach was classified as transverse bar-rip following Dimensionless Fall Velocity of Wright and Short (1984), dissipative following the Surf Scaling Parameter of Guza and Bowen (1976) and low-tide bar rip by the Relative Tidal Range of Masselink and Short (1993) by these models. Data from the wave buoy is used in this analysis here so comment can be made on the conditions during the experiment relative to previous and historical conditions. It is important to consider that all these models are sensitive to changes in conditions and that they are more indicative of whether the beach is accreting or eroding than the physical state of the beach at that precise time.

Following a similar process to the analysis of the wave climate, a time series of Ω is displayed for the month prior to and during each deployment in Figure 7.3 with the Ω summarised in Table 7.3. The analysis of Ω is supplemented with regular ARGUS images in Figure 7.4. The images are captured once every week for the four weeks prior to the experiment and once during the experiment, with the time at which each image was captured marked on Figure 7.3. For the month preceding each deployment, Ω often describes the beach as intermediate (Ω = 2 - 5) when Ω values are averaged, though this is interspersed with periods when Ω indicates the beach is subject to dissipative conditions.

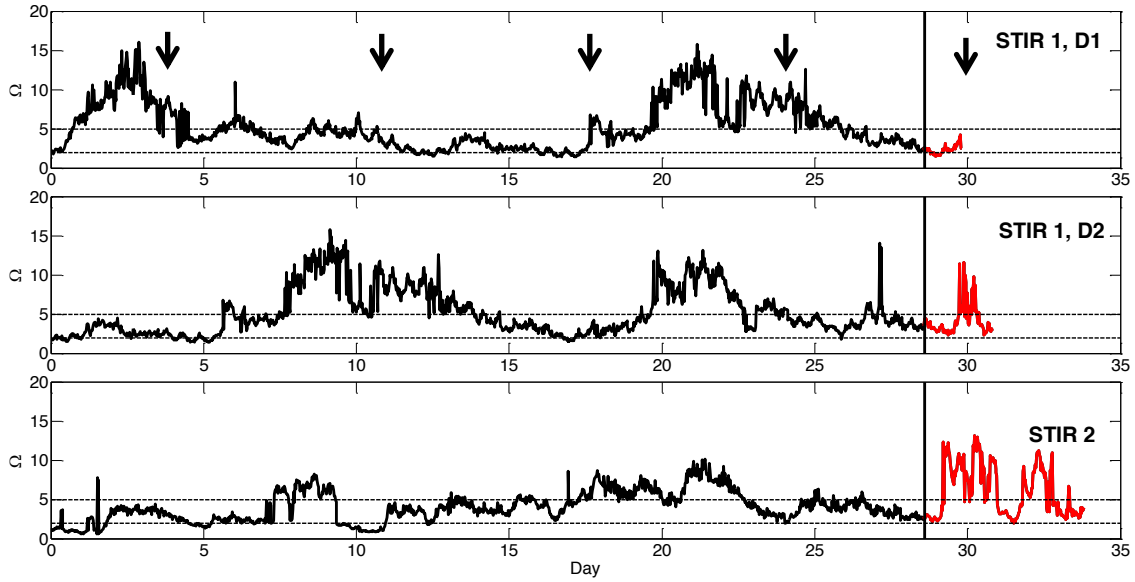

Figure 7.3: Dimensionless fall velocity (Ω) the month preceding and during each deployment. The beginning of each deployment is marked with a solid line. Horizontal dashed lines mark the intermediate classification, where Ω = 2 to 5. Conditions were dissipative when Ω > 5, and reflective when < 2. Ω was calculated from wave data collected at the DWR wave buoy, 1 km offshore of Perranporth. The vertical arrows mark the time at which further investigation of beach morphology is undertaken with use of ARGUS images.

Table 7.3: A comparison of dimensionless fall velocity (Ω) during and prior to the experiment and the historical average for the month of the deployment (from 2006 to 2014) calculated from wave data collected at the DWR wave buoy, 1 km offshore of Perranporth.

Deployment		During	Monthly Pre	Historical
STIR 1	Deployment 1 Oct 14-15, 2011	2.3	5.3	4.5
STIR 1	Deployment 2 Oct 26 to 28, 2011	4.1	5.2	4.5
STIR 2	Deployment 3 April 25 – 30, 2013	6.0	4	3.8

Throughout the first deployment, the beach is classified as intermediate, with a mean Ω value (Ω = 2.3) of around half the preceding month (Ω = 5.3) and historical monthly average values (Ω = 4.5). This supports the earlier suggestion, that based on the wave climate during the first deployment Perranporth was under low energy, and potentially accretionary, conditions. This is when conditions favour the development of the three dimensional morphology (Masselink and Hughes, 2003). This is further supported by examining the ARGUS images in the first column of Figure 7.4. In each image wave breaking patterns indicate developed three-dimensional morphology with cross-shore incised rip channels that appears similar in all 5 images. During this period suspended sediment transport was limited by a lack sediment suspension due to smaller waves. This is an important result, suggesting in low energy conditions; rip currents may have a reduced impact due to reduced sediment transport rates.

During the second deployment, Ω indicates an intermediate beach state (Ω = 4.1), though there is a spike in the time series where Ω > 10. The Ω during this deployment is less than that of the average for the preceding month (Ω = 5.2) and similar to the historical average for the month (Ω = 4.5). In Figure 7.4, wave breaking patterns indicate that the beach exhibited three-dimensional morphology and cross-shore orientated rip channels throughout the lead up to the experiment and were approximately similar between the lead up to the experiment and during the experiment. During the experiment significant offshore directed transport occurred.

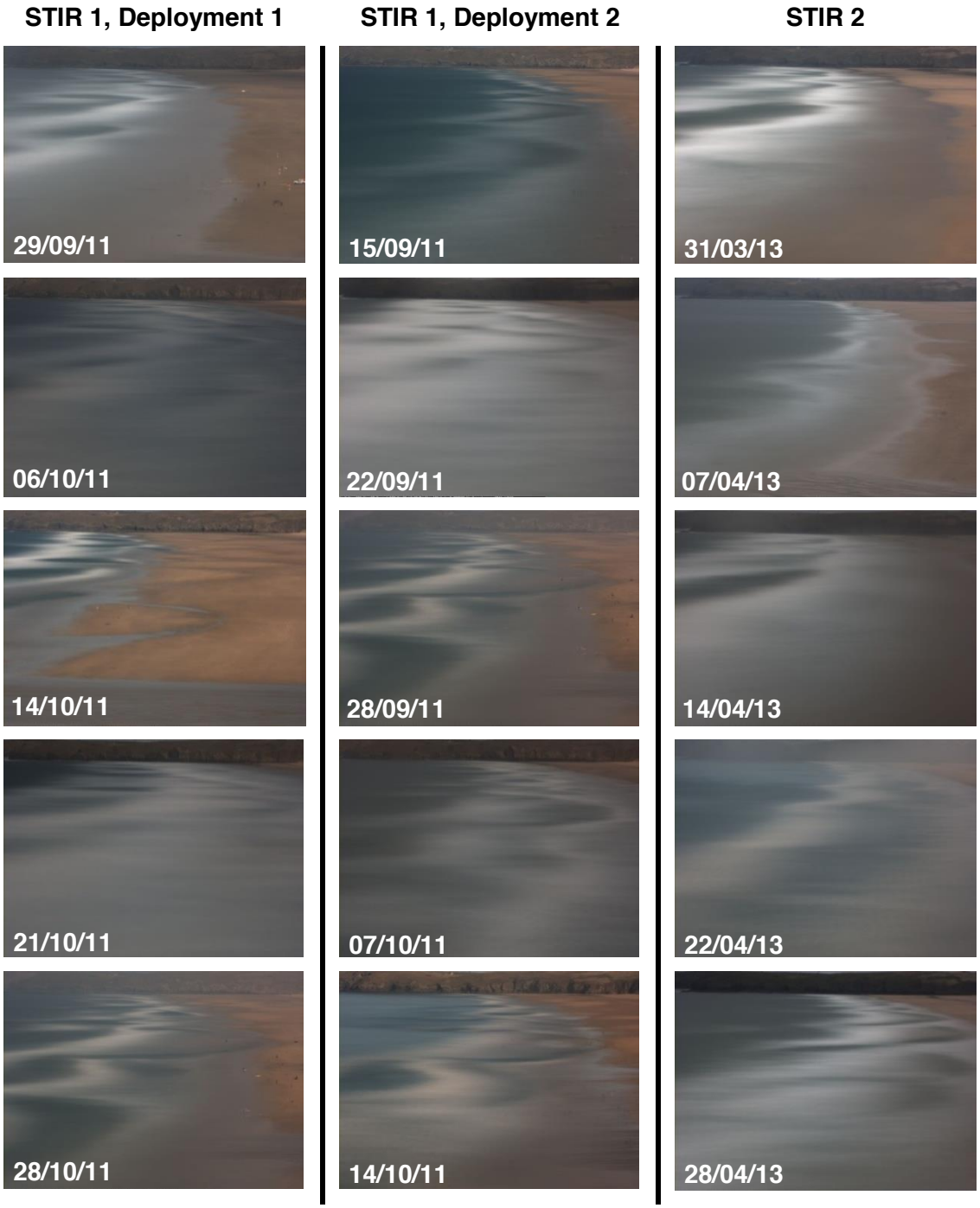

Figure 7.4: Four ARGUS images captured each week in the four weeks leading up to each deployment and one ARGUS image during each period of data collection. *STIR 1*, deployment 1 took place on the 14th and 15th October, 2011, *STIR 1*, deployment 2 took place between 26th and 28th October 2011 and *STIR 2* took place between 25th and 30th April, 2013. The time at which each image was captured is marked on Figure 7.3 with vertical arrows.

Figure 7.4 appears to show that the beach morphology changed significantly in the month leading up the experiment (*STIR 2*). The first set of images show that the beach appears to be exhibiting a longshore bar, though it meanders slightly. In the second image there is what appears to be a very small cross-shore orientated channel, and by the last image, the beach appears to exhibit large, pronounced low tide bar rip morphology with deep cross-shore orientated rip channels. Referring to Figure7.3, for

the month preceding the experiment the beach was regularly classified as being in an intermediate classification; it is possible that during this period the conditions existed for the development of a low tide bar – rip morphology. During the final deployment, there were several periods where Ω > 10**.** This is caused by the large wave heights combined with short period swell, leading to dissipative conditions. Figure 7.2 shows that the situation is more complex than this, because although the peak period was dominated by a wind sea component there was also a swell component. Table 7.4 summarises the wave conditions and Ω based on the peak period and significant wave height from the wind-sea and swell components of the wave spectra example presented in Figure 7.2. This makes a considerable difference to the predicted beach state, it is therefore reasonable to expect that the Ω predicted in the Figure 7.3 is at times over estimated and that the beach is in less of an erosional state than predicted. Offshore directed sediment transport was shown to be largest during this period, rip strength was slightly stronger in *STIR 2*, which may have increased suspension, though this could have been a result of increased wave height. The ratio of rip transport to bar transport may be similar to *STIR 1,* deployment 2 due to the potential for increased transport on the bar crest as a result of larger waves.

Table 7.4: Summary of sea conditions for the peak period and significant wave height from the wave spectra example (from *STIR* 2) displayed in Figure 7.3.

	% contribution	**H_o (m)**	**T_p (s)**	**Ω**
Peak period/ significant wave	-	1.8	6.7	8.4
Wind –sea component	77.2	1.69	6.7	7.8
Swell component	12.8	0.65	11.1	1.8

Visual observations made during both experiments, ARGUS images (Figure 4.4 and Figure 7.4) and morphological surveys indicated that the beach exhibited pronounced three-dimensional morphology and a large, well defined rip channel that was more evident in *STIR 2*. Figure 7.5 shows that in both October and April, Perranporth regularly exhibits well defined rip channels.

October 2010	October 2011	October 2012	October 2014
		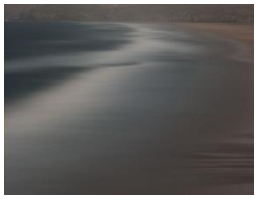	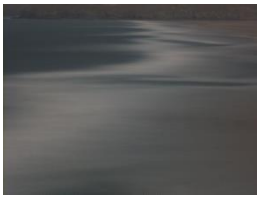
April 2011	April 2012	April 2013	April 2014
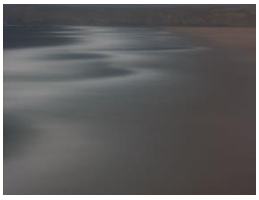			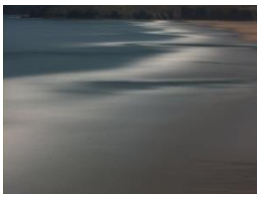

Figure 7.5: ARGUS images captured at low tide showing low tide morphology at Perranporth during *STIR 1* (October, 2011) and *STIR 2* (April 2013) and for three other years during the same months.

Perranporth is regarded as a representative example of a typical low tide bar-rip morphology that exists on the west facing coasts of Cornwall and Devon and also on high energy macro-tidal coasts in general (Scott et al., 2014). ARGUS images show that the low tide bar – rip morphology at Perranporth is typical of the beach.

It is reasonable to assume that the data collected at Perranporth is broadly representative of other sandy low tide bar – rip beaches when considering the key results from this study. Several process based observations lead to this conclusion:

- The dominance of the mean flux as the most important mode of suspended sediment transport is likely to apply to all rip currents, as the relatively strong mean flows are a defining feature of rip currents and provide a route for offshore sediment transport.

- The requirement for waves to suspend sediment prior to its offshore directed transport is likely to apply to all rip currents. Finer sediment and an increase in flow velocity could result in more sediment being suspended in lower wave heights. Velocities measured in this study are comparable to measurements made in many other studies (Bowman et al., 1989; Aagaard et al., 1997; Brander, 1999b; MacMahan et al., 2005; Austin et al., 2010; Austin et al., 2012; Austin et al., 2014). Also, Brander (1999b) observed a similar result, with waves being found to be important for sediment suspension.

- Suspended sediment transport at different time scales (infra-gravity and very low frequency) is a key result from this study. As infra-gravity (Aagaard et al.,

1997; MacMahan et al., 2004a) and very low frequency (MacMahan et al., 2004b; Reniers et al., 2007) oscillations have been observed in rip currents in other studies it is reasonable to assume they contribute to rip current sediment transport in other rip systems.

- Bedforms are widely acknowledged to exist in rip currents (Nielsen, 1992; Sherman et al., 1993; Thornton et al., 1998; Brander, 1999b) and they are likely to migrate in offshore mean flows and contribute to bedform transport when the flow velocity reaches a critical value.

The main difference that potentially exists between this study site and others is the macro-tidal range. This has the effect of switching the rip current on and off .relatively quickly. However, this is unlikely to affect sediment transport rates or processes in the rip current when it is running.

Data used in this study were collected in a varied wave climate that is typical of Perranporth. This included high energy conditions and relatively calmer periods. Using the dimensionless fall velocity to describe the expected beach state found that when averaged, conditions were generally indicative of an intermediate state beach, with short-term high energy conditions occurring sporadically that moved the beach toward a dissipative state.

During the first deployment data were collected in what can be considered typical of low energy summer conditions. During this period suspended sediment transport in the rip appeared to be limited by a lack of wave driven sediment suspension. Therefore it is reasonable to assume that in low energy conditions suspended sediment transport will be limited. The dependence on wave action to suspend sediment was also observed by Brander (1999b) and is well illustrated in data presented here by the correlation with a form of the mobility number that includes information on mean and oscillatory flows.

During the second and third deployments data were collected in higher energy conditions that, although variable, are felt to be representative of ‘normal’ conditions for the time of year and can be described as ‘moderate energy conditions’. During these periods suspended sediment transport was significant and is similar to other measurements of depth integrated suspended sediment transport made in the nearshore (e.g. Masselink et al., 2007; Aagaard et al., 2012) and in rip currents (Brander 1999b).

In large waves suspended sediment transport by rip currents is likely to eventually be restricted. Initially, an increase in wave height from that measured in this study may lead to an increase in transport with larger waves initiating more sediment suspension

and larger waves breaking on the adjacent bar driving stronger rip flows. However, when waves exceed a certain size, it is likely they will outsize the beach morphology. At this point larger waves will break further offshore and potentially through the rip channel. This may cause the rip flow to be limited and material to be retained within the surfzone (MacMahan et al., 2010). Therefore the ability of the rip current to drain excess water will be diminished and it is likely offshore sediment transport by undertow will become increasingly more important (Aagaard and Vinther, 2008). Also, although rip current transport rates may increase in larger waves, the relative importance of rip current transport within the bar-rip system may be diminished in larger waves. This is because the large surfzone width in comparison to the rip channel size could see transport on the bar become relatively more important. Also, if high energy conditions persist or the angle of wave incidence is large, the bar – rip morphology may be flattened and this would initially limit rip flow, and may ultimately stop it altogether. A return to lower energy conditions would be required for the formation of intermediate beach morphology.

7.4: Mode of Transport

In this section a comparison is made between the suspended load transport and the transport associated with migrating bedforms with the aim of assessing their individual importance. This is followed with an assessment of the importance of all components of transport ($\langle uc \rangle$, $\langle u'c' \rangle_{VLF}$, $\langle u'c' \rangle_{IG}$ $\langle u'c' \rangle_{G}$ *and* Q_b) based on a representative example.

7.4.1: Total suspended load and bedform transport

In Figure 7.5 the bedform transport rate (Q_b) is plotted alongside the depth integrated suspended sediment rate (Q_s), both with the units of kg/m/s. Comparison was possible using mostly *STIR 1* data due to a malfunction of the SRP during *STIR 2* (no bedform data was logged beyond the flood of the first tide). A summary of the mean and maximum values of bedform sediment transport rate (for periods when bedform data were collected) and depth integrated suspended sediment transport (during *STIR 1* and *STIR 2*) is provided in Table 7.5. It can be seen that the suspended sediment flux is much larger than the bedform transport rate throughout all periods when the rip current is active. For the period when simultaneous measurements of bedform transport rate and depth integrated transport were made, the mean bedform transport rate in rip current conditions (0.002 kg/m/s) was ~6% of the mean depth integrated transport (0.03 kg/m/s). The maximum bedform transport rate (0.054 kg/m/s) was also much less than the maximum depth integrated suspended sediment transport rate (0.76 kg/m/s). The largest bedform transport rates coincide with the largest suspended sediment

transport rates (run 155 and run 404). Generally depth integrated suspended sediment transport is larger in *STIR 2* than in *STIR 1,* where mean and maximum transport rate during rip current conditions were 0.08 kg/m/s and 0.78 kg/m/s respectively.

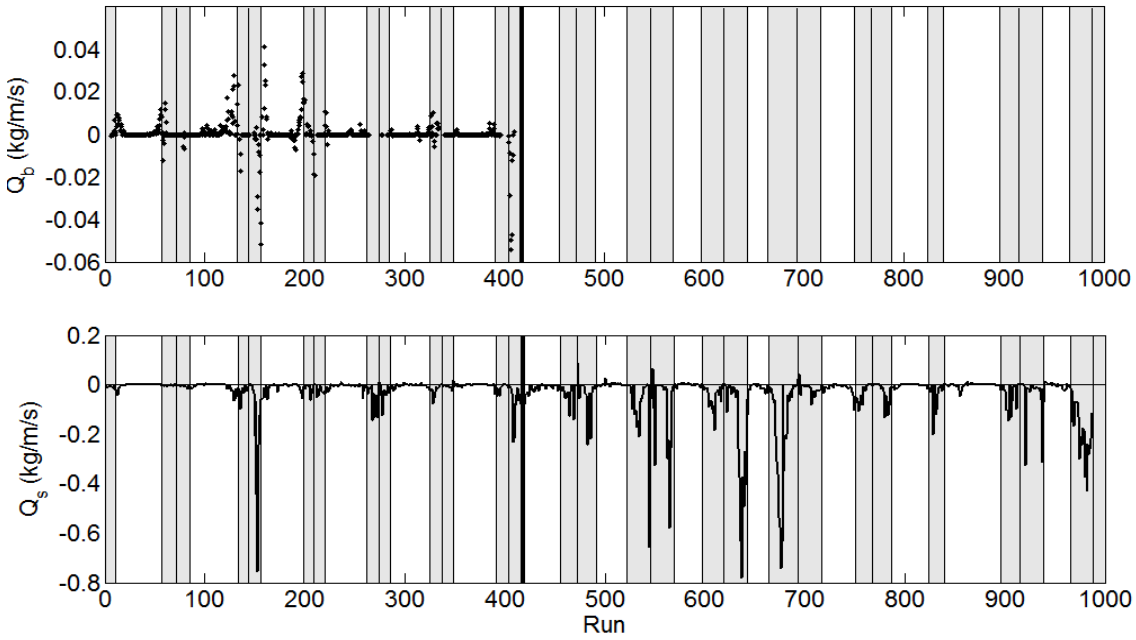

Figure 7.6: Bedform transport rate (Q_b) for periods when bed scans were collected (indicated by the solid thick line) and depth integrated suspended sediment transport rate (Q_s) for the entire study period. *STIR 2* commences at run 400. The shaded areas mark periods when the rip current was deemed to be active, the centre line in the shaded area represents the boundary between tides.

Table 7.5: Mean and maximum Q_b and Q_s during all periods the rip current was active and when bed data were. Mean and maximum Q_s also displayed for periods when bedform data were not collected.

Bedform (kg/m/s)		**Suspended (kg/m/s)**	
Mean	-0.002	**Mean**	When simultaneous bedform data collected = -0.03
			When no bedform data = -0.08
Max	-0.054	**Max**	When simultaneous bedform data collected = -0.76
			When no bedform data = -0.78

It is clear that the suspended load is by the far the dominant mode of sediment transport in a rip current, with bedform transport accounting for approximately 6% of suspended sediment transport in a rip current. It was originally hypothesised by Komar (1976) that the bedload was more important than suspended load sediment transport. However, later studies found that suspended sediment transport dominates in the entire surf and swash zone (Hanes, 1988; Thornton and Abdelrahman, 1991), thus agreeing with results presented here. Aagaard et al. (2013) found on a steep beach that suspended sediment flux was approximately an order of magnitude larger than bedform transport and often occurred in opposing directions in a range of conditions.

Similarly Miles and Thorpe (2015) found the suspended flux to be the dominant mode of transport, with transport associated with migrating bedforms accounting for around 15% of the total load.

Although the contribution of migrating bedforms to sediment transport is small, their presence is likely to play a significant role in the dynamics of suspended sediment transport. Bedforms will increase the bed roughness and lead to enhanced vorticity, therefore sediment will be mixed higher up in the water column (Osborne and Vincent, 1996).

7.4.2: All modes of suspended sediment transport and bedload

The contribution from all modes of transport ($\langle uc \rangle$, $\langle u'c' \rangle_{VLF}$, $\langle u'c' \rangle_{IG}$ $\langle u'c' \rangle_{G}$ and Q_b) is examined by using data from when the rip was active during the flood of Tide 3, *STIR 1* (run 144 to 156 in Figure 7.5). This section of data was chosen as it exhibited a strong mean rip flow, clear VLF oscillations, and moderate wave height and period. The hydrodynamics for this example are displayed in Table 7.6. Comparable sediment transport rates for different processes were achieved by partitioning the depth integrated transport based on the percentage contribution measured at z = 0.25 m. This relies on the assumption that the mean and oscillatory components are in phase through the water column.

Table 7.6: Hydrodynamics of rip conditions on the flood tide of Tide 3, *STIR 1*

	H_o (m)	$H_{o\ max}$ (m)	T_p (s)	U (m/s)	U_{max} (m/s)	U_m (m/s)	$U_{m\ max}$ (m/s)
Example	1.2	1.5	10.6	0.38	0.63	0.8	1.1

Table 7.7 shows the suspended flux is the dominant mode of transport (94%) compared to the bedform transport. The mean component of the suspended flux is dominant (82%) over the oscillatory flux. The oscillatory flux is often offshore in rip conditions though it makes up only a small percentage of the net offshore transport.

Table 7.7: Percentage contribution to (net) total sediment transport from mean transport, oscillatory transport and bedform transport for rip current data from the flood of Tide 3, *STIR 1*.

	UC	uc	Qb
Example	82%	12%	6%
	94%		

Table 7.8 compares all modes of transport and their contribution to total gross transport (and therefore does not account for directionality, however, occasions where transport

is onshore/offshore is indicated by a '+/-' symbol). It can be see that the mean flux is still the most important mode of transport. VLF oscillations can account for over a quarter of all total gross sediment transport (26%). Bedform transport accounts for up to 4 % of the total gross transport in the example presented. The contribution from infra-gravity transport is generally small. Gravity frequency transport is often an important mode of transport, operating in the opposite direction to the VLF transport, and therefore resulting in a low net oscillatory flux.

Table 7.8: Percentage contribution to (gross) total sediment transport from mean transport, VLF, IG, G frequency transport and bedform transport for an example of rip current data from Tide 3, *STIR 1*. '+' / '-' indicates onshore / offshore directed transport

	UC	Q_b	VLF	IG	G
Example	(-) 52 %	(-) 4 %	(-) 26 %	(-) 1 %	(+) 17 %

7.5 Overall Relevance of Results

At low tide, in a rip current sediment is transported offshore as suspended load and by migrating bedforms. It is likely that in low energy and normal conditions that sediment is simultaneously transported onshore due to an onshore mean flow as a result of mass transport across the bar (Aagaard et al., 1998; Kroon and De Boer, 2001; MacMahan et al., 2005). In this section, an attempt is made to answer the research question of 'how important are rip currents for offshore sediment transport and beach erosion?' by calculating typical mass transport rates on the bar and in the rip channel.

In Table 5.4, the bedform transport rate is presented from this study and other studies. These values are either quoted directly from the literature or are calculated following measurements of bedform geometry presented in the literature. The magnitudes of transport associated with migrating bedforms found in the literature are similar to the measurements made in this study (where literature values range from 0.008 to 0.07 kg/m/s compared to a mean of 0.0020 kg/m/s and a maximum 0.054 kg/m/s in this study). In strong mean flows migration is in the direction of the flow (Sherman et al., 1993; Hoekstra et al., 2004), though in the surfzone and shoaling zone migration is often onshore directed (Gallagher et al., 1998a; Aagaard et al., 2000) due to wave skewness (Crawford and Hay, 2003; Gallagher, 2003) or orbital velocity (Ngusaru and Hay, 2004).

In Table 6.13 depth integrated suspended sediment transports rates identified in the literature are summarised for a range of environments, including rip currents, the swash zone, the inner surf zone and the shoaling zone. Typically in lower energy conditions transport is onshore at rates that are comparable to transport rates

measured in this study (Table 7.4). In higher energy conditions, the results in the literature, including data collected at Perranporth (Miles and Thorpe, 2015), indicate net transport is offshore directed within the surfzone.

To compare transport rates on the bar and in the rip that can be considered typical of Perranporth during low tide when the beach is exhibiting low tide bar-rip morphology a mass transport rate was calculated. To do this the sediment transport rates (kg/m/s) measured in this study and those recorded in the literature are multiplied by the mean longshore width of the rip channel, (for sediment transport measurements made in the rip current), and the mean longshore width of the adjacent bar (for sediment transport measurements that may occur on the bar). This gives a mass transport rate of transport occurring on the bar and in the rip current, and is termed the longshore integrated cross-shore sediment transport rate (kg/s). Using 6 years' worth of ARGUS video images Scott et al. (2014) found mean bar spacing was 363.5 m and mean rip width was 27.5 m. These values are used as they are representative of the long term morphology of Perranporth. The longshore integrated cross-shore sediment transport rates are summarised in Table 7.8.

Table 7.8: A comparison of longshore integrated cross-shore sediment transport rates (kg/s) calculated from measurements made in this study and measurements reported in the literature. Column 1 gives values averaged over when the rip current was active. Column 2 indicates values for the adjacent bar. The longshore rip channel width was assumed to be 27.5 m, and the longshore bar width was assumed to be 363.5 m. The transport per unit beach length (kg/m/s) is also displayed in brackets.

Rip Channel Transport (kg/s)		Bar Transport (from surfzone data) (kg/s)		
			ONSHORE	**OFFSHORE**
		Swash		
		Miles et al. (2006)	25.5 (0.07)	
Suspended		**Suspended**		
This study	*STIR 1 =*- 0.8 (-0.03) *STIR 2 =* -2.2 (-0.08) Max. = -13.7	Aagaard et al. (2006)	29 (0.08)	-
		Grasijmer and Van Rijn (2001)	36.4 (0.1)	-
Brander, 1999	-1.38 (-0.05) Max. = -4.7 (-0.17)	Beach & Sternberg (1992)	10.9 (0.03)	-
		Tinker et al. (2009)	9.1 (0.025)	-10.9 (-0.03)
		Miles & Thorpe (2015)	-	-58.2 (-0.16)
Bedform Transport		**Bedform Transport**		
This study	-0.08 (-0.002); Max. = -1.4 (-0.054)	Gallagher et al. (1998)	10.9 (0.03)	
Sherman et al. (1993)	-1.9 (-0.07)	Aagaard et al. (2000)	25.4 (0.07)	
		Ngusaru and Nay (2004)	2.9 (0.004)	

The integrated longshore cross-shore sediment transport rates displayed in Table 7.8 can be considered indicative of a bar – rip system, though it is important to note that these measurements were not necessarily made on the made on the bar of a bar – rip system. The results of Miles and Thorpe (2015) and Tinker et al. (2009) show offshore directed transport, these measurements were made in the surf zone and in higher energy conditions. Onshore directed longshore integrated cross-shore transport over the bar is generally larger than that of the offshore transport measured in the rip current. This is likely, at least in part, to be because the bar width is 13 times longer than the

width of the rip channel. Maximum possible total offshore directed transport in the rip current was 15.1 kg/s based on the figures in Table 7.8, whereas maximum total transport due to onshore processes may be up to 80 kg/s (using maximum values of suspended transport + bedform transport + swash zone transport rates). Although sediment transport associated with rip currents were smaller than the potential transport from transport over the bar, at 19% of transport on the bar, it can be still be considered a significant exporter of sediment, even though the beach may be in an overall accretionary phase.

7.6 Limits of Applicability

This study focuses on temporal changes, processes and relative sediment fluxes in rip currents using techniques that are well established in the literature. This section reviews and assesses sources of error, the level of certainty about the relative importance of the processes observed and the limits of applicability of the whole experiment. Aspects to do with the method and the instrumentation are considered separately in Sections 7.6.1 and 7.6.2.

7.6.1: Method

Although the relative position of the instrument changes with tidal elevation data presented shows that the frame was deployed in the centre of rip channel during both *STIR 1* and *STIR 2* (Figures 4.5 to 4.7) and drifter measurements showed at this location that the flow was directed offshore (Figure 4.8).

In *STIR 1* suspended sediment flux was calculated from an ADV (z = 0.45 m) and OBS (z = 0.25 m) that were separated in the vertical plane. Ogston and Sternberg (1995) identified problems associated with calculating sediment flux with vertically separated velocity measurements. In *STIR* 2 a second ADV was deployed at z = 0.25 m allowing a comparison to be made between velocity measurements at z = 0.25 m and z = 0.45 m. It was shown in Figure 4.17 that the velocity measured at these two heights is very close to vertically uniform (R^2 = 0.95). This gives confidence in the results presented here regarding the concerns of.

Point measurements of suspended sediment concentration and velocity were used to calculate depth integrated suspended sediment fluxes. The method used is recommended by Van Rijn (1993) and is a pragmatic solution based on the instrumentation available (Miles and Thorpe, 2015). This is a conservative estimate of depth integrated transport, as concentration at the bed is assumed to be that of the lowest sensor (z = 0.25 m) and velocity is reduced to zero at the bed.

There are uncertainties associated with methods used to estimate the spectra in the data. These uncertainties principally affect whether a peak in the spectra is positioned at exactly the correct frequency. This mostly affects the low frequency peaks. A longer time series would allow increased confidence in the spectra. Observations from spectra show similar frequency oscillations to those evident in the time series (Sections 4.6 and 6.4). This provides confidence in the techniques used.

7.6.2: Instrumentation

The SRP was positioned at z = 0.8 m (*STIR 1*) and 0.7 m (*STIR 2*) giving an approximate scanning foot print of 2.4 and 3.1 m per scanner respectively. The length scale of the bedforms measured was often of a similar size to the footprint of the scanner; therefore in some cases a complete bedform wavelength was not captured in the scans. Bedform scans were examined rigorously to check that the minimum requirement of at least half a bedform was present in each scan. Raising the elevation of the SRP scanner was not an option as it would be submerged for a shorter time period and therefore reduces the amount of bedform data collected from a rip current. The height was chosen as a balance between scan footprint size and the scanner being sufficiently submerged for the longest possible duration. In *STIR 2* a second SRP was deployed, and was orientated so that both were aligned in the same cross-shore axis. This worked well giving a footprint of 4.4 m. Unfortunately, an equipment malfunction meant that only 90 minutes of data were collected.

The horizontal resolution of the SRP was sufficient for the measurement of bedforms of the length scales measured in this study. The horizontal resolution was 1.4 and 1.1 cm directly below the scanner and 7.4 and 3 cm at the far edges of the scan when deployed in *STIR 1* and *STIR 2* respectively.

The errors associated with the velocity measurements made with the ADV are small relative to the measurements made in this study. Experimentally the maximum has been found to be up to 5% for velocities > 0.02 m/s (Snyder and Castro, 1999). The accuracy of the ADV is +/- 0.5% of the measured value or 1 mm/s, whichever is larger (Nortek, 2010). Long-term errors depends on internal signal processing, especially filters the beam geometry and are typically a fraction of 1 cm/s (Nortek, 2010).

The errors associated with the concentrations measurements made with OBSs are small relative to the concentrations measurements made in this study. The accuracy of the OBSs is 4% or 10 mg/L (whichever is larger) in sand concentrations ranging from 50 to 100 g/L (Cambell Scientific, 2013). This values are approximately similar to the highest measured in the nearshore, found in the swash zone (Miles et al., 2006). Additionally, OBSs perform well in the surfzone (Downing, 2006), compared to acoustic

backscatter sensors that have problems associated with the scattering of sound by bubbles (Webb and Vincent, 1999).

7.7: Suggestions for Further Work

Throughout this study many potentially important aspects of sediment transport in rip currents have been identified. Some would benefit from being studied in greater detail. The following list identifies areas suggested for further study, with possible routes for taking the project forward.

- An attempt has been made to put the measurements in a morphological context, however to achieve this aim it would be necessary to make similar measurements as in this study, but to supplement them with regular measurements of morphology across the entire bar – rip system. In addition to this, making simultaneous sediment flux measurements on the bar would provide a full context of transport in a bar-rip system.
- Many of the measurements and processes identified in this experiment are new. The next logical step would be to use them in a model such as Xbeach or Delft 3D to predict shoreline change and beach morphology. It is indicated here that the rip current is potentially an important transporter of sediment and is therefore likely to play a significant role in beach morphodynamics. It would be useful to test the models capability to replicate this.
- An interesting and unexpected find during this study was the presence of rip current pulsing on VLF time scales and its importance for sediment transport. This was observed in all three deployments though due to the experimental design it was not possible to identify mechanism responsible for rip pulsing. To investigate this further an array of PTs and/or velocity sensors deployed throughout the rip system, and offshore of the rip neck, would be needed to identify the mechanism responsible for the observed rip pulsing.
- Initial results of grain size show that fine grains were stripped from the rip channel. Brander (1999) found that finer grains where transported higher in the water column, whilst Cook (1970) suggested that rip channels should be preserved in the geological record as coarse bands of sediment. It would be useful to investigate the role of the rip current in transporting different size fractions.

- Data were collected in wave heights ranging from 0.5 to 3 m, it would be of interest to extend this to include both larger and smaller waves and assess the effect this has on sediment transport.
- Data were collected on a stretch of open coast that exhibited rhythmic low tide bar-rip morphology. However, rip currents are known to exist as topographically constrained features that develop alongside headlands and man-made structures. They also occur in high energy conditions in small embayments as mega-rips where they can drain the whole bay (Short, 1985). It would be of interest to extend the study to assess the impacts of rips on sediment transport and morphology change in different rip scenarios.

CHAPTER 8: CONCLUSIONS

From a comprehensive review of the literature it was apparent that whilst the potential for rip currents to transport sediment is acknowledged, little is known about the processes responsible and their relative contribution. Only several studies have been published specifically on sediment transport in rip currents (Cook, 1970; Aagaard et al., 1997; Brander, 1999b). The following gaps in literature were identified:

- Limited work has been carried out on examining sediment transport in rip currents
- Much of the work in general on rip currents has been done in micro/meso tidal environments and in low energy conditions.
- The processes and mechanisms responsible for sediment transport in rip currents and their relative importance are not well understood.
- Whilst bedforms are known to exist in rip channels, they have only ever been fully quantified in a feeder channel and not in the rip neck.
- Whilst rip currents have been recognised as a potentially important mode of transport, they have not been placed in context of other transport processes that may occur in the nearshore.

Data were collected from a rip channel at Perranporth in SW England, a high energy, macro-tidal beach that is known to exhibit low tide bar – rip morphology. It is considered representative of similar beaches in SW England and globally (Scott et al., 2014). Simultaneous measurements were made of water depth, waves, velocities, bedform profiles and suspended sediment concentrations over three deployments spanning two field campaigns. This accounted for 14 tidal cycles, which included 27 occurrences of rip currents. *In-situ* measurements were supplemented with ARGUS images and spatial data from morphological and bathymetric surveys.

The conclusions of this study are;

- Spatial data indicated that for the entirety of the experiment, the beach exhibited a large flat inter-tidal zone and pronounced low tide bar – rip morphology with well-defined rip channels that were slightly skewed to the south (the direction of the ebb tide). The beach morphology was classified as Transverse Bar-Rip, Low Tide Bar-Rip and Dissipative using the Dimensionless Fall Velocity (Wright and Short, 1984), Relative Tidal Range (Masselink and Short, 1993) and Surf Scaling Parameter (Guza and Bowen, 1976) conceptual models. The classification of low tide bar – rip is most applicable as the Relative

Tidal Range model of Masselink and Short (1993) accounts for the macro-tidal range.

- Offshore significant wave height and peak period during the data collection period ranged from 0.5 to 3 m and 6.5 to 15 s respectively. Analysis of the wave climate prior to the deployment, and of historical data for Perranporth showed that conditions could generally be considered to be 'normal' for Perranporth, and representative of a high energy, macro-tidal beach. The exception was that during the first deployment where conditions were much lower energy (H_o = 0.76 m) than the average for the preceding month (H_o = 1.64 m) or the historical average for that month (H_o = 1.5 m) and therefore the beach was considered to be in a low energy and potentially accretionary phase for that deployment.

- Rip current hydrodynamics, bedform dynamics and suspended sediment transport were all modulated by the tidal elevation. At lower tidal elevations, the low tide bar – rip morphology provided the longshore variation in wave breaking that forced the rip current. In turn, the presence of rip flow had a sigifnifcant impact on suspended sediment and bedform dynamics.

- 10-minute mean cross-shore flows were between 0.14 and 0.74 m/s. The largest instantaneous velocities of ~ 2 m/s occurred in *STIR 2* when waves were breaking on the adjacent bar. 10-minute mean longshore velocities were between -0.1 to 0.5 m/s (where negative is towards the North) at lower tidal elevations. The maximum 10-minute mean resolved velocity was 0.8 m/s. Rip currents were identified as being active by comparing measured flows with a model designed to predict undertow velocity (Masselink and Black, 1995).

- Wave breaking on the bar was identified as an important process for driving rip current flow, as also observed by MacMahan et al. (2005) and Austin et al. (2010). Rip flow also persisted once the adjacent bar had dried out due to morphological constriction.

- The observed beforms are best decribed as megaripples. When the rip current was active, mean bedform length was 1.45 m with a maximum of 3.11 m and mean bedform height was 0.06 m, with a maximum of 0.19 m. Bedforms appeared to be larger when the rip current was active compared to when the rip was not active (where mean dimensions were: λ = 1.09 m, Δ 0.06).

- Bedforms were found to migrate in an offshore direction at a mean rate of 0.16 cm/min (max = 4.6 cm/min) in a rip current and appeared to be forced by the mean flow of the rip. In non-rip conditions mean and maximum migration rates

were 0.09 cm/min and 2.2 cm/min respectively. This correlated well with incident wave skewness, as also observed by Crawford and Hay (2003); Gallagher (2003) and to a lesser extent, orbital velocity as observed by Ngusaru and Hay (2004). However, during non-rip condtions, the bedforms exhibited two migration behavours; they migrated onshore when h = ~ 2.5 to 5 m and when h = > 5 m the bedforms generally did not migrate.

- Sediment transport rates associated with migrating bedforms (termed bedform sediment transport) occurred in an offshore direction at a mean rate of 0.0020 kg/m/s (max = 0.054 kg/m/s) when the rip current was active. When rip flow ceased, bedform transport occurred in an onshore direction at mean rates of 0.0015 kg/m/s (max = 0.041 kg/m/s). When considered over a whole tidal cycle, net offshore bedform transport in the rip current was small, due to the onshore migration of bedforms when the rip was inactive.

- The presence of waves can be a limiting factor in suspended sediment transport because waves are required to suspend sediment prior it to being transported in the rip current. In smaller waves suspended sediment transport was less than in larger waves, even though rip current strength was generally similar. The importance of waves to suspend sediment is demonstarted by the correlation of total suspended sediment transport with the mobility number, where R^2 = 0.67 – 0.77.

- The net suspended sediment transport was always offshore directed when the rip current was active.

- The mean suspended sediment flux was found to be the dominant mode of suspended sediment transport. The mean component of suspended sediment was always offshore directed and accounted for > 70% of the total flux (<uc> + <u'c'>) on 19 of the 27 occurrences of rip currents in this study.

- Very low frequency offshore pulses were observed in the rip flow. These correlated with mean flows and were greatest when wave breaking occurred on the adjacent bar, suggesting that their presence is linked to the exsistence of the rip current. Offshore directed VLF pulses correlated with increases in sediment suspension. They were also found to be an important mode of offshore suspended sediment transport, that was secondary only to the mean component. Transport at VLF was offshore directed on 23 of the 27 occurrences of rip currents and accounted for > 10% of the total flux (when

considering all modes of suspended sediment transport) on 22 of the 27 occurrences of rip currents.

- Suspended sediment transport at incident wave frequencies was usually onshore when the rip current was active (on 22 of the 27 occurrences of rip currents) and accounted for > 10% of the total suspended flux on 21 of the 27 occurrences of rip currents. Onshore suspended sediment transported at incident wave frequencies correlated with offshore directed VLF transport. Therefore, although they were both of significant magnitudes, they were in opposing directions and had the net effect of cancelling one another out.

- Mean depth integrated suspended sediment flux averaged over all periods when the rip current was active was 0.03 kg/m/s in *STIR 1* and 0.08 kg/m/s in *STIR 2,* with maximum rates of > 0.7 kg/m/s. These fluxes were comparable to other depth intergrated suspended sediment rates that occurred within the swash zone (Miles et al., 2006), inner surfzone (Aagaard et al., 2012) and shoaling zone (Tinker et al., 2009). In non-rip conditions the mean depth integrated suspended sediment flux was 0.005 kg/m/s in both *STIR 1* and *STIR 2*. Therefore on average, depth integrated suspended sediment transport was 6 to 16 times larger when the rip was active compared to when it was not active.

- In an active rip current the mean offshore bedform transport accounted for ~6% of the mean total suspended sediment transport.

The above conclusions specifically address all of the original objectives of the study, as laid out in Section 1.3 With respect to the broad research questions (Section 1.3); rip currents have been shown to be an important component contributing to sediment transport in the nearshore system with the mean flux being the most significant mode of transport. Data presented here has advanced the understanding of sediment transport processes in rip currents and their relative importance within the nearshore zone.

References

Aagaard, T., Black, K.P., Greenwood, B., 2002. Cross-shore suspended sediment transport in the surf zone: a field-based parameterization. Marine Geology, 185, 283-302

Aagaard, T., Greenwood, B., 1994. Suspended sediment transport and the role of infragravity waves in a barred surf zone. Marine Geology, 118, 23-48

Aagaard, T., Greenwood, B., 1995a. Longshore and cross-shore suspended sediment transport at far infragravity frequencies in a barred environment. Continental Shelf Research, 15, 1235-1249. 10.1016/0278-4343(94)00072-u

Aagaard, T., Greenwood, B., 1995b. Suspended sediment transport and morphological response on a dissipative beach. Continental Shelf Research, 15, 1061-1086

Aagaard, T., Greenwood, B., Larsen, S.M., 2013. Total cross-shore sediment transport under shoaling waves on a steep beach. Coastal Dynamics, Bordeaux, France, 39-50

Aagaard, T., Greenwood, B., Nielsen, J., 1997. Mean currents and sediment transport in a rip channel. Marine Geology, 140, 25-45

Aagaard, T., Greenwood, B., Nielsen, J., 2000. Bedlevel changes and megaripple migration on a barred beach. Journal of Coastal Research SI, New Zealand, 110-116

Aagaard, T., Hughes, M., Baldock, T., Greenwood, B., Kroon, A., Power, H., 2012. Sediment transport processes and morphodynamics on a reflective beach under storm and non-storm conditions. Marine Geology, 326, 154-165

Aagaard, T., Hughes, M., Møller-Sørensen, R., Andersen, S., 2006. Hydrodynamics and sediment fluxes across an onshore migrating intertidal bar. Journal of Coastal Research, 22, 247-259

Aagaard, T., Hughes, M.G., 2010. Breaker turbulence and sediment suspension in the surf zone. Marine Geology, 271, 250-259

Aagaard, T., Nielsen, J., Greenwood, B., 1998. Suspended sediment transport and nearshore bar formation on a shallow intermediate-state beach. Marine Geology, 148, 203-225

Aagaard, T., Vinther, N., 2008. Cross-shore currents in the surf zone: Rips or undertow? Journal of Coastal Research, 24, 561-570

Allen, J.R.L., 1968. Current Ripples: Their relation to patterns of water and sediment motion. North-Holland Publishing Co., Amsterdam. 433

Allen, J.R.L., 1985. Principles of Physical Sedimentology. George Allen & Unwin Ltd, London. 272

Anthony, E.J., 1998. Sediment-wave parametric characterization of beaches. Journal of Coastal Research, 14, 347-352

Austin, M., Masselink, G., O'Hare, T., Russell, P., 2007. Relaxation time effects of wave ripples on tidal beaches. Geophysical Research Letters, 34, 1-5

Austin, M., Masselink, G., O'Hare, T., Russell, P., 2009. Onshore sediment transport on a sandy beach under varied wave conditions: Flow velocity skewness, wave asymmetry or bed ventilation? Marine Geology, 259, 86-101

Austin, M., Scott, T., Brown, J., Brown, J., MacMahan, J., Masselink, G., Russell, P., 2010. Temporal observations of rip current circulation on a macro-tidal beach. Continental Shelf Research, 30, 1149-1165

Austin, M.J., Masselink, G., Scott, T.M., Russell, P.E., 2014. Water-level controls on macro-tidal rip currents. Continental Shelf Research, 75, 28-40

Austin, M.J., Scott, T.M., Russell, P.E., Masselink, G., 2012. Rip current prediction: Development, validation, and evaluation of an operational tool. Journal of Coastal Research, 29, 283-300

Bagnold, R., 1963. Mechanics of marine sedimentation. The sea, 3, 507-528

Bagnold, R., 1977. Bed load transport by natural rivers. Water Resources Research, 13, 303-312

Bailard, J.A., 1981. An energetics total load sediment transport model for a plane sloping beach. Journal of Geophysical Research: Oceans, 86, 10938-10954

Beach, R.A., Sternberg, R.W., 1988. Suspended sediment transport in the surf zone: response to cross-shore infragravity motion. Marine Geology, 80, 61-79

Beach, R.A., Sternberg, R.W., 1991. Infragravity driven suspended sediment transport in the swash, inner and outer surf zone. Coastal Sediments, Seattle, Washington, 114-128

Beach, R.A., Sternberg, R.W., 1996. Suspended-sediment transport in the surf zone: response to breaking waves. Continental Shelf Research, 16, 1989-2003

Blondeaux, P., Foti, E., Vittori, G., 2000. Migrating sea ripples. European Journal of Mechanics - B/Fluids, 19, 285-301

Boguchwal, L.A., Southard, J.B., 1990. Bed configurations in steady unidirectional water flows. Part 1. Scale model study using fine sands. Journal of Sedimentary Research, 60, 649-657

Bonneton, N., Bonneton, P., Senechal, N., Castelle, B., 2006. Very Low Frequency rip current pulsations during high energy conditions on a meso-macro tidal beach. 30th International Conference on Coastal Engineering, San Diego, CA, 1087-1096

Bowen, A., Holman, R.A., 1989. Shear instabilities of the mean longshore current: 1. Theory.

Bowen, A.J., 1969. Rip Currents: 1. Theortical Investigations. Journal of Geophysical Research, 74, 5467-5478

Bowen, A.J., Inman, D.L., 1969. Rip Currents: 2. Laboratory and Field Observations. Journal of Geophysical Research, 74, 5479-5490

Bowman, D., Rosen, D.S., Kit, E., Arad, D., Slavicz, A., 1989. Flow characterisitcs at rip current neck under low energy conditions. Marine Geology, 79, 41-54

Brander, R.W., 1999a. Field observations on the morphodynamic evolution of a low-energy rip current system. Marine Geology, 157, 199-217

Brander, R.W., 1999b. Sediment transport in low energy rip current systems. Journal of Coastal Research, 15, 839-849

Brander, R.W., 2001. Flow kinematics of low energy rip current systems. Journal of Coastal Research, 17, 468-481

Brander, R.W., Short, A.D., 2000. Morphodynamics of a large-scale rip current system at Muriwai Beach, New Zealand. Marine Geology, 165, 27-39

Bruneau, N., Castelle, B., Bonneton, P., Pedreros, R., Almar, R., Bonneton, N., Bretel, P., Parisot, J.-P., Sénéchal, N., 2009. Field observations of an evolving rip current on a meso-macrotidal well-developed inner bar and rip morphology. Continental Shelf Research, 29, 1650-1662

Bruun, P., Chiu, T., Gerritsen, F., Morgan, W., 1962. Storm tides in Florida as Related to coastal topography. Engineering Programme, Gainesville, Florida, p. 76.

Butt, T., Miles, J., Ganderton, P., Russell, P., 2004a. A simple method for calibrating optical backscatter sensors in high concentrations of non-cohesive sediments. Marine Geology, 192, 419-424

Butt, T., Russell, P., 1999. Suspended sediment transport mechanisms in high-energy swash. Marine Geology, 161, 361-375

Butt, T., Russell, P., Puleo, J., Miles, J., Masselink, G., 2004b. The influence of bore turbulence on sediment transport in the swash and inner surf zones. Continental Shelf Research, 24, 757-771

Butt, T., Russell, P., Turner, I., 2001. The influence of swash infiltration–exfiltration on beach face sediment transport: onshore or offshore? Coastal Engineering, 42, 35-52

Callaghan, D.P., T. E. Baldock, P. Nielsen, M., D. Hanes, K.A.H., and , MacMahan, J.H., 2005. Pulsing and circulation in a rip current system. 29th International Conference Coastal Engineering, New York, 1493–1505

Cambell Scientific, 2013. OBS-3+ and OBS300: Suspended Solids and Turbidity Monitors, 11th June, 2012. https://s.campbellsci.com/documents/eu/manuals/obs3_obs300.pdf

Camenen, B., 2009. Estimation of the wave-related ripple characteristics and induced bed shear stress. Estuarine, Coastal and Shelf Science, 84, 553-564

Cant, D.J., Walker, R.G., 1978. Fluvial processes and facies sequences in the sandy braided South Saskatchewan River, Canada. Sedimentology, 25, 625-648

Castelle, B., Bonneton, P., 2006. Modelling of a rip current induced by waves over a ridge and runnel system on the Aquitanian Coast, France. Comptes Rendus Geoscience, 338, 711-717

Castelle, B., Bonneton, P., Senechal, N., Dupuis, H., Butel, R., Michel, D., 2006. Dynamics of wave-induced currents over an alongshore non-uniform multiple-barred sandy beach on the Aquitanian Coast, France. Continental Shelf Research, 26, 113-131

Castelle, B., Coco, G., 2012. The morphodynamics of rip channels on embayed beaches. Continental Shelf Research, 43, 10-23

Castelle, B., Reniers, A., MacMahan, J., 2013. Numerical modelling of surfzone retention in rip current systems: on the impact of the surfzone sandbar morphology. Coastal Dynamics, Bordeaux, France

Channel Coast Obsevatory, 2015. Regional coastal monitoring programmes - Perrranporth, Accessed: March, 2015. http://www.channelcoast.org/data_management/real_time_data/charts/?chart=76

Chatfield, C., 2013. The analysis of time series: an introduction. CRC press, London. 352

Church, J.A., Clark, P.U., Cazenave, A., Gregory, J.M., Jevrejeva, S., Levermann, A., Merrifield, M., Milne, G., Nerem, R., Nunn, P., 2013. Climate change. Chapter 13: Sea level change - IPCC Report, pp. 1137-1216.

Clarke, L.B., Werner, B.T., 2004. Tidally modulated occurrence of megaripples in a saturated surf zone. Journal of Geophysical Research: Oceans, 109, 2156-2202. 10.1029/2003jc001934

Clifton, H., 1976. Wave-generated structures—a conceptual model. Beach and Nearshore Processes, 24, 126-148

Clifton, H.E., Dingler, J.R., 1984. Wave-formed structures and paleoenvironmental reconstruction. Marine Geology, 60, 165-198

Coco, G., Murray, A.B., 2007. Patterns in the sand: from forcing templates to self-organization. Geomorphology, 91, 271-290

Conley, D.C., Beach, R.A., 2003. Cross‐shore sediment transport partitioning in the nearshore during a storm event. Journal of Geophysical Research: Oceans, 108. 10.1029/2001JC001230

Conley, D.C., Inman, D.L., 1992. Field observations of the fluid‐granular boundary layer under near‐breaking waves. Journal of Geophysical Research: Oceans, 97, 9631-9643

Cook, D.O., 1970. The occurrence and geologic work of rip currents off southern California. Marine Geology, 9, 173-186

Cooley, J.W., Tukey, J.W., 1965. An algorithm for the machine calculation of complex Fourier series. Mathematics of computation, 19, 297-301

Crawford, A., Hay, A., 2001. Linear transition ripple migration and wave orbital velcoity skewness: Observations. Journal of Geophysical Research, 106, 14133-14128

Crawford, A., Hay, A., 2003. Wave orbital veloctiy skewness and linear transition ripple migration: Comparison with weakly non-linear theory. Journal of Geophysical Research, 108. 10.1029/2001JC001254

Dalrymple, R.A., 1978. Rip currents and their causes. International Conference of Coastal Engineering, Hamburg, Germany, 1414-1427

Dalrymple, R.A., MacMahan, J.H., Reniers, A.J., Nelko, V., 2011. Rip currents. Annual Review of Fluid Mechanics, 43, 551-581

Davidson, M.A., O'Hare, T.J., George, K.J., 2008. Tidal modulation of incident wave heights: Fact or Fiction? Journal of Coastal Research, 24, 151-159

Davidson, M.A., Russell, P., Huntley, D.A., Hardisty, J., A, C., 1992. An overview of the British Beach And Nearshore Dynamics (B-Band) programme. 23rd International Conference Coastal Engineering, Venice, Italy, 1987-2000

Davidson, M.A., Russell, P.E., Huntley, D.A., Hardisty, J., 1993. Tidal asymmetry in suspended sand transport on a macrotidal intermediate beach. Marine Geology, 110, 333-353. 10.1016/0025-3227(93)90092-a

Davis Jr, R.A., 1985. Beach and nearshore zone, Coastal sedimentary environments. Springer, New York, pp. 379-444.

Deigaard, R., Drønen, N., Fredsøe, J., Jensen, J.H., Jørgensen, M.P., 1999. A morphological stability analysis for a long straight barred coast. Coastal Engineering, 36, 171-195

Dingler, J.R., Inman, D.L., 1976. Wave-formed ripples in nearshore sands. 15th International Conference on Coastal Engineering, Honolulu, Hawaii, 2109-2126

Dodd, N., Blondeaux, P., Calvete, D., De Swart, H.E., Falqués, A., Hulscher, S.J., Różyński, G., Vittori, G., 2003. Understanding coastal morphodynamics using stability methods. Journal of Coastal Research, 19, 849-865

Downing, J., 2006. Twenty-five years with OBS sensors: The good, the bad, and the ugly. Continental Shelf Research, 26, 2299-2318

Downing, J.P., Beach, R.A., 1989. Laboratory apparatus for calibrating optical suspended solids sensors. Marine Geology, 86, 243-249

Downing, J.P., Sternberg, R., Lister, C., 1981. New instrumentation for the investigation of sediment suspension processes in the shallow marine environment. Marine Geology, 42, 19-34

Drake, T.G., Calantoni, J., 2001. Discrete particle model for sheet flow sediment transport in the nearshore. Journal of Geophysical Research: Oceans, 106, 19859-19868

DRIBS, 2013. DRIBS: Dynamics of Rips and Implications for Beach Safety, Accessed: 3rd January, 2014. http://www.ripcurrents.co.uk

Dronen, N., Karunarathna, H., Fredsoe, J., Sumer, B.M., Deigaard, R., 2002. An experimental study of rip channel flow. Coastal Engineering, 45, 223-238

Dugan, J., Vierra, K., Morris, W., Farruggia, G., Campion, D., Miller, H., 1999. Unique vehicles used for bathymetry surveys in exposed coastal regions. Proceedings of the US Hydrographic Conference Society National Meeting, Alabama Hydrographic Society of America

Dumas, S., Arnott, R., Southard, J.B., 2005. Experiments on oscillatory-flow and combined-flow bed forms: implications for interpreting parts of the shallow-marine sedimentary record. Journal of Sedimentary Research, 75, 501-513

Dyer, K.R., 1986. Coastal and estuarine sediment dynamics. John Wiley & Sons, Inc, Chichester, England. 358

Elgar, S., Gallagher, E.L., Guza, R., 2001. Nearshore sandbar migration. Journal of Geophysical Research: Oceans, 106, 11623-11627

Elgar, S., Guza, R., Freilich, M., 1988. Eulerian measurements of horizontal accelerations in shoaling gravity waves. Journal of Geophysical Research: Oceans, 93, 9261-9269

Fowler, R.E., Dalrymple, R.A., 1990. Wave group forced nearshore circulation. 22nd International Conference Coastal Engineering, Delft, The Netherlands, 729-742

Fredsoe, J., Deigaard, R., 1993. Mechanics of coastal sediment transport. World Scientific, London. 369

Gallagher, E.L., 2003. A note on megaripples in the surf zone: evidence for their relation to steady flow dunes. Marine Geology, 193, 171-176. 10.1016/s0025-3227(02)00662-x

Gallagher, E.L., 2011. Computer simulations of self-organized megaripples in the nearshore. Journal of Geophysical Research: Earth Surface, 116. 10.1029/2009jf001473

Gallagher, E.L., Elgar, S., Guza, R., 1998a. Megaripple migration in a natural surf zone. Nature, 394, 165-168

Gallagher, E.L., Elgar, S., Guza, R., 1998b. Observations of sand bar evolution on a natural beach. Journal of Geophysical Research: Oceans, 103, 3203-3215

Gallagher, E.L., MacMahan, J., Reniers, A.J.H.M., Brown, J., Thornton, E.B., 2011. Grain size variability on a rip-channeled beach. Marine Geology, 287, 43-53. DOI 10.1016/j.margeo.2011.06.010

Gonzalez-Rodriguez, D., Madsen, O.S., 2007. Seabed shear stress and bedload transport due to asymmetric and skewed waves. Coastal Engineering, 54, 914-929

Goring, D., Nikora, V., 2002. Despiking Acoustic Doppler Velocimeter Data. Journal of Hydraulic Engineering, 128, 117-126. 10.1061/(ASCE)0733-9429(2002)128:1(117)

Grasmeijer, B.T., Van Rijn, L.C., 2001. Sand transport in the surf zone of a dissipative beach. 4th Coastal Dynamics Conference, Lund, Sweden, 102-111

Greenwood, B., Brander, R., Perez, B., Joseph, E., Li, J., 2013. Water level modulation of current vectors and sediment flux in a transverse bar-rip cell. 3rd International Conference on Physical Coastal Processes, Management and Engineering, Las Palmas, Canary Islands

Greenwood, B., Davidson-Arnott, R.G.D., 1979. Sedimentation and equilibrium in wave-formed bars: a review and case study. Canadian Journal of Earth Sciences, 16, 312-332. 10.1139/e79-030

Guza, R., Thornton, E.B., 1985. Observations of surf beat. Journal of Geophysical Research: Oceans, 90, 3161-3172

Guza, R.T., Bowen, A.J., 1976. Resonant Interactions for Waves Breaking on a Beach 15th International Conference Coastal Engineering Proceedings, Honnlulu, Hawaii 560-579

Haas, K.A., Svendsen, I.A., Brander, R.W., Nielsen, P., 2002. Modelling of a Rip Current System on Moreton Island. 28th International Conference of Coastal Engineering, Wales, UK, 784-796

Haller, M.C., 1999. Rip current dynamics and nearshore circulation, PhD Thesis University of Delaware

Haller, M.C., Dalrymple, R., Svendsen, I., 1997. Rip channels and nearshore circulation. 3rd Coastal Dynamics Conference, Plymouth, UK, 594-603

Haller, M.C., Dalrymple, R.A., 2001. Rip current instabilities. Journal of Fluid Mechanics, 433, 161-192

Haller, M.C., Dalrymple, R.A., Svendsen, I.A., 2002. Experimental study of nearshore dynamics on a barred beach with rip channels. Journal of Geophysical Research: Oceans, 107. 10.1029/2001JC000955

Hanes, D.M., 1988. Intermittent sediment suspension and its implications to sand tracer dispersal in wave-dominated environments. Marine Geology, 81, 175-183

Hanes, D.M., Huntley, D.A., 1986. Continuous measurements of suspended sand concentration in a wave dominated nearshore environment. Continental Shelf Research, 6, 585-596

Hardisty, J., 1990. Beaches: Form and processes. Unwin Hyman Ltd, London, UK. 348

Harris, T.F.W., Jordaan, J., McMurray, W., Verwey, C., Anderson, F., 1964. Mixing in the surf zone. South African Council for Scientific and Industrial Research, Pretoria, South Africa.

Hay, A.E., Bowen, A.J., 1993. Spatially correlated depth changes in the nearshore zone during autumn storms. Journal of Geophysical Research: Oceans, 98, 12387-12404

Hay, A.E., Mudge, T., 2005. Principal bed states during SandyDuck97: Occurrence, spectral anisotropy, and the bed state storm cycle. Journal of Geophysical Research: Oceans, 110. 10.1029/2004JC002451

Hegge, B.J., Masselink, G., 1996. Spectral analysis of geomorphic time series: Auto-spectrum. Earth Surface Processes and Landforms, 21, 1021-1040

Hino, M., 1974. Theory on formation of rip-current and cuspidal coast. 14th International Conference Coastal Engineering, Copenhagen, Denmark, 901-919

Hoefel, F., Elgar, S., 2003. Wave-induced sediment transport and sandbar migration. Science, 299, 1885-1887

Hoekstra, P., Bell, P., van Santen, P., Roode, N., Levoy, F., Whitehouse, R., 2004. Bedform migration and bedload transport on an intertidal shoal. Continental Shelf Research, 24, 1249-1269. DOI 10.1016/j.csr.2004.03.006

Holman, R.A., Symonds, G., Thornton, E.B., Ranasinghe, R., 2006. Rip spacing and persistence on an embayed beach. Journal of Geophysical Research: Oceans, 111. 10.1029/2005JC002965

Hsu, T.-J., Elgar, S., Guza, R., 2006. Wave-induced sediment transport and onshore sandbar migration. Coastal Engineering, 53, 817-824

Hsu, T.J., Hanes, D.M., 2004. Effects of wave shape on sheet flow sediment transport. Journal of Geophysical Research: Oceans, 109. 10.1029/2003JC002075

Huntley, D.A., Amos, C.L., Williams, J.J., Humphery, J.D., 1991. Estimating bedload transport on continental shelves by observations of ripple migration - an assessment, in: Soulsby, R., Bettes, R. (Eds.), Sand Transport in Rivers, Estuaries and the Sea. Balkema, Rotterdam, p. 291.

Huntley, D.A., Hanes, D.M., 1987. Direct measurement of suspended sediment transport. Coastal Sediments New Orleans, USA, 723-737

Huntley, D.A., Short, A.D., 1992. On the spacing between observed rip currents. Coastal Engineering, 17, 211-225

Ingle Jr, J.C., 1966. The movement of beach sand. An analysis using fluorescent grains. University of Southern California Los Angeles Dept of Geology.

Inman, D., Bowen, A.J., 1963. Flume experiments on sand transport by waves and currents. Proc. 8th Conference on Coastal Engineering, 137-150

Inman, D.L., 1957. Wave-generated ripples in nearshore sands, Technical Report Scripps Institution of Oceanography Scripps, CA, p. 42.

Inman, D.L., Tunstall, E.B., 1972. Phase dependent roughness control of sand movement. 13th Coastal Engineering Conference, Vancouver, Canada, 1155-1171

Jaffe, A., Sternberg, R.W., Sallenger, J.A.H., 1984. The Role of suspeneded sediment in shore-normal beach profile change. 19th International Conference on Coastal Engineering, Houston, Texas, 1983-1996

Jamal, M., Simmonds, D., Magar, V., 2014. Modelling gravel beach dynamics with XBeach. Coastal Engineering, 89, 20-29

Jenkins, G.M., Watts, D.G., 1968. Spectral analysis and its applications. Holden-Day, San Francisco, California 526

Kachel, N.B., Sternberg, R.W., 1971. Transport of bedload as ripples during an ebb current. Marine Geology, 10, 229-244

Komar, P., 1976. Boundary layer flow under steady unidirectional currents. Marine sediment transport and environmental management, 1, 91-106

Komar, P., D, 1998. Beach processes and sedimentation: 2nd Edition. Prentice Hall, Upper Saddle River. 544

Kraus, N.C., Gingerich, K.J., Rosati, J.D., 1989. DUCK85 surf zone sand transport experiment, Surf zone sediment transport processes work unit US Army Corps of Engineers, Washington, DC.

Kroon, A., De Boer, A., 2001. Horizontal flow circulation on a mixed energy beach. Proceedings of Coastal Dynamics, Lund, Sweden, 548-557. 10.1061/40566(260)56

Kroon, A., De Kruif, A., Quartel, S., Reintjes, C., 2003. Influence of storms on the sequential behavior of bars and rips. Proceedings of Coastal Sediments, Clearwater Beach, Florida, (on CD)

Kroon, A., Masselink, G., 2002. Morphodynamics of intertidal bar morphology on a macrotidal beach under low-energy wave conditions, North Lincolnshire, England. Marine Geology, 190, 591-608. http://dx.doi.org/10.1016/S0025-3227(02)00475-9

Lab, C.I., 2009. The ARGUS programme, Accessed: August, 2011. http://cil-www.coas.oregonstate.edu/

Leatherman, S., Fletemeyer, J., 2011. Rip Currents: Beach Safety, Physical Oceanography, and Wave Modeling. CRC Press. 310

Lippmann, T., Herbers, T., Thornton, E., 1999. Gravity and shear wave contributions to nearshore infragravity motions. Journal of physical oceanography, 29, 231-239

Lippmann, T., Smith, G., 2008. Shallow surveying in hazardous waters. Shallow Water Survey Conference, Durham, USA, 118-118

Longuet-Higgins, M.S., Stewart, R., 1964. Radiation stresses in water waves; a physical discussion, with applications. Deep Sea Research and Oceanographic Abstracts, 11, 529-562. 10.1016/0011-7471(64)90001-4

MacMahan, J., 2001. Hydrographic surveying from personal watercraft. Journal of surveying engineering, 127, 12-24

MacMahan, J., Brown, J., Brown, J., Thornton, E., Reniers, A., Stanton, T., Henriquez, M., Gallagher, E., Morrison, J., Austin, M.J., Scott, T.M., Senechal, N., 2010. Mean Lagrangian flow behavior on an open coast rip-channeled beach: A new perspective. Marine Geology, 268, 1-15

MacMahan, J., Reniers, A., Brown, J., Brander, R., Thornton, E., Stanton, T., Brown, J., Carey, W., 2011. An introduction to rip currents based on field observations. Journal of Coastal Research, 27. http://dx.doi.org/10.2112/JCOASTRES-D-11-00024.1

MacMahan, J.H., Reniers, A.J.H.M., Thornton, E.B., Stanton, T.P., 2004a. Infragravity rip current pulsations. Journal of Geophysical Research-Oceans, 109. 10.1029/2003jc002068

MacMahan, J.H., Reniers, A.J.H.M., Thornton, E.B., Stanton, T.P., 2004b. Surf zone eddies coupled with rip current morphology. Journal of Geophysical Research-Oceans, 109. 10.1029/2003jc002083

MacMahan, J.H., Thornton, E.B., Reniers, A.J.H.M., 2006. Rip current review. Coastal Engineering, 53, 191-208

MacMahan, J.H., Thornton, E.B., Reniers, A.J.H.M., Stanton, T.P., Symonds, G., 2008. Low-Energy Rip Currents Associated With Small Bathymetric Variations. Marine Geology, 255, 156-164

MacMahan, J.H., Thornton, E.B., Stanton, T.P., Reniers, A.J.H.M., 2005. RIPEX: Observations of a rip current system. Marine Geology, 218, 113-134

Marine-Electronics, 2006. Sand Ripple Profiler, Accessed: 12th October, 2010. http://www.marine-electronics.co.uk/sand_ripple_profiling.html

Mariño‐Tapia, I., Russell, P., O'Hare, T., Davidson, M., Huntley, D., 2007. Cross‐shore sediment transport on natural beaches and its relation to sandbar

migration patterns: 1. Field observations and derivation of a transport parameterization. Journal of Geophysical Research: Oceans, 112. 10.1029/2005JC002893

Martin, V., Fisher, T., Millar, R., Quick, M., 2002. ADV data analysis for turbulent flows: Low correlation problem. Proceedings of Hydraulic Measurements and Experimental Methods Conference, Colorado, USA, 1-10

Masselink, G., Austin, M., O'Hare, T., Russell, P., 2007. Geometry and dynamics of wave ripples in the nearshore of a coarse sandy beach. Geophysical Research Letters, 112. 10.1029/2006JC003839

Masselink, G., Austin, M., Scott, T., Poate, T., Russell, P., 2014. Role of wave forcing, storms and nao in outer bar dynamics on a high-energy, macro-tidal beach. Geomorphology, 226, 76-93

Masselink, G., Austin, M., Tinker, J., O'Hare, T., Russell, P., 2008. Cross-shore sediment transport and morphological response on a macrotidal beach with intertidal bar morphology, Truc Vert, France. Marine Geology, 251, 141-155

Masselink, G., Black, K.P., 1995. Magnitude and cross-shore distribution of bed return flow measured on natural beaches. Coastal Engineering, 25, 165-190. http://dx.doi.org/10.1016/0378-3839(95)00002-S

Masselink, G., Evans, D., Hughes, M.G., Russell, P., 2005. Suspended sediment transport in the swash zone of a dissipative beach. Marine Geology, 216, 169-189

Masselink, G., Hughes, M.G., 2003. Introduction to Coastal Processes & Geomorphology. Hodder Education, London. 354

Masselink, G., Pattiaratchi, C., 2000. Tidal asymmetry in sediment resuspension on a macrotidal beach in northwestern Australia. Marine Geology, 163, 257-274

Masselink, G., Russell, P., 2006. Flow velocities, sediment transport and morphological change in the swash zone of two contrasting beaches. Marine Geology, 227, 227-240

Masselink, G., Short, A.D., 1993. The effect of tide range on beach morphodynamics and morphology: a conceptual beach model. Journal of Coastal Research, 9, 785-800

MathsWorks, 2014. MATLAB.

McCarroll, R.J., Brander, R.W., MacMahan, J.H., Turner, I.L., Reniers, A.J., Brown, J.A., Bradstreet, A., Sherker, S., 2014. Evaluation of swimmer-based rip current escape strategies. Natural hazards, 71, 1821-1846

McKenzie, P., 1958. Rip-current systems. The journal of geology, 66, 103-113

Miles, J., 2013. Wave shape effects on sediment transport. Journal of Coastal Research SI, 65, 1803-1808

Miles, J., Butt, T., Russell, P., 2006. Swash zone sediment dynamics: A comparison of a dissipative and an intermediate beach. Marine Geology, 231, 181-200. 10.1016/j.margeo.2006.06.002

Miles, J., Thorpe, A., 2015. Bedform contributions to cross-shore sediment transport on a dissipative beach. Coastal Engineering, 98, 65-77. http://dx.doi.org/10.1016/j.coastaleng.2015.01.007

Miles, J., Thorpe, A., Russell, P., Masselink, G., 2014a. Megaripple dynamics on a dissipative sandy beach. Journal of Coastal Research SI, 65, 187-192

Miles, J., Thorpe, A., Russell, P., Masselink, G., 2014b. Observations of bedforms on a dissipative macrotidal beach. Ocean Dynamics, 64, 225-239. 10.1007/s10236-013-0677-2

Miles, J.R., Russell, P.E., Ruessink, B.G., Huntley, D.A., 2002. Field observations of the effect of shear waves on sediment suspension and transport. Continental Shelf Research, 22, 657-681. 10.1016/s0278-4343(01)00095-4

Miller, M.C., Komar, P.D., 1980. A field investigation of the relationship between oscillation ripple spacing and the near-bottom water orbital motions. Journal of Sedimentary Research, 50, 183-191

Munk, W.H., 1949. The solitary wave theory and its application to surf problems. Annals of the New York Academy of Sciences, 51, 376-424

Ngusaru, A.S., Hay, A.E., 2004. Cross ‐ shore migration of lunate megaripples during Duck94. Journal of Geophysical Research: Oceans, 109. 10.1029/2002JC001532

Nichols, G., 2009. Sedimentology and stratigraphy. Jon Wiley & Sons, UK. 419

Nielsen, P., 1981. Dynamics and geometry of wave ‐ generated ripples. Journal of Geophysical Research: Oceans, 86, 6467-6472

Nielsen, P., 1986. Suspended sediment concetrations under waves. Coastal Engineering, 10, 23-31

Nielsen, P., 1992. Coastal bottom boundary layers and sediment transport. World Scientific, London. 324

Nielsen, P., 2006. Sheet flow sediment transport under waves with acceleration skewness and boundary layer streaming. Coastal Engineering, 53, 749-758

Noda, E.K., 1974. Wave-Induced Nearshore Circulation. Journal of Geophysical Research, 79. 10.1029/JC079i027p04097

Nortek, 2010. Acousitc Doppler Current Profilers, Accessed: 12th October, 2010. http://www.nortek-as.com/en/products/velocimeters/acoustic-doppler-current-profilers-adcp

Nuttal, A.H., 1971. Spectral estimation by means of overlapped FFT processing of windowed data. Naval Underwater Systems Center Report No. 4169, New London, CT, USA, p. 49.

O'Hara Murray, R., Thorne, P., Hodgson, D., 2011. Intrawave observations of sediment entrainment processes above sand ripples under irregular waves. Journal of Geophysical Research: Oceans, 116. 10.1029/2010JC006216

Oltman-Shay, J., Howd, P., Birkemeier, W., 1989. Shear instabilities of the mean longshore current: 2. Field observations. Journal of Geophysical Research: Oceans, 94, 18031-18042

Orzech, M.D., Reniers, A.J.H.M., Thornton, E.B., MacMahan, J.H., 2011. Megacusps on rip channel bathymetry: Observations and modeling. Coastal Engineering, 58, 890-907. http://dx.doi.org/10.1016/j.coastaleng.2011.05.001

Orzech, M.D., Thornton, E.B., MacMahan, J.H., O'Reilly, W.C., Stanton, T.P., 2010. Alongshore rip channel migration and sediment transport. Marine Geology, 271, 278-291

Osborne, P.D., Greenwood, B., 1992a. Frequency dependent cross-shore suspended sediment transport. 1. A non-barred shoreface. Marine Geology, 106, 1-24

Osborne, P.D., Greenwood, B., 1992b. Frequency dependent cross-shore suspended sediment transport. 2. A barred shoreface. Marine Geology, 106, 25-51

Osborne, P.D., Vincent, C.E., 1996. Vertical and horizontal structure in suspended sand concentrations and wave-induced fluxes over bedforms. Marine Geology, 131, 195-208

Pattiaratchi, C., Olsson, D., Hetzel, Y., Lowe, R., 2009. Wave-driven circulation patterns in the lee of groynes. Continental Shelf Research, 29, 1961-1974

Poate, T., Kingston, K., Masselink, G., Russell, P., 2009. Response of High-energy, Macrotidal Beaches to Seasonal Changes in Wave Conditions: Examples from North Cornwall, UK. Journal of Coastal Research SI, 56, 747-751

Puleo, J., Blenkinsopp, C., Conley, D., Masselink, G., Russell, P., Turner, I., Buscombe, D., Lanckriet, T., McCall, R., Poate, T., 2012. Comprehensive study of swash-zone hydrodynamics and sediment transport. 33rd International Conference on Coastal Engineering, Santander, Spain. http://dx.doi.org/10.9753/icce.v33.sediment.1

Ranasinghe, R., Symonds, G., Black, K., Holman, R., 2000. Processes governing rip spacing, persistence and strength in a swell dominated, microtidal environment. 27th International Conference on Coastal Engineering Sydney, Australia, 455-467

Reniers, A., Battjes, J., 1997. A laboratory study of longshore currents over barred and non-barred beaches. Coastal Engineering, 30, 1-21

Reniers, A.J., Roelvink, J., Thornton, E., 2004a. Morphodynamic modeling of an embayed beach under wave group forcing. Journal of Geophysical Research: Oceans, 109. 10.1029/2002JC001586

Reniers, A.J., Roelvink, J., Thornton, E., 2004b. Morphodynamic modeling of an embayed beach under wave group forcing. Journal of Geophysical Research: Oceans, 109. 10.1029/2002JC001586

Reniers, A.J.H.M., MacMahan, J.H., Thornton, E.B., Stanton, T.P., 2007. Modeling of very low frequency motions during RIPEX. Journal of Geophysical Research, 112, C07013. 10.1029/2005jc003122

Richardson, H., 2011. Longshore variability in 3D bar-rip morphology on a macrotidal beach, Perranporth, UK., MSc Thesis, Plymouth University

Roelvink, D., Reniers, A., van Dongeren, A., de Vries, J.v.T., McCall, R., Lescinski, J., 2009. Modelling storm impacts on beaches, dunes and barrier islands. Coastal Engineering, 56, 1133-1152

Roelvink, D., Reniers, A., Van Dongeren, A., Van Thiel de Vries, J., Lescinski, J., McCall, R., 2010. XBeach model description and manual, Unesco-IHE Institute for Water Education, Deltares and Delft University of Tecnhology, p. 208.

Rosati, J.D., Kraus, N.C., 1989. Development of a portable sand trap for use in the nearshore, Surf zone sediment transport processes. US Army Corps of Engineers, p. 180.

Ruessink, B., Coco, G., Ranasinghe, R., Turner, I.L., 2007. Coupled and non-coupled behavior of three ‐ dimensional morphological patterns in a double sandbar system. Journal of Geophysical Research: Oceans, 112. 10.1029/2006JC003799

Ruessink, B., Houwman, K., Hoekstra, P., 1998. The systematic contribution of transporting mechanisms to the cross-shore sediment transport in water depths of 3 to 9 m. Marine Geology, 152, 295-324

Ruessink, B., Van den Berg, T., Van Rijn, L., 2009. Modeling sediment transport beneath skewed asymmetric waves above a plane bed. Journal of Geophysical Research: Oceans, 114. 10.1029/2009JC005416

Ruessink, B., Van Enckevort, I., Kingston, K., Davidson, M., 2000. Analysis of observed two-and three-dimensional nearshore bar behaviour. Marine Geology, 169, 161-183

Ruskin, 2011. Pressure Transducer Data Logger Manual Oct 2012, 2012. rbr-global.com

Russell, P., Huntley, D., 1999. A cross-shore transport" shape function" for high energy beaches. Journal of Coastal Research, 15, 198-205

Russell, P.E., 1990. Field studies of suspended sand transport on a high energy dissipative beach, PhD Thesis University College of Swansea

Russell, P.E., 1993. Mechanisms for Beach Erosion during Storms. Continental Shelf Research, 13, 1243-1265

Schmidt, W.E., Woodward, B.T., Millikan, K.S., Guza, R.T., Raubenheimer, B., Elgar, S., 2003. A GPS-Tracked Surf Zone Drifter*. Journal of Atmospheric and Oceanic Technology, 20, 1069-1075. 10.1175/1460.1

Scott, T., Austin, M., 2012. DRIBS data.

Scott, T., Austin, M., Masselink, G., Russell, P., 2016. Dynamics of rip currents associated with groynes—field measurements, modelling and implications for beach safety. Coastal Engineering, 107, 53-69

Scott, T., Masselink, G., Austin, M.J., Russell, P., 2014. Controls on macrotidal rip current circulation and hazard. Geomorphology, 214, 198-215

Scott, T., Masselink, G., Russell, P., 2011. Morphodynamic characteristics and classification of beaches in England and Wales. Marine Geology, 286, 1-20

Scott, T., Russell, P., Masselink, G., Wooler, A., 2009a. Rip current variability and hazard along a macro-tidal coast. Journal of Coastal Research SI, 56, 895-899

Scott, T., Russell, P., Masselink, G., Wooler, A., Short, A., 2007. Beach rescue statistics and their relation to nearshore morphology and hazards: a case study for southwest England. Journal of Coastal Research, 50, 1-6

Scott, T., Russell, P., Masselink, G., Wooler, A., Short, A., 2009b. High volume sediment transport and its implication for recreational beach risk. Coastal Engineering, 1-5, 4250-4262

Shepard, F., Emery, K., La Fond, E., 1941. Rip currents: a process of geological importance. The journal of geology, 49, 337-369

Shepard, F., Inman, D., 1950. Nearshore water circulation related to bottom topography and wave refraction. Transactions, American Geophysical Union, 31, 196-196

Sherman, D.J., Short, A.D., Takeda, I., 1993. Sediment Mixing Depth and Bedform Migration in Rip channels. Journal of Coastal Research, 15, 39-48

Short, A., Hogan, C., 1994. Rip currents and beach hazards: their impact on public safety and implications for coastal management. Journal of Coastal Research SI, 12, 197-209

Short, A.D., 1985. Rip-current type, spacing and persistence, Narrabeen Beach, Australia. Marine Geology, 65, 47-71

Short, A.D., Brander, R.W., 1999. Regional Variations in Rip Density. Journal of Coastal Research, 15, 813-822

Smith, J.A., Largier, J.L., 1995. Observations of nearshore circulation: rip currents. Journal of Geophysical Research: Oceans, 100, 10967-10975

Snyder, W.H., Castro, I.P., 1999. Acoustic Doppler velocimeter evaluation in stratified towing tank. Journal of Hydraulic Engineering, 125, 595-603

SonTek, 2009. Acousitc Doppler Profiler, Accessed: 13th October, 2010. http://www.sontek.com/10mhzadv.php

Sonu, C.J., 1972. Field observation of nearshore circulation and meandering currents. Journal of Geophysical Research, 77, 3232-3247

Soulsby, R., 1997. Dynamics of marine sands. Thomas Telford Publications, London. 249

Southard, J.B., Boguchwal, L.A., 1990. Bed configurations in steady unidirectional water flows. Part 2. Synthesis of flume data. Journal of Sedimentary Research, 60, 658-679

Stokes, C., Russell, P., Conley, D., Beaumont, E., Greaves, D., 2013. Exploring Monthly To Seasonal Beach Morphodynamics Using Empirical Orthogonal Functions. Journal of Coastal Research SI, 65, 1868-1873

Swales, A., Oldman, J.W., Smith, K., 2006. Bedform geometry on a barred sandy shore. Marine Geology, 226, 243-259. 10.1016/j.margeo.2005.10.001

Tang, E.C.S., Dalrymple, R., 1989. Nearshore circulation: Rip currents and wave groups. Plenum Press, New York. 205-229

Thorne, P.D., Davies, A.G., Williams, J.J., 2003. Measurements of near‐bed intra‐wave sediment entrainment above vortex ripples. Geophysical Research Letters, 30. 10.1029/2003GL018427

Thornton, E.B., Abdelrahman, S., 1991. Sediment transport in the swash due to obliquely incident wind-waves modulated by infragravity waves. Coastal Sediments, Seattle, Washington, 100-113

Thornton, E.B., MacMahan, J., Sallenger, J.A.H., 2007. Rip currents, mega-cusps, and eroding dunes. Marine Geology, 240, 151-167

Thornton, E.B., Swayne, J.L., Dingler, J.R., 1998. Small-scale morphology across the surf zone. Marine Geology, 145, 173-192. 10.1016/s0025-3227(97)00114-x

Thorpe, A., Miles, J., Masselink, G., Russell, P., 2014. Bedform Dynamics in a Rip Current. Journal of Coastal Research SI, 66, 700-705

Thorpe, A., Miles, J., Masselink, G., Russell, P., Scott, T., Austin, M., 2013. Suspended sediment transport in rip currents on a macrotidal beach. Journal of Coastal Research. SI, 65, 1880-1885

Thorpe, A., Miles, J., Masselink, G., Russell, P., Scott, T., Austin, M., 2012. Field Measurements of Bedforms in a Rip Channel on a Macro-tidal Beach. 33rd International Conference on Coastal Engineering, Santander, Spain

Tinker, J., O'Hare, T., Masselink, G., Butt, T., Russell, P., 2009. A cross-shore suspended sediment transport shape function parameterisation for natural beaches. Continental Shelf Research, 29, 1948-1960

Traykovski, P., Hay, A.E., Irish, J.D., Lynch, J.F., 1999. Geometry, migration, and evolution of wave orbital ripples at LEO‐15. Journal of Geophysical Research: Oceans, 104, 1505-1524

Trimble, 2013. Trimble 5600 Series Manual Accessed: 25th September, 2014. ftp://ftp.trimble.com/pub/tmsupport/5600_Geodimeter/5600%20User%20Guide%20571702011%20ver0600%20ENG.pdf

Turner, I.L., Whyte, D., Ruessink, B.G., Ranasinghe, R., 2007. Observations of rip spacing, persistence and mobility at a long, straight coastline. Marine Geology, 236, 209-221

Turner, R.K., Luisetti, T., 2015. Toward adaptive management in coastal zones, in: Glavovic, B.C.K., M.; Kay, R.; Travers, A. (Ed.), Climate Change and the Coast: Building Resilient Communities. CRC Press, Boca Raton, pp. 417-434.

van Rijn, L.C., 1984. Sediment transport, part III: bed forms and alluvial roughness. Journal of Hydraulic Engineering, 110, 1733-1754

Van Rijn, L.C., 1993. Principles of sediment transport in rivers, estuaries and coastal seas. Aqua Publications Amsterdam, Netherlands. 1200

Vincent, C., Marsh, S., Webb, M., Osborne, P., 1999. Spatial and temporal structures of suspension and transport over megaripples on the shore face. Journal of Geophysical Research: Oceans, 104, 11215-11224

Vincent, C.E., Osborne, P., 1995. Predicting suspended sand concentration profiles on a macro-tidal beach. Continental Shelf Research, 15, 1497-1514

Vincent, C.E., Osborne, P.D., 1993. Bedform dimensions and migration rates under shoaling and breaking waves. Continental Shelf Research, 13, 1267-1280

Webb, M., Vincent, C., 1999. Comparison of time-averaged acoustic backscatter concentration profile measurements with existing predictive models. Marine Geology, 162, 71-90

Welch, P.D., 1967. The use of fast Fourier transform for the estimation of power spectra: a method based on time averaging over short, modified periodograms. IEEE Transactions on audio and electroacoustics, 15, 70-73

Werner, B., Kocurek, G., 1999. Bedform spacing from defect dynamics. Geology, 27, 727-730

Whitehouse, R., Sutherland, J., 2001. COAST3D data report-3D experiment, Teignmouth, UK. HR Wallingford Report, 119

Wiberg, P.L., Harris, C.K., 1994. Ripple geometry in wave‐dominated environments. Journal of Geophysical Research: Oceans, 99, 775-789

Wright, L.D., Short, A.D., 1984. Morphodynamic variability of surf zones and beaches: A synthesis. Marine Geology, 56, 93-118

Yalin, M.S., 1964. Geometrical Properties of sand waves. Journal of the Hydraulics Division, 90, 105-109

APPENDIX

1. Thorpe, A., Miles, J., Masselink, G., Russell, P., Scott, T., Austin, M., 2013. Suspended sediment transport in rip currents on a macrotidal beach. Journal of Coastal Research. SI, 65, 1880-1885

2. Thorpe, A., Miles, J., Masselink, G., Russell, P., 2014. Bedform Dynamics in a Rip Current. Journal of Coastal Research. SI, 66, 700-705

3. Thorpe, A., Miles, J., Masselink, G., Russell, P., Scott, T., Austin, M., 2012. Field Measurements of Bedforms in a Rip Channel on a Macro-tidal Beach. 33rd International Conference on Coastal Engineering, Santander, Spain.

FIELD MEASUREMENTS OF BEDFORMS IN A RIP CHANNEL ON A MACRO-TIDAL BEACH

Antony Thorpe[1], Jon Miles, Gerd Masselink, Paul Russell, Tim Scott and Martin Austin

A Sand Ripple Profiler (SRP) was deployed in a rip channel on a dissipative sandy beach to measure bedform height (Δ), length (λ) and migration rate (M_r) throughout a macro-tidal cycle with an offshore significant wave height of 0.7 m and peak period of 10 s. At lower tidal elevations in the strong offshore flow of the rip current (maximum = 0.4 m/s) bedforms (Δ = 0.15 m, λ = 3 m) were found to migrate offshore (M_r = 0.21 m/hr). Outside of active rip current conditions (water depth (h) = >~2.5 m) bedforms were found to be of smaller scale (Δ = 0.09 – 0.12 m, λ = 1 – 1.2 m) migrating onshore at a rate of 0.35 m/hr at mid tide (h = 3.3 m) and 0.03 m/hr at high tide (h = 6.3 m). Onshore migration rates were found to increase with increased wave skewness and velocity variance.

Keywords: rip currents, bedforms, megaripples

INTRODUCTION

Rip currents are a unique feature of the nearshore environment exhibiting a channel of strong, quasi-steady, offshore directed flow (in the order of 0.5 m/s) that dissects the wave dominated surfzone and dissipates beyond the breaker zone (MacMahan et al., 2005). Rips are a mass balance response to wave induced onshore transport. Wave breaking is focused on sandbars and minimized in the rip channel; as a consequence of this, water travels alongshore in feeder channels before flowing seaward within the rip neck (MacMahan et al., 2006)**.** They are typically found at lower tidal elevations where they are associated with the bar/rip morphology of intermediate state beaches (Brander, 1999a).

Megaripples are large ripples or small dunes with heights (Δ) of 0.1 – 0.5 m and lengths (λ) of 1 – 5 m (Gallagher, 2003). They are generally present within the nearshore environment. Field observations suggest that megaripples exist in rip currents (Aagaard et al., 1997), migrate offshore (Greenwood & Davidson-Arnott, 1979) and that they are current dominated (Nielsen, 1992). Sherman et al. (1993) observed megaripples in a rip feeder channel by visually measuring a pre-selected megaripple with a 'meter long aluminium comb'. They observed lunate bedforms of megaripple dimension (Δ = 0.16 m, λ = 1.6 m) migrating at 0.99 m/hr in the direction of flow.

Gallagher et al. (1998) found megaripples (Δ = 0.2 – 0.3 m, λ = 2 – 5 m) present 60 percent of the time in the surfzone (in a trough where h = 1.5 – 2 m) during a 6 week field work campaign. The megaripple generally took the form of oval shaped holes and occurred under a wide range of wave conditions (H_s = 0.5 – 4 m). Onshore migration was attributed to wave skewness with typical migration rates of 0.3 m/hr (maximum = 1.5 m/hr). Gallagher (2003) proposed that megaripples found in the combined flow environment of the surfzone were dynamically similar to asymmetric, steady flow features present in rivers, estuaries and deserts.

In this study, results are presented of bedform dynamics measured in a rip channel on an exposed sandy beach over a macro-tidal cycle. The large change in water level at the site allows a comparison between bedform dynamics at lower tidal elevations when there is an active rip current with those at higher tidal elevations when the rip becomes inactive.

STUDYSITE & METHODOLOGY

Study Site

The study site was Perranporth, a 3.5 km long beach (Figure 1) located on the North Coast of Cornwall, UK (Figure 2).

[1]School of Marine Science and Engineering, Plymouth University, Drake's Circus, Plymouth, Devon, PL4 8AA, UK

Figure 1: Panoramic photo of Perranporth beach, looking form south to north.

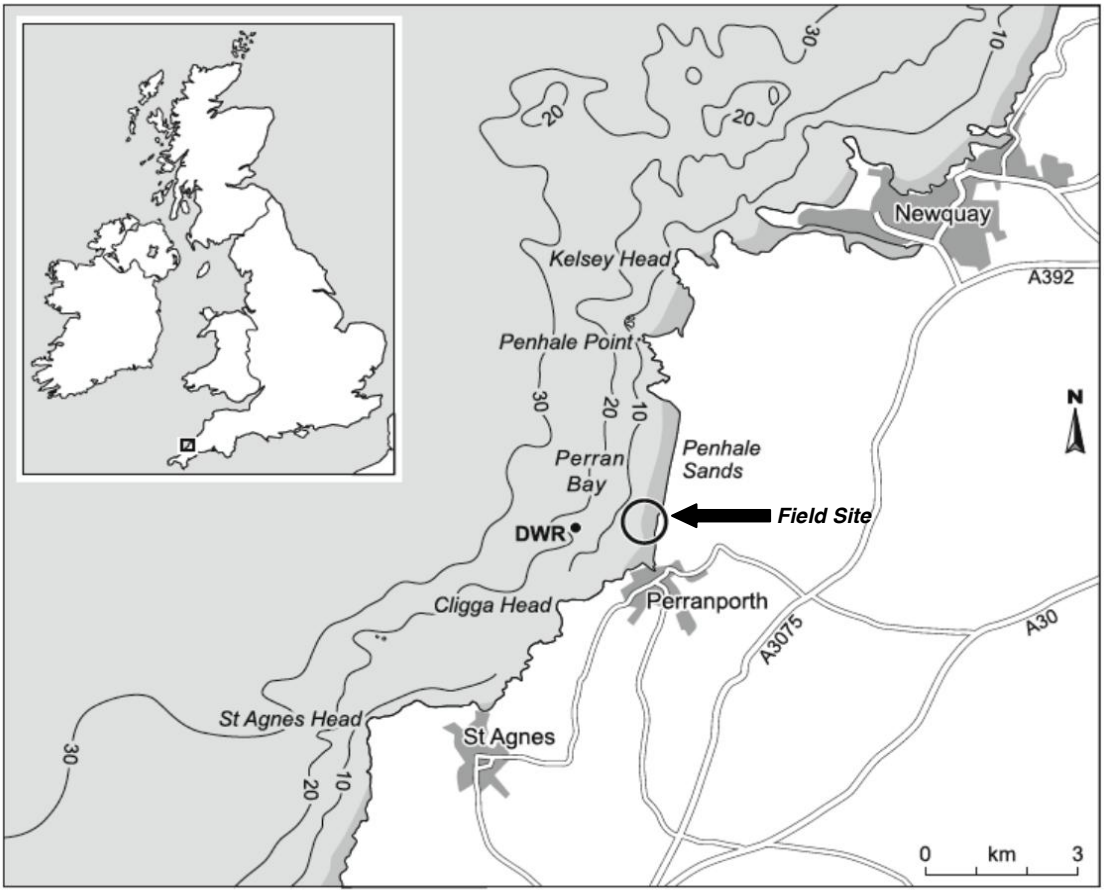

Figure 2: Map showing location of the study site and within the UK the location of the directional wave rider buoy (DWR) (Austin et al., 2010).

Perranporth is a highly energetic beach with an annual significant wave height (H_s) of 1.6 m and a peak period (T_p) of 10.5 s (CCO, 2012). It faces west-northwest, is exposed to Atlantic swell and also receives locally generated wind waves. It is a macro-tidal beach with a mean spring range of 6.3 m and consists of medium sized sand (D_{50} = 0.28 – 0.34 mm). The beach lies on the boundary of the intermediate and dissipative classifications with pronounced bar/rip morphology on a seasonal time scale (Austin et al., 2010).

Figure 3 shows a time-averaged image captured with an ARGUS camera of Perranporth beach at spring low tide at the time of the experiments described in this paper. The rhythmic nature of the bar/rip system is evident throughout the length of the beach. The rip used for the study and the location of the instrumentation is marked on the image. This rip was chosen because it offered a clearly defined channel with offshore flow dissecting the intertidal bar.

Figure 3: Time averaged image of bar-rip morphology at Perranporth beach (arrow marks rip system used in study; circle marks position of instrumentation).

Methodology

Offshore wave data were collected from a Directional Wave Rider (DWR) wave buoy located approximately 1 km offshore (see Figure 2) of the study site (CCO, 2012). In-situ data were collected using a range of instruments secured to a mobile rig. The rig was assembled prior to deployment and carried into the rip channel at spring low tide.

The flow velocities, waves and tidal elevation in the rip channel were recorded with a Nortek Vector 3D-Acoustic Doppler Velocimeter (ADV) fitted with an external pressure transducer (PT). The head of the ADV was carefully aligned to measure cross-shore and longshore flows at a height of 0.55 m above the bed. The PT, used to measure wave statistics and tidal elevation was housed in the ADV casing unit with the sensor positioned at a height of 0.2 m above the bed. Data from both instruments were logged autonomously at 8 Hz.

A Sand Ripple Profiler (SRP) was used to measure bedform dynamics. The SRP is a pencil beam sonar scanner that collects data as a range and angle from the scanner, for analysis this is processed to obtain an 'x' (cross-shore distance) and 'z' (distance below the scanner) co-ordinate system. The data can be post-processed to produce a profile of the bed from which Δ, λ and M_r can be deduced. The SRP was aligned to scan in the cross-shore direction, and was positioned 0.9 m above the bed with a horizontal resolution of 14 mm directly below the scanner. The data logger was programmed to log autonomously scanning the bed once every minute. The SRP does not give reliable data in breaking waves, due to excessive amounts of bubbles in the water column. Bedform data are therefore only available for water depths of over approximately 1 m.

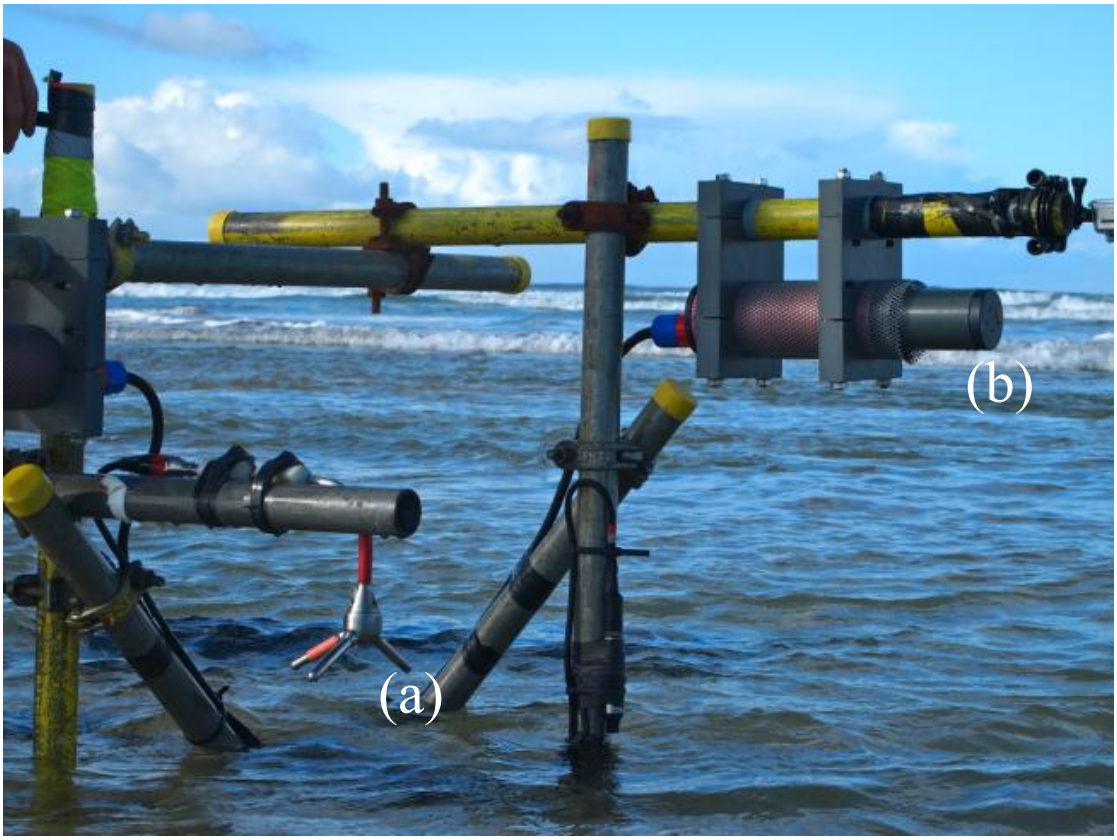

Figure 4: Rig design and position of instruments; (a) ADV head, (b) SRP. The picture was taken at low tide; at mid and high tide the rig is completely submerged.

The SRP data was post processed by first applying a five minute averaging routine in which five consecutive scans were combined. Spurious '*z*' axis data points were identified as those with a difference of 50 mm or over in elevation from neighbouring points and were removed. The gaps in the data this created were treated by applying linear interpolation over a 2 m range.
Bedform height was obtained by measuring the difference between crest and trough height of the same bedform. A value for half a wavelength was obtained by finding the cross-shore distance between the crest and trough, this value was then doubled. Bedform wavelength was measured in such a way as the bedform length scale is occasionally similar or greater than the SRP footprint; therefore the complete bedform is not always visible in the SRP scan. The limitation of this is that the wavelength may be under or overestimated if the bedform is not symmetrical. Migration rate was calculated measuring the distance of crest-crest or trough-trough positions over consecutive scans and dividing by the elapsed time.

Intertidal surveys of the beach elevation were carried out at low tide using a Real Time Kinematic GPS (RTK-GPS) mounted on an All-Terrain Vehicle (ATV). Sub-tidal surveys were carried out using a RTK-GPS in conjunction with a single beam echo sounder mounted on a Jet Ski, overlapping the intertidal surveys. The two sets of survey data were combined and interpolated onto a normal grid and fitted to a local co-ordinate system (Austin et al, 2010).

Lagrangian drifters, based on a design by Schmit (2003), were used to measure rip flows and to identify the overall location of the rip current.. The drifters were fitted with GPS receivers and data loggers capable of recording raw carrier phase satellite data at 1 Hz, which were subsequently processed against a survey grade base station. The data provided estimates of rip flow with a positional accuracy of <0.4 m and an accuracy of the flow velocity estimates of 0.01 m/s (Austin et al., 2010).

RESULTS

Environmental Conditions

Data were collected over six tidal cycles in October 2011. Data in this paper are presented from two tidal cycles over the 14th and 15th (referred to from here on as Tide 1 and Tide 2). The maximum water depths for Tide 1 and Tide 2 were 6.5 m and 6.3 m respectively. Wave heights and period were

measured at the offshore wave buoy of H_s = 0.6 m and a T_p = 9.5 s for Tide 1 and H_s = 0.7 m and a T_p = 10 s for Tide 2.

The morphology of the study area is shown in Figure 5. The rip channel is clearly defined by the mean low water spring (MLWS) position (bold line). It is aligned so that the channel is shore normal, and is situated between two sand bars. At its largest the rip was visually observed to be approximately 50 m wide and 150 m in length.

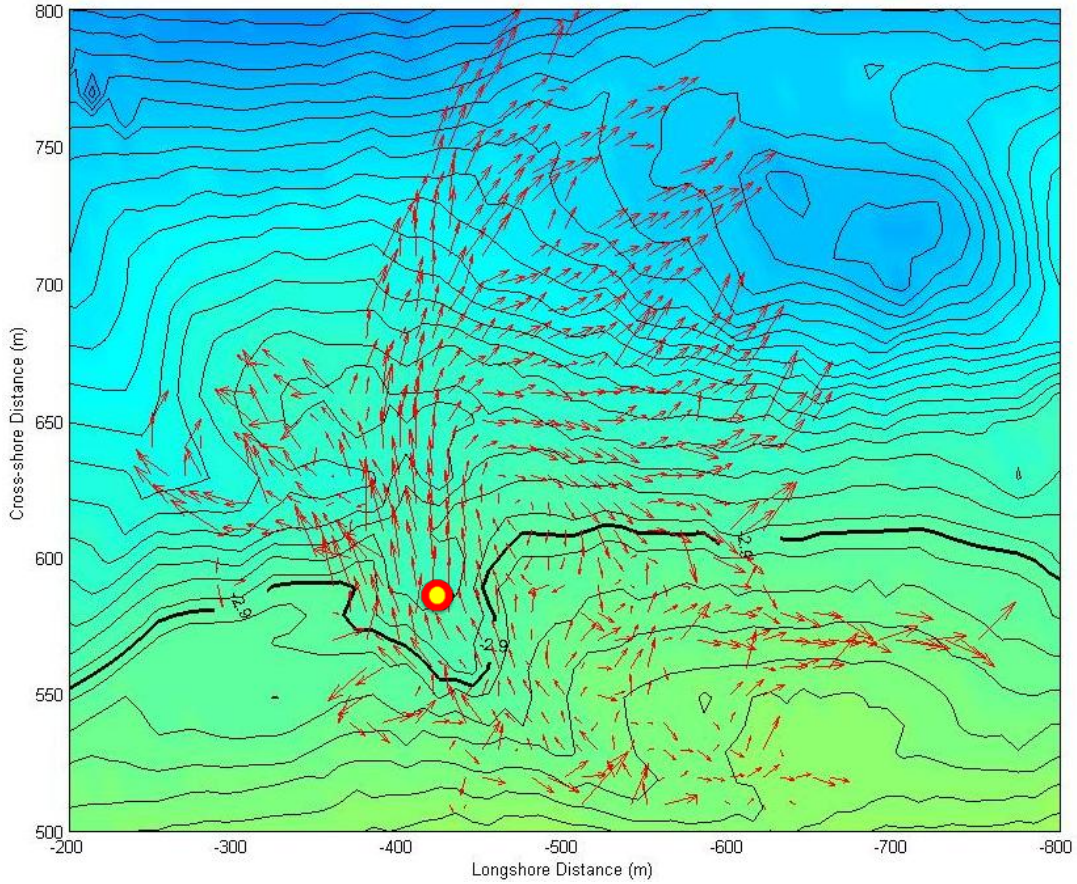

Figure 5: Beach morphology and averaged GPS drifter tracks from when bedform measurements in the rip were taken. The bold line represents the MLWS position; the circle indicates the rig position.

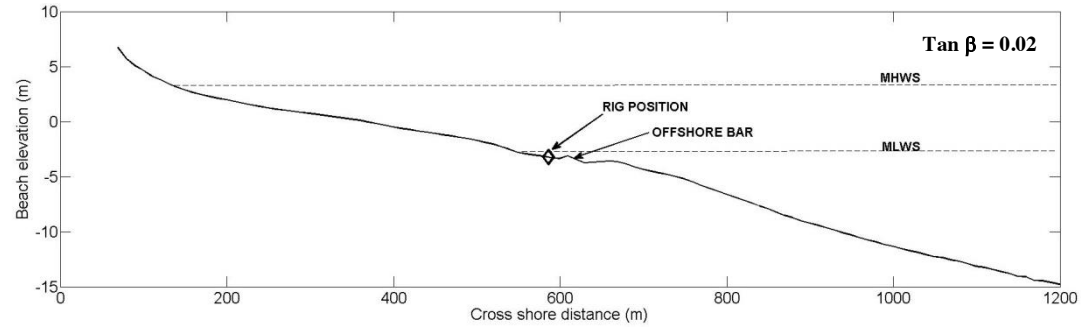

Figure 6: Beach profile through instrument position. Tan β of 0.02 indicates a gently sloping beach.

To process the drifter data, the nearshore zone surrounding the rip system was divided into 10 m x 10 m bins. The drifter observations (position and velocity) were averaged within each bin. Bins with over five drifter observations were deemed statistically significant. The resulting quiver plot is superimposed on the bathymetric map in Figure 5 and shows the rip flows in and around the rip system for approximately 2 hours either side of low tide. As H_s was small, wave breaking was minimized on the bar allowing drifters to exit the surfzone and flow up to 250 m offshore of the MLWS position. There was also evidence of circulation (especially to the south) of the rip channel. At the position of the instrumentation, flow was directly offshore.

In-situ hydrodynamic data are presented for Tides 1 and 2 as 10 minute means in Figure 7. The bedform dynamics are presented as three individual cases (Figure 8) chosen as they represent three distinct phases of bedform behaviour that are consistent throughout the whole data set. These cases are discussed in detail in the following section. The larger waves occurred in the ebb cycle of Tide 2 where H_s exceeded 1 m. At water depths of over approximately 2.5 m the mean flow is negligible. At all times in shallower water depths there is offshore flow at times reaching a maximum of 0.4 m/s. These are assumed to be rip current conditions; visual observations and comparison with lagrangian GPS drifter tracks support this assertion.

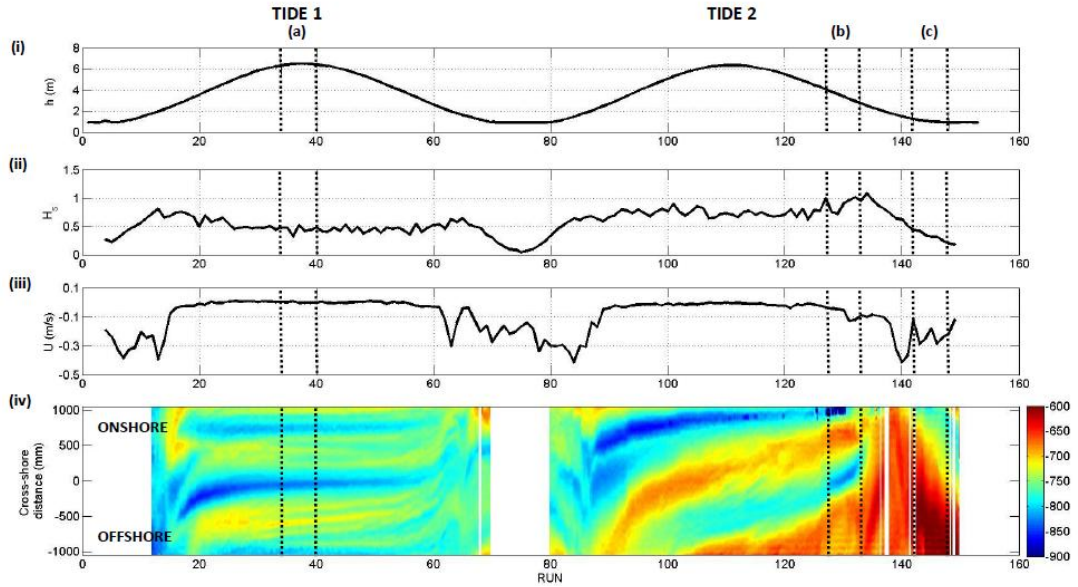

Figure 7: Time series over two tidal cycles of (i) *h* (m), (ii) H_s (m), (iii) *U* (m/s) and (iv) bed evolution. The colour bar is a reference for the bed height as a measurement of the distance below the scanner (mm). The three vertical bars mark out the high tide case (*a*), mid tide (*b*) case and rip current case (*c*).

Plot *iv* provides an overview of the bed and its evolution over time in relation to the hydrodynamic conditions. The 'hot' colours represent bedform crests and the 'cool' colours represent troughs. The blank spaces are where the water level was below the height of the SRP or where bubbles in the water inhibit the recording of the bed. Around high tide (represented by case *a*) stable (Tide 1) or slowly onshore migrating (Tide 2) bedforms of $\lambda = 1 - 1.5$ m occur in negligible mean flow and small waves. At mid tide (represented by case *b*), bedforms are of a similar size to those observed at high tide, but they migrate onshore at a much faster rate in weak offshore mean flow and larger waves. At lower tidal elevations, the instrument rig is in the rip current (small waves, strong offshore flow) and this is represented by case *c*. Under these conditions there is offshore migration of small features ($\lambda = \sim 0.5$ m) in the flood tide of Tide 2 and offshore migration of a much larger feature ($\lambda = \sim 3$ m) during the ebb tide. Bedform development during the three cases is discussed in more detail below.

Bedform Results

Each case (*a, b* and *c)* consists of one hour of data and is categorised based on tidal elevation as high tide (HT), mid tide (MT) and low tide (LT), with only the low tide case representing 'true' rip current conditions. The hydrodynamic conditions for each tide are presented in Table 1. The high tide case is characterised by negligible flow and a relatively small velocity variance (σ^2) and wave skewness (*S*). Wave skewness was calculated following Elgar et al. (1988), see Equation 1 below. At high tide the conditions may be considered to be in a low energy state. As tidal elevation decreased towards mid tide, represented by case *b*, H_s, *S* and σ^2 all increased, representing the transition to a higher energy state. During this time there was also a mean offshore flow of 0.07 m/s. As the tidal elevations fell further, the rip current became active and the values of H_s, T_p, *S* and σ^2 decreased slightly, and offshore mean flow of 0.26 m/s (upper 10 percentile of the mean flow (U_{10}) of 0.42 m/s) became the dominant hydrodynamic process.

$$S = \frac{<u(t)^3>}{<u(t)^2>^{3/2}} \qquad (1)$$

Table 1: Summary of key hydrodynamic parameters ($h, H_s, T_p, U, U_{10}, \sigma^2$, and S) for HT, MT and LT case

Case	Location	h (m)	H_s (m)	T_p (s)	U (m/s)	U_{10} (m/s)	σ^2 (m^2s^2)	S
a	HT	6.3	0.44	9.0	0.00	-0.01	0.02	0.13
b	MT	3.3	0.90	10.0	-0.07	-0.12	0.12	0.80
c	LT	1.2	0.42	6.6	-0.26	-0.42	0.08	0.77

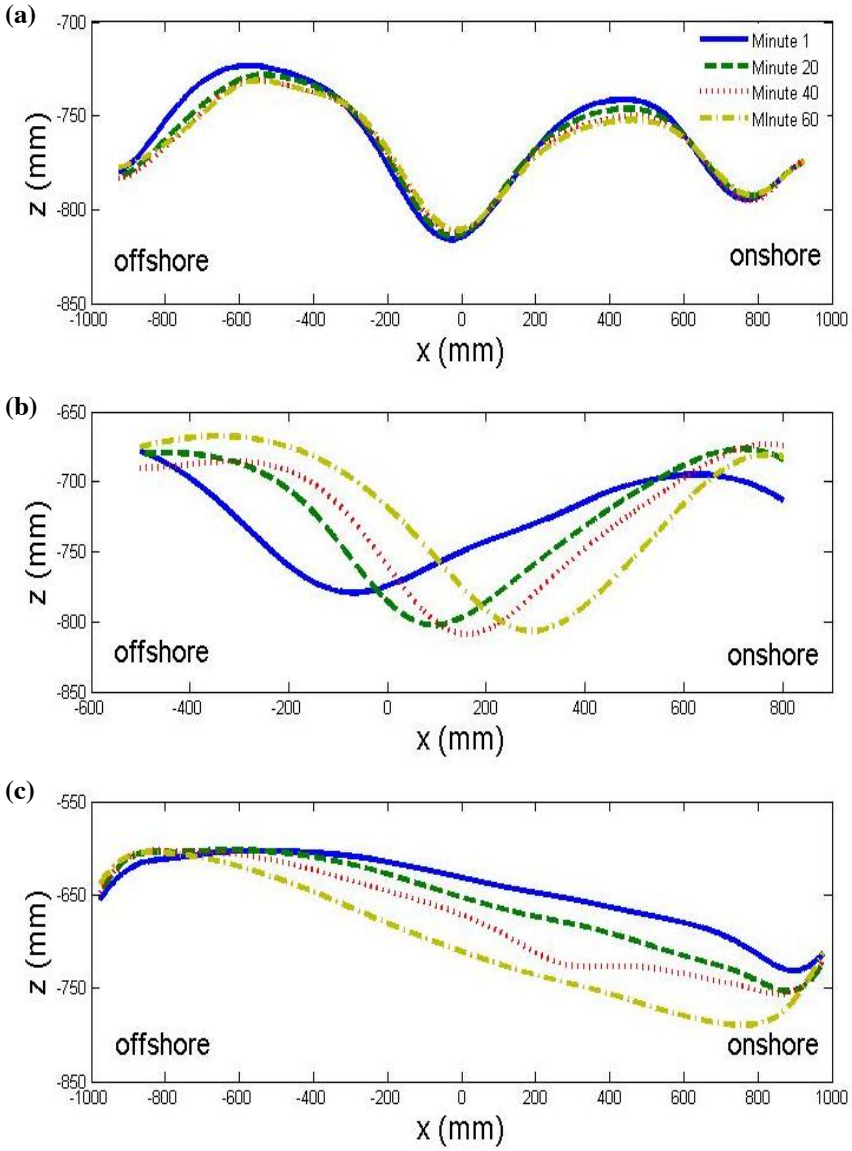

Figure 8: Individual bed scans at (a) high tide; (b) mid tide and (c) at low tide, 20 minutes apart over a one hour period. Note that the plots are not all of same scale.

Figure 8 shows the bed profiles derived from SRP scans for each identified case. During high (*a*) and mid tide (*b*) the bedforms appear to be symmetric and are at the lower end of the megaripple size range (during high tide: Δ = 0.09 m, λ = 1 m; during mid tide: Δ = 0.12 m, λ = 1.20 m). The main difference between these two cases is that at high tide the bed migrates very slowly onshore (M_r = 0.03 m/hr) and at mid tide there is significant onshore migration (M_r = 0.35 m/hr). During low tide, when measurements are being made in the rip current, the bedform height and length increases significantly to approximately 0.15 m and 3 m respectively and the bedform migrates offshore at a rate of 0.21 m/hr.

Table 2: Summary of bedform dynamics (Δ, λ and M_r) for HT, MT and LT cases.				
Case	Location	Δ (m)	λ (m)	M_r (m/hr)
a	HT	0.09	1.0	0.03
b	MT	0.12	1.2	0.35
c	LT	0.15	3.0	-0.21

Figure 9 highlights the change in migration dynamics with respect to water level and mean cross-shore velocity. Migration rate is calculated from individual scans 10 minutes apart of which the time of the first and last scan correspond to the start and end of each 'run' of hydrodynamic data. Negative migration is in the offshore direction. In the strong offshore flow of the rip current migration is offshore, at mid tide in weak offshore flows it is onshore, and at high tide it is very slow in the onshore direction. It appears that there is a threshold mean flow velocity of approximately -0.2 m/s around which the bedform migration changes direction, though it is likely that wave processes will affect this value.

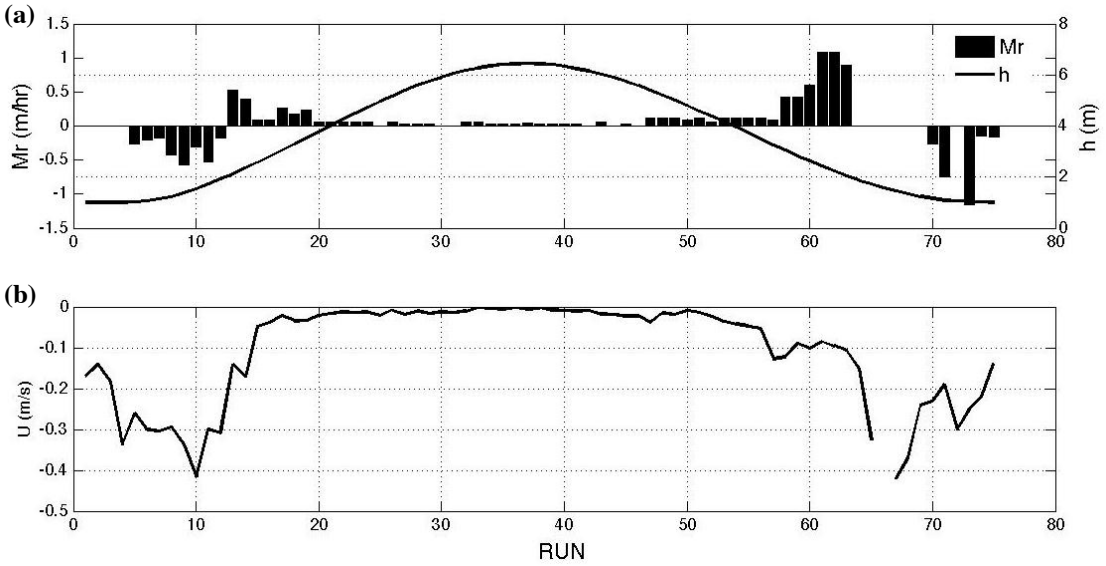

Figure 9: (a) Overview of migration rate (M_r) and direction (-ve = offshore) and rate in relation to water depth and (b) mean cross-shore velocity (taken from Tide 2).

DISCUSSION

Measurements of bedforms in a rip channel over a macro-tidal cycle have shown that there are a range of bedform behaviours and this appears to be in response to a variation in hydrodynamic conditions.

During active rip current conditions, measurements conformed well to observations reported in the literature (Aagaard et al., 1997; Brander, 1999b; Greenwood & Davidson-Arnott, 1979; Nielsen, 1992). Bedforms were of megaripple dimension, migrated offshore and had an asymmetric profile. The change of the profile of the megaripples at the onset of strong offshore flow from symmetric to asymmetric (with the stoss face downstream of the flow origin) supports Nielsen's (1992) observation that they are current dominated. Though the asymmetric profile indicates a current dominated regime, comparison between migration rates in this study and results obtained by Sherman et al. (1993) in a feeder channel suggests that waves may still have an influence. Sherman et al. (1993) recorded average migration rates of 0.99 m/hr, compared to the 0.21 m/hr recorded in this study at similar mean flow velocities (mean of 0.5 m/s). The key difference between these two environments is that in a feeder channel wave energy has been fully dissipated as waves break on the sandbar and that the current is generally at right angles to the wave direction, whereas in the rip waves propagate shoreward in opposition to the rip flow. This may have the effect of slowing the offshore migration of megaripples and may explain the difference in migration rates recorded in an otherwise similar environment.

Outside of rip current conditions the bedforms were observed to be symmetrical. Gallagher (2003) suggested this was due to the oscillatory motion of the waves. During the onshore stroke of a wave the sediment is moved shoreward along the ripple crest where it tumbles down the slip face into the trough.

Flow separation occurs just prior to the beginning of the offshore stroke of the wave which creates turbulence and suspends sediment; the offshore stroke then transports sediment offshore. Due to sediment moving in both directions a symmetrical profile occurs. If the waves are skewed the onshore stroke of the wave is stronger than the offshore stroke resulting in net sediment transport occurring in the onshore direction. Gallagher (2003) proposed this may result in onshore migration of bedforms. An initial investigation into skewness and velocity variance suggests that these may influence bedform migration rates in the non-rip cases. At mid tide, high values of wave skewness and velocity variance coincided with onshore bedform migration. At high tide wave skewness and velocity variance were found to be much lower and subsequently bedform migration was very slow in the onshore direction or non-existent. This suggests that both skewness and velocity variance are important processes outside of active rip current conditions in terms of bedform migration dynamics even though at mid-tide there was a weak mean offshore flow opposing the migration direction.

The megaripple length scale was found to be up to three times greater in active rip currents compared to non-rip conditions. At this stage it appears that an increase in wavelength is a response to the onset of strong offshore flow. Hoekstra et al. (2004) described a similar result of rapid bedform growth with increasing current velocities.

The results presented here show megaripples migrating at significant rates in both the onshore and offshore directions. It has been suggested that this may be an important mechanism for sediment transport (Gallagher et al., 1998). The migration of small scale bedforms (Δ = 0.015 m, λ = 0.15 m) (Kachel & Sternberg, 1971) and larger scale features (Δ = 0.4 – 0.1 m, λ = 0.6 – 1.7 m) (Hoekstra et al., 2004) have both been used as a proxy for bedload sediment transport.

In this study the net transport of the megaripples over a tidal cycle is a balance between onshore transport when the water is deep and the rip is not operating and offshore in the rip current when the water is shallow.

CONCLUSIONS

New measurements within a rip channel have found bedform dynamics to be dependent on waves, water depth and the occurrence of offshore directed flows in the rip channel. In an active rip current (U_{10} = -0.41 m/s) bedforms were found to be current dominated, exhibiting an asymmetric profile and migrating offshore (M_r = -0.21 m/hr). The increase in current velocity at the onset of rip current conditions also seems to have the effect of increasing megaripple length scale (Δ = 0.15 m, λ = 3 m) by up to three times the lengths recorded in non-rip conditions (Δ = 0.09 – 0.12 m, λ = 1 – 1.2 m). In non-rip conditions bedforms were observed to be symmetrical due to the back and forth movement of sediment driven by oscillatory wave motion. At mid tide skewed waves and an increased velocity variance appear to induce significant onshore megaripple migration (M_r = 0.35 m/hr), which was reduced at high tide (M_r = 0.03 m/hr) when wave skewness and velocity variance decreased.

REFERENCES

Aagaard, T., Greenwood, B. & Nielsen, J. 1997. Mean currents and sediment transport in a rip channel, *Marine Geology*, 140 (1-2), 25-45.

Austin, M., Scott, T., Brown, J., Brown, J., MacMahan, J., Masselink, G. & Russell, P. 2010. Temporal observations of rip current circulation on a macro-tidal beach, *Continental Shelf Research*, 30 (9), 1149-1165.

Brander, R. W. 1999a. Field observations on the morphodynamic evolution of a low-energy rip current system, *Marine Geology*, 157 (3-4), 199-217.

Brander, R. W. 1999b. Seiment Transport in Low Energy Rip Current Systems, *Journal of Coastal Research*, 15 (3), 839-849.

CCO 2012. Channel Coast Observatory, [Online]. Available at: http://www.channelcoast.org/data_management/real_time_data/charts/?chart=76 (Accessed: 23/11/2011).

Elgar, S., Guza, R. T. & Freilich, M. H. 1988. Eulerian Measurements of Horizontal Accelerations in Shoaling Gravity Waves, *Journal of Geophysical Research*, 93 (C8), 9261-9268.

Gallagher, E. L. 2003. A note on megaripples in the surf zone: evidence for their relation to steady flow dunes, *Marine Geology*, 193 (3-4), 171-176.

Gallagher, E. L., Elgar, S. & Thornton, E. B. 1998. Megaripple migration in a natural surf zone, *Nature*, 394 (6689), 165-168.

Greenwood, B. & Davidson-Arnott, G. D. 1979. Sedimentation and equilibrium in wave-formed bars: a review and case study, *Journal of Earth Science*, 312-332.

Hoekstra, P., Bell, P., van Santen, P., Roode, N., Levoy, F. & Whitehouse, R. 2004. Bedform migration and bedload transport on an intertidal shoal', *Continental Shelf Research*, 24 (11), 1249-1269.

Kachel, N. B. & Sternberg, R. W. 1971. Transport of bedload as ripples during an ebb current', *Marine Geology*, 10 (4), 229-244.

MacMahan, J. H., Thornton, E. B. & Reniers, A. J. H. M. 2006. Rip current review, *Coastal Engineering*, 53 (2-3), 191-208.

MacMahan, J. H., Thornton, E. B., Stanton, T. P. & Reniers, A. J. H. M. 2005. RIPEX: Observations of a rip current system, *Marine Geology*, 218 (1-4), 113-134.

Nielsen, P. 1992. *Coastal bottom boundary layers and sediment transport*. Advanced series on ocean engineering. London: World Scientific.

Schmit, W. B., Woodward, K., Millikan, R., Guza, R. T., Raubenheimer, B. & Elgar, S. 2003. A GPS-tracked surf zone drifter, *Journal of Atmospheric and Ocean Technology*, 1069-1075.

Sherman, D. J., Short, A. D. & Takeda, I. 1993. Seiment Mixing-Depth and Bedform Migration in Rip channels, *Journal of Coastal Research*, 39-48.

Suspended Sediment Transport in Rip Currents on a Macrotidal Beach

www.cerf-jcr.org

Antony Thorpe, Jon Miles, Gerd Masselink, Paul Russell, Tim Scott and Martin Austin

School of Marine Science and Engineering,
University of Plymouth, Plymouth,
PL4 8AA, UK
athorpe1@plymouth.ac.uk
j.r.miles@plymouth.ac.uk
gerd.masselink@plymouth.ac.uk
p.russell@plymouth.ac.uk
timothy.scott@plymouth.ac.uk
martin.austin@plymouth.ac.uk

www.JCRonline.org

ABSTRACT

Thorpe, A., Miles, J., Masselink, G., Russell, P., Scott, T., Austin, M., 2013. Sediment Transport In Rip Currents on a Macrotidal Beach, *Proceedings 12th International Coastal Symposium* (Plymouth, England), *Journal of Coastal Research*, Special Issue No. 65, pp. xxx-xxx, ISSN 0749-0208.

Rip currents are offshore-directed flows in the surf zone that may be responsible for significant offshore transport of sediment. In this study high frequency surface elevation and current velocity data were collected alongside suspended sediment concentrations in a rip channel on a high energy, macro-tidal beach. At low tide (water depth over the rip channel (h) = 0.9 m), when the rip current was active (maximum offshore directed flow = ~ 0.4 m/s), net suspended sediment transport was directed offshore, and 88% of the flux was due to the mean flow component. The rip current was found to pulse at very low frequencies (VLF) and this contributed significantly to offshore sediment transport, accounting for 48% of total oscillatory flux (not considering direction). Infra-gravity (IG) frequency oscillations had a marginal contribution to offshore sediment transport within the rip (10% of total oscillatory flux) and incident wave transport was onshore (42% of total oscillatory flux). The relative influence of the wave component increased as tidal elevations increased and the rip current became inactive. For comparison, at mid-tide (h = 3.5 m) the total suspended sediment flux was in the offshore direction and four times less than during low tide. The mean flux accounted for 34% of the total transport at mid-tide. At high tide (h = 6.1 m) the total sediment transport was in the onshore direction due to the incident waves, with a 0% contribution from the mean flux.

ADDITIONAL INDEX WORDS: *Rip Currents, Suspended Sediment Transport, Megaripples, Field Measurements*

INTRODUCTION

Rip currents are a unique feature of the nearshore environment typically exhibiting a narrow, strong, quasi-steady, offshore flow (in the order of 0.5 m/s) that dissects the wave dominated surf zone and dissipates beyond the breaker zone (MacMahan et al., 2005). Rips are a mass balance response to wave induced onshore transport. Wave breaking is focused on sandbars and minimized in the rip channel; as a result water travels alongshore in feeder channels before flowing seaward within the rip neck (MacMahan et al., 2006). Rips are typically found at lower tidal elevations where they are associated with the bar/rip morphology of intermediate state beaches (Brander, 1999a).

Although there is limited research on the quantification of sediment transport in rips (Aagaard et al., 1997; Brander, 1999b), there is a consensus among coastal scientists that rips are an important mechanism for the offshore transport of sediment (Cook, 1970; Short, 1985; MacMahan et al., 2005) and ultimately affect the beach morphology (Brander, 1999a; Thornton et al., 2007). Both Aagaard et al. (1997) and Brander (1999b) observed mean suspended sediment flux to be maximised around low tide when mean flow velocities were greatest. Aagaard et al. (1997) found the mean flux was the dominant mode of suspended sediment transport. Infra-gravity oscillations were found to be efficient at entraining sediment and had a small contribution to offshore transport, with incident wave component being responsible for onshore transport. Offshore sediment flux ceased as tidal elevation increased and the rip became inactive with weak onshore transport taking place as a result of weak onshore mean flow and gravity waves.

The aim of this paper is to investigate further the processes driving sediment transport within an active rip current in order to quantify the relative contribution of incident waves, infra-gravity waves and very low frequency oscillations to the total suspended load transport.

METHODS

Study Site

The study site, Perranporth, is a 3.5 km long beach located on the North Coast of Cornwall, UK (Figure 1). Perranporth is a highly energetic beach with an annual significant wave height (H_s) of 1.6 m and a peak period (T_p) of 10.5 s (Austin et al., 2010). It faces west-northwest, is exposed to Atlantic swell and also receives locally generated wind waves. It is a macro-tidal beach with a mean spring range of 6.3 m and consists of medium sized sand (D_{50} = 0.28 – 0.34 mm). The beach lies on the boundary of the intermediate and dissipative classifications with pronounced

DOI: 10.2112/SI65-xxx.1 received Day Month 2012; accepted Day Month 2013.

low tide bar/rip morphology on a seasonal time scale (Austin et al., 2010).

During the fieldwork the beach exhibited a rhythmic bar/rip system throughout the length of the beach. The rip used for the study was chosen because it offered a clearly defined channel with offshore flow dissecting the intertidal bar.

Field Measurements

Offshore wave data were collected from a Directional Wave Rider (DWR) wave buoy located approximately 1 km offshore of the study site (see Figure 1). In-situ data were collected using a range of instruments secured to a mobile rig (Figure 2). The rig was assembled prior to deployment and carried into the rip channel at spring low tide.

The flow velocities, waves and tidal elevation in the rip channel were recorded with a Nortek Vector 3D-Acoustic Doppler Velocimeter (ADV) fitted with an internal Pressure Transducer (PT). The head of the ADV was carefully aligned to measure cross-shore and longshore flows with the sensing volume set at 0.55 m above the bed. The PT, used to measure wave statistics and tidal elevation was housed in the ADV casing unit with the sensor positioned at a height of 0.2 m above the bed. Suspended sediment measurements were made with Optical Backscatter Sensors (OBS), deployed at 0.25 and 0.4 m above the bed. The OBSs were pre- and post-calibrated at a range of 0–4000 Nephelometric Turbidity Units (NTU) with a known concentration of local sediment suspended in glycerol using the method developed by (Butt et al., 2004). Data from the ADV, PT and OBS were logged autonomously at 8 Hz.

Intertidal surveys of the beach elevation were carried out at low tide using a Real Time Kinematic GPS (RTK-GPS) mounted on an All-Terrain Vehicle (ATV). Sub-tidal surveys were carried out using a RTK-GPS in conjunction with a single beam echo sounder mounted on a Jet Ski, overlapping the intertidal surveys. The two sets of survey data were combined and interpolated onto a normal grid and fitted to a local co-ordinate system (Austin et al., 2010). Lagrangian drifters, based on a design by Schmit et al. (2003), were used to measure rip flows and to identify the overall location of the rip current.. The drifters were fitted with GPS receivers and data loggers capable of recording raw carrier phase satellite data at 1 Hz, which were subsequently processed from a survey grade base station. The drifter data provided estimates of rip flow with a positional accuracy of <0.4 m and an accuracy of the flow velocity estimates of 0.01 m/s (Austin et al., 2010).

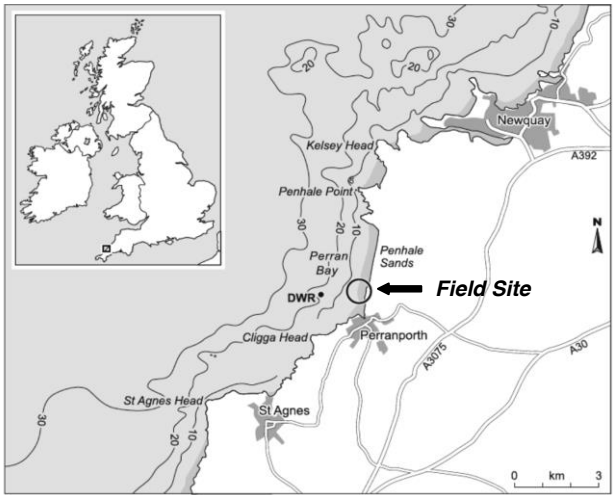

Figure 1. Map showing location of the study site and location within the UK and the position of the Directional Wave Rider buoy (DWR) (Austin et al., 2010).

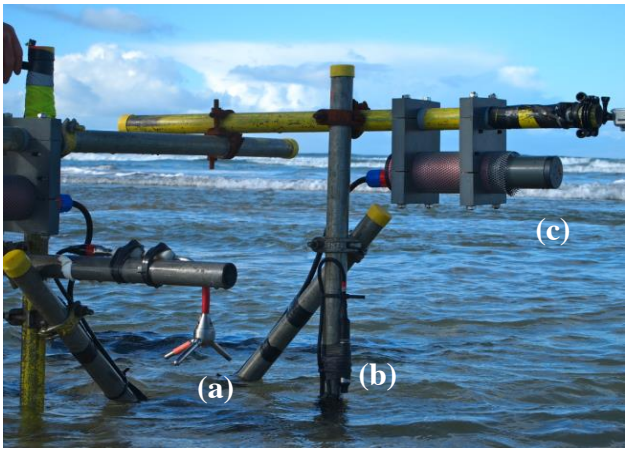

Figure 2. Rig design and position of instruments; (a) ADV head, (b) OBS and (c) a Sand Ripple Profiling Sonar (SRPS). The picture was taken at low tide; at mid-tide and high tide the rig is completely submerged.

RESULTS

Environmental Conditions

Data are presented from one tidal cycle over the 15th October, 2011, when a clear rip current was present centred on the instrument rig. The maximum water depth over the rip channel was 6.3 m. Wave conditions measured at the offshore wave buoy were characterised by H_s = 0.7 m and T_p = 10 s. Figure 3 shows the in-situ hydrodynamic conditions. The largest waves occurred during the ebb phase of the tide when H_s exceeded 1 m giving rise to the largest amount of wave stirring ($U_m = \sqrt{\delta\sigma_u}$). At water depths in excess of approximately 2.5 m the mean flow (U) is negligible. At all times in shallower water depths there is a mean offshore flow, at times reaching a maximum of 0.4 m/s (calculated as an average of 10 minute sections of data). This is considered to be rip current conditions. Visual observations and comparison with Lagrangian GPS drifter tracks support this assertion. The morphology of the study area is shown in Figure 4. The landward margin of the rip channel is clearly defined by the shoreward bend in the mean low water spring (MLWS) position (bold line). The channel is shore-normal, and is situated between two sand bars. At its largest the rip was visually observed to be approximately 50 m wide and 150 m in length. To process the drifter data, the nearshore zone and surrounding the rip system was divided into 10 m x 10 m bins. The drifter observations (position and velocity) were averaged within each bin. Bins with over five drifter observations were deemed statistically significant (Austin et al., 2010). The resulting quiver plot is superimposed on the bathymetric map in Figure 4 and shows the rip flows in and around the rip system for approximately 2 hours either side of low tide. As H_s was small, wave breaking was minimized on the bar allowing drifters to exit the surfzone and flow up to 250 m offshore of the MLWS position. There was also evidence of circulation (especially to the south) of the rip channel. At the position of the instrumentation, the mean drifter tracks indicated a

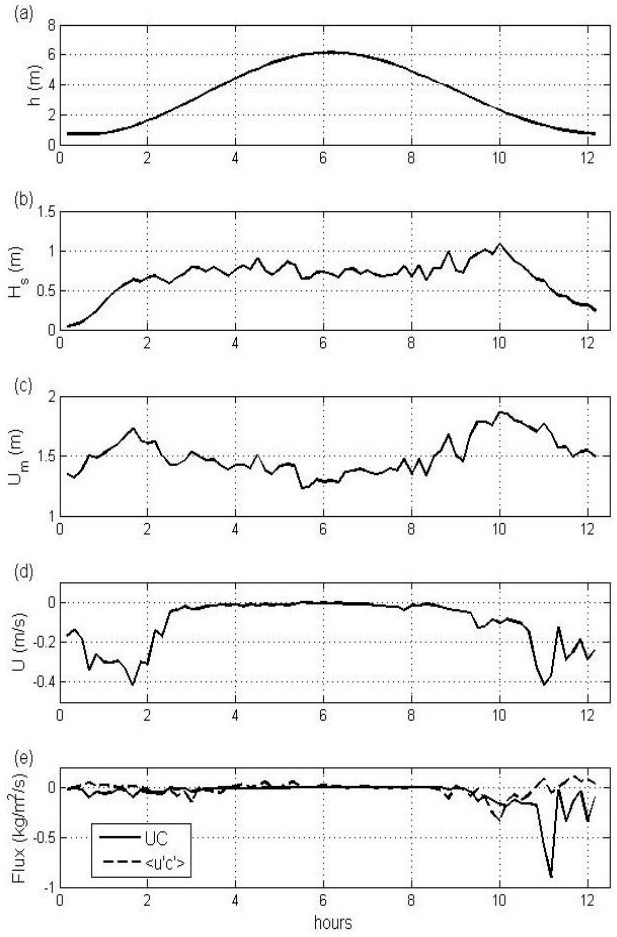

Figure 3. Hydrodynamic variables and suspended sediment flux as 10 minute means; (*a*) water depth (*h*), (*b*) significant wave height (H_s), (*c*) wave stirring (U_m), (*d*) mean cross-shore velocity (*U*), and (*e*) mean flux (*UC*) and oscillatory flux <u'c'> calculated from the ADV and OBS (z = 0.55 m and 0.25 m respectively).

mean offshore flow. For more detailed description of rip circulation patterns, refer to (Austin et al., 2010).

Suspended Sediment Flux

Following Jaffe et al. (1984) suspended sediment flux is partitioned into a mean flux (*UC*) and oscillatory flux <*u'c'*> and presented alongside the hydrodynamic parameters for the whole tide in Figure 3e. Sediment concentration data were collected at 0.25 m and velocity data were collected at 0.55 m. Velocity was assumed to be vertically uniform. The sediment flux is minimal for both modes of transport on the flood tide, though during the ebb tide sediment transport is significantly larger (coinciding with an increase in H_s and U_m (Figures 3b & 3c)) and dominated by the mean flux with the oscillatory flux fluctuating between the onshore and offshore direction. The maximum mean flux (~ 0.9 kg/m^2/s) was obtained during the fastest offshore flows (~ 0.4 m/s) in water depths and wave heights of approximately 1 m and 0.5 m respectively.

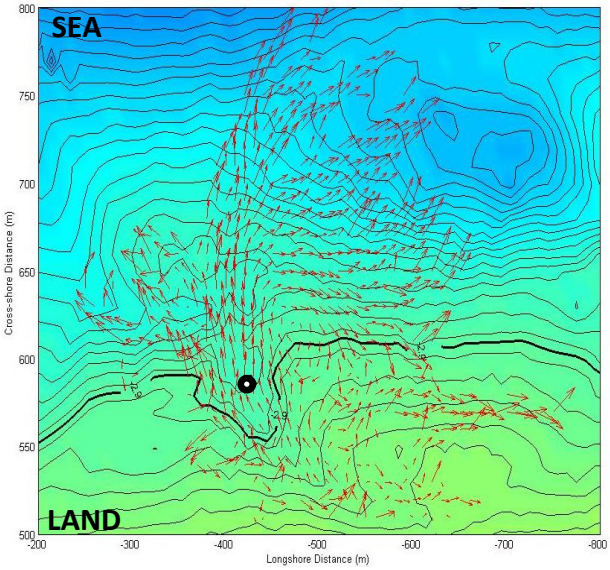

Figure 4. Beach morphology and averaged GPS drifter tracks. The bold line represents the MLWS position; the circle indicates the rig position.

Due to the macrotidal range of the beach the nearshore conditions changed considerably during a tidal cycle. The mean variables are presented for 60 minutes of data collected at low tide, mid-tide (both during the flood tide) and high tide in Table 1. At low tide (h = 0.9 m), rip current conditions dominated, characterised by small waves and strong offshore mean flow. At mid-tide (h = 3.5 m) waves were larger and a weak offshore flow existed. At high tide (h = 6.1 m) waves were of intermediate size and rip flow was negligible. Table 1 also shows the percentage contribution to sediment flux from the mean component (*UC*) and the oscillatory component <*u'c'*>. During rip conditions 88% of the total transport was due to the mean flux; at mid-tide this was 34%. At high tide 100% of the flux was due to the oscillatory component.

In Figure 5, instantaneous cross-shore velocity data with a 1-minute running mean and simultaneous concentration data are presented for low tide, mid-tide and high tide (for the time corresponding to the variables presented in Table 1). The rip current velocities at low tide were found to pulse at very low frequencies (VLF) with a period of approximately 15 to 20 minutes. These pulses can be seen in the instantaneous data (Figure 5d) and appear to be efficient in suspending sediment (Figure 5*a*) with peak concentrations of 10-40 g/l (compared to a mean of 1 g/l), coinciding, with offshore pulses. Infra-gravity (IG)

Table 1. Overview of the hydrodynamic variables and sediment flux. H_s = significant wave height; T_p = peak wave period; h = water depth; δh = change in water depth over 60 minutes; U = mean cross-shore velocity and U_{10} = upper 10 percentile of U, *UC* = mean flux and *uc* = wave driven flux.

	h (m)	H_s (m)	T_p (s)	δh (m)	U (m/s)	U_{10} (m/s)	*UC* (%)	*u'c'* (%)
LT	0.9	0.40	6.5	0.5	-0.25	-0.40	88	12
MT	3.5	0.93	10	1.3	-0.05	-0.10	34	66
HT	6.1	0.70	9.7	0.0	0.00	-0.02	0	100

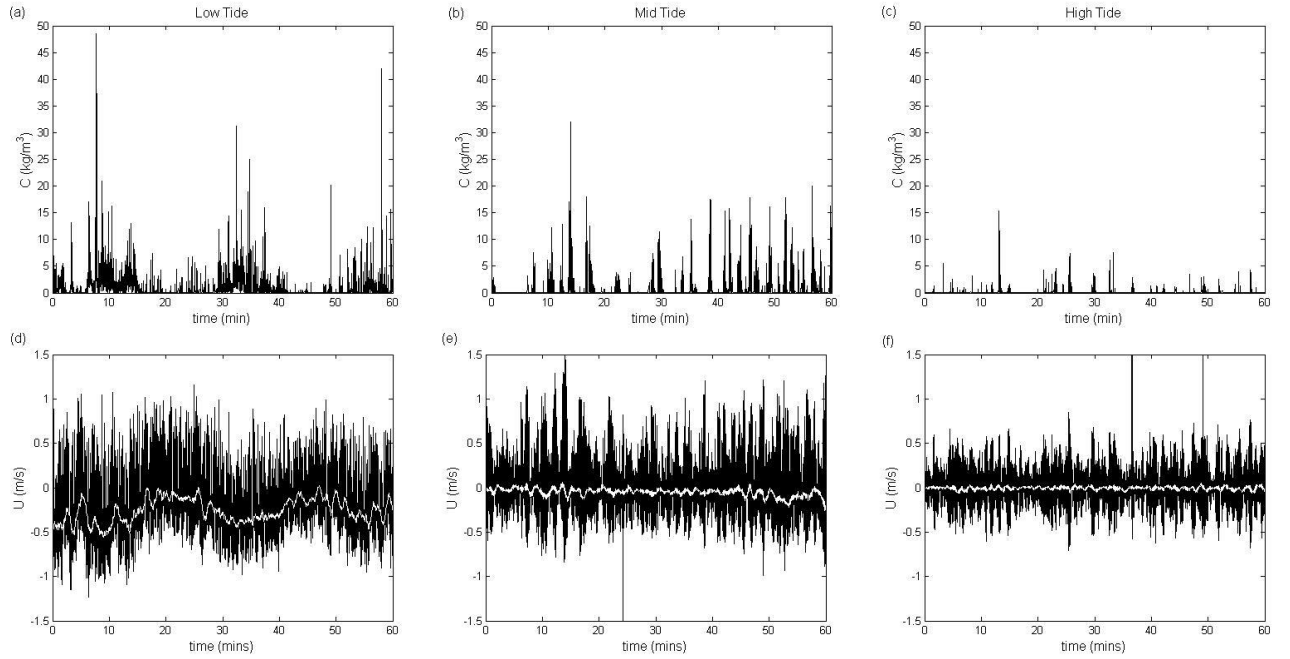

Figure 5. Instantaneous sediment concentration at 0.25 m above the bed for (*a*) low tide, (*b*) mid-tide and (*c*) high tide and instantaneous cross-shore velocity (*U*) data for (*d*) low tide, (*e*) mid-tide and (*f*) high tide. The white line is a 1-minute running mean.

pulses are also present within the raw velocity data; these are of approximately a 2 minute period.

At mid-tide VLF pulses and rip flow were absent; however IG pulses were present within the velocity data. Sediment suspension appears to be synchronous with IG oscillations. At high tide, the raw velocity time series is dominated by gravity waves with no VLF or IG frequency oscillations present. Sediment suspension is much lower than during low tide and mid-tide and appears to be in response to incident waves.

To investigate further the contribution of the oscillatory component to the sediment flux, cross-spectral analysis was undertaken on the 60 minutes of data from low tide, mid-tide and high tide (Figure 6). For the analysis, 4 non-overlapping and 3 overlapping windows were used giving 12 degrees of freedom (Nuttal, 1971). For the co-spectral analysis 95% confidence in the coherence was obtained for coherences greater than 0.45. At low tide, during rip current conditions (Figure 6*a*), a dip in the cross-shore velocity spectra (*u*) exists at 0.0039 Hz. This point is nominally used as the boundary between the VLF and IG bands (> 256 s).

The spectra show that the energy peak in the VLF band was greater than any other band and that VLF oscillations are the largest component of the oscillatory flow during low tide. The spectrum for the sediment concentration (*c*) also shows the highest energy in the VLF band. The IG band encompassed frequencies from 0.0039 Hz to 0.03 Hz (256-33 s). A trough at 0.03 Hz was chosen as the boundary between IG and G frequencies as it also exists at mid-tide and high tide. Within the IG and G bands peaks are present in the spectra of *u* and *c*. At low tide the co-spectra of *u* and *c* show significant offshore transport in the VLF band. The co-spectra crosses zero very close to the VLF – IG boundary. In the IG band sediment transport direction fluctuates between onshore and offshore, but the net is in the offshore direction. In the gravity band there is relatively small amount of onshore transport.

At mid-tide, no VLF signature is detected in the spectra of *u* or *c*. However, the spectra for both *u* and *c* have peaks in the IG and G bands. The co-spectra for the mid-tide *u* and *c* data shows offshore transport in the IG band and a fluctuating transport direction in the G band. At high tide the *u* and *c* spectra are dominated by a peak in the gravity band, though of lower energy than the peak at mid-tide. The co-spectra for *u* and *c* show a small amount of onshore transport at G frequencies.

The oscillatory components of *u* and *c* were filtered and used to calculate the contributions to the sediment flux at VLF, IG and G frequencies. A high-pass filter was applied with a cut off of 0.03 Hz to isolate the G band. A low-pass filter was used at 0.0039 Hz

Table 2. Suspended sediment transport rates ($kg/m^2/s$) for the mean component (*UC*), oscillatory component $\langle u'c' \rangle$, the VLF, IG and G bands and the total transport (UC_{TOTAL}) for low tide, mid-tide and high tide.

	UC	$\langle u'c' \rangle$	$\langle u'c' \rangle_{VLF}$	$\langle u'c' \rangle_{IG}$	$\langle u'c' \rangle_{G}$	UC_{TOTAL}
LT	-0.246	-0.034	-0.102	-0.021	0.089	-0.280
MT	-0.026	-0.050	-0.007	-0.025	-0.018	-0.076
HT	0.000	0.006	0.000	-0.002	0.008	0.006

Table 3. Percentage contribution to the total oscillatory flux from VLF, IG and G frequency oscillations (transport direction not considered).

	$\langle u'c' \rangle_{VLF}$ (%)	$\langle u'c' \rangle_{IG}$ (%)	$\langle u'c' \rangle_{G}$ (%)
LT	48	10	42
MT	14	50	36
HT	0	20	80

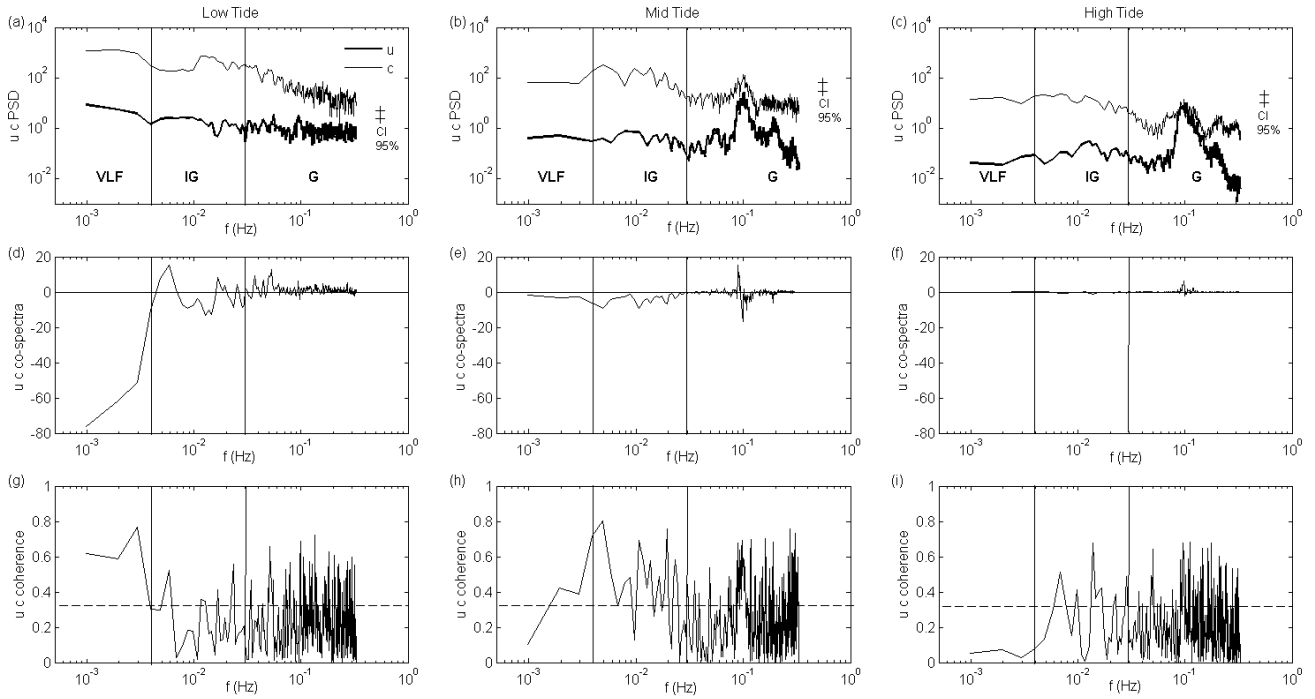

Figure 6. Power spectral density (PSD) of cross-shore velocity (*u)* ($m^2/s^2/Hz$) and concentration (*c*) ($(kg/m^3)^2/Hz$) for (*a*) low tide, (*b*) mid-tide and (*c*) high tide; Co-spectra for *u* and *c* ($kg/m^2/s/Hz$) for (*d*) low tide, (*e*) mid-tide and (*f*) high tide and coherence (*g*, *h* and *i*) corresponding to the co-spectra with the 95% confidence interval marked with dashed horizontal line. Vertical lines mark the boundaries of VLF, IG and G frequencies.

to separate the VLF band. A band-pass filter was used to isolate the IG component. This is presented in Table 2 alongside the total flux and the contribution from the mean flux.

At low tide the mean flux associated with the offshore flow of the rip was found to be the dominant mode of transport, with a significant offshore contribution from the VLF component and a minor contribution from the IG component whilst at gravity frequencies transport was onshore. At mid-tide the mean flux was an order of magnitude less than during low tide. The VLF signature is negligible whilst a small amount of offshore transport occurred at IG and G frequencies. At high tide there was weak onshore transport due to incident waves. Table 3 shows the contribution to the total oscillatory flux. VLF oscillations account for 48%, highlighting their importance to sediment transport. As the tidal elevation increases VLF and IG frequency oscillations decrease in importance

DISCUSSION

Suspended sediment transport in rip currents was found to principally be a result of the quasi-steady offshore mean flows of the rip with oscillatory flows playing a secondary role. Results presented here agree with both Aagaard et al. (1997) and (Brander, 1999b) that sediment flux increases with increasing current velocity at lower tidal elevations.

Over the tidal cycle there is asymmetry in the suspended flux (Figure 3e) with a much larger flux in the ebb tide than the flood tide. This may be due to increased wave stirring on the ebb tide as a result of an increase in wave height. Another explanation may be due to changes in the OBS sensor height above the bed due to the presence of bedforms. Simultaneous bedform measurements (see Thorpe et al. (2012) found megaripples with lengths and heights of 3 m and 0.15 m respectively to be present in the rip channel.

The rip was found to exhibit velocity oscillations at very low frequencies reaching up to 1 m/s on a timescale of 15 – 20 minutes. The presence of strong VLF velocity signals in rip in both high and low energy conditions have been observed by Bruneau et al. (2009), Bonneton et al. (2006), MacMahan et al. (2004a) and Reniers et al. (2007). Here we showed, using co-spectral analysis, that the VLF oscillations are responsible for significant amounts of sediment transport. Instantaneous data showed sediment suspension to be synchronous with offshore VLF velocity pulses, with suspension occurring at VLF frequencies. Model results obtained by Orzech et al. (2011) showed that whilst sediment transport was principally dominated by mean flows, VLF oscillations in both sediment concentration and flow were significant.

Filtering of the wave driven component of the flux found transport at VLF frequencies to be the biggest contributor to wave driven flux and accounted for approximately a third of the mean flux component. VLF oscillations acting as both a stirring and transport mechanism was also observed by Aagaard and Greenwood (1995) on a barred beach during a storm. Miles et al. (2002) identified that the offshore directed flows in shear wave oscillations at far infra-gravity frequencies (similar range to VLF identified here), on an intertidal bar on a micro-tidal beach, have the potential to enable sediment suspension by enhancing the mean current such that the velocity exceeds the threshold for suspension. It is possible that a similar mechanism is working here.

Within the rip current infra-gravity and gravity frequency signals were also present. The infra-gravity oscillations were of a

approximately a 2-minute period. MacMahan et al. (2004b) attributed the IG pulses to infra-gravity standing waves. The co-spectra of *u* and *c* show a varying direction of transport at IG frequencies and this is why the net IG flux is low. The gravity signal, attributed to incident waves was responsible for onshore transport. Aagaard et al. (1997) used a similar method to study suspended sediment transport in rip currents, finding a small offshore contribution from IG oscillations and a slightly larger, onshore contribution from incident waves. They did not identify any VLF signals. It appears that in the absence of VLF pulses net oscillatory transport is onshore, whereas the data presented here shows net wave driven transport is offshore. The presence of a VLF signal appears to be crucial in determining the direction of net oscillatory transport.

At mid-tide rip flow and VLF velocity pulses were absent. The total flux was offshore, of which the mean flux accounted for 34%, showing the diminishing influence of the rip flow at higher tidal elevations. In both the *u* and *c* spectra, peaks existed in the IG and G band. All modes of transport were offshore. At high tide the velocity spectra was dominated by a G frequency signal, sediment transport rates were low compared to low tide and in the onshore direction due to incident waves.

The data here suggest that rip currents play an important part in offshore transport of sediment. Morphologically, they are therefore likely to make an important contribution to processes such as the deepening of channels, and the re-distribution of sediment from the shoreward side of sandbars to regions outside the surf zone, and beyond the extent of the undertow. Further work is on-going to quantify the relative contribution of rip current sediment transport to the overall nearshore sediment transport budget.

CONCLUSION

Offshore suspended sediment transport in a rip was dominated by the mean flux component (88%). During times when the rip current was active sediment transport rates were at least four times greater than at higher tidal elevations when it was inactive and directed offshore.

The rip current was found to pulse at very low frequencies (VLF) with a timescale of 15 to 20 minutes. These pulses were the most important mode of oscillatory driven offshore sediment transport (0.102 kg/m^2/s) at low tide, accounting for 48% of the total oscillatory flux. Infra-gravity (IG) oscillations were also present, they transported sediment offshore at 0.021 kg/m^2/s, and incident waves transported sediment onshore at 0.089 kg /m^2/s. At higher tidal elevations rip flow and VLF pulses were absent, though IG oscillations were still present at mid-tide and contributed to the total sediment transport, which was in the offshore direction. At high tide incident waves were responsible for onshore transport.

ACKNOWLEDGEMENTS

This work is part of the first author's PhD. We would like to acknowledge the Natural Environment Research Council (NERC) for their funding of the PhD studentship (ref no: NE/I528550/1).

We would also like to thank the DRIBS (Dynamics of Rip Currents and Implications for Beach Safety) project (grant ref no: NE/H004262/1) for providing technical assistance and use of the infra-structure in place for their fieldwork.

LITERATURE CITIED

Aagaard, T. & Greenwood, B. 1995. Longshore and cross-shore suspended sediment transport at far infragravity frequencies in a barred environment. *Continental Shelf Research*, 15, 1235-1249.

Aagaard, T., Greenwood, B. & Nielsen, J. 1997. Mean currents and sediment transport in a rip channel. *Marine Geology*, 140, 25-45.

Austin, M., Scott, T., Brown, J., Brown, J., MacMahan, J., Masselink, G. & Russell, P. 2010. Temporal observations of rip current circulation on a macro-tidal beach. *Continental Shelf Research*, 30, 1149-1165.

Bonneton, N., Bonneton, P., Senechal, N. & Castelle, B. 2006. Very Low Frequency rip current pulsations during high energy conditions on a meso-macro tidal beach, *International Conference on Coastal Engineering*. San Diego, USA.

Brander, R. W. 1999a. Field observations on the morphodynamic evolution of a low-energy rip current system. *Marine Geology*, 157, 199-217.

Brander, R. W. 1999b. Seiment Transport in Low Energy Rip Current Systems. *Journal of Coastal Research*, 15, 839-849.

Bruneau, N., Castelle, B., Bonneton, P., Pedreros, R., Almar, R., Bonneton, N., Bretel, P., Parisot, J.-P. & Sénéchal, N. 2009. Field observations of an evolving rip current on a meso-macrotidal well-developed inner bar and rip morphology. *Continental Shelf Research*, 29, 1650-1662.

Butt, T., Miles, J., Ganderton, P. & Russell, P. 2004. A simple method for calibrating optical backscatter sensors in high concentrations of non-cohesive sediments. *Marine Geology*, 192, 419-424.

Cook, D. O. 1970. The occurrence and geologic work of rip currents off southern California. *Marine Geology*, 9, 173-186.

Jaffe, A., Sternberg, R. W. & Sallenger, J. A. H. 1984. The Role of suspeneded sediment in shore-normal beach profile change, *International Conference on Coastal Engineering*. Houston.

MacMahan, J. H., Reniers, A. J. H. M., Thornton, E. B. & Stanton, T. P. 2004a. Surf zone eddies coupled with rip current morphology. *Journal of Geophysical Research-Oceans*, 109

MacMahan, J. H., Reniers, A. J. H. M., Thornton, E. B. & Stanton, T. P. 2004b. Infragravity rip current pulsations. *Journal of Geophysical Research-Oceans*, 109

MacMahan, J. H., Thornton, E. B. & Reniers, A. J. H. M. 2006. Rip current review. *Coastal Engineering*, 53, 191-208.

MacMahan, J. H., Thornton, E. B., Stanton, T. P. & Reniers, A. J. H. M. 2005. RIPEX: Observations of a rip current system. *Marine Geology*, 218, 113-134.

Miles, J. R., Russell, P. E., Ruessink, B. G. & Huntley, D. A. 2002. Field observations of the effect of shear waves on sediment suspension and transport. *Continental Shelf Research*, 22, 657-681.

Nuttal, A. H. 1971. *Spectral estimation by means of overlapped FFT processing of windowed data*. New London, CT, USA: Naval Underwater Systems Center Report No. 4169. Available.

Orzech, M. D., Reniers, A. J. H. M., Thornton, E. B. & MacMahan, J. H. 2011. Megacusps on rip channel bathymetry: Observations and modeling. *Coastal Engineering*, 58, 890-907.

Reniers, A. J. H. M., MacMahan, J. H., Thornton, E. B. & Stanton, T. P. 2007. Modeling of very low frequency motions during RIPEX. *Journal of Geophysical Research*, 112, C07013.

Schmit, W. B., Woodward, K., Millikan, R., Guza, R. T., Raubenheimer, B. & Elgar, S. 2003. A GPS-tracked surf zone drifter. *Journal of Atmospheric and Ocean Technology*, 20, 1069-1075.

Short, A. D. 1985. Rip-current type, spacing and persistence, Narrabeen Beach, Australia. *Marine Geology*, 65, 47-71.

Thornton, E. B., MacMahan, J. & Sallenger, J. A. H. 2007. Rip currents, mega-cusps, and eroding dunes. *Marine Geology*, 240, 151-167.

Thorpe, A., Miles, J., Masselink, G., Russell, P., Scott, T. & Austin, M. 2012. Field Measurements of Bedforms in a Rip Channel on a Macro-tidal Beach, *International Conference on Coastal Engineering*. Santander, Spain.

Bedform Dynamics in a Rip Current

Antony Thorpe, Jon Miles, Gerd Masselink and Paul Russell

School of Marine Science and Engineering,
University of Plymouth, Plymouth,
PL4 8AA, UK
athorpe1@plymouth.ac.uk
j.r.miles@plymouth.ac.uk
gerd.masselink@plymouth.ac.uk
p.russell@plymouth.ac.uk

www.cerf-jcr.org

www.JCRonline.org

ABSTRACT

Thorpe, A., Miles, J., Masselink, G., Russell, P., 2014. Bedform Dynamics in a Rip Current, *Proceedings 13th International Coastal Symposium* (Durban, South Africa), *Journal of Coastal Research*, Special Issue No. 66, pp. xxx-xxx, ISSN 0749-0208.

A Sand Ripple Profiler (SRP) was deployed in a rip channel on a dissipative sandy beach to measure bedform height (Δ), length (λ) and migration rate (M_r) throughout a macro-tidal cycle.
Data were collected in significant wave heights ranging from 0.5 m to 2.1 m and water depths of between 0.9 m and 7.4 m. Periods when the rip current was active were identified by comparing measured cross-shore velocity (U) with predicted cross-shore velocity from a bed return flow model. Rip flow was found to commence when offshore velocities reached approximately 0.1 m/s, maximum rip velocity as a 5 minute mean was 0.74 m/s.
At lower tidal elevations (h < 2.5 m), in the strong offshore flow of the rip current megaripples were found to migrate offshore (M_r = 0 – 4 cm/min). When migration occurred in a rip current migration rates were correlated with U with the highest migration rates found in the strongest flows.
In non-rip current conditions megaripples exhibited two types of migration behaviour; (*1*) migrating onshore at a maximum rate of 2.1 cm/min when h was in the range of 2.5 m to 5 m and wave skewness was high and (*2*) megaripples were stable when mean flows and skewness were low, this occurred at higher tidal elevations when h > 5m.

ADDITIONAL INDEX WORDS: *Rip Currents, Megaripples, Field Measurements, Bedform Migration*

INTRODUCTION

Rip currents are a unique feature of the nearshore zone exhibiting a channel of strong, quasi-steady, offshore-directed flow (in the order of 0.5 m/s) that dissects the wave dominated surfzone and dissipates beyond the breaker zone (MacMahan *et al*., 2005; Austin *et al*., 2010). Wave breaking is focused on sandbars and minimized in the rip channel; as a consequence of this water travels alongshore in feeder channels before flowing seaward within the rip neck (MacMahan *et al*., 2006). Rip currents are typically found at lower tidal elevations where they are associated with bar/rip morphology (Brander, 1999a).

Bedform dynamics are principally governed by the flow characteristics, and to a lesser extent grain size and the water depth in which they are situated (Allen, 1985). In the combined flows of the surfzone (waves > currents), Gallagher *et al*. (1998) found megaripples (height (Δ) = 0.2 – 0.3 m, length (λ) = 2 – 5 m) present 60 % of the time (in a trough where h = 1.5 – 2 m) during a 6 week field work campaign. The megaripples generally took the form of oval shaped holes and occurred under a wide range of wave conditions (H_s = 0.5 – 4 m). Onshore migration was attributed to wave skewness with typical migration rates of 0.5 cm/min (maximum = 2.5 cm/min). Gallagher *et al*. (2003) proposed that megaripples found in the surfzone were dynamically similar to asymmetric, steady flow features present in rivers and estuaries.

In a tidal shoal of an estuary mouth (currents > waves) Hoekstra *et al*. (2004) found megaripples (Δ = 0.03 – 0.05 m, λ = 0.6 – 1 m) were consistently present and were shown to increase in wavelength with increasing mean flows and migrated in the direction of tidal flow (maximum = 0.5 m/s) at maximum rates of 1.1 to 1.4 cm/min.

Megaripples have also been observed to be present in rip currents (Greenwood and Davidson-Arnott, 1979; Nielsen, 1992; Aagaard *et al*., 1997; Brander, 1999b). Field observations suggest that in rip currents megaripples migrate offshore and are current dominated (Nielsen, 1992). Sherman *et al*. (1993) observed megaripples in a rip feeder channel (V = 0.4 to 0.6 m/s) by visually measuring a pre-selected megaripple with a 'meter long aluminium comb'. They observed lunate bedforms of megaripple dimension (Δ = 0.16 m, λ = 1.6 m) migrating at an average of 1.65 cm/min in the direction of flow.

The aim of this paper is to quantify bedform dynamics, with particular focus on bedform migration, in a rip current and to investigate the processes responsible. This is achieved by comparing bedforms and their behaviour in an active rip current to that in non-rip conditions.

DOI: 10.2112/SI70-118.1 received 20 November 2013; accepted 21 February 2014.

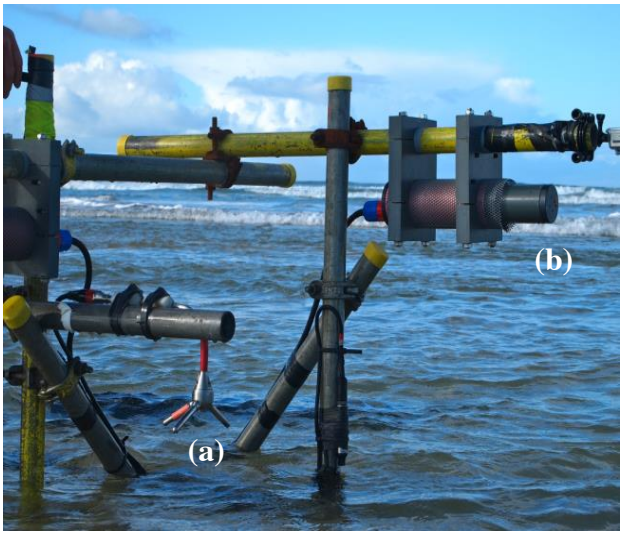

Figure 1. Mobile instrument frame and position of instruments; (a) ADV head and (b) Sand Ripple Profiler (SRP). The picture was taken at low tide in the first field experiment; at mid tide and high tide the rig is completely submerged.

METHODS

Study Site

The data in this study were collected from Perranporth on the North Cornwall Coast, UK during two separate experiments. Perranporth is a highly energetic beach with an annual significant wave height (H_s) of 1.6 m and a peak period (T_p) of 10.5 s (Austin *et al*., 2010). It faces west-northwest, is exposed to Atlantic swell and also receives locally generated wind waves. It is a macro-tidal beach with a mean spring range of 6.3 m and consists of medium sized sand (D_{50} = 0.28 – 0.34 mm). The beach is dissipative with pronounced low tide bar/rip morphology on a seasonal time scale (Austin *et al*., 2010).

During both fieldwork campaigns the beach exhibited a low tide rhythmic bar/rip system throughout its length. The rip used for the study was chosen because it offered a clearly defined channel with offshore flow dissecting the intertidal bar.

Field Measurements

Offshore wave data were collected from a wave buoy located approximately 1 km offshore of the study site. *In-situ* data were collected using a range of instruments secured to a mobile frame (Figure 1). The frame was assembled prior to deployment and carried into the rip channel at spring low tide.

The flow velocities, waves and tidal elevation in the rip channel were recorded with a Nortek Vector 3D-Acoustic Doppler Velocimeter (ADV) fitted with an internal Pressure Transducer (PT). The head of the ADV was carefully aligned to measure cross-shore and longshore flows with the sensing volume set at 0.55 m above the bed. The PT, used to measure wave statistics and tidal elevation was housed in the ADV casing unit with the sensor positioned at a height of 0.2 m above the bed. Data from the ADV, PT and OBS were logged autonomously at 8 Hz during the first experiment and 4 Hz in the second deployment.

A Sand Ripple Profiler (SRP) was used to measure bedform dynamics. The SRP is a pencil beam sonar scanner that collects data as a range (R) and angle (θ) from the scanner. Data processing involved transforming the (R, θ) data to polar co-ordinates (x = cross-shore distance; z = distance below the scanner). The data were post-processed to produce a profile of the bed from which Δ, λ and M_r were deduced. The SRP was aligned to scan in the cross-shore direction positioned 0.9 m above the bed, giving a footprint of approximately 2 m with a horizontal resolution of 14 mm directly below the scanner. In the second experiment a second SRP was deployed, also with a cross-shore orientation, giving a 4.4 m footprint. The data logger was programmed to log autonomously scanning the bed once every minute. Analysis is limited to sections of data where the acoustic scans by the SRP are unaffected by aeration in the water column from breaking waves

Bedform statistics were calculated following Masselink *et al*. (2007). Bedform length was found using the auto-correlation of the scan where the wavelength is twice the spatial lag corresponding to the strongest negative auto-correlation peak. For this method to work, at least half a megaripple wavelength should be captured in the scan. Bedform height was estimated as the root mean square of the bed elevation using, $\sqrt{8}\sigma$, where σ is the standard deviation of the bed level profile (Crawford and Hay, 2001). Migration rate was determined by cross-correlating scans 5 minutes apart, with the strongest positive correlation assumed to represent migration distance. This value was divided by the elapsed time to give migration rate in centimetres per minute.

RESULTS

Environmental Conditions

Data presented here were collected from six full tidal cycles (during the first field experiment) and the flood of a seventh (during a second field experiment), thus giving 13 periods when the rip current was active (accounting for flood and ebb parts of the tidal cycle). Offshore H_s ranged from 0.5 to 1.9 m and peak period was between 10 to15 seconds.

In-situ hydrodynamic parameters were calculated as 5-minute means and synchronised to periods when good SRP data were collected (Figure 2). Water depths ranged from 0.9 m (the depth at which the SRP was deployed) to a maximum of 7.4 m. Wave heights (H_s) were corrected for depth attenuation and ranged from 0.5 m in Tide 1 to 2.1 m in Tide 5. In relatively shallow water, the rip current is active and offshore-directed flows are typically in excess of 0.3 m/s, with a maximum of 0.74 m/s in run number 294. Mean cross-shore flows (U) are close to zero in relatively deep water. Wave skewness is a measure of wave shape, with positively shaped waves having a faster onshore than offshore stroke and therefore having the potential to induce onshore sediment transport or onshore bedform migration (Gallagher *et al*., 1998). Normalised short-wave skewness was calculated as $S = <U^3>/<U^2>^{2/3}$ following Elgar *et al*. (1988) using velocity data high-pass filtered at 0.05 Hz. The mobility number (ψ), calculated following Gallagher *et al*. (2003), includes both the mean and the oscillatory component of the velocity time series where; $\psi = (u^2 + v^2)/(s-1)gD$, and s is the specific gravity (a ratio of sediment to water density, 2.65 for quartz sand), g is acceleration due to gravity and D is grain diameter. Wave skewness and mobility number exhibit a similar trend with the highest values found at lower tidal elevations and in larger waves.

To define when the rip current was active, a simple model by Masselink and Black (1995) was used to predict cross-shore velocities (as a result of bed return flow) and compared to measured cross-shore velocities (Figure 3). To consistently isolate the rip from non-rip conditions it was deemed that four

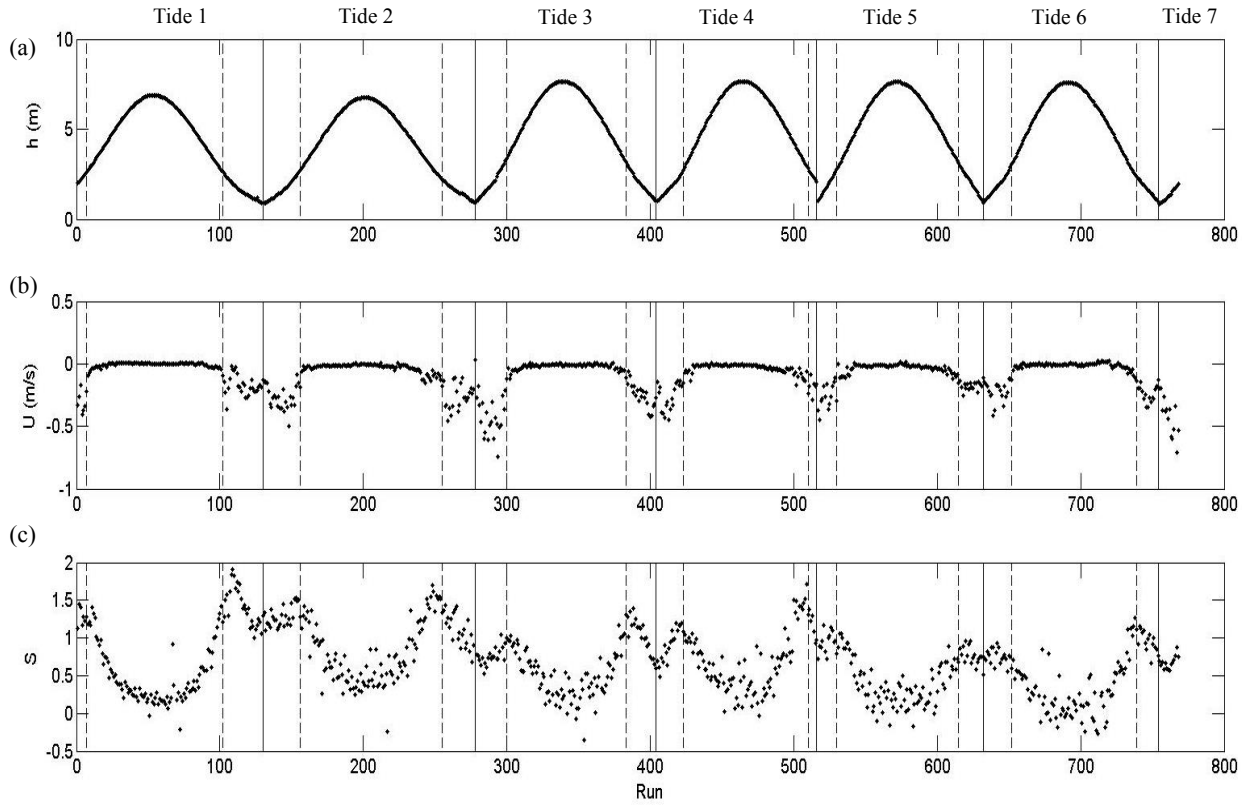

Figure 2. Hydrodynamic parameters calculated form 5 minute bursts. (a) Water depth (h), (b) mean cross-shore velocity (U) and (c) wave skewness (S). The solid lines represent the boundaries between individual tides; the dashed lines mark the rip boundaries.

consecutive observations of measured U exceeding predicted U were rip current conditions, and similarly four consecutive observations where predicted U exceeded measured U (after a period of rip conditions) was a return to non-rip conditions.

Periods of rip current conditions are marked with a vertical dashed line in the time series plots of hydrodynamic conditions in Figure 2.

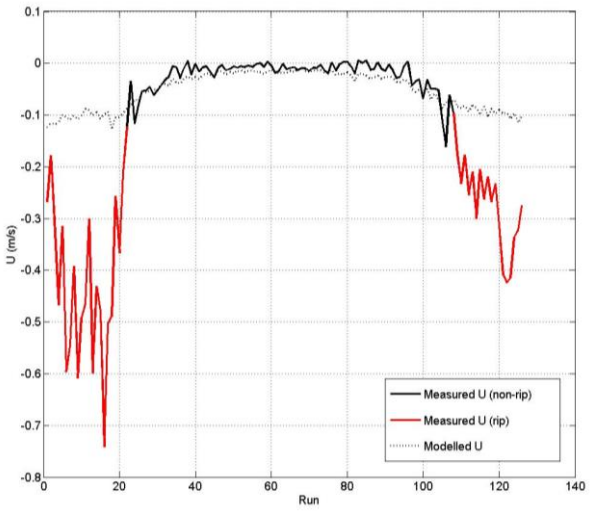

Figure 3. Rip identification. Measured U against modelled U with rip and non-rip conditions marked (-ve is offshore).

Bedform Dimensions

During the study bedforms of megaripple scale were found to be present in the rip channel throughout the tidal cycle (Figure 4). Bedform length and height in non-rip conditions were found to be stable with minimal change during each tide and consistent values between each tide, with λ ranging from 0.92 to 1.35 m and Δ from 0.04 to 0.09 m (though in Tide 5, megaripple height is as high as 0.15 m).

During rip current conditions measurements of λ was found to be quite variable, though the observed trend is an increase in λ compared to non-rip conditions, with λ often of the order of 2 m, and in some cases in excess of 3 m. Bedform Δ in the rip current was of similar scale as in non-rip conditions, with heights ranging from 0.04 to 0.20 m.

Bedform Migration

Megaripple migration direction and speed varied over the tidal cycle, but the variation was consistent between tides. This is shown in Figure 5*a*, which was produced by collapsing 5 tides of data (from Tides 3 to 7, all of which were of similar tidal range, allowing each data run to be averaged) onto one plot.

Typically in rip current conditions, megaripple migration was offshore at rates ranging from 0 to 4 cm/min, with the majority of offshore migration occurring at h = < 2.5 m. Figure 6 shows an example of 60 minutes of bed data collected from within the rip current, with h increasing from 0.8 to 1.7 m and U peaking at 0.6

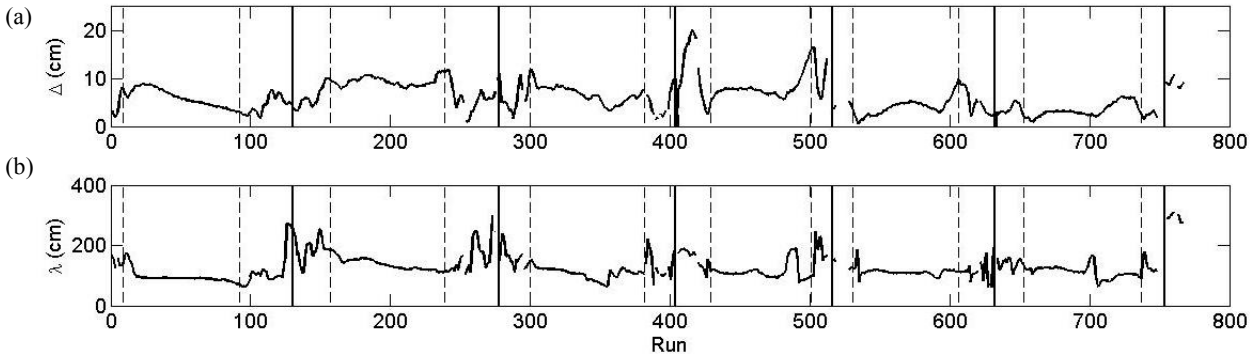

Figure 4. Time series of (a) bedform height (Δ) and (b) length (λ). The solid lines represent the boundaries between individual tides; the dashed lines mark the rip boundaries.

m/s. The average λ and Δ were 2.9 m and 0.1 m, respectively (far exceeding the typical measurements made in the non-rip conditions, where λ = 0.92 to 1.35 m and Δ = 0.04 to 0.09 m) and average migration rate for the period was 0.75 cm/min with a 5 minute maximum of 2.1 cm/min.

In non-rip conditions megaripples showed two different forms of migration behaviour. As tidal elevation increased (h = 2.5 to 5 m) and mean flows became weaker as the rip became inactive the

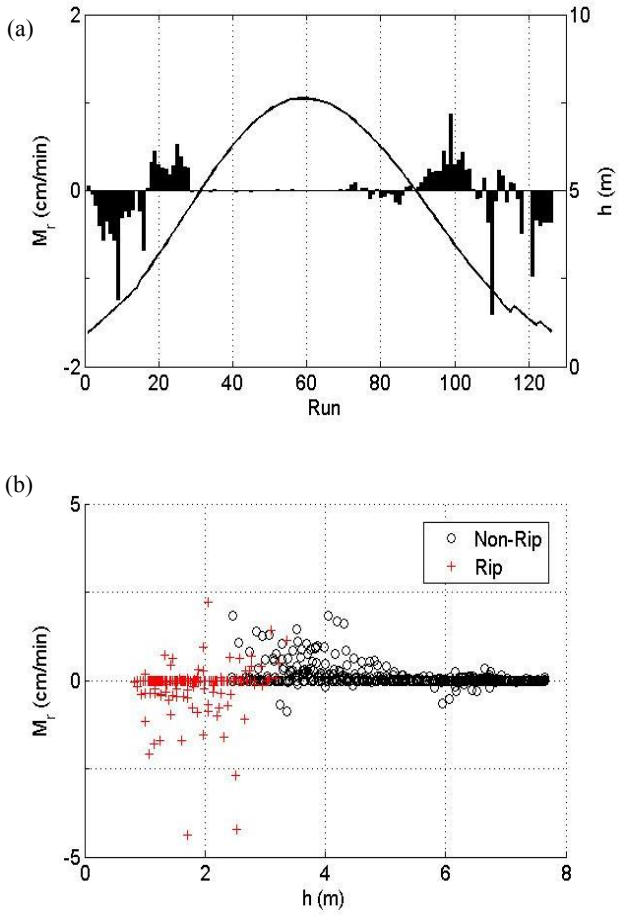

Figure 5. (a) Migration rate and direction (-ve is offshore) alongside water depth. Data from Tides 3 to 7 collapsed onto one plot. (b) Migration rate and direction as a function of water depth.

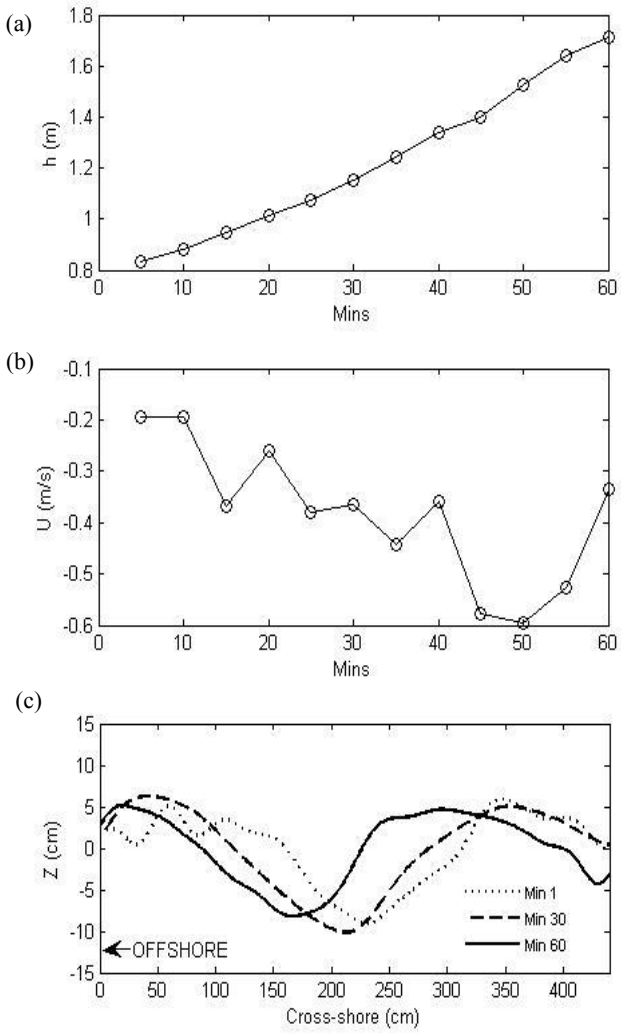

Figure 6. (a) Water depth (h), (b) cross-shore velocity (U) and (c) individual SRP bed scans (every 30 minutes) showing offshore megaripple migration.

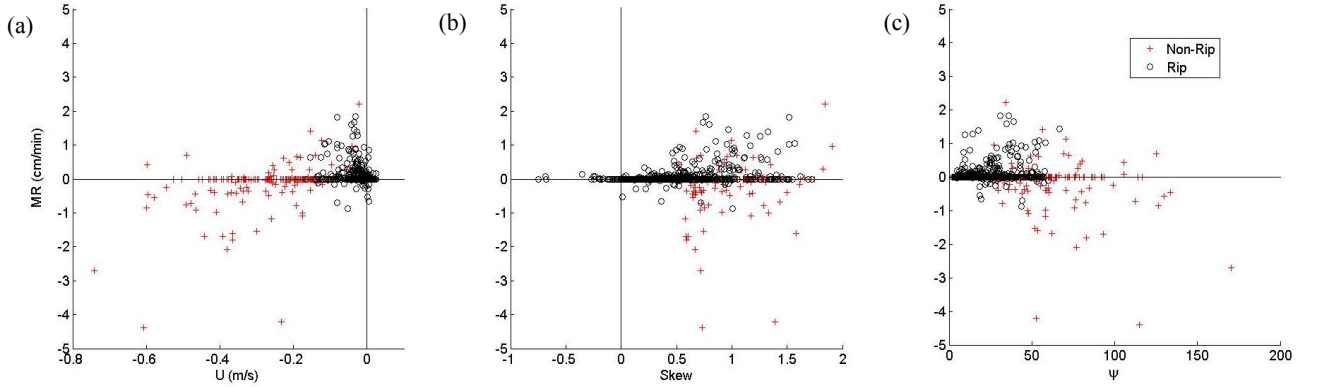

Figure 7. Hydrodynamic forcing on megaripple migration; (a) Wave skewness, (b) cross-shore velocity and (c) mobility number.

direction of migration switched to onshore at similar speeds as the offshore migration (M_r = 0 to 2.1 cm/min). As the tidal elevation increased further (h > 5m), the megaripples remained stable until the process was reversed on the flooding tide. The importance of water depth with regard to migration behaviour is shown in Figures 5*a* and 5*b*. The partitioning of data into rip and non-rip conditions (Figure 5*b*) describes offshore migration in rip conditions well.

The hydrodynamic variables responsible for the different megaripple migration behaviours are investigated in Figure 6. The rip flow shows a reasonable relationship with megaripple migration. The fastest offshore migration is found in the strongest offshore flows, with little offshore migration occurring when U = < 0.2 m/s and all onshore migration taking place in weaker flows of < 0.3 m/s. At wave skewness values of below 0.5 there is no migration in any direction, whilst beyond this onshore migration rate shows an increase with increasing skewness for non-rip conditions. In rip conditions migration shows no relationship with wave skewness and there are periods of reasonably high skewness values (1.2 to 1.6) and moderate flow (0.2 – 0.4 m/s) when offshore migration occurs (Figure 6*b*). The fastest offshore migration rates are found at mobility numbers of above 50. The majority of onshore migration was found to occur at lower mobility numbers.

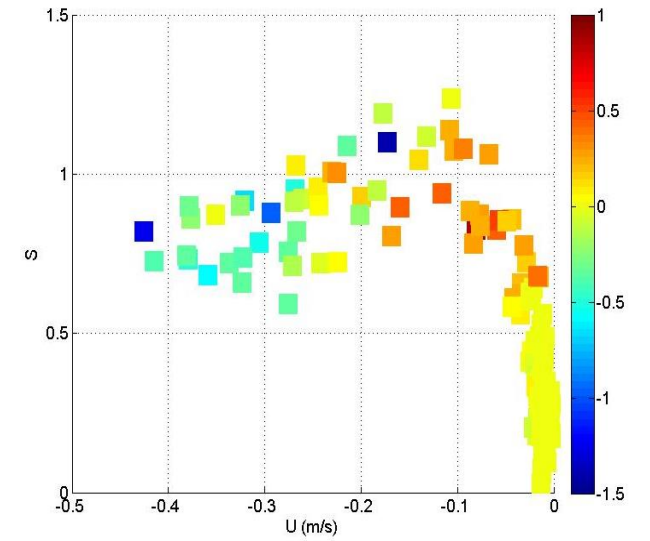

Figure 8. Migration rate (cm/min) and direction (represented by the colour bar; 'cool' colours indicating offshore migration) as a function of cross-shore velocity and wave skewness. Data from Tides 3 to 7.

The combined forcing of megaripple migration by mean offshore flows and wave skewness is investigated in Figure 8. Following figure 5*a*, the same method has been applied for U and S. There are three well defined parameter spaces within the figure with low S and weak U resulting in a stable bed. Weak U and high S result in onshore migration and strong offshore directed U and low S resulting in offshore migration.

DISCUSSION

Bedforms of megaripple scale were found to be consistently present in rip currents in the data collected, confirming field observations by Greenwood and Davidson-Arnott, (1979), Aagaard *et al*. (1997) and Brander (1999b). The megaripples in the rip were, at times, over twice the length of the bedforms in non-rip conditions, suggesting an increase in wavelength was the result of conditions becoming increasingly current dominated, agreeing with observations made by Hoekstra *et al*. (2004) in a tidal inlet.

The partitioning of the data into rip and non-rip conditions based on a comparison with predicted offshore flows works well as a means of identifying rip flow, with the boundary between rip and non-rip conditions closely matching the change in migration direction. Rip flow ceased at velocities weaker than 0.1 m/s but this value would possibly depend on the hydrodynamic forcing of the rip and the scale of the controlling morphology.

Bedform migration in a rip current was found to undergo three phases over an entire tidal cycle; offshore migration in the strong offshore flows of the rip, onshore migration when skewness was high and mean flows were low and stable around high tide (h > 5 m) when both mean flows and skewness was low.

Though offshore migration did not always occur in a rip the migration rate was positively correlated to the rip velocity, supporting the assertion by Nielsen (1992) that bedforms in a rip current are current dominated. The rates of migration in a rip current recorded in this study (0 to 4 cm/min) compare favourably to measurements made by Sherman *et al*. (1993) in a feeder channel of an average of 1.35 cm/min with similar mean flows.

If the waves are positively skewed the onshore stroke of the wave is stronger than the offshore stroke resulting in net onshore sediment transport. Gallagher *et al*. (2003) proposed this may result in onshore migration of bedforms. In the data presented

here, skewness values are low in deep water, and peak when $h = 2$ to 3 m, coinciding with periods of onshore migration. Migration rates of megaripples in non-rip conditions increase with increasing skewness. Wave skewness and strong offshore-directed mean flows peak at similar times and the clear change in migration direction at $h = \sim 2.5$ m suggests that they compete for control over megaripple migration and there is a fine balance between which is the dominant forcing**.** However, the fact that offshore migration is shown to take place in relatively high skewness values suggests that mean flows can dominate even if skewness is high.

The apparent change in hydrodynamic forcing over the tidal cycle is not possible to describe with a single parameter. The form of mobility number used by Gallagher *et al*.(2003) was chosen as it includes both an oscillatory and mean flow component. It shows a reasonable relationship with offshore migration, though no correlation with onshore migration. This may be because skewness is a measure of wave shape and not oscillatory flow.

CONCLUSION

New measurements within a rip channel have found bedform migration rate and direction to be dependent on the occurrence of offshore directed flows of the rip current, wave skewness and water depth. In an active rip current (U = 0.1 to 0.74 m/s) bedforms were found to migrate offshore at rates of 0 to 4 cm/min, with migration rates showing an approximately linear relationship with rip velocity. In non-rip conditions bedforms were observed to migrate onshore in water of intermediate depths (h = 2.5 to 5 m) and when skewness was high (> 0.5). When h > 5 m and both skewness and mean flows were low the bed was stable.

ACKNOWLEDGEMENTS

This work is part of the first author's PhD. We would like to acknowledge the Natural Environment Research Council (NERC) for their funding of the PhD studentship (ref no: NE/I528550/1).

We would also like to thank the DRIBS (Dynamics of Rip Currents and Implications for Beach Safety) project (grant ref no: NE/H004262/1) for providing technical assistance and use of the infra-structure in place for their fieldwork.

LITERATURE CITED

Aagaard, T., Greenwood, B. & Nielsen, J. 1997. Mean currents and sediment transport in a rip channel. *Marine Geology*, 140, 25-45.

Allen, J. R. L. 1985. *Principles of Physical Sedimentology*. London: George Allen & Unwin Ltd.

Austin, M., Scott, T., Brown, J., Brown, J., MacMahan, J., Masselink, G. & Russell, P. 2010. Temporal observations of rip current circulation on a macro-tidal beach. *Continental Shelf Research*, 30, 1149-1165.

Brander, R. W. 1999a. Field observations on the morphodynamic evolution of a low-energy rip current system. *Marine Geology*, 157, 199-217.

Brander, R. W. 1999b. Sediment Transport in Low Energy Rip Current Systems. *Journal of Coastal Research*, 15, 839-849.

Crawford, A. & Hay, A. 2001. Linear transition ripple migration and wave orbital velcoity skewness: Observations. *Journal of Geophysical Research*, 106, 14133-14128.

Elgar, S., Guza, R. T. & Freilich, M. H. 1988. Eulerian measurements of horizontal accelerations in shoaling gravity waves. *Journal of Geophysical Research: Oceans*, 93, 9261-9269.

Gallagher, E. L., Elgar, S. & Thornton, E. B. 1998. Megaripple migration in a natural surf zone. *Nature*, 394, 165-168.

Gallagher, E. L., Thornton, E. B. & Stanton, T. P. 2003. Sand bed roughness in the nearshore. *Journal of Geophysical Research: Oceans*, 108, 3039.

Greenwood, B. & Davidson-Arnott, R. G. D. 1979. Sedimentation and equilibrium in wave-formed bars: a review and case study. *Canadian Journal of Earth Sciences*, 16, 312-332.

Hoekstra, P., Bell, P., van Santen, P., Roode, N., Levoy, F. & Whitehouse, R. 2004. Bedform migration and bedload transport on an intertidal shoal. *Continental Shelf Research*, 24, 1249-1269.

MacMahan, J. H., Thornton, E. B. & Reniers, A. J. H. M. 2006. Rip current review. *Coastal Engineering*, 53, 191-208.

MacMahan, J. H., Thornton, E. B., Stanton, T. P. & Reniers, A. J. H. M. 2005. RIPEX: Observations of a rip current system. *Marine Geology*, 218, 113-134.

Masselink, G., Austin, M., O'Hare, T. & Russell, P. 2007. Geometry and dynamics of wave ripples on th nearshore of a coarse sandy beach. *Geophysical Research Letters*, 112

Masselink, G. & Black, K. P. 1995. Magnitude and cross-shore distribution of bed return flow measured on natural beaches. *Coastal Engineering*, 25, 165-190.

Nielsen, P. 1992. *Coastal bottom boundary layers and sediment transport*. Advanced series on ocean engineering. London: World Scientific.

Sherman, D. J., Short, A. D. & Takeda, I. 1993. Sediment Mixing-Depth and Bedform Migration in Rip channels. *Journal of Coastal Research*, 15, 39-48.